In situ therapeutic response imaging using a novel fluorescence imaging platform –TRIPODD

By

Nathan P. McMahon
B.S., Illinois Institute of Technology, 2015

A DISSERTATION

Presented to the Department of Biomedical Engineering
of the Oregon Health & Science University School of Medicine
in partial fulfillment of the requirements for the degree
of Doctor of Philosophy in Biomedical Engineering

July 2021

TABLE OF CONTENTS

LIST OF FIGURES

LIST OF TABLES

ACKNOWLEDGEMENTS

I would to thank my mentor, Summer Gibbs, for her tireless support and guidance in my development as a scientist. I would also like to thank all of those who contributed to the work through experimental work or insightful discussion including Jocelyn Jones, Dr. Allison Solanki, Dr. Lei Wang, Dr. Kimberley Samkoe, Dr. Kenneth Tichauer and all of the members of the Gibbs lab. Finally, I would like to thank my family and friends for their love and support throughout this process.

This work was funded by grants from the National Institute of Health/National Cancer Institute (R44CA224994), The Prospect Creek Foundation and Mark Foundation for Cancer Research.

ABSTRACT

Successful cancer treatment continues to elude modern medicine and its arsenal of therapeutic strategies. Therapy resistance is driven by tumor heterogeneity, complex interactions between malignant, microenvironmental and immune cells and signaling pathway cross talk. Advances in molecular characterization technologies such as next generation sequencing have helped unravel this interaction network and identify therapeutic targets. Tyrosine kinase inhibitors (TKI) are a class of molecularly targeted therapeutics seeking to inhibit signaling pathways critical to sustaining proliferative signaling, resisting cell death, and other hallmarks of cancer. While tumors may initially respond to TKI therapy, disease progression is inevitable due to acquired resistance largely involving cellular signaling pathway reprogramming. With the ultimate goal of improved molecularly targeted therapeutic efficacy, we have developed and optimized a fluorescence imaging platform termed **TRIPODD** (**T**herapeutic **R**esponse **I**maging through **P**roteomic and **O**ptical **D**rug **D**istribution), resulting in the only methodology capable of simultaneous quantification of single-cell drug target availability and protein expression with preserved spatial context within a tumor. TRIPODD combines intracellular paired agent imaging (iPAI) to quantify drug target interactions and oligonucleotide conjugated antibody (Ab-oligo) cyclic immunofluorescence (cyCIF) imaging to characterize perturbed signaling pathways in response to therapy. Importantly, iPAI and cyCIF data is collected on the same tissue sections facilitating spatial registration of the two datasets. iPAI employs spectrally distinct, fluorescently labeled targeted and untargeted drug derivatives, which correct for untargeted uptake and facilitate quantitative *in situ* assessment of drug target engagement. Ab-oligo cyCIF exploits *in situ* hybridization of complementary oligonucleotides for biomarker labeling, while oligo modifications facilitate signal removal for sequential rounds of fluorescent tagging. Ab-oligo cyCIF is capable of generating multi-parametric images to quantify protein expression, phosphorylation and spatial distribution. To date, we have quantified and evaluated our iPAI toolbox using a suite of functional assays, where initial *in vitro* screening confirmed biological functionality. Subsequent *in vivo* validation studies successfully performed ratiometric iPAI quantification after systemic iPAI probe administration, followed by sequential cyCIF imaging on the same xenograft tissue sections for single-cell quantification of drug target availability, EGFR pathway signaling and cell viability. TRIPODD will enable an improved mechanistic understanding of clinically-relevant treatment regimens through spatially resolved single-cell quantification of drug concentration and proteomic response to identify mechanisms of resistant subclonal population outgrowths driving therapeutic resistance.

Chapter 1

The promise and challenges of targeted, small-molecule cancer therapeutics

INTRODUCTION

Deregulation of kinase function in cell signaling pathways is implicated in numerous cancers.[2] In response, highly specific tyrosine kinase inhibitors (TKIs) have been developed for personalized therapy.[3] Though nearly 50 TKIs have been FDA-approved,[4] TKI monotherapy is seldom curative, often owing to intratumoral subclonal cell population heterogeneity and poor drug target engagement that can both be drivers of acquired resistance. For example, it is now understood that binary designations of a tumor as positive or negative for a biomarker is insufficient for interpreting the intricacies of tumor heterogeneity.[5-7] One example of this phenomena is in epidermal growth factor mutated (EGFRmut+) non-small cell lung cancer (NSCLC) where patients that receive multiple biopsies after acquiring resistance can display multiple resistance mechanisms (e.g., cell signaling pathway reprograming, change in EGFR mutation type) demonstrating intratumoral heterogeneity and variation in population size of resistant clones.[8-10] Further, poor drug target engagement can lead to an observed lack of therapeutic efficacy. Retrospective studies of phase II clinical trials have revealed that nearly 20% of trial failures attributed to poor drug efficacy failed to demonstrate adequate drug target engagement.[11-13] In addition, treatment of sensitive tumor cells may coincide with deleterious outgrowth of resistant stem cell-like persister cells.[14-16] To combat these therapeutic challenges in the complex tumor microenvironment, fully realized personalized therapy must be tailored to resistance mechanisms and include curated drug selection for mono- and combination therapy designed to efficiently and effectively engage with their targets to exploit cellular vulnerabilities.[17, 18] To be successful, a therapeutic must engage with its drug target in the dynamic and complex disease setting, where subsequent efficacy is dictated by the duration, completeness and homogeneity of drug target availability (DTA).[13, 19] Despite its integral role, *in situ* DTA quantification is not routine when evaluating a therapeutic's efficacy. Standard pharmacokinetic or biochemical drug screening tools are typically bulk in nature (e.g., plasma analysis, western blot [WB]) and not representative of cell-to-cell variability in drug distribution, target binding and off-target effects.[20-22] Additionally, proteomics has emerged as a powerful tool in cancer therapy prediction and evaluation, where the significance of protein expression, function, protein-protein interactions, and spatial organization of key tumor biomarkers has been directly validated. Despite these advances, significant challenges still exist to translate our knowledge of cancer proteomics into personalized medicine, including: identification of druggable targets, interpreting the role of drug target availability in assessing proteomic therapeutic response and designing durable therapeutic regimens.[23-26] Importantly, no established technology exists to quantify TKI target availability, concomitant with single-cell protein expression and response heterogeneity, a critically unmet analytical need.[13, 19]

INTRACELLULAR PAIRED AGENT IMAGING (iPAI)

Tumor microenvironments (TME) are complex and highly dynamic with dysfunctional vasculature, hypoxic regions, dense extracellular matrix, immune infiltrate, epithelial to

mesenchymal transition [EMT], cancer stem cells [CSC], etc. Drug delivery characterization in the multifaceted TME is a crucial missing component in most drug efficacy studies as it requires *in situ* spatial interpretation that exceeds current analytical capabilities.[27] Furthermore, therapeutic efficacy can be correlated to the spatial organization of tumor, immune, and stromal cells. As such, significant efforts are underway to interpret therapeutic response within these dynamic environments.[28-32] Numerous labeled small molecule drugs have been generated (e.g., fluorescent, biotin, photoclickable labels) to facilitate direct visualization of tissue distribution and target engagement.[20, 33-36] Conversely, druggable protein targets have also been genetically modified to enable direct visualization.[19, 37] While useful, modifications can vastly alter drug distribution or target engagement. To overcome this difficulty, various label-free methods have been developed, including mass spectrometry imaging (MSI), cellular thermal shift assay (CETSA) and positron emission tomography (PET).[38-43] However, quantification of available drug targets necessitates accounting for both on-target drug binding and non-specific accumulation in the cells and tissues due to drug affinity, biodistribution, pharmacokinetics and metabolism.[28, 44, 45] To facilitate quantification of specific and non-specific targeted drug accumulation in tissue, we have adapted a technique from autoradiography termed Paired Agent Imaging (PAI). PAI was created for quantitative *in vivo* imaging, where non-specific accumulation of protein-based, radiolabeled affinity reagents dominated malignant tissue signals, but could be corrected for by normalizing the targeted signal to the signal of a co-administered, control antibody labeled with an isotope of different energy.[46] This technique has been reinvigorated by our lab and others, where spectrally-distinct targeted and untargeted imaging agents are used to correct for non-specific uptake to quantify drug target availability (DTA; also called "binding potential").[47-63] Notably, DTA is a relative measure of number proteins available for treatment, rather than a measure of protein concentration performed by immunostaining or western blotting. We have expanded the PAI technique to be capable of measuring intracellular targets with the use of spectrally-distinct, fluorescently-labeled drug derivatives, such as TKIs (**Fig. 1.1**). DTA is calculated by collecting images of targeted and untargeted agents in order to perform ratiometric imaging between the two fluorescent signals. The ratiometric imaging performed in iPAI satisfies the requirement of accounting for both the drug that binds to its target as well as the drug that accumulates in the cells and tissues in a non-specific or untargeted manner when calculating DTA. The goal of a targeted therapeutic is to achieve on-target binding, but in the complex tumor setting there is always some degree of untargeted accumulation which can vary on a cell-by-cell basis in heterogeneous diseases such as NSCLC. Notably, although our technique relies on fluorescently-labeled drugs for quantification, all treatment is completed with the parent drug and is thus classified as a label-free method with quantitative assessment of the interaction of the parent drug with its native target. Quantification of DTA will facilitate analyses of intra- and inter-tumoral heterogeneity of available

drug targets as well as provide a mechanistic understanding of therapeutic response in developing innovative treatment strategies.

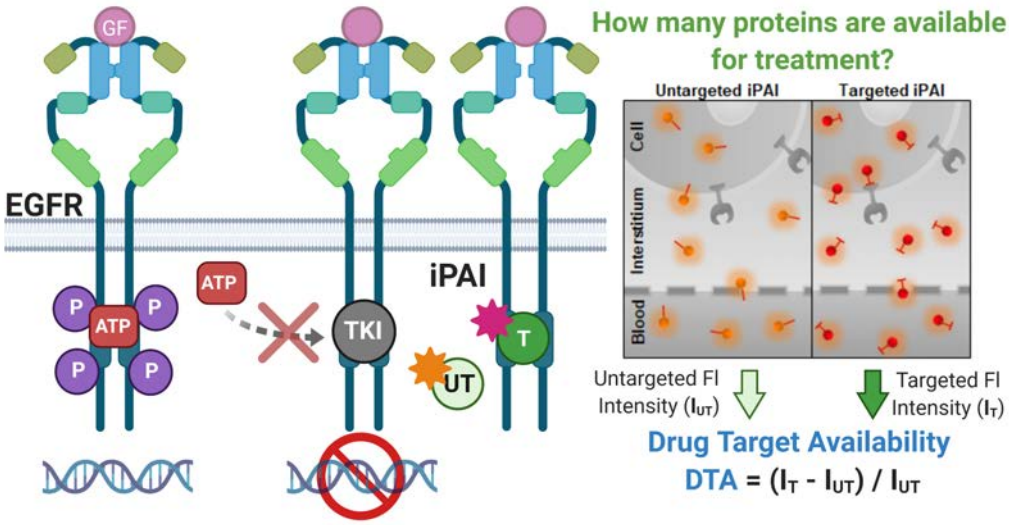

Fig 1.1: *iPAI quantification of DTA.* Drug target availability (DTA) is related to the number of proteins available for a particular concentration of drug to bind. DTA does not necessarily equal total protein concentration, which is typically measured with immunostaining or western blot. DTA is calculated by subtracting the intensity of the untargeted image from the targeted image and dividing by the intensity of the untargeted image, accounting for off-target drug accumulation.

HIGHLY MULTIPLEXED SPATIAL PROTEOMICS

While histological and genomic differences between tumors guide cancer diagnosis and treatment selection, it has become clear that spatially distinct clonal evolution and TME properties drive inter- and intra-patient heterogeneity, hindering therapeutic efficacy.[64-66] In response, highly-multiplexed immunostaining techniques have evolved as a popular means for quantitative spatial proteomics using two main methods: (1) conventional antibody staining (i.e., immunofluorescence [IF] or immunohistochemistry [IHC]) in a cyclic fashion[67, 68] or (2) mass spectroscopy imaging (MSI) using rare earth metal labeled antibodies.[30, 69-79] The IF and IHC strategies have seen widespread adoption due to their detection using conventional microscopy.[67, 68] In order to generate high-dimensional IF or IHC images, cycles of staining, imaging and signal removal (e.g., antibody stripping[86, 92, 93] or fluorophore bleaching[69, 73, 76]) are required. While effective, these protocols generally require weeks to complete and can be destructive to samples.[88] MSI (i.e., mass cytometry by time-of-flight [CyTOF],[72] multiplexed ion beam imaging [MIBI],[30, 71] etc.) does not require cycling resulting in reduced highly multiplexed dataset generation times. However, MSI resolution is restricted by laser spot size, limiting single-cell detection, and presents difficulties for detecting low abundance antigens (e.g., phosphoproteins).[68] In response, hybrid techniques use unique antibody tags, such as DNA barcodes,[80] analogous to the rare earth metal tagged antibodies. This permits one staining step with a "master mix" of antibodies. Antibody barcoding techniques (e.g., Nanostring Digital Spatial Profiler [DSP],[80, 81] Akoya co-detection by indexing [CODEX],[67]

DNA Exchange Imaging [DEI],[82] and Immuno-SABER[83]) have demonstrated the ability for highly multiplexed immunostaining using non-destructive signal removal techniques. We have optimized a oligonucleotide conjugated antibody (Ab-oligo) cyclic IF (cyCIF) technique, where a complementary, fluorescently labeled oligonucleotide sequence is used for detection (**Fig. 1.2**).[84]

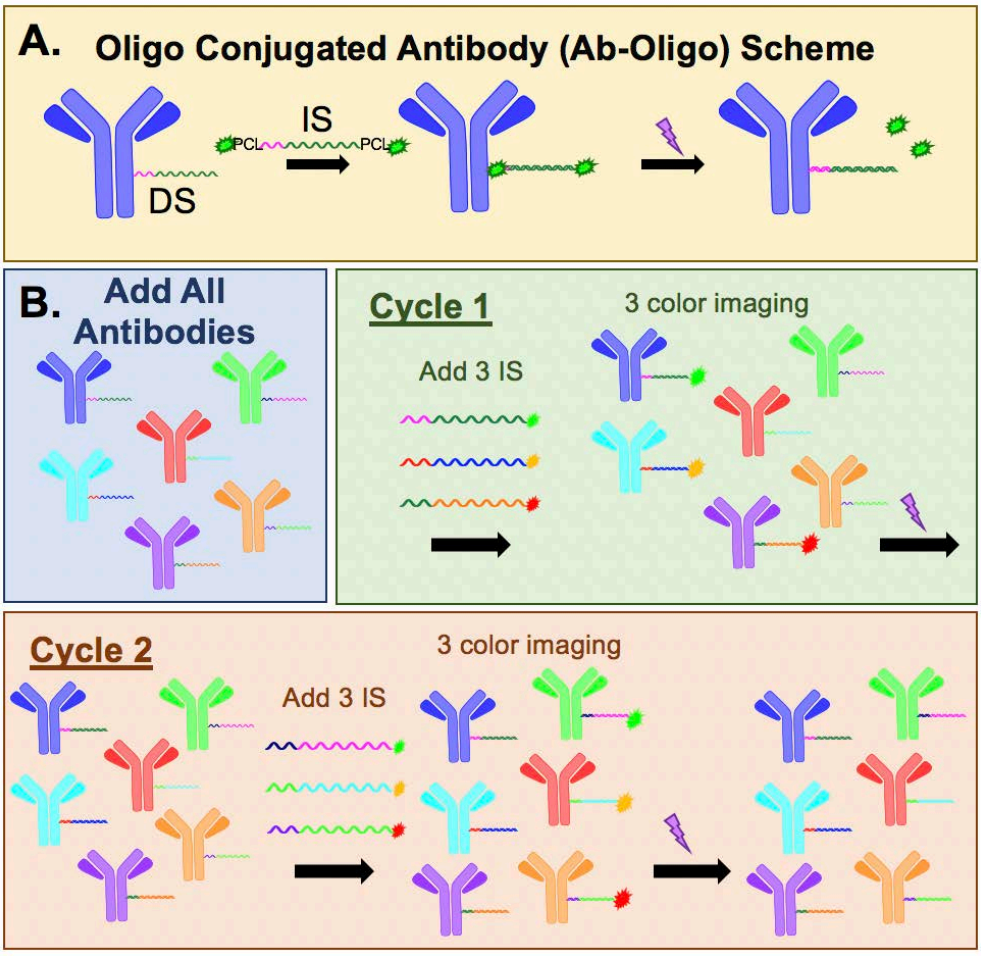

Fig. 1.2: *Ab-oligo Scheme.* **A.** Primary antibodies are conjugated to single stranded oligos (DS = docking stand) termed Ab-oligo. After Ab-oligo sample labeling, the complementary oligo (IS = imaging strand) conjugated to two fluorophores through photocleavable linkers (PCL) is used for *in situ* labeling via DS/IS hybridization. After imaging, UV light is applied to cleave the PCLs so that fluorophores can be washed from the sample. **B.** An illustrative example of a three color, two cycle Ab-oligo staining experiment, where each Ab-oligo has a unique DS. The complementary IS are labeled with spectrally distinct fluorophores. The sample is stained with a mixed cocktail of the six Ab-oligos. In cycle one, three Ab-oligos are labeled with their complementary IS. Three color imaging is completed, then the signal is removed with UV light. This is followed by a second cycle with complementary IS using the same three fluorophores that hybridize to the other three Ab-oligos for imaging followed by UV light induced signal removal.

Specifically, a master mix solution of all Ab-oligo conjugates, each labeled with a unique docking strand (DS) oligo sequence are incubated on a tissue section in a single step. Then cyclic rounds of imaging are performed through the addition of sets of fluorophore-labeled, imaging strand (IS) oligos each complementary to a specific Ab-oligo conjugate. Then to remove fluorescence signal between rounds, the stained tissue is exposed to ultraviolet (UV) light that cleaves the fluorophores

from the IS due to the presence of a photocleavable linkers (PCL) adjacent to the fluorophores. Our Ab-oligo cyCIF platform is capable of quantifying tumor plasticity/stemness, cell signaling pathway and phenotypic changes on a single-cell basis while retaining spatial organization in the dynamic TME, which is critical to understanding therapeutic response and resistance heterogeneity.

TRIPODD: A NOVEL FLUORESCENCE IMAGING PLATFORM

TRIPODD (**T**herapeutic **R**esponse **I**maging through **P**roteomics and **O**ptical **D**rug **D**istribution and binding) facilitates characterization of DTA and proteomic therapeutic response, leveraged by our iPAI and cyCIF imaging technologies (**Fig. 1.3**). The result is the only fluorescence imaging platform to simultaneously quantify the complex interactions of drug distribution (iPAI) and proteomics (cyCIF) at the single-cell level on a single tissue section and correlate these relationships to efficacy by spatially registering the iPAI and cyCIF data, an unmet analytical need. In the targeted therapy era, genetic screening motivates therapeutic recommendations; however, it is now evident that gene profiling doesn't guarantee initial, or lasting, treatment success. Further, standard proteomic, pharmacokinetic or biochemical drug screening tools are typically bulk in nature (e.g., plasma analysis, WB) inherently limited metrics for a mechanistic understanding of therapeutic response by heterogeneous tumors in the context

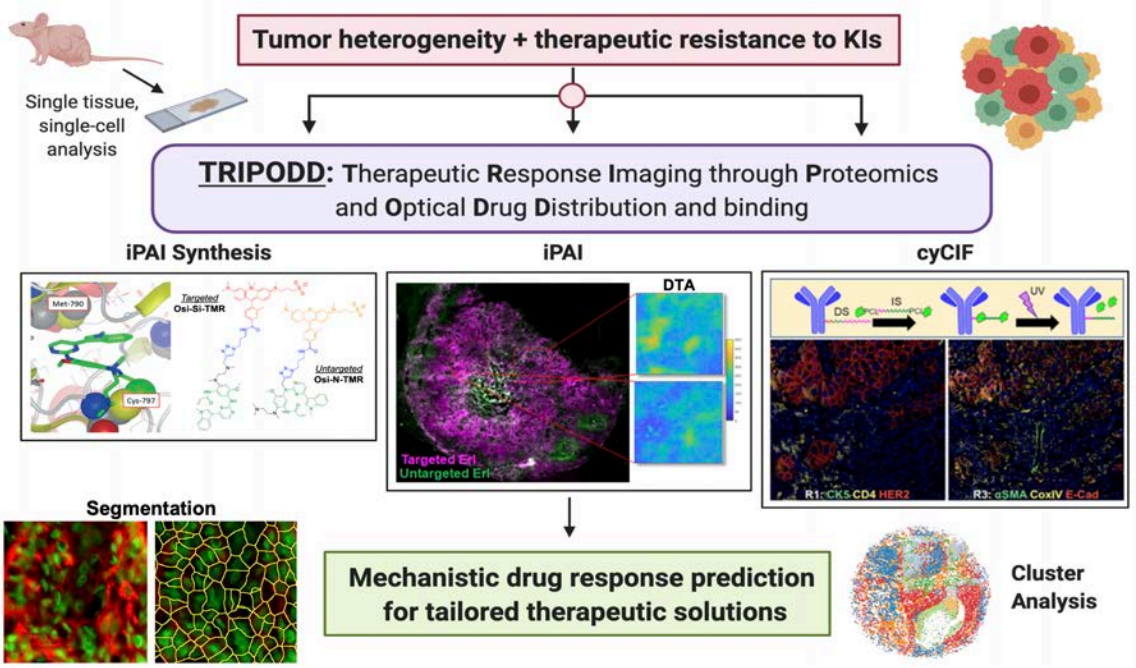

Fig. 1.3: *TRIPODD.* The novel fluorescence image toolbox capable of interpreting tumor heterogeneity through therapeutic response imaging. TRIPODD therapeutic response imaging is enabled using the combination of iPAI and Ab-oligo cyCIF imaging technologies on a single tissue section to measure *in situ* DTA and spatially intact proteomic signatures, respectively. Spatial registration of the two image datasets facilitates single-cell resolution quantification with spatial context preserved in order to perform high dimensional analysis to identify unique signatures of therapeutic response.

of their complex microenvironments. Specifically, in the case of NSCLC clinical trials, the majority of phase III clinical trials fail to meet their primary endpoints where a lack of drug efficacy is a major contributor to therapeutic failure.[85, 86] Further exacerbating the issue is the lack of correlation of preclinical therapeutic efficacy to clinical success.[87] This demonstrates the need for improved preclinical technologies in assessing novel therapeutic strategies that will enable correlation between drug accumulation and therapeutic success. TRIPODD bridges the analytical gap between drug distribution and proteomic therapeutic response assessment as the first technology capable of *in situ* single-cell resolution therapeutic response imaging for a mechanistic understanding of treatment response.

ADVANCED CANCERS LACK CURATIVE THERAPEUTIC REGIMENS

One example of a cancer lacking curative therapy where TRIPODD could be applied to develop novel treatment strategies is lung cancer. Lung cancer is an aggressive disease and the leading cause of cancer death worldwide, with ~1.8 million fatalities in 2018.[88] The combination of asymptomatic presentation and insufficient screening methods accounts for the near uniformly late stage-diagnoses, leaving most lung cancer patients with few curative options. While smoking is the number one predictor of disease occurrence, 15% of all lung cancer patients have never smoked,[89] where non-small cell lung cancer (NSCLC) is the most commonly diagnosed subtype in this population. The discovery of NSCLC dependence on EGFR signaling (i.e., EGFRmut+) and the development of targeted EGFR TKIs has revolutionized treatment outcomes for patients harboring these genetic abnormalities. Phase III trials have consistently shown superior efficacy of first- (i.e., gefitinib or erlotinib) and second-generation (i.e., afatinib) TKIs over standard chemotherapies (i.e., platinum-based) for patients with EGFRmut+ NSCLC, improving progression-free survival (PFS) from 6 to up to 15 months.[90-94] However, tumor evolution and subsequent disease progression are still inevitable, most commonly the result of a T790M mutation in EGFR exon 20, which sterically hinders binding of both first- and second-generation EGFR TKIs.[17] A third-generation EGFR TKI, osimertinib, overcame this resistance mechanism, binding to a different domain on EGFR resulting in superior efficacy and lower toxicity, and garnered FDA approval in 2018 as a first-line treatment option regardless of T790M mutation status.[95, 96] As with the vast majority of targeted therapies, enthusiasm for initial robust response rates was tempered by inexorable disease progression. Three distinct adaptive resistance mechanisms limit the duration of NSCLC response to osimertinib treatment: (1) cell signaling pathway reprogramming (e.g., *MET* or *HER2 a*mplifications, **Fig. 1.4**), (2) additional EGFR mutations (e.g., C797S) and (3) phenotypic changes (e.g., transition from NSCLC to small cell lung cancer).[97] Further, the heterogeneous nature of EGFRmut+ NSCLC makes it particularly vulnerable to the emergence of resistant subpopulations that are difficult to treat with second-line therapies.[16] Overexpression of the downstream protein, MEK, through the MAPK pathway serves as a representative example of acquired resistance to osimertinib in NSCLC (**Fig. 1.4.**). A tumor evading treatment through this mechanism is utilizing cell signaling pathway reprogramming to avoid cell death. Additionally, the treatment of only osimertinib sensitive cells through osimertinib monotherapy applies selective

pressures that has the potential to promote the outgrowth of intrinsically osimertinib resistant cell subpopulations. Activation of MEK through the MAPK pathway is mediated through MET amplification, where clinical trials studying the efficacy of combining osimertinib with the MEK TKI, selumetinib, are ongoing (e.g., NCT03392246, NCT02143466, NCT02143466). However, mechanistic understanding of how drug target availability influences proteomic therapeutic response is not fully understood. Notably, while the listed osimertinib resistance mechanisms are the most recognized, they do not represent the full spectrum of resistance put forth by the TME, which is diverse and not yet fully characterized.[98] This diversity is further reinforced by the 10-

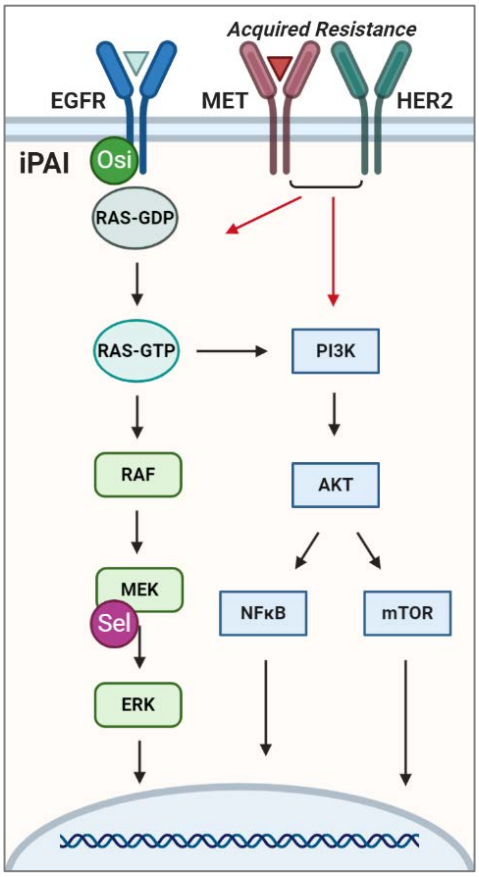

Fig. 1.4: *NSCLC TKI collateral sensitivity.* Cell signaling reprogramming can result in EGFR bypass and loss of osimertinib (Osi) efficacy. A common mechanism of cell signaling reprogramming is MET amplification, which can reactivate the MEK pathway. MEK activation can be targeted using selumetinib (Sel). Red arrows indicate route of cell signaling reprogramming to bypass EGFR and activate MEK.

20% of EGFRmut+ patients that do not respond to first-line EGFR therapy, where intrinsic resistance mechanisms are not understood.[99] Similar therapeutic issues plague other cancers where a lack of durable response limits patient survival. Other cancers lacking curative treatments include breast and colon cancer where recent studies have uncovered the significance of spatial organization of the tumors, but lack correlation of spatial proteomics to drug distribution.[32, 100] It has been proposed that contributing factors to therapeutic failure in advanced cancer patients include insufficient drug target engagement and off-target activity, however, effective tools to quantify and validate intracellular drug delivery and engagement are lacking.[11, 38]

THESIS OUTLINE

This thesis describes the work undertaken to develop TRIPODD, a novel fluorescence imaging platform, capable of *in situ* quantification of drug target availability and proteomic therapeutic response. The work presented herein represents significant progress in the development and application of TRIPODD in elucidating mechanistic understanding of therapeutic response. TRIPODD as a platform combines two complementary technologies, Ab-oligo cyCIF and iPAI. **Chapter 2** describes the variety of methods evaluated for conjugating oligonucleotides to antibodies as well as the fluorescence signal removal techniques tested in the development of Ab-oligo cyCIF. In **Chapter 3**, the fully validated and optimized Ab-oligo cyCIF methodology is outlined and highly multiplexed characterization of multiple breast cancer subtypes presented. **Chapter 4** reports on a procedure for amplifying the fluorescence signal produced by Ab-oligo cyCIF in order to increase the sensitivity of the technology to low abundance antigens. In **Chapter 5,** the TRIPODD platform is validated where first methods of *ex vivo* analysis of tissues after systemic iPAI probe administration are established. Then the process for combining of iPAI and Ab-oligo cyCIF analysis on the same tissue section is described as well as validation of the capability of TRIPODD to produce single-cell resolution drug target availability and protein expression data. **Chapter 6** describes the application of the TRIPODD platform in the analysis of treated tissues to perform therapeutic response imaging for a mechanistic understanding of erlotinib therapeutic effect kinetics. **Chapter 7** provides a summary of the results presented herein and gives perspectives into future work.

Chapter 2

Optimization of oligonucleotide conjugation of antibodies and signal removal methodology

ABSTRACT

Significance: A number of highly multiplexed immunostaining and imaging methods have advanced spatial proteomic characterization of cancer for improved therapeutic strategy design. Two popular methods employ antibodies directly labeled with either fluorophores or unique rare earth metal tags. While widely used, these methods are limited by harmful signal removal techniques, difficult reagent production and sensitivity. Growing in popularity is highly multiplexed imaging employing oligonucleotide (oligos)-barcoded antibodies. However, challenges remain in consistent conjugation of oligos to antibodies with maintained antigenicity as well as non-destructive, robust and cost-effective signal removal methods.

Aim: We tested a variety of oligo conjugation and signal removal methods in the development of our oligo conjugated antibody cyclic immunofluorescence (Ab-oligo cyCIF) methodology to identify the optimal conjugation and signal removal strategies.

Approach: We employed both non-specific and site-specific conjugation strategies to label antibodies with unique oligo sequences, termed the docking sequence (DS). DS were hybridized *in situ* with their complementary imaging strand (IS) oligo sequence tagged with a conventional fluorophore. Fluorescence signal removal methods tested involved either a modification to the IS sequence or exploitation of intrinsic properties of oligo hybridization to remove IS. Signal removal strategies were optimized and validated to be incorporated into our Ab-oligo cyCIF strategy.

Results: We identified an optimal site-specific conjugation method to generate Ab-oligo reagents with minimal perturbation of binding affinity or staining pattern. We also found incorporation of photocleavable linkers (PCL) into the IS design permitting signal removal with ultraviolet (UV) light treatment cleaved the oligo at the PCL site and unbound fluorophore was readily removed from samples.

Conclusion: Herein, we assessed the utility of both non-specific and specific oligo conjugation to antibody methods in the development of Ab-oligo cyCIF where an optimal method was identified. We tested a number of fluorescence signal removal methods where cost, speed and potential damage to the sample over numerous cycles were assessed. This resulted in an optimized Ab-oligo cyCIF platform capable of generating high dimensional images of cancer to characterize the spatial proteomics of the hallmarks of cancer.

INTRODUCTION

The emergence of high throughput technologies has revolutionized our view of cancer from a static disease of malignant cells undergoing unchecked proliferation to a complex disease consisting of multifaceted interactions between tumor and immune cells in the context of the tumor microenvironment (TME).[25, 101-104] While large-scale cancer genome studies have identified novel cancer genes and advanced our understanding of drug response, analogous single-cell proteome analysis has been limited in scope.[105, 106] Importantly, proteins are the basic functional units in biological processes and most targeted drugs act directly on protein function.[107] Further, post-transcriptional modifications, such as phosphorylation status in cancers with known dysregulated signaling pathways, is a crucial variable when unraveling mechanisms of resistance to therapeutics. Additionally, the TME must be characterized to understand the multiple evolving obstacles that hamper effective drug delivery and response, including immune cell infiltrate, dysfunctional vasculature and dense extracellular matrix.[108] In response to this analytical need, a number of highly-multiplexed immunostaining techniques have been developed as a means for quantitative, spatial proteomics to fully elucidate and characterize proximity interactions between cells of all functions that drive tumor evolution.

Two main methods of high dimensional immunostaining employ (1) conventional antibody staining (i.e., immunohistochemistry [IHC] or immunofluorescence [IF]) or (2) mass spectrometry imaging (MSI) using rare earth metal-labeled antibodies.[30, 69-73, 75-79, 109] Cyclic immunostaining produces precise spatial proteome maps by repeated staining, imaging, and signal removal (e.g., fluorophore bleaching[73, 69, 76] or antibody stripping[78, 110, 111]) of a single sample. Since this approach can be readily integrated into the conventional histopathological workflows, it has been widely explored. However, these studies can take weeks to complete due to repeated antibody incubation steps and the number of detectable biomarkers is limited by chemical fluorescence quenching or antibody stripping methods, which can damage tissue integrity and antigenicity.[79] Conversely, in mass spectrometry imaging (e.g., MIBI,[70, 71] CyTOF,[72] etc.) all antibodies are applied in a single step as a "master-mix," where each antibody is labeled with a unique rare earth metal tag allowing detection of unique mass-to-charge ratios. While this eliminates the need for cycles of antibody incubation, imaging and signal removal, spatial resolution is limited by the laser spot size, limiting detection of single cells and low abundant antigens (e.g., phosphoproteins). In response to these challenges, hybrid techniques that use unique antibody tags, such as oligonucleotide "barcodes," analogous to the rare earth metal-tagged antibodies have been developed.[80] This permits one staining step with a DNA-barcoded antibody "master-mix," similar to MSI. Antibody barcoding techniques (e.g., DNA-Exchange Image,[82] Immuno-SABER,[83] Nanostring[80, 81] and CODEX[67]) have demonstrated the ability for highly multiplexed immunostaining using non-destructive signal removal techniques. We have optimized a barcoded antibody cyclic IF (cyCIF) technique where a complementary fluorophore-labeled DNA strand is used for *in situ* detection, facilitating collection of high-dimensional proteomic data.[112] Notably, signal removal of complementary fluorophore-labeled DNA strands can be achieved through a variety of non-destructive methods, making this technique advantageous over fluorophore-labeled antibody-based cyCIF and MSI.

While the advent of sophisticated, highly multiplexed immunostaining techniques is a relatively new field, methodologies to label antibodies with various detection reagents have been used widely for decades. Techniques for antibody labeling can be divided into two main categories: (1) non-specific labeling, which targets abundant molecular moieties that are widely distributed across immunoglobin G (IgG) antibodies and (2) site-specific labeling targeting specific molecular components including native moieties and engineered unnatural amino acids. In general, a frequent challenge to antibody labeling is reduced affinity and specificity vs. the unlabeled antibody, resulting in off-target staining and decreased signal to background ratios. Restricting the labeling site and number of labels can minimize these difficulties. The most widely employed non-specific antibody labeling method is N-Hydroxysuccinimide (NHS) ester reaction chemistry in which amine-reactive, NHS ester-modified molecules (e.g., fluorophores, oligonucleotides) react with the abundant free amine groups present on lysine groups within antibodies.[113] Fluorophore-labeling of antibodies using NHS ester chemistry is common and kit-based options for oligo-labeling of antibodies using this conjugation method are commercially available. Maleimide chemistry is also a routine method for non-specific label conjugation to antibodies through cysteine moiety labeling. While both NHS ester and maleimide labeling strategies can produce stable and functional bioconjugates, their non-specific nature can disrupt the antigen binding site. Click chemistry methods have been developed for site specific antibody labeling, where click chemistry reactions form a covalent bond between an alkyne and an azide group.[114] Copper (Cu)-free click chemistry overcomes the limitations of standard Cu-based click chemistry where copper ions can disrupt the specificity of biofunctional molecules such as antibodies. Cu-free click chemistry labeling kits have been developed enabling site-specific addition of azide groups to the antibodies reducing labeling at the antigen binding site.

Another crucial component to successful cyCIF is selection of a signal removal technique that balances complete signal removal with maintenance of tissue integrity and antigenicity for staining in subsequent rounds. DNA-barcoded antibodies have distinct advantages over other cyclic IF techniques, in that their versatility provides for a variety of signal-removal options, all of which are relatively gentle to tissue integrity and antigenicity. Notably, DNA barcodes can be denatured from their target using, electric charge, pH, heat or denaturants like formamide.[115-117] The length and nucleotide composition of the oligonucleotide sequences additionally allow for annealing factors, such as temperature, to be optimized to better preserve tissue integrity and antigenicity. For example, shorter DNA duplexes, and those with less guanine (G) and cytosine (C) content require lower temperature to denature, and subsequently remove DNA barcodes from their antibody targets.[118-120] Described herein, we review the optimization of Ab-oligo cyCIF to facilitate quantitative proteomics with specific attention focused on antibody labeling methods and signal removal techniques for successful cyCIF studies.

MATERIALS & METHODS

Oligonucleotides, Fluorophores & Antibodies. Oligonucleotides (oligos) used for all studies were purchased from Integrated DNA Technologies (IDT Coralville, IA). Docking strands (DS) were modified on the 5' end for subsequent attachment to primary IgG antibodies. DS contained either a 5' C6-amino or 5' Dibenzocyclooctyne triethylene glycol spacer arm (DBCO-TEG) modification for antibody conjugation using NHS ester or Cu-free click chemistry, respectively. Complementary imaging strands (IS) were labeled with fluorophore on the 5', 3', or both 5' and 3' ends for fluorescence imaging. Fluorophores used for labeling included Alexa Fluor (AF) 488, AF546, AF647 and AF750. In some cases, IS contained modifications specific for the different methods of fluorescence signal removal as described below. In the case of IS containing photocleavable linker (PCL) modifications, the PCL was inserted between the fluorophore and 5', 3', or both 5' and 3' ends. Strand Mediated Displacement (SMD) studies were performed using DS, IS, and Capture Strands (CS) based on previously published studies.[121] With the exception of the SMD studies, DS length was 28 nucleotides (nt), which was selected based on preliminary studies using sequences designed from previous work.[122] IS length varied from 13-28 nt for optimal DS/IS hybridization *in situ*, as well as to evaluate signal removal strategies. Primary HER2 IgG antibody (Herceptin, Genentech, San Francisco, CA), anti-c-ErbB2/c-Neu mouse monoclonal (HER2, OP15, IgG1 antibody, MilliporeSigma, St. Louis, MO), Lamin B1 (rabbit polyclonal [pRb], AbCam, Cambridge, MA), TOMM20 (pRb, AbCam), and E-Cadherin (E-Cad, EP700Y, AbCam), Cytokeratin-19 (CK19, 3E11, Biolegend, Sand Diego, CA) were used for oligo conjugation and staining studies in the reported studies.[112]

Samples for DNA-Barcoded Antibody Validation & Signal Removal Evaluation. SK-BR-3 cells were purchased from ATCC (Old Town Manassas, VA). All human formalin fixed paraffin embedded (FFPE) tissues were obtained from the OHSU Knight Biolibrary as deidentified human tissue blocks. Ab-oligo conjugates were validated in cells and FFPE tissue as previously described.[112] Ab-oligo conjugate optimization studies also were performed in FFPE MCF7 subcutaneous xenografts grown in mice for unrelated studies. Signal removal evaluation studies were performed in SK-Br-3 cells, FFPE cell buttons made from MCF7 or MDA-MB-468 breast cancer cell lines as well as FFPE normal tonsil, normal breast, and HER2 positive (HER2+) breast cancer tissues.

Ab-oligo Staining Protocol. SK-Br-3 cells were seeded onto 96-well glass bottom plates (Cellvis, Mountain View, CA) at 10,000 cells per well and grown to ~70% confluence for ~60 hours (h) at 37 °C and 5% CO_2. Cells were fixed for 15 minutes (min) in 4% paraformaldehyde (PFA, MilliporeSigma) at room temperature (RT). PFA was removed and cells were washed with 1X PBS, pH 7.4 (3 x 5 min) and stored in 1X PBS containing 0.05% sodium azide (NaN_3) at 4 °C. Prior to staining, the cells were washed with PBS (3 x 5 min) to remove NaN_3. In pilot studies, the cells were permeabilized in 0.5% polyoxyethylene(10) octylphenyl ether (Triton X-100, MilliporeSigma) for 15 min at RT followed by washing in PBS (3 x 5 min). This step was omitted following completion of staining optimization studies. The cells were blocked for 30 min at RT in

"blocking buffer" composed of 2% bovine serum albumin (BSA, Bioworld Dublin, OH), 0.5 mg/mL sheared salmon sperm DNA (ThermoFisher), 0.5% dextran sulfate, and 0.05% Tween 20 (MilliporeSigma). Notably, Lamin B1 staining pattern was negatively affected by the presence of Tween 20, so it was omitted during subsequent Lamin B1 staining studies. However, interestingly Triton X-100 could be utilized for permeabilization without affecting Lamin B1 staining patterns. Ab-oligos were diluted to 10-15 µg/mL in blocking buffer and incubated with SK-BR-3 cells overnight at 4 °C. Staining solution was removed and cells were washed in PBS (3 x 5 mins). Cells were post-fixed in 2% PFA for 15 min at RT, followed by washing in 2X saline-sodium citrate (SSC, VWR, Radnor, PA, 3 x 5 min). IS incubation concentration ranged from 6.25-350 nM, diluted in "labeling buffer," which consisted of 2X SSC containing 2% BSA, 0.5 mg/mL sheared salmon sperm DNA and 0.5% dextran sulfate at pH 7. IS was incubated with the cells for 1 h at RT with gentle shaking, protected from light. The staining solution was removed and the cells were washed with PBS or 2X SSC (3 x 5 min). The cells were stained with 300 nM DAPI for 10 min at RT after which they were washed with PBS or 2X SSC (2 x 5 min) prior to imaging. FFPE tissue sections (4-5 µm thickness) were stained as previously described.[112, 123] Stained slides were mounted in Fluoromount G (Southern Biotech, Birmingham, AL) or Prolong Gold Antifade with DAPI (ThermoFisher) prior to cover slipping.

Fluorescence Microscopy, Visualization & Analysis. Stained cells were imaged on a Zeiss AxioObserver microscope with an AxioCam 506 camera. FFPE tissue experiments were imaged on the Zeiss AxioObserver or a Zeiss AxioImager.M2 microscope equipped with an XY motorized scanning stage (Carl Zeiss AG, Oberkochen, Germany) and a 14-bit CCD CoolSNAP HQ2 camera (Photometrics, Tucson, AZ). The following bandpass (BP) filters were used to filter excitation light: 470/40, 545/25, 620/60, ET710/75x for AF488, AF546, AF647 and AF750 imaging, respectively. The following BP filters were used to filter emission light: 525/50 nm, 605/70 nm, 700/75 nm and ET810/90 nm for AF488, AF546, AF647 and AF750 imaging, respectively. To collect DAPI images, excitation light was filtered using a Zeiss 405/40 or 390/40 BP filter. All images were collected at 20X (Plan-Apochromat, 0.8A) or 40X (Plan-Apochromat, 0.95A) magnification.[112] Signal to background ratio (SBR) calculations were performed to quantify differences between staining and signal removal conditions as previously described.[112] The fluorescence imaging channels were registered using QiTissue software (Quantitative Imaging Systems, LLC, Pittsburgh, PA).

Oligonucleotide Antibody Conjugation & Optimization Strategies. Both non-specific and site-specific conjugation methods were used to generate the Ab-oligo conjugates. Except where noted, excess modification reagents or oligos were purified using 0.5 mL 100 kDa Amicon spin filters (MilliporeSigma Burlington, MA). DBCO reagents were diluted from DMSO stocks to maintain <1% DMSO in the presence of antibody to prevent antibody degradation. Conjugates were resuspended in 1X PBS, pH 7.4 and absorbance was measured by spectroscopy to estimate the concentration of oligo, antibody and oligo to antibody conjugation ratio.

(1) *Non-specific antibody conjugation using Maleimide or NHS Ester.* To label antibodies with fluorophore or oligonucleotide, 200-300 µg of primary antibody was added to Cyanine 7

(Cy7) NHS ester dye (Lumiprobe, Hunt Valley, MA) at a molar ratio of 1:1 in 1 mL 1X PBS, pH 8.3. The antibody-fluorophore mixture was then gently mixed for 3 h at RT. Excess dye was removed with a 0.5 mL 10 kDa spin filter. In the maleimide reaction, the antibody was reduced by the addition of 50X molar excess Tris(2-carboxyethyl)phosphine hydrochloride (TCEP, MilliporeSigma) in 1X PBS, pH 7.2 supplemented with 1 µL 0.5 M ethylenediaminetetraacetic acid disodium salt dihydrate (EDTA, Fisher Scientific Waltham, MA), pH 8.0. The reduction reaction was incubated at RT for 1 h. Meanwhile, a NAP5 column (Cytiva, Marlborough, MA) was equilibrated to RT with 10 mL of 1X PBS, pH 7.4. Following antibody reduction, it was eluted from the NAP5 column and the antibody fraction was collected directly into a tube containing the fluorophore or oligo containing a DBCO maleimide (MilliporeSigma) for modification. For NHS ester conjugation of antibody, 10 µL of 1M sodium bicarbonate ($NaHCO_3$, ThermoFisher Scientific) was added in 1X PBS, pH 7.4 prior to modification by DBCO sulfo-NHS ester (MilliporeSigma). For both maleimide and NHS Ester reactions, the antibody was modified at a molar ratio of 6:1 DBCO to antibody and ~30:1 oligo to antibody. The resultant DBCO-antibody products were incubated with gentle shaking for 3 h at RT. Docking strands (DS) with an azide moiety on the 5' end were subsequently added to the DBCO-antibody product and the conjugation reaction was run overnight at 4 °C. NHS-ester Ab-oligo conjugates were also generated according to the protocol provided with the Solulink kit (S-9011-1, Trilink Biotechnologies, San Diego, CA). Briefly, oligos were modified with NHS ester-4-formylbenzamide (4FB) to an amino group on the 5' end. The antibody was modified with succinimidyl-6-hydrazino-nicotinamide (HyNic). Combining the modified oligo and antibody in solution at a target molar ratio of 20:1 oligo to antibody resulted in a stable bis-arylhydrazone bond with peak absorbance at 354 nm and extinction coefficient of 29,000 $M^{-1}cm^{-1}$.

(2) *Specific Ab-oligo conjugation.* Ab-oligo conjugates were generated according to the protocol provided with the SiteClick Kit (Thermo Fisher). Briefly, antibodies were buffer exchanged into 1X Tris, pH 7 and then carbohydrate domains on the F_c region of antibodies were cleaved with ß-galactosidase, which allowed the remaining residues to be modified with an azide moiety in the presence of the GalT(Y289L) enzyme. Oligos were resuspended in 1X Tris, pH 7. The oligos were added to the azide-modified antibodies at molar ratios of 4-20 oligos per antibody and incubated overnight at 25 °C. Excess unbound oligo was removed with a 0.5 mL 30 kDa Amicon spin filter.

(3) *Ab-oligo Conjugate Optimization & Purification.* Validation of the functionality of the Ab-oligo conjugates was performed by comparing the staining pattern of the Ab-oligo conjugate to that produced by conventional indirect staining. Initial staining results for some Ab-oligo conjugates showed non-specific fluorescence signal in the Ab-oligo + IS samples compared to Ab-oligo + secondary antibody staining. Subsequently, these Ab-oligo conjugates was subjected to additional purification using a 100 kDa spin filter, blocked with 1% BSA. Washing spins were repeated 5-10X, adding 1X PBS, pH 7.4 after

each wash spin to result in a final volume of 500 μL for each wash. The flow-through from each spin was collected in a separate tube. After washing was completed, absorbance was measured at 260 and 280 nm for the purified and flow-through fractions to quantify removal of unbound DS and antibody loss. As a representative example, serial FFPE MCF7 xenograft tissue sections were stained with the titrations of the washed E-Cadherin Ab-oligo conjugate to compare the relative fluorescence signal and antigen specificity in washed and unwashed Ab-oligo conjugates.

Signal Removal Methods. A variety of methods were used to remove the Ab-oligo staining pattern back to the level of tissue autofluorescence, explained as follows.

(1) *Strand-Mediated Displacement (SMD).* Oligo sequence design for these studies was based on previous work.[121] SK-BR-3 cells were stained with HER2 Ab-oligo conjugated to the EP-2 oligo sequence as previously described. Subsequently, the complementary oligo sequence, CP-2, labeled with AF647, was incubated with the Ab-oligo-stained cells and allowed to hybridize *in situ*. Following imaging for total fluorescence signal, the cells were either incubated with displacement probes DP-1 or DP-2 at RT, (DP-2: specific, displaces CP-2; DP-1: non-specific, does not displace CP-2). Images were taken collected 2, 5, 10, 20 and 30 mins after displacement probe incubation to monitor fluorescence signal removal. The plate was then washed and imaged again in a different field of view (FOV) to quantify fluorescence signal intensity.

(2) *Restriction Enzyme (RE).* RE and buffers were purchased from New England Biolabs (NEB, Ipswich, MA). Following Ab-oligo conjugate incubation, the complementary IS was incubated with the cells as previously described. Following staining and imaging, the cells were washed twice briefly in 1X Cut Smart Buffer, which was also used to dilute the RE stock solutions and for all subsequent washes. RE were kept at -20 °C throughout the experiment in a benchtop cooler (Thermo Fisher). Stained cells were incubated with RE (2 x 5 min) at 37 °C and 5% CO_2 prior to sustained RE treatment for 30 min at 37 °C and 5% CO_2. Cells were washed twice briefly and incubated with fresh RE for 30 min at 37 °C and 5% CO_2. Cells were washed and imaged to quantify signal removal. To validate specificity, BamHIA-HER2 and SalIA-CK19 conjugates were hybridized to complementary IS labeled with AF647 and AF488, respectively. The cells were then treated with BamHI and SalI high fidelity (HF) RE. The same FOV was imaged in each channel, and DAPI was also imaged for registration. RE concentration titration was performed using the NheIA-Lamin B1 Ab-oligo conjugate and IS labeled with AF546. NheI HF RE was applied at 200, 500, or 1000 units (U) per well. Additionally, four rounds of RE treatment at three concentrations were tested using the PstIA-TOMM20 Ab-oligo conjugate and IS labeled with AF546. PstIA-HF RE was applied at 200, 500, or 1000 U per well.

(3) *Thermal Denaturation Using the Oligonucleotide Melting Temperature (T_m).* The thermal denaturation method was validated in HER2+ breast cancer tissue stained with SalIA-CK19, NheIA-Lamin B1 and BamHIA-HER2 Ab-oligo conjugates hybridized with their complementary IS labeled with AF488, AF546 and AF647, respectively. The same FOV

was imaged in each channel. DAPI was also imaged for registration and to monitor for any tissue damage. To determine the minimum T_m required to remove the full complement of IS, FFPE MCF7 cell buttons were stained with SalIA-CK19 Ab-oligo conjugate and hybridized to 28 nt IS labeled with AF647 for imaging. The coverslips were floated off in 0.1X SSC at RT prior to immersion in a glass Coplin staining dish (Fisher) with 0.1X SSC preheated to 70, 65, 60, 55, or 50 °C. The temperature was monitored throughout the experiment with a digital thermometer (Keynice, Fulling Way Technologies Ltd, Hong Kong). Following heating, the slides were washed 10 times in 0.1X SSC at RT and then remounted, cover slipped and imaged to quantify all remaining fluorescence signal.

Using the same SalIA-CK19 Ab-oligo conjugate and additional tissue sections from the same block, IS of varying lengths were tested to elucidate the relationship between IS length, the resulting fluorescence signal intensity and completeness of signal removal through thermal denaturation. SalIA-CK19 was hybridized with IS of 28, 17, 15 or 13 nt labeled with AF647, where vendor-specified T_m of each IS was 62.7, 60.5, 55.1, 50.5, and 46.3 °C, respectively. Following staining, imaging and removal of the coverslip, the slides hybridized with 28, 17, 15 or 13 nt IS were heated to 70, 60, 55 or 50 °C, respectively. To monitor potential tissue and antigenicity degradation after multiple rounds of heating, HER2+ breast cancer FFPE tissue sections were cut from a single block and stained as previously described.[123] The SalIA-CK19, Nhe-Lamin B1 and BamHIA-HER2 conjugates were each hybridized to 28 nt or 13 nt IS. The slides were imaged prior to thermal denaturation to establish baseline fluorescence signal and then heated to remove fluorescence signal at 70 °C for the 28 nt IS or 50 °C for the 13 nt IS. The slides were then re-imaged to evaluate fluorescence signal. The process of blocking, staining, imaging and heating was repeated for six total cycles on the same tissues.

(4) *Disulfide cleavage using TCEP.* Assessment of fluorescence signal removal by application of TCEP to cleave disulfide linkers of fluorophores on IS was performed in FFPE breast cancer tissue stained with the BamHIA-HER2 Ab-oligo conjugate. Ab-oligo staining was performed as described, while IS application and signal removal through cleavage of disulfide linkers was performed as previously described.[67] Briefly, after deparaffinization, antigen retrieval, blocking and Ab-oligo incubation, slides were washed 2 x 5 min with buffer 405 (10 mM Tris, pH 7.5, 650 mM NaCl, 0.1% Triton X-100). Slides were subsequently incubated with 50 mM TCEP diluted in buffer 405 for 4 min and then washed 3 x 5 min with buffer 405. Tissues were then blocked with freshly made 100 mM iodacetamide for 1 h in buffer 405 adjusted to pH 8.0. After removing excess blocking buffer, complementary IS modified with a disulfide linker adjacent to AF647 were diluted with buffer 4 (10 mM Tris, pH 7.5, 10 mM $MgCl_2$, 150 mM NaCl, 0.1% Triton X-100) and applied to the tissue for 45 min at RT. Unbound IS was removed with 3 x 5 min washes with buffer 405. DAPI was applied followed by tissue mounting and cover slipping as described above. Images were collected in the AF647 and DAPI channels. Total fluorescence signal intensity in the AF647 channel was quantified. After imaging, the coverslip was floated off in 0.1X SSC at RT. To cleave the disulfide linkers and remove

fluorescence signal, slides were incubated for 2 min in 50 mM TCEP diluted in buffer 405 followed by 2 x 5 min washes with buffer 405 and a 1 min incubation in 100 mM iodoacetamide diluted in buffer 405. The same FOV was imaged to evaluate fluorescence signal removal through TCEP cleavage. To confirm antigenicity was preserved, the tissue was then incubated with 15 μg/mL of HER2 conjugated to AF555 (HER2-AF555) for 1 h. The tissue was washed 3 x 5 min with 2X SSC and cover slipped prior to imaging of the same FOV in AF647, AF555 and DAPI channels.

(5) *Photocleavable Linker (PCL).* Cleavage of fluorophore from the IS was completed through the integration of a photocleavable linker on the IS immediately adjacent to the fluorophore. Signal removal was completed with ultraviolet (UV) light treatment. FFPE normal breast tissue was stained using the SalIA-CK19 Ab-oligo conjugate to evaluate fluorescence signal removal following UV light treatment. Fluorescence signal of the Ab-oligo conjugate was assessed prior to treatment with UV light (~350 nm) with a handheld UVGL-55 UV lamp (UVP, Upland, CA) at 5 min increments for up to 15 min total treatment time. Images were collected after each 5 min UV light treatment to monitor signal removal. MCF7 FFPE cell button sections were stained with the SalIA-CK19 conjugate and IS either with or without a PCL to determine the signal removal by PCL vs. UV light photobleaching. Samples were imaged before and after 15 UV light treatment in representative FOVs to evaluate signal change in each sample.

RESULTS

Ab-Oligo Conjugation Strategies. Conjugation of antibodies has become standard laboratory practice, with a variety of available strategies. Herein, we investigated four strategies for oligo conjugation to antibodies (**Fig. 2.1**), where conjugation ratio, retained antibody binding affinity and staining specificity were used as metrics of success. Two of the most common antibody conjugation methods, maleimide and NHS ester, were employed for antibody modification with a Cu-free click chemistry linker (i.e., DBCO) permitting covalent attachment of the azide-modified oligos (**Fig. 2.1A & 2.1B**). While both methods are common and relatively simple, Ab-oligo conjugate production with maintained binding affinity and specificity had high variability. Two commercial kit-based approaches were investigated including the Solulink and SiteClick kits (**Fig. 2.1C & 2.1D**). The Solulink kit uses NHS ester modification of the antibody to add an S-HyNic group and addition of a 5'-4FB group to the oligo. Once modified, the antibody and oligo were covalently attached through formation of a stable bis-arylhydrazone bond (**Fig. 2.1C**). The SiteClick kit provided a means of site-directed conjugation, where the antibody was modified to contain an azide moiety on the F_c region. Oligos containing an alkyne group in the form of a DBCO-TEG modification on the 5' end permitted Cu-free click chemistry-mediated covalent attachment (**Fig. 2.1D**). While both the Solulink and SiteClick kits resulted in Ab-oligo conjugates with maintained affinity and specificity, retention of binding affinity was substantially higher for

the site-specific SiteClick kit compared to the non-specific Solulink kit (~90% vs. ~50%, respectively).

Quantification of antibody retention and Ab-oligo conjugation ratio using standard spectroscopy methods was not possible due to the proximity in peak absorbance of the oligos (260 nm) and antibodies (280 nm), where the oligo peak was dominant. To more accurately quantify conjugation ratios, NHS ester conjugation of Cy7 was employed prior to oligo conjugation (**Fig. 2.1C**). The fluorophore to antibody ratio could be accurately quantified due to the spectral separation between the peak antibody absorbance (280 nm) and Cy7 absorbance (750 nm). Following oligo conjugation, the fluorophore concentration was used as a surrogate for the antibody concentration, permitting quantification of the oligo to antibody conjugation ratio using standard spectral methods.

Staining patterns of the Ab-oligo conjugates were periodically overwhelmed by nuclear background, which could be mitigated through additional washing of the conjugate to remove unconjugated oligo (**Fig. 2.2**). As a representative example, the functionality of the EcoRIA-E-Cad Ab-oligo conjugate + IS was compared to Ab-oligo + secondary antibody and found to have increased non-specific fluorescence signal in the nucleus relative to the indirect immunofluorescence staining (**Fig. 2.2B**). This non-specific background staining was diminished after the E-Cad Ab-oligo conjugate was subjected to additional washing, which was thought to remove unconjugated DS, however overall fluorescence signal intensity also declined (**Fig. 2.2B**). To estimate the number of unconjugated DS that was removed and antibody loss during the washing process, absorbance was measured at 260 and 280 nm in the 5X and 10X retained fractions, as well as the flow-through from each wash step (**Fig. 2.2A**). The peak absorbance signal observed at 280 nm was increased in the 5X washed sample compared to the unwashed sample (i.e., the original Ab-oligo conjugate). BSA was loaded into the filter prior to washing in an effort to block the filter from capturing antibody non-specifically which increases antibody loss through the washing procedure. Therefore, the increased 280 nm signal was likely due to excess BSA being removed from the filter during the washing procedure (**Fig. 2.2A**). However, decreased E-Cad-specific fluorescence signal intensity in the 10X washed

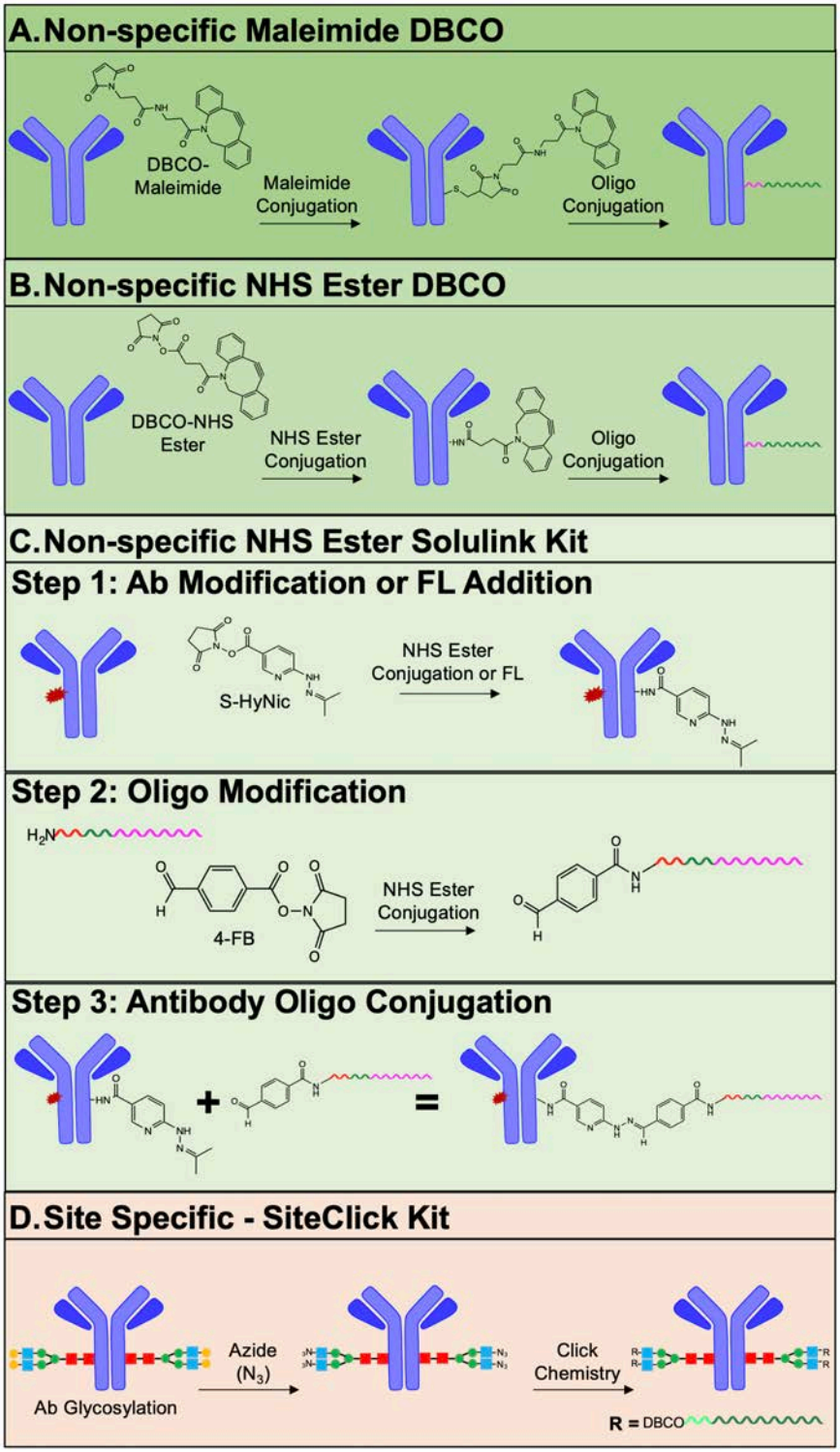

Fig. 2.1: *Oligo conjugation methods.* Non-specific Ab-oligo conjugations were tested where **A.** maleimide Cu-free click chemistry, **B.** NHS ester Cu-free click chemistry and **C.** NHS ester conjugation with the Solulink kit (Trilink Biotechnologies) were compared. To enable conjugation ratio quantification, Cy7 (red explosion) was pre-conjugated to some antibodies. **D.** The site-specific SiteClick Kit (Thermo Fisher) was also evaluated where modification was limited to the F_c region of antibodies.

compared to 5X washed and unwashed Ab-oligo conjugate images indicated that some E-Cad antibody was also lost during the purification process. Notably, titrating the Ab-oligo conjugate helped restore the fluorescence signal intensity in the 10X washed conjugate, while non-specific nuclear fluorescence remained low (**Fig. 2.2C**) demonstrating the utility of the washing method to improve overall staining pattern.

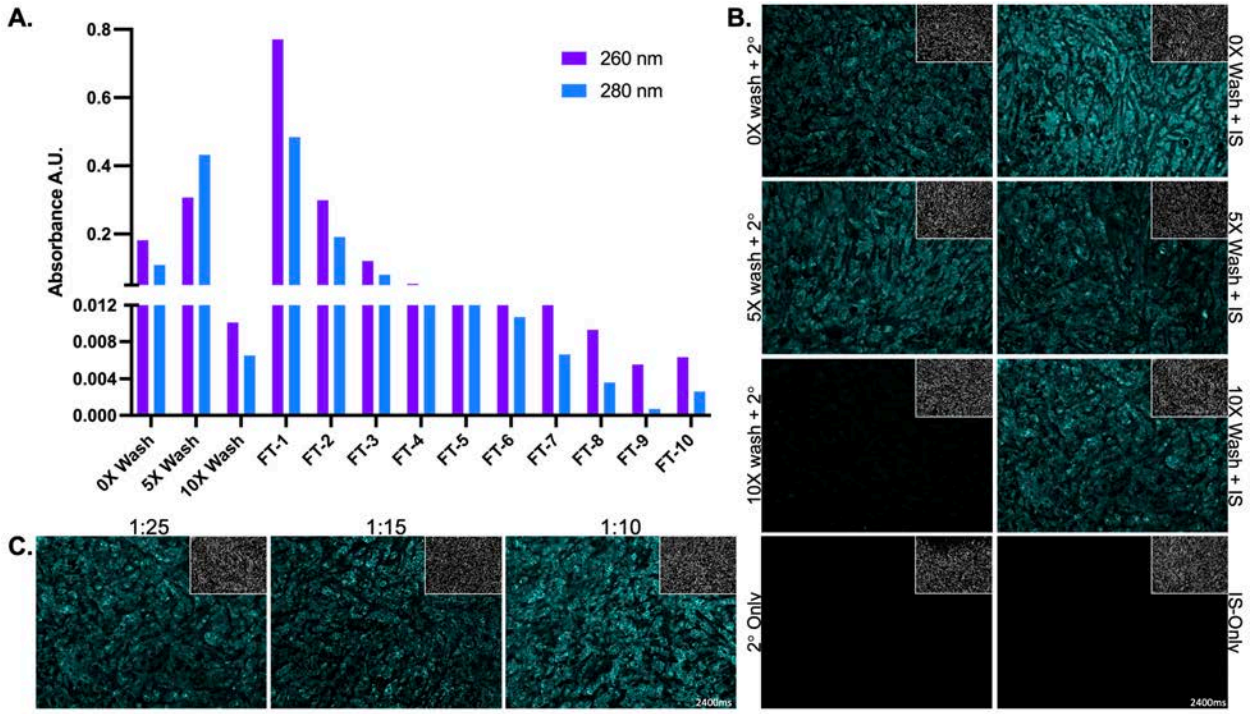

Fig. 2.2: *Ab-oligo conjugate purification.* **A.** After Ab-oligo conjugation, unbound DS was removed through a series of 5-10 washes where oligo and antibody loss were tracked through absorbance measurements at 260 and 280 nm, respectively. **B.** The functionality the EcoRIA-E-Cad Ab-oligo conjugate after 0, 5 and 10 washes were compared to conventional indirect immunofluorescence staining. **C.** Ab-oligo conjugate concentration titration after purification restored marker specific staining. Images in each panel are displayed with equivalent contrast settings.

Strand-Mediated Displacement (SMD) Signal Removal. SMD employed the use of oligo sequences based on previous work.[121] The antibody conjugated sequence (EP-2) contained 16 bp complementarity to the labeling sequence, CP-2. Moreover, the CP-2 sequence also contained an additional 6 nucleotides, termed the toe-hold region. This toe-hold region permitted the third sequence, DP-2, with 22 nt complementary to CP-2, to completely hybridize with CP-2 sequence, facilitating the removal of CP-2 from EP-2 and eliminating fluorescence signal (**Fig. 2.3A**). To validate the specificity and robustness of this signal removal strategy, SK-BR-3 cells were stained with the EP-2-HER2 Ab-oligo conjugate, followed by incubation with CP-2 labeled with AF647 fluorophore. Images collected prior to signal removal showed membrane-specific HER2 staining. Fluorescence intensity was monitored during incubation with the either the specific DP-2 or the non-specific DP-1 sequences. While signal to background ratio decreased in all tested conditions, signal reduction was greater for the cells incubated with the specific DP-2 than cells incubated with the non-specific DP-1. Signal to background ratio was measured by segmenting the foreground for signal and measuring the ratio of the signal and background mean intensities.

Additionally, fluorescence signal remained for cells incubated with DP-1 after washing and imaging of a new FOV. The opposite was true for cells incubated with DP-2 (**Fig. 2.3B** & **2.3C**). These findings illustrate that while repeatedly imaging the same FOV caused a decrease in fluorescence signal over time, likely due to photobleaching of the AF647, specific fluorescence signal removal was only achieved via specific DP-2/CP-2 hybridization and washout.

Restriction Enzyme (RE) Signal Removal. The DS and fluorophore conjugated IS were

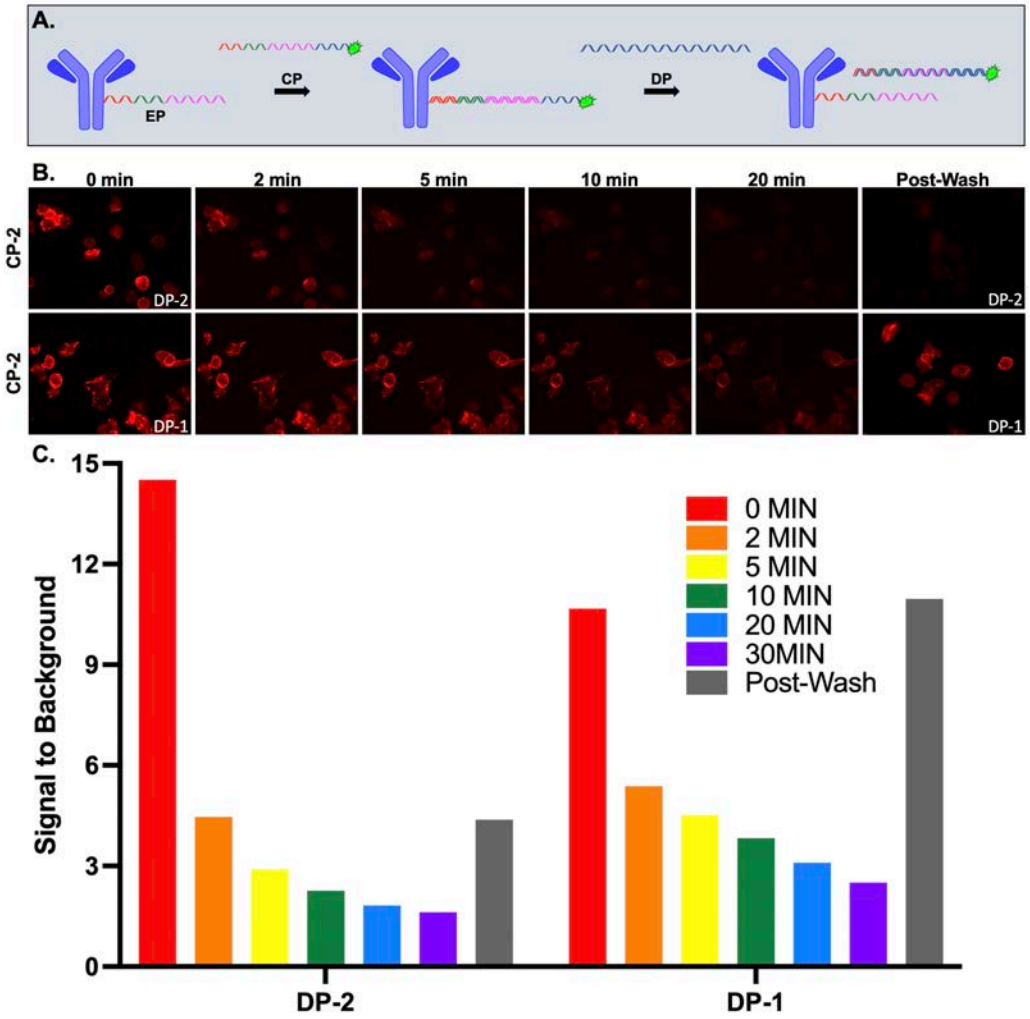

Fig. 2.3: *Strand-mediated displacement signal removal.* **A.** The EP oligo docking strand (DS) sequence was conjugated to an antibody. The capture strand (CP) oligo, labeled with a fluorophore, contained 16 bp complementarity to EP while also having a 6 nt toe-hold region not complementary to the EP sequence. After image capture, the displacement oligo (DP) that had full 22 nt complementarity to the CP was incubated on the tissue. The DP and CP strands completely hybridize in order to remove fluorescence signal. **B.** SK-BR-3 cells stained with EP-2-HER2 Ab-oligo conjugate were labeled with the fluorophore labeled CP-2 sequence. Stained cells were then incubated either with the specific DP-2 or non-specific DP-1 with images being collected at 0 min, 2 min, 5 min, 10 min, 20 min, 30 min and after washing at the 30 min time. **C.** Signal changes in the specific and non-specific staining were quantified.

each designed to contain a 6 nt section that could be recognized and cleaved by a specific RE upon hybridization. After imaging of the Ab-oligo-stained sample, specific RE was added and the

hybridized DS/IS was cleaved and washed from the sample (**Fig. 2.4A**). Multiplexed staining using Ab-oligos targeted to HER2 and CK19 were detected using IS labeled with AF647 and AF488, respectively (**Fig. 2.4B**), demonstrating both staining specificity and signal removal using distinct RE's. While membrane and cytosolic Ab-oligo signal was readily removed by RE application, organelle- and nuclear-specific staining patterns were more challenging to fully remove. For example, while Lamin B1 Ab-oligo staining pattern was reduced after increasing RE concentration, it remained above background autofluorescence levels (**Fig. 2.4C** & **2.4D**). This result was recapitulated with an Ab-oligo conjugate targeted to the mitochondrial protein TOMM20, where neither increased concentration nor multiple rounds of RE application fully

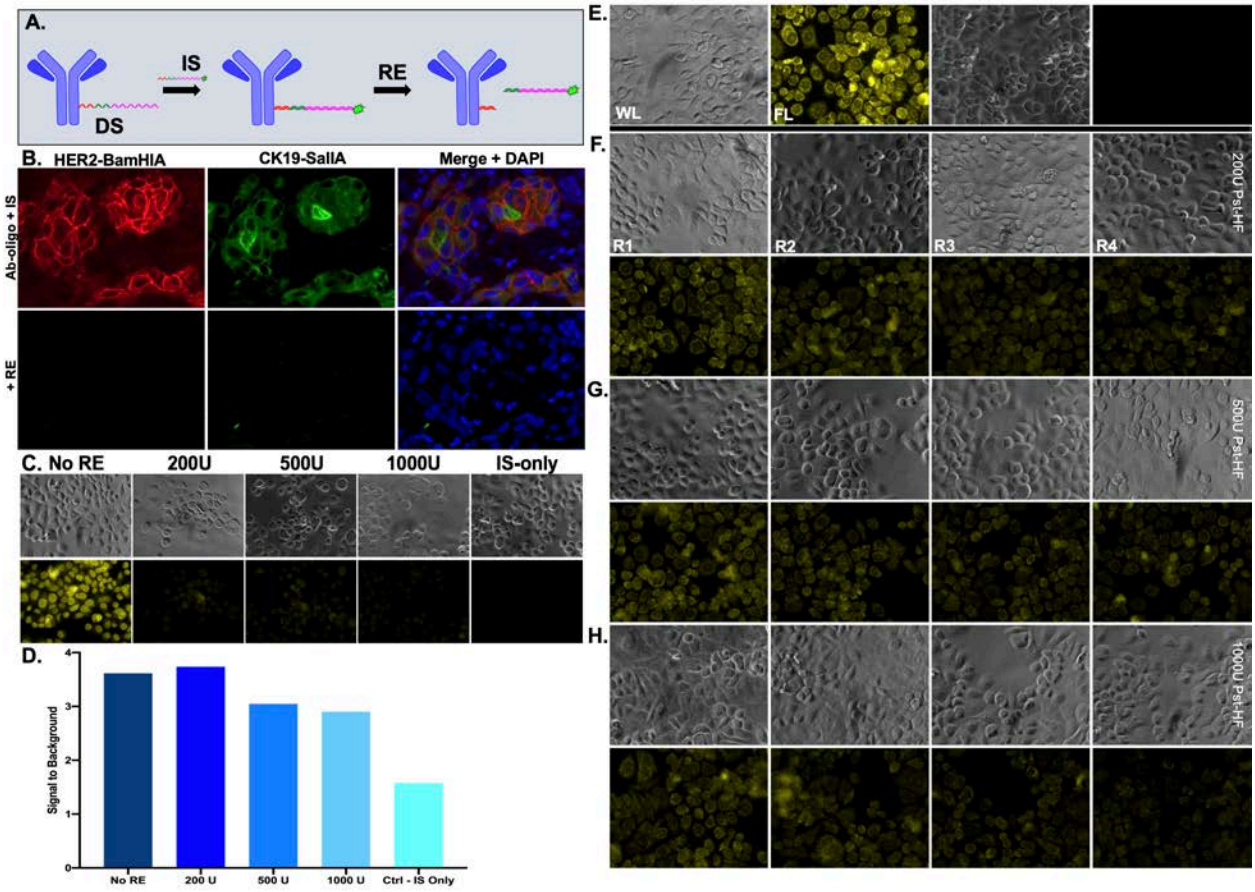

Fig. 2.4: *Restriction enzyme signal removal.* **A.** The DS of the Ab-oligo conjugate contains a region that is recognized by RE once hybridized to its complementary IS for fluorescence signal removal. **B.** Tissue stained with Ab-oligo conjugates for membrane and cytosolic markers, HER2 and CK19, respectively, had complete signal removal after RE incubation. **C.** Fluorescence signal from the Lamin B1 Ab-oligo conjugate, an organelle-specific marker, was reduced, **D.** but remained above background autofluorescence levels. **E.** Fluorescence signal from the Ab-oligo conjugate for the mitochondrial protein, TOMM20, was also not reduced to background levels after **G.** multiple rounds and **H.** increased concentration of RE incubation.

removed the fluorescence staining pattern to the level of tissue autofluorescence (**Fig. 2.4E-2.4H**).

Thermal Denaturation Signal Removal. The specific melting temperature (T_m) of the hybridized DS/IS pair was tested as a method to remove fluorescence signal. The T_m of each respective IS varied according to oligo length and the percentage of guanine (G) and cytosine (C)

bases.[119, 120] Other factors that affect T_m, such as salt concentration,[118] were kept constant during these studies. Heating Ab-oligo + IS stained slides to a temperature above the IS-specific T_m resulted in denaturation of the DS/IS complex labeling the target antigen, and the fluorophore-labeled IS was removed from the sample by washing (**Fig. 2.5A**). HER2+ breast cancer samples stained with CK19, Lamin B1 and HER2 Ab-oligo conjugates showed the expected staining

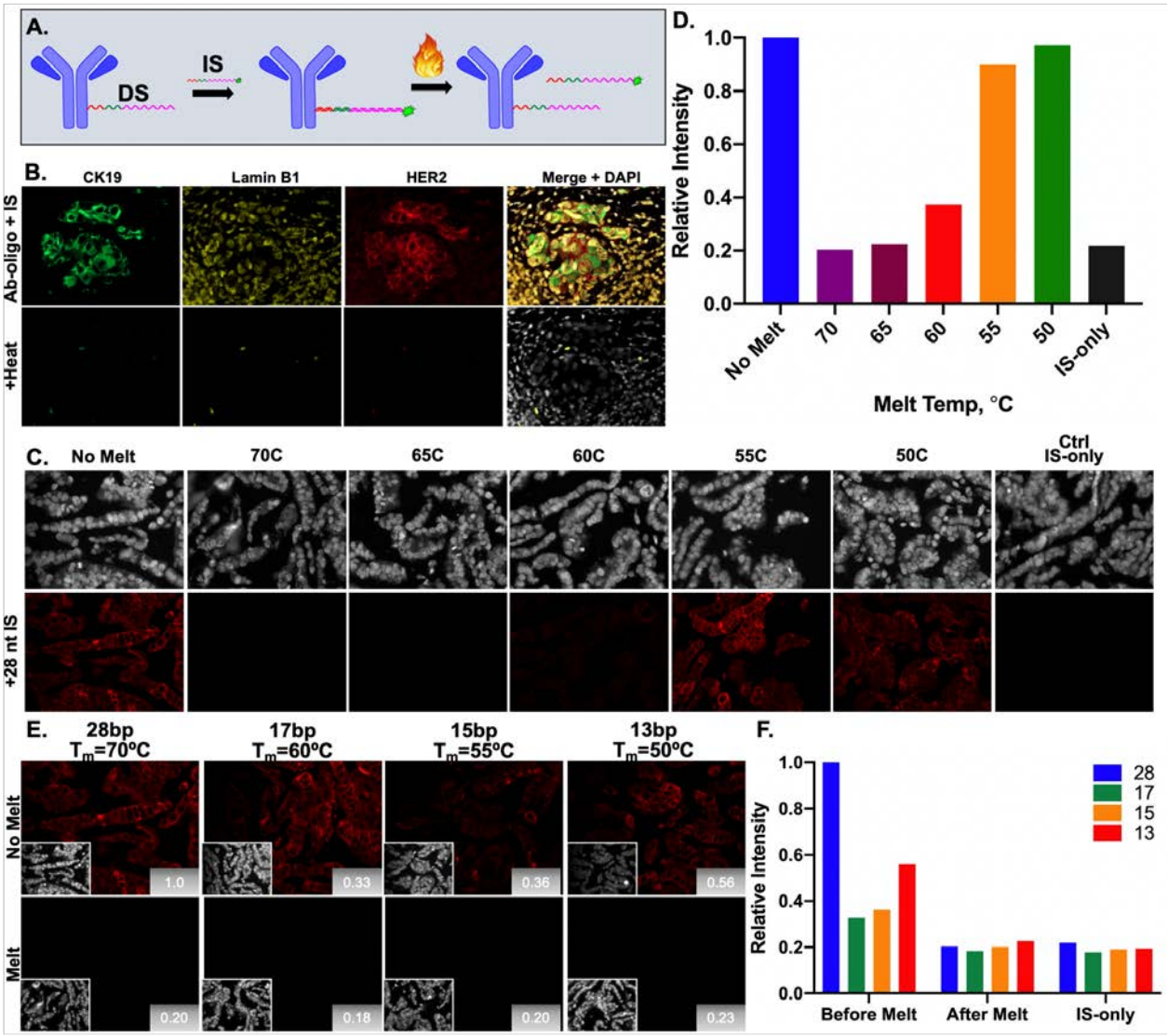

Fig. 2.5: *Thermal denaturation signal removal.* **A.** After Ab-oligo conjugate staining with a fluorophore labeled IS, signal removal is achieved by heating the slide to a temperature above the IS-specific T_m to denature the DS/IS complex, where the IS can be readily washed from the sample. **B.** Heating of a tissue section to 70 °C stained with Ab-oligo conjugates for CK19, Lamin B1 and HER2 resulted in removal of marker specific staining. **C.** Tissues stained with the CK19 Ab-oligo conjugate were exposed to varied temperatures to find a minimum temperature needed to denature 28 nt IS. Image contrast levels are set to that of the no melt image and **D.** relative fluorescence intensity at each temperature quantified. **E.** Tissues stained with CK19 Ab-oligo conjugate were incubated with IS of varying length and then heated to T_m specific to each IS length. **F.** Relative intensity was quantified for each length IS (i.e., 28, 17, 15 or 13 nt) before melt, after melt and for the IS-only control.

patterns after incubation with their respective 28 nt complementary IS, each labeled with a

spectrally distinct fluorophore. The specific fluorescence staining was fully removed by heating the slide to 70 °C (**Fig. 2.5B**).

Identification of a minimum required DS/IS melting temperature for complete signal removal was investigated to both optimize and generalize this signal removal strategy. FFPE cell buttons were stained with the CK19 Ab-oligo conjugate and hybridized *in situ* to its full length (i.e., 28 nt) complement IS with a calculated T_m = 62.7 °C. Imaging comparing samples that were not heated to those heated to 50-70 °C showed that heating above the calculated melting temperature was required to reduce the fluorescence intensity to the level of IS-only stained tissues (**Fig. 2.5C** & **2.5D**). Based on these results, the temperature selected for optimization using thermal removal studies was ~5 °C above the calculated T_m of each specific IS. While heating to at least 65 °C successfully denatured 28 nt DS/IS hybridization, there was concern that repeat heating to such high temperatures could either damage tissue or cause antibodies to be removed from their antigen. To address this concern, shorter IS lengths of 17, 15 or 13 nt were compared to the 29 nt length used to detect the CK19 Ab-oligo conjugate. These studies allowed evaluation of staining

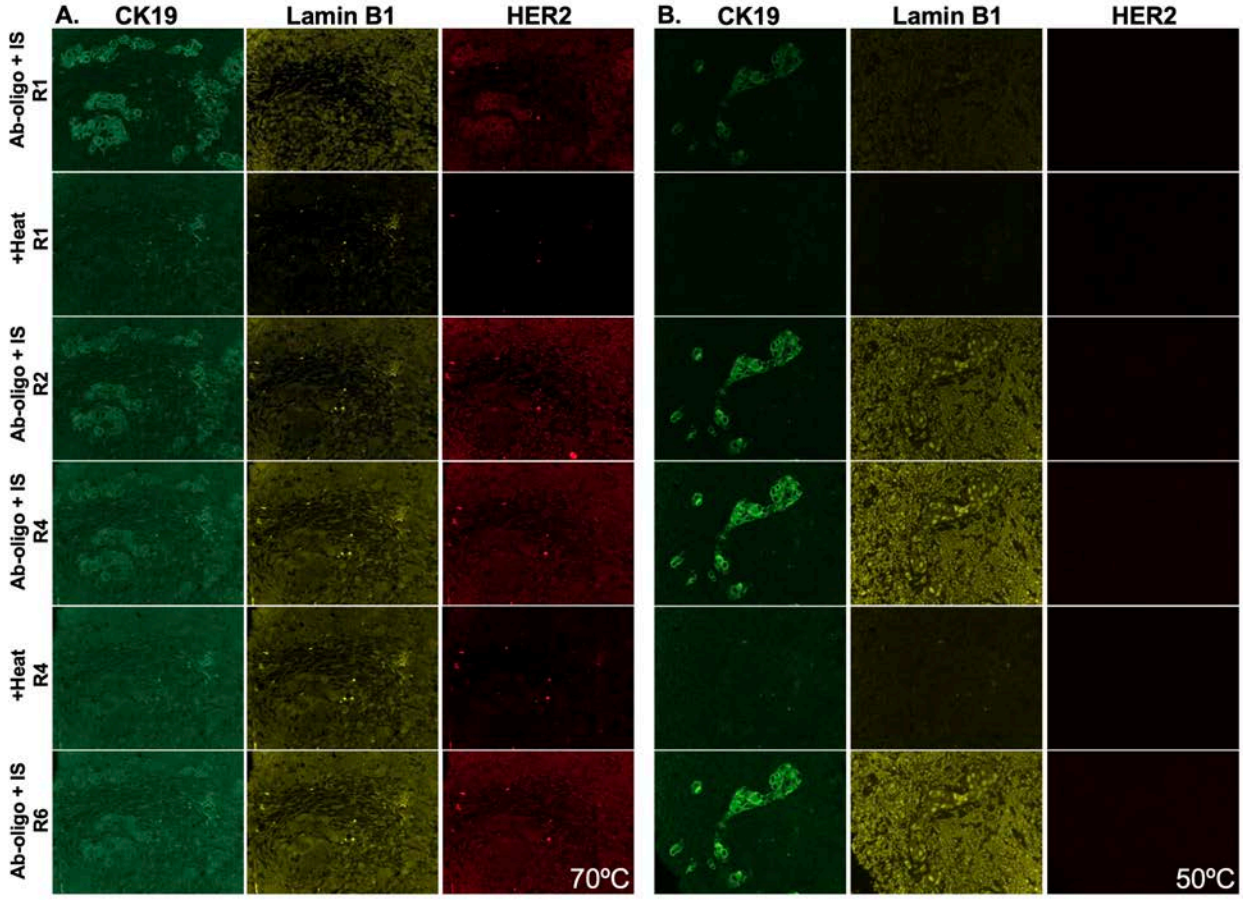

Fig. 2.6: *Effect of thermal denaturation on background autofluorescence.* Tissues were stained with CK19, Lamin B1 and HER2 Ab-oligo conjugates and then incubated with **A.** 28 nt or **B.** 13 nt length IS and heated for signal removal to either 70 °C or 50 °C, respectively. Each sample was subjected to six rounds of IS application, imaging and thermal denaturation.

specificity using shorter IS as well as ability to remove Ab-oligo specific signal using lower temperatures. Fluorescence signal intensity was the highest for the longest (i.e., 28 nt) tested IS, however all tested IS lengths provided specific CK19 staining. Fluorescence signal for DS/IS pairs of all lengths was readily reduced to IS-only levels after heating to denature DS/IS duplexes at ~5 °C above the calculated T_m (**Fig. 2.5E** & **2.5F**).

To assess the utility of thermal denaturation for signal removal over multiple rounds of staining, a HER2+ breast cancer tissue was stained with CK19, Lamin B1 and HER2 Ab-oligo conjugates. *In situ* IS hybridization with either 28 or 13 nt length IS were used for detection (**Fig. 2.6**). The slides were subjected to six rounds of IS staining, imaging and fluorescence signal removal by heating at 70 and 50 °C for the 28 and 13 nt IS, respectively. While antigen-specific

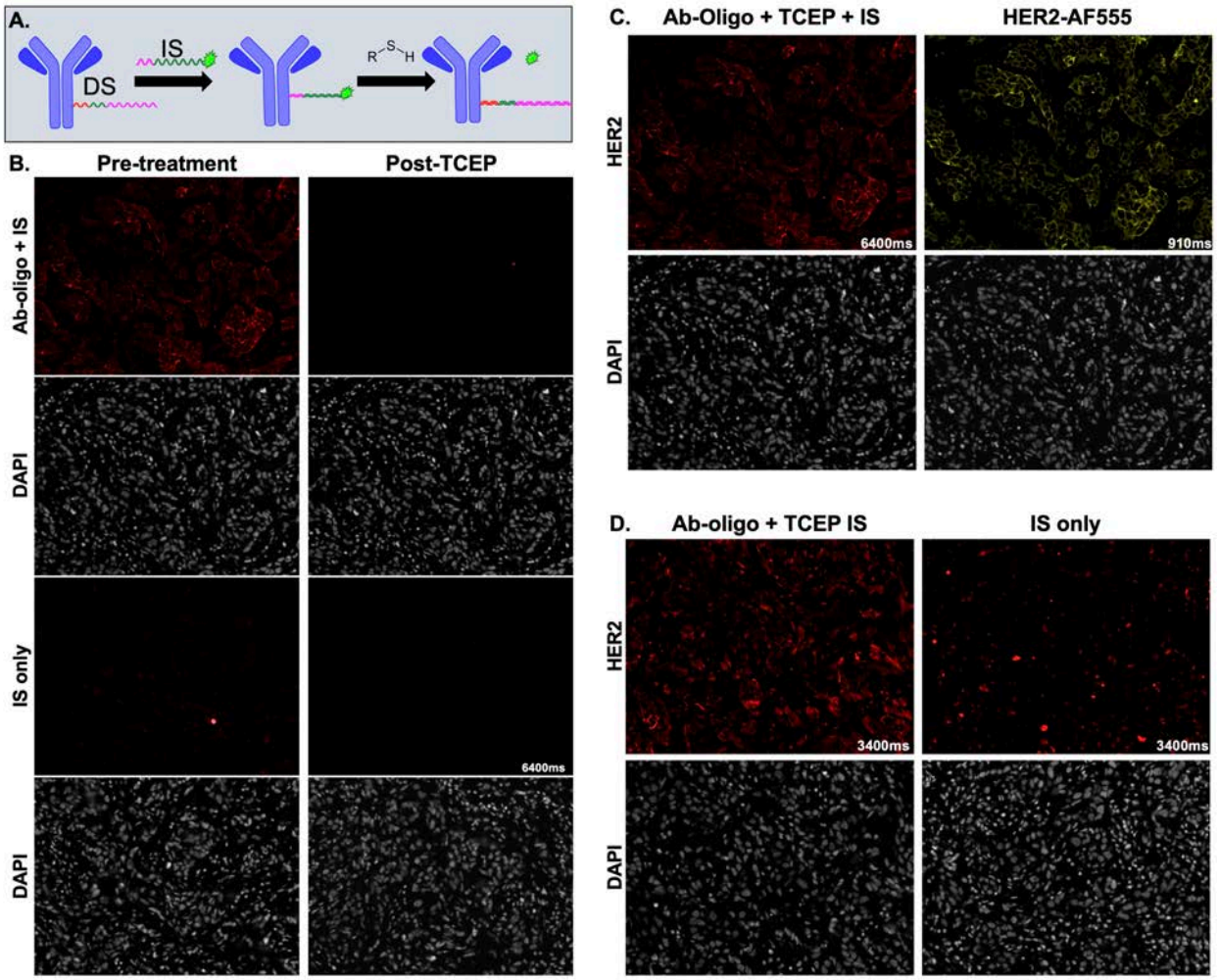

Fig. 2.7: *TCEP disulfide cleavage for signal removal.* **A.** Ab-oligo conjugates were incubated with a fluorophore-labeled IS modified with a disulfide modification adjacent to the fluorophore. Incubation with TCEP cleaves the disulfide region and the fluorophore can be readily washed away for signal removal. **B.** Tissues stained with the HER2 Ab-oligo conjugate and disulfide modified IS saw complete signal removal after TCEP incubation. **C.** After HER2 Ab-oligo signal removal, the tissue was stained with HER2 labeled with AlexaFluor555 and the same FOV imaged to confirm preserved tissue antigenicity. **D.** Increased background was observed in subsequent tissues stained with the HER2 Ab-oligo conjugate and disulfide modified IS.

staining pattern was removed for both IS lengths with heating to their respective T_m, reapplication of 28 nt IS and imaging over multiple rounds showed a general increase in background fluorescence intensity as cycle number increased. The CK19 Ab-oligo stained with the 13 nt IS and thus only heated to 50 °C maintained distinct and specific fluorescent staining pattern through the six rounds, with a potential increase in contrast in R2 (**Fig. 2.6B**). Lamin B1 staining was visible after both 28 and 13 nt IS staining, but overwhelmed by increased background using either 70 and 50 °C melting in subsequent cycles. Interestingly, HER2 staining was only visible in R1 using the 28 nt IS and was also overwhelmed by increase background following R1 staining using either melting temperature (**Fig. 2.6**).

TCEP Disulfide Cleavage Signal Removal. A disulfide modification on the 3' end of the IS adjacent to the fluorophore was used to release the fluorophore for signal removal after a brief incubation with the reducing agent TCEP (**Fig. 2.7A**). Initial testing showed specific staining using the HER2 Ab-oligo conjugate, where fluorescence signal was removed to the level of tissue autofluorescence (i.e., IS-only control) following TCEP treatment (**Fig. 2.7B**). Additionally, antigenicity was unaffected by TCEP treatment, as shown by addition of fluorophore-labeled HER2 (i.e., HER2-AF555) to the same tissue following TCEP cleavage (**Fig. 2.7C**). However, in subsequent staining studies, substantially increased background was observed in both DS/IS stained tissues as well as in IS-only controls, demonstrating the variability experienced using this signal removal method (**Fig. 2.7D**).

Photocleavable Linker Signal Removal. The addition of a PCL between the terminal nucleotide and the fluorophore label on the IS facilitated signal removal after exposure to UV light (~350 nm, **Fig. 2.8A**). A time-course study of UV light treatment showed that at least 10 min was required to completely remove the Ab-oligo specific fluorescent staining pattern to the level of autofluorescence (i.e., IS-only control, **Fig. 2.8B**). Ab-oligo CK19 and HER2 conjugates were stained and hybridized to IS containing PCL and compared to IS identical in design, but without a PCL. In all cases, fluorescence signal intensity was completely removed in the PCL IS groups, and remained in the IS group without a PCL, showing the specificity of this signal removal methods (**Fig. 2.8C**).

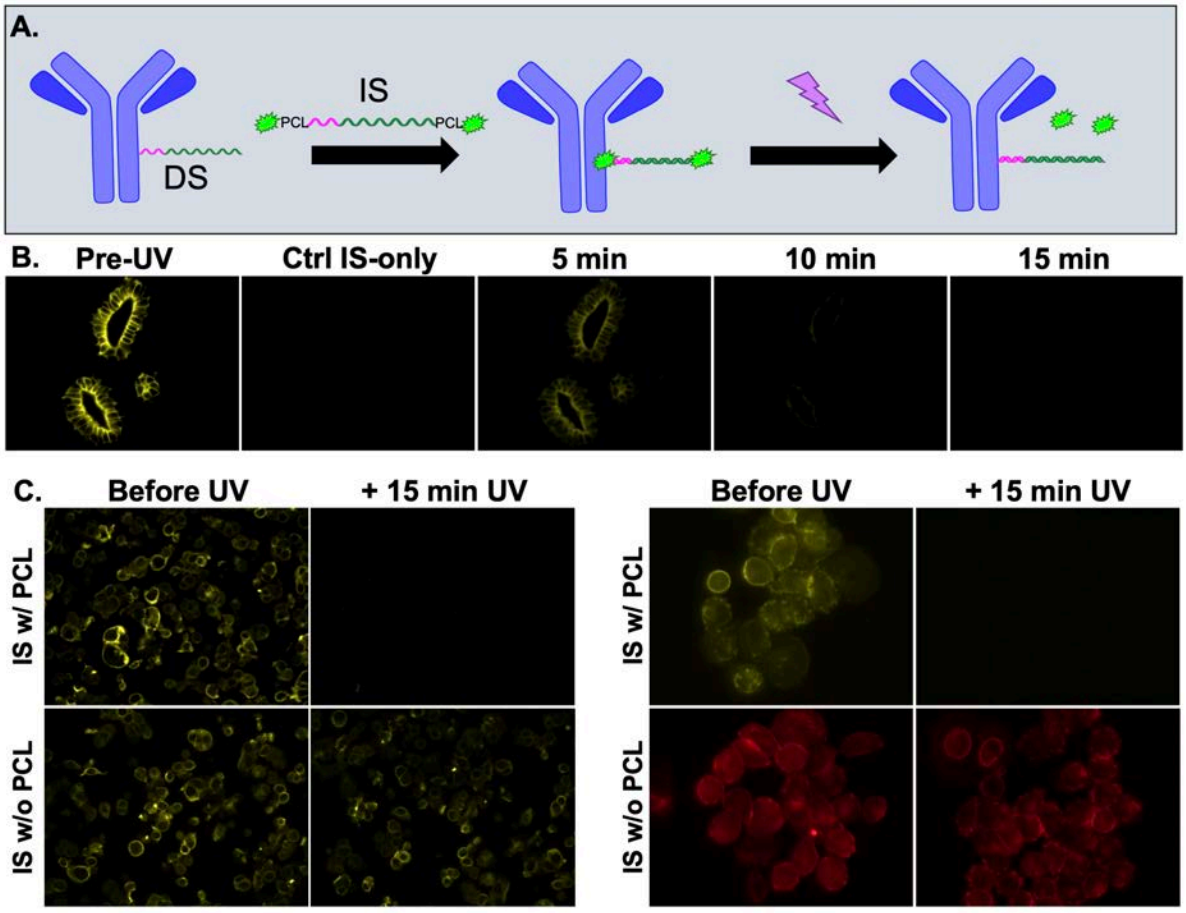

Fig. 2.8: *Photocleavable linker (PCL) facilitated signal removal.* **A.** Ab-oligo conjugates are stained with an IS containing fluorophores at each terminal end conjugated through a PCL. After imaging, exposure to UV light cleaves the fluorophore at the PCL so that it can be readily washed from the sample. **B.** Tissues stained with CK19 Ab-oligo conjugate and PCL-containing IS were imaged and then treated with UV-light for 15 min with imaging performed of the same FOV every 5 min. **C.** CK19 (left) and HER2 (right) conjugates were stained with either IS with or without a PCL, imaged, treated with UV light and re-imaged.

DISCUSSION

Over the past few decades, immunofluorescence imaging tools have remained limited by both the number of markers that can be measured on a single tissue section and spectral detection space on a single sample, both of which prevent high dimensional imaging of biomarkers expressed in tissues. Cyclic immunofluorescence (cyCIF) has emerged as a versatile solution to this challenge, where cycles of staining, imaging and signal removal enable the generation of highly multiplexed images, facilitating quantification and correlation of expression and spatial distribution of large numbers of proteins. This technique holds the potential for broad application to a wide range of biological questions previously beyond the limits of immunolabeling methodologies. In the context of highly multiplexed imaging of cancer tissues, the primary goal is to interpret the multifaceted interactions between tumor, stromal and immune cells at play in the tumor microenvironment and how these interactions influence therapeutic efficacy through imaging a high dimension of biomarkers. While a variety of cyclic immunostaining techniques have been developed, methodologies utilizing DNA barcoding have distinct methodological advantages. However, success of these methods relies on oligo modification of antibodies without disruption of its antigen affinity and the ability to completely remove antibody-specific staining. Herein, we surveyed commonly used non-specific and specific oligo conjugation strategies for the optimization of our Ab-oligo cyCIF methodology, with the goal of identifying the method that most reliably produced oligo-modified antibodies with retained antigen affinity. We also evaluated a variety of signal removal techniques to assess their ability to completely remove antibody-specific staining with minimal disruption to tissue integrity and antigenicity.

The non-specific Ab-oligo conjugation methods employed were maleimide or NHS ester DBCO-based approaches and NHS ester via the commercial Solulink kit (**Fig. 2.1A-2.1C**). The DBCO-maleimide and NHS ester strategies covalently labeled the available cysteines or lysine moieties, respectively with DBCO, which was followed by Cu-free click chemistry with azide-modified oligos (**Fig. 2.1A & 2.1B**). Alternatively, the Solulink kit reacted an oligo modified to contain a 5' terminal amine group with the free lysines to form stable, covalent bonds (**Fig. 2.1C**). Notably, neither of the DBCO conjugation methods reliably produced Ab-oligo conjugates with retained antigen affinity and were not further explored in the development of Ab-oligo cyCIF. The Solulink kit was more successful than the DBCO methods, but variability in generation of functional Ab-oligo conjugates remained high. The inconsistency in production of functional Ab-oligo conjugates was thought to be due to the potential of these non-specific methods to conjugate oligos to the F_{ab} region of the antibody, degrading the antibody's affinity for its native antigen. While non-specific conjugation strategies can be quite successful for fluorophore labeling of antibodies, the substantially larger size of the oligo labels likely contributed to the difficulties using non-specific labeling methods. As a solution to this challenge, the site-specific SiteClick conjugation kit was used to attached azide moieties directly to the carbohydrate domains present only in the F_c region of the antibody, preventing labeling in the F_{ab} region and minimizing disruption of the antibody binding site (**Fig. 2.1D**). Given the improved functionality of Ab-oligo

conjugates generated using this strategy, it was selected as the optimal conjugation method for Ab-oligo cyCIF.

Quantification of the final antibody concentration and conjugation ratios in the Ab-oligo conjugate was hampered by the proximity in peak absorbance of the oligo(s) (260 nm) conjugated to the antibody (280 nm). To quantitatively evaluate antibody loss during conjugation and conjugation ratio, a Cy7 fluorophore was conjugated to a subset of antibodies prior to oligo conjugation (**Fig. 2.1C**) and acted as a surrogate for antibody absorbance for quantification of the Ab-oligo conjugate. Using this method, antibody loss due to SiteClick conjugation was estimated to be 10-25% and conjugation ratio was found to be 1-1.5 oligos per antibody. However, use of the Cy7 channel for antibody concentration calculation prevented its use for IS labeling for cyCIF studies decreasing the maximum throughput of the Ab-oligo cyCIF technique. Therefore, following estimation of antibody loss and Ab-oligo conjugation ratio for a variety of conjugates, Cy7 conjugation directly to the antibody was discontinued and not integrated as a standard step in the development of future Ab-oligo conjugates.

The use of the SiteClick kit allowed for a maximum of four DBCO-alkyne-modified oligo molecules to bind to an antibody. However, the molar ratio of oligo added to the antibody required strict control to prevent unconjugated oligo from causing off-target labeling and non-specific background fluorescence during cyCIF staining. One way to circumvent this was to limit the target molar ratio, where molar ratios of 4-20 oligos per antibody were evaluated. However, in practice maximum saturation of the conjugation sites was rarely achieved (i.e., conjugation ratios averaged 1-1.5 oligos per antibody) and unconjugated oligo remained in the final Ab-oligo product. For high antigenicity targets, such as CK19, non-specific background due to these unconjugated DS did not visibly affect the staining pattern. However, antibodies with lower affinity required additional purification for successful staining (**Fig. 2.2**). However, additional purification steps resulted in further Ab-oligo loss. To this end, we optimized the conjugation reaction by limiting the amount of added oligo to a molar excess of 4-5 oligos per antibody to achieve optimal Ab-oligo cyCIF staining (**Fig. 2.2C**). To further decrease non-specific background signal, blocking conditions were optimized to include sheared salmon sperm, dextran sulfate and SSC.

Optimal signal removal methods were investigated, balancing the need for complete staining pattern removal to the level of tissue autofluorescence while preserving tissue integrity and antigenicity. Herein, we examined six signal removal techniques to potentially be integrated into the Ab-oligo cyCIF workflow. In selecting the optimal signal removal method, we considered if signal could be reduced to background levels without damage to the tissue integrity through rounds of signal removal as well as cost and feasibility of the method to be scaled up for many biomarkers and tissue samples.

Strand-mediated displacement (SMD) employed removal of fluorescence via competition of oligo sequences to remove the fluorophore label. While this method provided specific Ab-oligo staining and signal removal, the addition of a third sequence to the workflow added substantial reagent cost, staining time and protocol complexity and was not further pursed (**Fig. 2.3**). Oligo sequences were designed to have a restriction enzyme (RE) recognizable sequence upon

hybridization of the DS/IS pair that could be cleaved to remove the fluorophore (**Fig. 2.4A**). RE-based Ab-oligo signal removal was sufficient for antigens localized to cell membranes and cytosol (**Fig. 2.4B**), but signal removal of organelle and nuclear localized antigens was frequently incomplete (**Fig. 2.4C-2.4H**). Notably, multiple rounds of RE treatment, increased RE concentrations and long incubation times were not adequate for full signal removal and also increased the time and cost of this method. Similar to SMD, these shortcomings caused fluorescence signal removal through RE site cleavage to be abandoned in lieu of more feasible signal removal options for Ab-oligo cyCIF.

Thermal denaturation of the hybridized DS/IS duplex as a method of fluorescence signal removal exploited the melting temperature (T_m) of the DS/IS bond which is influenced by both the length and G-C composition of the hybridized sequences.[118-120] Repeatable signal removal to the level of tissue autofluorescence was facilitated by heating the samples to ~5 °C above the calculated T_m. Antibodies can be stripped from tissue if subjected to high temperatures even after fixation, so IS of varied length were investigated since shorter IS have lower T_m and are thus potentially advantageous for preserving tissue integrity and antigenicity. However, the shorter IS were found to hybridize less efficiently to DS than the longer IS which resulted in a trade-off between Ab-oligo specific staining and successful signal removal (**Fig. 2.5E, 2.5F, 2.6B**). Under our experimental conditions, Ab-oligo specific staining over multiple rounds was only achieved for highly expressed targets, such as CK19, using the shorter IS (**Fig 2.6**). Notably, use of thermal denaturation improved Ab-oligo staining following the initial heating for certain targets (i.e., CK19). However, multiple rounds of heating and reapplication of IS largely resulted in increased background that overwhelmed the Ab-oligo specific staining pattern. Thus, while thermal denaturation-based signal removal was inexpensive and relatively rapid, given its disadvantages it was not further pursued.

The TCEP disulfide bond signal removal method had the fastest signal removal step, giving it a distinct advantage over the previously described methods (**Fig. 2.7B**). Additionally, this method was non-destructive as target antigenicity was maintained after incubation with TCEP for signal removal (**Fig. 2.7C**). However, the additional steps required for successful IS hybridization to the DS to avoid disulfide cleavage prior to image capture often increased background signal (**Fig. 2.7D**), which was problematic for acquiring marker specific labeling of Ab-oligo conjugates. The photocleavable linker (PCL) modification adjacent to fluorophore on the IS enabled rapid removal of the Ab-oligo staining pattern through UV light treatment (**Fig. 2.8**). This method had several distinct advantages over all other investigated signal removal methods. PCL-based signal removal had both a simpler workflow and faster signal removal compared to both SMD and RE cleavage. It had the advantage over thermal denaturation that full-complementary IS could be used, rather than shorter IS, equating to increased fluorescence signal and therefore sensitivity to the detection of lower abundance antigens. Additionally, the workflow was more streamlined and did not produce the background seen in the heating or TCEP signal removal methods making signal removal through PCL cleavage superior to all methods tested. Based on these advantages and its superior performance to all other methods tested, we integrated the PCL signal removal technique

into the Ab-oligo cyCIF workflow resulting in the generation of 12-color image data sets with complete signal removal between rounds of imaging and minimal tissue loss.[112] The simple workflow for staining, image acquisition and signal removal will allow for ready integration into an automated staining and imaging system in the future for increased throughput.

While the incorporation of photocleavable linkers (PCL) into the Ab-oligo cyCIF workflow offers a promising avenue for fluorescence signal removal in highly multiplexed image generation, there also exist some limitations to this technique. One limitation is the time required for complete signal removal which is longer than alternative signal removal strategies such as cleavage of disulfide linkers (i.e., Akoya Codex).[67] While PCL-based signal removal requires 15 minutes of UV light exposure, the Codex methodology is completed 5X faster in only 3 minutes. This represents the potential for more rapid data acquisition over the course of many cycles of imaging. An additional limitation to the employment of PCLs in the Ab-oligo cyCIF workflow is the additional costs associated with modifications to oligos of both fluorophores and PCLs. This is contrast to the Nanostring Digital Spatial Profiler platform where oligos with a single PCL are used to label antibodies.[124] In the Nanostring platform, the oligos are cleaved and the abundance of each antibody's unique oligo is measured, eliminating the need for multiple oligos and multiple oligo modifications. This results in a decreased reagent cost and a more streamlined antibody staining process where only a single step is necessary to label the tissue for measurement. These limitations of the Ab-oligo workflow should be considered and addressed for further advancement of the methodology to facilitate optimal scaling of the platform.

In summary, DNA barcoded antibodies are becoming a common tool used in cyclic immunostaining where multiplexed imaging studies seek to reveal the complex spatial proteomics of biological samples. DNA barcoded antibodies are a versatile option with multiple choices for both oligo conjugation and signal removal, many of which are described herein. Site specific labeling generated Ab-oligo conjugates that reliably and specifically labeled their target antigens. Additionally, we sought to optimize this method to improve fluorescence signal intensity and antibody retention for a variety of tested antibodies by carefully controlling the conjugation ratio and purification steps. All of the tested signal removal methods achieved the goal of fluorescence signal removal to permit additional rounds of staining with discussed advantages and disadvantages. Given its performance, our preferred signal removal method was PCL cleavage because the signal was removed to tissue autofluorescence levels, and it was easily integrated into our workflow. This method can be used alone, or in conjunction with other signal removal methods in order to generate highly multiplexed datasets requisite for complete characterization of tissues.

Chapter 3

Oligonucleotide conjugated antibodies permit highly multiplexed immunofluorescence for future use in clinical histopathology

This manuscript was originally published in *Journal of Biomedical Optics*. McMahon NP*, Jones JA*, Kwon S, et al. Oligonucleotide conjugated antibodies permit highly multiplexed immunofluorescence for future use in clinical histopathology. J Biomed Opt. 2020 Apr 24;25(5):1-18.

ABSTRACT

Significance: Advanced genetic characterization has informed cancer heterogeneity and the challenge it poses to effective therapy; however current methods lack spatial context which is vital to successful cancer therapy. Conventional immunolabeling, commonplace in the clinic, can provide spatial context to protein expression. However, these techniques are spectrally limited, resulting in inadequate capacity to resolve the heterogenous cell subpopulations within a tumor.

Aim: We developed and optimized oligonucleotide conjugated antibodies (Ab-oligo) to facilitate cyclic immunofluorescence (cyCIF), resulting in high dimensional immunostaining.

Approach: We employed a site-specific conjugation strategy to label antibodies with unique oligonucleotide sequences, which were hybridized *in situ* with their complementary oligonucleotide sequence tagged with a conventional fluorophore. Antibody concentration, imaging strand concentration and configuration as well as signal removal strategies were optimized to generate maximal staining intensity using our Ab-oligo cyCIF strategy.

Results: We successfully generated 14 Ab-oligo conjugates and validated their antigen specificity was maintained in single color staining studies. With the validated antibodies, we generated up to 14-color imaging data sets of human breast cancer tissues.

Conclusion: Herein, we demonstrated the utility of Ab-oligo cyCIF as a platform for highly multiplexed imaging, its utility to measure tumor heterogeneity, and potential for future use in clinical histopathology.

INTRODUCTION

Our understanding of cancer has evolved from a view of a collection of cells exhibiting unchecked proliferation to the realization that cancers include heterogenous genetic cell populations able to evade death through oncogenic dysregulation[25, 101] and complex interactions with the tumor microenvironment.[102-104] We owe much of our recent understanding to large cancer genome sequencing efforts that uncovered novel cancer genes and genetic diversity using molecular characterization technologies such as next generation sequencing and quantitative polymerase chain reaction (qPCR) sequencing studies. However, the translation of complex genomic analyses to gold standard pathological diagnoses remains challenging as conventional immunohistochemical (IHC) and immunofluorescence (IF) staining are limited to ~2-5 antigens per sample.[110] Additionally, while genomic analyses are a powerful therapeutic tool, they are deployed at the cost of spatial context of biomarker distribution. Recent discoveries have revealed the significance of the spatial relationships between cancer, immune, and microenvironmental cells in response and resistance to therapy,[125, 126] highlighting the importance of their preservation. Thus, to further understand the diagnostic and prognostic implications of these relationships, a molecular profiling technology to measure both expression and spatial context of biomarkers, while preserving both will be required.

While conventional immunolabeling techniques permit simultaneous expression and spatial context analysis of proteins, their spectral limit (i.e., ~2-5 antigens/sample) requires a modified solution to understand the complexity of cancer proteomics *in situ*. To overcome these limitations, a number of strategies have been developed to increase single sample specific antigen labeling, but to date, none of these methods can be seamlessly integrated into routine clinical histopathology. Mass spectroscopy techniques such as multiplexed ion beam imaging (MIBI)[30, 70, 71] and CyTOF[72] offer significant multiplexing capabilities using rare earth metal mass tags with simultaneous detection of up to 40 antigens in formalin fixed paraffin embedded (FFPE) tissues demonstrated.[70] However, integration into clinical histopathology will present significant challenges including (1) nontrivial generation of isotope labeled probes, (2) detection of low abundance antigens is generally poor, and (3) translation to the routine pathology lab will be difficult due to instrumentation expense and required technological expertise. IF permits higher dimensionality immunostaining than IHC, but the maximum number of fluorophores that can be visualized on a single sample using conventional fluorescence microscopy is five and using unmixing techniques is improved to seven.[75, 110, 127] Various techniques using sequential cycles of fluorescent tagging, imaging, and bleaching[73, 76, 128] or dissociation of affinity tags[78, 110, 129] have demonstrated multiplexing capabilities of up to 61 immunostained targets in a single sample.[73] Cyclic IHC techniques have also been developed, facilitating staining of up to 12 antigens on a single sample stained and imaged one-by-one.[74] Although these techniques improve multiplexing capabilities, they will be difficult to incorporate into clinical histopathology because (1) antigenicity of the tissue is affected by the bleaching and destaining methods[79] and (2) steric hindrance issues can occur as cycle number increases.[71, 130] Antibody barcoding techniques (e.g., Nanostrings,[80, 81] CODEX,[67] DNA Exchange Imaging (DEI),[82] Immuno-SABER[83]) have also been

developed, demonstrating the ability for highly multiplexed cyclic fluorescence imaging using non-destructive signal removal techniques. Nanostrings has been shown to visualize up to 90 antigens in a single cellular sample[80] and after extension of Nanostrings technology to tissue has been demonstrated to visualize 32 antigens, but is not yet feasible for whole tissue imaging.[81] Nanostrings assessment of entire tissue sections for clinical histopathology will be time consuming and costly, as spot scanning at 100x100μm resolution for detection is required and since barcodes are released from tissue for detection, subcellular resolution is not possible. In contrast, CODEX, DEI and Immuno-SABER have demonstrated the capability of subcellular resolution paired with high dimensional imaging. However, due to protocol complexity, instrumentation expense and the necessary technological expertise they are not amicable to integration with clinical workflow. Therefore, although multiplexed protein detection is possible, none of the current methods will readily translate to routine clinical histopathology.

Our novel, highly-multiplexable, cyclic IF (cyCIF) technique is capable of generating multi-parametric images for quantifying biomarker expression and distribution and is readily translatable to the clinical setting. While similar to other antibody barcoding techniques, the workflow described herein has minimal variation from indirect IF tissue staining procedures that are commonplace in the clinical laboratory setting. Termed antibody conjugated oligonucleotide (Ab-oligo) cyCIF, it preserves tissue antigenicity and lends itself to ready integration into clinical workflows. Similar to the Nanostrings technology, our Ab-oligo cyCIF exploits *in situ* hybridization of complementary oligonucleotides for biomarker labeling and the oligo modifications to facilitate signal removal for sequential rounds of fluorescent tagging and imaging. In our technology, a single stranded oligo (docking strand, DS) is conjugated to the primary antibody. Subsequent introduction of a complementary single stranded oligo (imaging strand, IS) conjugated to a conventional Alexa Fluor (AF) fluorophore (e.g., AF488, AF546, and AF647) facilitates specific on tissue fluorescent labeling through *in situ* hybridization and imaging with any conventional fluorescence microscope. The presence of a photocleavable linker (PCL) between the fluorophore and oligo sequence facilitates signal removal to levels of autofluorescence after ultraviolet (UV) light exposure and prior to subsequent staining cycles, while maintaining hybridization between the DS/IS pair after imaging to diminish the possibility for any cross-talk between staining cycles. The advantages of our method over other multi-staining methods include (1) all Ab-oligos are applied in a single mixed cocktail at the beginning of the study, preventing steric hindrance and (2) application of all Ab-oligos in a single staining step drastically reduces overall staining time, as only a single long antibody incubation step is required. Ab-oligo cyCIF is therefore able to visualize endogenous protein expression while maintaining spatial context *in situ*, which is critical to identifying heterogenous cell populations within tumors. Using our Ab-oligo cyCIF platform, we have generated up to 14 color images on multiple breast cancer FFPE samples as proof-of-concept of our cyCIF technology.

Quantification of protein signatures *in situ* could revolutionize cancer care in much the same way genomic analyses have changed the landscape of cancer diagnosis and therapy selection. Reliable and robust quantitative analysis of protein signatures will require a consistent,

multiplexed, *in situ* staining method with a coupled computational visualization and analysis platform that generates repeatable biomarker and clustering signatures. Additionally, to influence clinical decisions, this methodology must integrate seamlessly into the clinical histopathology workflow. Herein, we validate our Ab-oligo cyCIF methodology, demonstrating its capability to produce high dimensionality data from a single tissue sample with the potential to unravel the complexity of a tumor with the capability for ready translation into the clinical setting.

MATERIALS & METHODS

Primary Antibody Conjugation. Monoclonal antibodies were purchased from AbCam (Cambridge, UK), Thermo Fisher Scientific (Waltham, MA), Biolegend (San Diego, CA), or Cell Signaling Technology (Danvers, MA) to the following targets: cytokeratin 5 (CK5), cytokeratin 8 (CK8), cytokeratin 19 (CK19), proliferating cell nuclear antigen (PCNA), Ki-67, E-Cadherin (E-Cad), human epidermal growth factor receptor 2 (HER2), α smooth muscle antigen (α-SMA), CD44, CoxIV, CD4, and CD3 (**Table 3.1**). A unique dibenzocyclooctyne (DBCO) or amine-terminated single-stranded oligonucleotide (docking strand, DS, 28 mer in length) was obtained from Integrated DNA Technologies (IDT, Coralville, IA) to conjugate to each primary antibody. Prior to modification, the IgG antibodies were purified from storage buffers including excess azide reagent using 50 kDa Amicon filters (EMD Millipore, Burlington, MA). Antibody modification and oligonucleotide (oligo) conjugation were performed using either the SiteClick™ Antibody Azido modification kit (Thermo Fisher Scientific) or the Solulink™ antibody modification kit (TriLink Biotechnologies, San Diego, CA) following the manufacturer's instructions, explained briefly as follows. The SiteClick kit cleaved the carbohydrate domains on the heavy chains of the monoclonal IgG antibodies using β-galactosidase, enabling addition of an azido moiety. The DBCO-terminated DS was mixed with the azido modified whole immunoglobin G (IgG) and standard copper free click chemistry reagents resulting in site-specific labeling of the antibodies

Table 3.1: Oligonucleotide conjugated antibodies (Ab-oligos).

	Biomarker	Vendor	Ab-oligo CR	FL CR	Stained Tissue	DS Oligonucleotide Sequence
Cell State	CK5	AbCam	1.20	0.52	Normal Breast	5'-AATATGGAATTCGTCCGAGCCCGTCAAG-3'
	CK8	AbCam	1.27	0.58	Normal Breast	5'-CCCAAAGGTACCCGTCGTAGTAACAAAG-3'
	CK19	Biolegend	0.85	1.74	Normal Breast	5'-AATAATGTCGACTACGCCTGACCGTCGT-3'
	PCNA	AbCam	1.24	0.95	MDA-MB-468	5'-ATTTACGGTACCAGTCGTACAAGACGGG-3'
	Ki-67	AbCam	1.15	0.74	MDA-MB-468	5'-AAGAAGCTGCAGTGCGATTTAAGGTCGG-3'
	E-Cadherin	AbCam	1.13	0.48	Normal Breast	5'-TTATATCCATGGCCGCAATCGCCTCGAT-3'
Breast Cancer	HER2	Thermo	1.09	1.72	Sk-Br-3	5'-AAAATTCGGCCGTGAAGTCGTTCGCCAG-3'
Stroma	α-SMA	AbCam	1.24	0.62	Normal Breast	5'-ATATATGGATCCCTGGCGTGGTTCGTCG-3'
	CD44	AbCam	1.30	0.70	MDA-MB-468	5'-AATATAGTCGACCGCCGATGCTTCGTGG-3'
Architecture	Cox IV	CST	1.26	1.38	Sk-Br-3	5'-TTAATTCGGCCGCGCTTACGGACTCAGT-3'
Immune	CD4	AbCam	1.20	0.88	Tonsil	5'-ATCTTTCAGCTGCGAACGTAAACCTCGG-3'
	CD3	AbCam	1.48	0.91	Tonsil	5'-TACACCAAGCTTTAAACTGCGAGCGACA-3'

*CR = Ab-oligo conjugation ratio, FL CR = antibody to fluorophore conjugation ratio for direct immunofluorescence comparison with Ab-oligo cyCIF.

with their unique oligo sequence (Ab-oligo). Using the Solulink kit, the antibody was modified at the available lysine residues, where a S-HyNic (part# S-9011-1-01, TriLink Biotechnologies) small molecule was conjugated. Simultaneously, the amine-terminated DS was covalently modified to contain a 4-FB (part# S-9011-1-02, TriLink Biotechnologies) small molecule on the 5' end. The 4-FB modified DS and S-HyNic conjugated antibody were mixed together at a molecular target ratio of 20 oligos to 1 antibody and the N-Hydroxysuccinimide (NHS) ester reaction occurred in the presence of the Turbolink™ catalyst (part# S-9011-1-05, TriLink Biotechnologies). Excess oligo was removed from the Ab-oligo conjugates using molecular weight cut off (MWCO) spin columns. After purification, the absorbance of the Ab-oligo conjugate was measured on a Spectramax M5 (Molecular Devices, San Jose, CA). The maximum absorbance of the antibody and conjugated DS were measured at 280 and 260 nm, respectively. Using the estimated extinction coefficient of 210,000 $M^{-1}cm^{-1}$ for all antibodies and the manufacturer reported extinction coefficient for each DS, the approximate Ab-oligo conjugation ratios (CR) were calculated to quantify the average number of oligos conjugated to an antibody.

An aliquot of the same primary antibody used for oligo conjugation was directly conjugated to Alexa Fluor 555 NHS ester (AF555 NHS, Thermo Fisher Scientific). The starting antibody concentration was determined by measuring the absorbance at 280 nm prior to any conjugation chemistry. The primary antibody was again purified of any storage buffers (e.g., sodium azide) and buffer exchanged into 1X PBS, pH 8.3 with a 10 kDa Amicon filter. AF555 NHS was resuspended at 10 mM in anhydrous dimethyl sulfoxide (DMSO) and added to the antibody at a ratio of 10 fluorophore molecules to 1 antibody in a reaction volume of 1 mL. The mixture was rocked gently at 4 °C for 3 hours protected from light. The antibody conjugate was then purified with a 10 kDa Amicon filter. Absorbance was measured at 280 and 555 nm to calculate the antibody and fluorophore concentrations, respectively enabling quantification of the conjugation ratio or the average number of fluorophores conjugated to an antibody (FL CR).

Formalin Fixed Paraffin Embedded (FFPE) Tissue & Cell Samples for Antibody Validation. Deidentified human FFPE tissue blocks were obtained from the Oregon Health and Science University (OHSU) Knight Biolibrary. The functionality of oligonucleotide and fluorophore conjugated antibodies were validated on FFPE blocks of normal breast tissue, normal tonsil tissue and FFPE cell buttons generated from MDA-MB-468 or SK-BR-3 breast cancer cell lines. All cell lines were originally purchased from ATCC (Old Town Manassas, VA) and maintained at <25 passages for all experiments. The tissue or cell button type known to express the target of interest was used for validation of each primary antibody (**Table 3.1**). 5 μM sections of the selected FFPE block were captured onto 1x3-inch Superfrost™ Plus slides (Thermo Fisher Scientific), which were baked at 65 °C in a hybridization oven for 30 minutes to overnight prior to commencing staining.

Antibody Staining on FFPE Samples. The baked FFPE slides were deparaffinized at room temperature (RT) in xylenes (2 x 10 min washes). The tissue was then gradually rehydrated in ethanol and water solutions as follows: 100% ethanol (2 x 10 min), 95% ethanol (1 x 5 min), 70% ethanol (1 x 5 min), then 50% ethanol (1 x 5 min). The tissue was then rinsed in 100%

deionized water (diH_2O) followed by a wash in 1X PBS, pH 7.4 for 10 minutes. A two-step antigen retrieval procedure was performed in a Pascal Pressure Cooker (Dako, Santa Clara, CA). RT solutions of 10 mM sodium citrate, pH 6, 1X tris hydrochloride (HCl), pH 8 and diH_2O were placed in the pressure cooker in three individual plastic buckets immersed in 500 mL of diH_2O, which covered the bottom of the chamber. The slides were immersed in the sodium citrate buffer and the pressure cooker lid was secured. The temperature was increased to 125 °C over a 15 min period, where the pressure reached ~15 psi. The pressure cooker was removed from heat, and the temperature and pressure were allowed to decrease to 90 °C and 0 psi respectively over ~25 min. The residual pressure was released as the lid was removed and the slides were rinsed in the hot diH_2O. The slides were immediately placed in the hot tris-HCl buffer, where they were incubated for 10 min with the lid on the pressure cooker. The slides were then transferred back to the hot diH_2O and brought back to RT by slow addition of RT water to the vessel. After 5 min in RT diH_2O, the slides were washed in PBS, pH 7.4 at RT for an additional 5 min.

Antibody staining studies were completed using four groups for staining pattern validation including: (1) conventional indirect immunofluorescence with unconjugated primary and fluorophore conjugated secondary antibody, (2) the Ab-oligo conjugate plus the same fluorophore conjugated secondary antibody, (3) the Ab-oligo conjugate plus the complementary fluorophore conjugated imaging strand (IS) and (4) the fluorophore labeled primary. The same overall staining procedure was used for each group, explained as follows. The antigen retrieved slides were blocked at RT for 30 min in Ab-oligo blocking and dilution buffer which contained 2% bovine serum albumin (BSA, bioWORLD, Dublin, OH), 0.5 mg/mL sheared salmon sperm DNA (Thermo Fisher Scientific) and 0.5% dextran sulfate (Sigma-Aldrich, St. Louis, MO) in 1X PBS, pH 7.4. The Ab-oligo conjugate was diluted in the Ab-oligo blocking and dilution buffer to a final protein concentration of 15 μg/mL. The tissue sections were covered with 40-100 μL of the diluted Ab-oligo conjugate and incubated at 4 °C overnight in a humidified chamber. The next day, the sections were washed with 2X saline-sodium citrate (SSC) buffer, pH 7 (VWR, Radnor, PA) for 3 x 5 min. The sections were fixed in 2% paraformaldehyde (PFA, Sigma-Aldrich) for 15 min at RT, then washed again in 2X SSC buffer (3 x 5 min).

For groups (1) and (2), AF555 conjugated secondary antibody was added at 350 nM. For group (3), complementary IS labeled with Alexa Fluor 546 (AF546), diluted to 350 nM in IS dilution buffer containing 2% BSA, 0.5 mg/mL sheared salmon sperm DNA and 0.5% dextran sulfate in 2X SSC buffer was added. The sections were incubated with IS at RT protected from light for 45 min. The IS was removed and the sections were washed in 2X SSC buffer (3 x 5 min). The slides were protected from light for the remainder of the staining procedure. Group (4) did not require any secondary detection reagent. DAPI (Thermo Fisher Scientific) was applied to all stained sections at 300 nM for 10 min at RT and the slides were then washed in 2X SSC buffer (2 x 5 min). The stained slides were mounted in Fluoromount-G (Southern Biotech, Birmingham, AL) and cover-slipped for imaging.

Fluorescence Microscopy, Image Visualization & Image Analysis. Antibody-stained slides were imaged on a Zeiss AxioImager.M2 with motorized XY scanning stage (Carl Zeiss AG,

Oberkochen, Germany) equipped with a CoolSNAP HQ2 14-bit CCD camera (Photometrics, Tucson, AZ). Fluorescence images were collected using three channels for IS visualization. Depending on the fluorophore used for IS labeling, the following Zeiss filter sets were used: 38HE (Cy2/AF488), 43HE (Cy3/AF555) and 50 (Cy5/AF647). Excitation light was filtered using the following bandpass (BP) filters 470/40 (HE), 550/25 (HE) and 640/30, for AF488, AF546/AF555 and AF647 respectively. Emission light was filtered using the following BP filters 525/50 (HE), 605/70 (HE) and 690/50, for AF488, AF546/AF555 and AF647 respectively. DAPI was imaged using Zeiss filter set 49 (UV/DAPI), where excitation was filtered at 365 nm and emission was filtered using a 445/50 BP filter. Single color, single field of view images were collected using an X-Cite 120Q (Excelitas Technologies Corporation, Waltham, MA) light source at 40X (Plan-Apochromat, 0.95NA) magnification. Images of the entire FFPE section were collected with 10% overlap at 20X (Plan-Apochromat, 0.8NA) magnification, where overlapping images were tiled into a single tissue map. Each fluorescence channel was registered using QiTissue Software (Quantitative Imaging Systems, Pittsburg, PA).

Signal-to-background ratio (SBR) was calculated from collected images using a Python script to extract mean fluorescence intensity of marker specific fluorescent signal and separate the background from each image (DOI: 10.5281/zenodo.3738745). To quantify the marker specific signal, a threshold was established to create a binary mask to extract mean fluorescent intensity from only pixels in positively stained regions of the image. The threshold was established manually using ImageJ v1.51 (NIH) where the histogram minimum and maximum was adjusted to only display positive pixels. Positive pixels were displayed white and equal to one in the image array while negative pixels were black and equal to zero. For example, a binary mask for a membrane specific marker would be created where only tissue membrane pixels were white. The binary image array of ones and zeros was used to filter pixels to be counted if their binary image array location had a value of one. To measure background fluorescence, the binary mask was inverted to measure fluorescent signal from pixels not in positively stained regions of the tissue where now the background pixels previously valued as zero in the binary array were equal to one and included in the background fluorescence quantification. SBRs were calculated for image data sets by dividing the signal fluorescent intensity by the background fluorescent signal intensity. Mean fluorescence intensity was used in lieu of SBR for data reporting signal removal in which signal is only present prior to signal removal making SBR an inappropriate metric for image analysis after signal removal.

Ab-oligo conjugate titration. The previously detailed FFPE antibody staining procedure was used to stain normal breast tissue with CK8 Ab-oligo conjugate after being diluted in Ab-oligo dilution buffer to final concentrations of 15μg/mL, 5 μg/mL, 1.5 μg/mL and 0.15 μg/mL. Images were collected at 60 ms with varying contrast settings to display positive staining at all Ab-oligo concentrations. The images were then used to calculate mean intensity of CK8 specific positive staining, as previously described, to evaluate the optimal staining concentration.

Ab-oligo IS titration. The previously detailed FFPE antibody staining procedure was used to stain normal breast tissue with E-Cad or α-SMA Ab-oligo conjugates and triple negative breast

cancer tissue with the Ki67 Ab-oligo conjugate. The complementary IS was diluted in IS dilution buffer, and added to the Ab-oligo-stained slides at 100, 250, 350, 500, 750 or 1000 nM. Images were collected at 300 ms for E-Cad, 10 ms for α-SMA and 500 ms for Ki67 Ab-oligo conjugates. The displayed images have varying contrast settings to exhibit positive staining pattern at all IS concentrations. The images were used to calculate SBR as previously described, which was used to evaluate the optimal staining concentration.

Optimal IS fluorophore configuration. SK-BR-3 cell buttons were stained with the HER2 Ab-oligo conjugate and normal breast tissue was stained with the E-Cad Ab-oligo conjugate using the previously described FFPE staining protocol. IS with fluorophore labeled on either the 5' (i.e., one fluorophore) or both the 5' and 3' ends (i.e., two fluorophore) were used for detection. Ab-oligo-stained cell buttons or tissues were subsequently stained with 250 nM of the one fluorophore or two fluorophore labeled IS. Images of each stained tissue were collected at 3000 ms for HER2 and 175 ms for E-Cad and used to calculate SBR to determine the optimal IS configuration.

Signal Removal using Photocleavable Linkers with Varied IS Length. Normal breast tissue was stained with the E-Cad Ab-oligo conjugate using the previously described FFPE staining protocol. IS of varied length (28, 27 and 26 mer) that contained a photocleavable linker and AF546 fluorophore on both the 3' and 5' ends were used for staining at 350 nM. As a positive control, a 28 mer IS with AF546 on both the 3' and 5' end without photocleavable linkers was used. Images of the stained tissues were collected at 600 ms. The mean fluorescence intensity of each image was calculated to determine the optimal IS length. Following imaging, the slides were treated with ultraviolet (UV) light for 15 minutes on a UVGL-55 Handheld UV lamp (UVP Upland, CA) through the cover glass. The UV treated slides were placed vertically in 0.1X SSC for 5 minutes, allowing removal of the cover glass. The slides were then washed 10 times with 0.1X SSC and mounted using Fluoromount-G prior to imaging using the same settings. The mean fluorescence intensity of the image was again quantified to determine the amount of retained signal.

Multiplexed Ab-oligo Staining and Imaging. HER2+ BC and BC tissue microarray (TMA) FFPE samples were stained with a cocktail of the 14 Ab-oligo conjugates using the previously described staining protocol. The 12 antibodies outlined in **Table 3.1** as well as oligo conjugated estrogen receptor and PD-1 antibodies were mixed at a concentration of 15 μg/mL per antibody into a single cocktail for staining. The tissues stained with the Ab-oligo conjugates were labeled with IS in rounds, where IS labeled with distinct fluorophores and complementary to three Ab-oligos were stained at 350 nM in each staining round. Serial sections were used for staining with the Ab-oligo cocktail or IS only as a negative control. Images were collected in all three channels (AF488, AF546 and AF647), followed by a separate image of the DAPI channel. All stained slides were treated with UV light for 15 minutes followed by washing 10 times with 0.1X SSC and remounted with Fluoromount-G. Finally, the slides were imaged with the same settings used prior to UV treatment to quantify any remaining signal. Subsequent rounds of IS addition, imaging and signal removal were repeated until all Ab-oligo conjugates were imaged.

Tissue Damage Quantification of Ab-oligo cyCIF. DAPI images from each round of cyclic staining were analyzed using ilastik[131] v1.3.3 (European Molecular Biology Laboratory) to quantify the number of nuclei present in first round and quantify tissue loss in subsequent rounds. First, a pixel classifier was developed in the Pixel Classification pipeline. The classifier was trained and applied on the full tissue image for each tissue sample to stratify pixels as either a pixel of a cell nucleus or as a background pixel. A map where each pixel was identified as either a nuclear or background pixel was then used in the Boundary-based Segmentation with Multicut pipeline to create objects from the classified pixels. A watershed algorithm was applied to plant watershed seeds inside of each nucleus. The boundary of each watershed object was then exported as the object segmentation map. The object segmentation map was put into the Object Classification pipeline where a classifier was trained to identify each object as either background or a cell. After applying the classifier to the full tissue image, a comma-separated values (csv) table was exported identifying each object as either background or cell. The number of cell objects for each image were then counted to quantify tissue loss per round of cyclic staining.

RESULTS

Staining pattern validation of Ab-oligo conjugates. Optimal Ab-oligo conjugate staining concentrations was evaluated on tissue positive for CK8 (**Fig. 3.1A**) where titration of the Ab-oligo conjugate was performed from 0.15-15 μg/mL. Quantification of CK8 specific fluorescent signal of the same structure in serial FFPE tissue sections showed the highest mean intensity using 15 μg/mL of Ab-oligo conjugate (**Fig. 3.1B**). Subsequently, the optimal IS staining concentration was assessed on tissues positive for α-SMA, E-Cad and Ki67 (**Fig. 3.1C**), where IS was titrated from 100-1000 nM. The resulting images were qualitatively and quantitatively assessed showing increased SBR from 100-350 nM IS concentrations, with little SBR increase with further increase in IS concentration (**Fig. 3.1D**), resulting in selection of 350 nM IS as the optimal staining concentration. A panel of 12 antibodies, selected to elucidate the cell state, breast cancer epithelial cells, stromal compartment, tissue architecture and immune infiltrate of HER2+ breast cancers (**Table 3.1**), were conjugated to unique DS. The staining pattern of each Ab-oligo conjugate with its complementary IS was confirmed using qualitative comparison to conventional indirect IF staining with an unconjugated primary, indirect IF staining using the Ab-oligo conjugate as the primary antibody and direct IF staining using a fluorophore-conjugated primary antibody. Negative control tissue was stained with secondary only, IS only or without any detection reagent (**Fig. 3.2**). The staining patterns for all 12 antibodies were qualitatively similar between conventional indirect IF, Ab-oligo indirect IF, Ab-oligo with IS detection and direct IF staining, demonstrating that oligonucleotide conjugation did not substantially change the affinity of the primary antibody. Four of the 12 antibodies showed similar SBR between conventional indirect IF and Ab-oligo indirect IF staining (**Fig. 3.2A**, **3.2E**, **3.2L**, & **3.2M**). Five of the 12 antibodies resulted in a lower SBR when comparing Ab-oligo indirect IF to conventional indirect IF staining (**Fig. 3.2B**, **3.2C**, **3.2D**, **3.2H** & **3.2I**). The other three Ab-oligo conjugates stained with secondary

antibody had higher SBRs than conventional indirect IF staining (**Fig. 3.2F**, **3.2J** & **3.2K**). As expected, Ab-oligo with IS staining required longer exposure times than either indirect IF method,

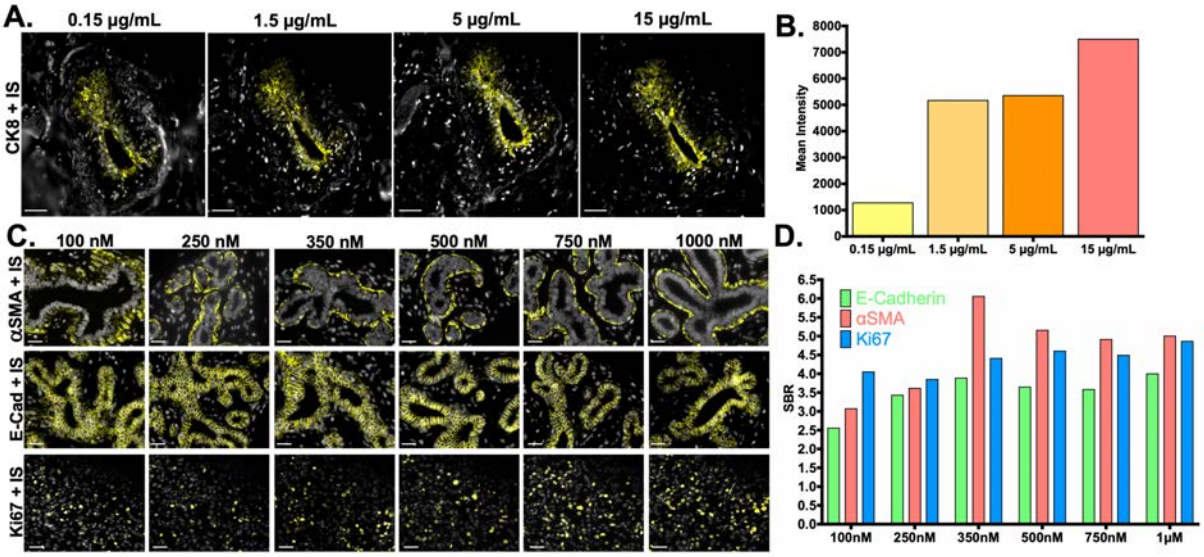

Fig. 3.1: *Ab-oligo conjugate and IS titration for optimal staining.* A. The CK8 Ab-oligo conjugate was titrated (0.15-15 µg/ml) onto serial sections of normal breast FFPE tissue and equivalent concentrations of IS were applied to all tissue samples for visualization. Images are displayed with contrast and gain optimized for visualization of the positive CK8 staining pattern generated at each antibody conjugate concentrations. B. Image quantification showed the highest mean fluorescence intensity using 15 µg/ml antibody concentration for tissue staining. C. IS was titrated (100-1000 nM) onto FFPE tissue with equivalent Ab-oligo conjugate concentrations present of αSMA (staining completed on normal breast tissue, top), E-Cad (staining completed on normal breast tissue, middle) and Ki-67 (staining completed on breast cancer tissue, bottom). D. The signal to background ratio (SBR) was calculated for each concentration tested for all biomarkers. 40 µm scale bars are displayed in all images.

generally resulting in decreased SBRs as compared to indirect IF. This required increase in exposure time can be attributed to the signal gain obtained using secondary antibodies that was not possible using the Ab-oligo with our IS staining strategy. As a more direct comparison, primary antibody directly conjugated to AF555 was used to stain serial sections and SBR was quantified for comparison. Overall similar SBRs were calculated for Ab-oligo detected with IS and direct IF staining, however, there were still sizable differences depending on the stained antigen. For all 12 selected antibodies, the negative control demonstrated that minimal nonspecific background contributed to the overall signal as only nuclear DAPI fluorescence was visible in the normalized control images (**Fig. 3.2**). Thus, all 12 Ab-oligo conjugates provided positive staining for the antigen of interest and were able to generate sufficient signal for visualization by conventional fluorescence microscopy.

Optimal IS Design. The measured average conjugation ratio (CR) of the 12 Ab-oligo conjugates was near one (average Ab-oligo CR = 1.22, **Table 3.1**). Thus, a single IS was expected to hybridize to each Ab-oligo conjugate during staining, accounting for the relatively long exposure times compared with indirect or direct IF, where multiple secondary antibodies or fluorophores were available for signal detection, respectively. In an effort to increase the Ab-oligo staining intensity, the IS was modified to contain a fluorophore on both the 3' and 5' ends (i.e.,

two fluorophore design). The Ab-oligo staining intensity was quantitatively compared using identical IS sequences with the one or two fluorophore design for HER2 (**Fig. 3.3A**) and E-Cad (**Fig. 3.3B**). As expected, the additional fluorophore increased the staining intensity resulting in improved SBR (SBR improvement with two fluorophores vs. one fluorophore design: E-Cad = 27.4% and HER2 = 29.9%, **Fig. 3.3D**). Due to the SBR increase for both HER2 and E-Cad, the IS design with fluorophore labeled on both the 3' and 5' ends (i.e., two fluorophore) was selected for all future studies.

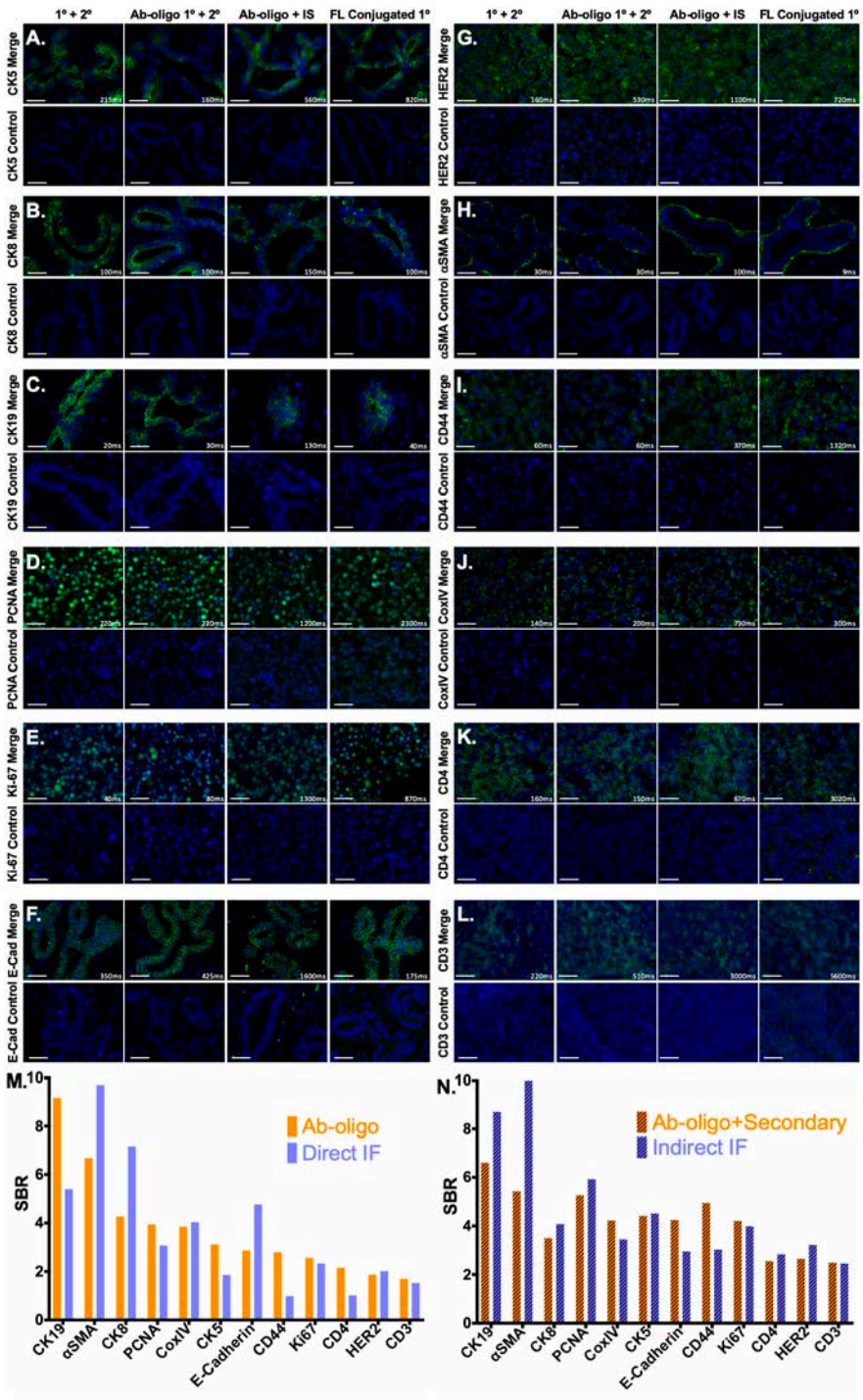

Fig. 3.2: *Ab-oligo conjugate staining validation.* The staining pattern of each Ab-oligo conjugate was validated by staining serial sections using conventional indirect IF (1°+2°), the Ab-oligo conjugate (1°) detected with a conventional fluorophore labeled secondary antibody (2°), the Ab-oligo conjugate detected using the complementary imaging strand (Ab-oligo + IS), and direct IF using fluorophore (FL) conjugated 1° antibody. The appropriate negative control image is located below their corresponding antibody-stained image. Ab-oligo staining pattern was verified for **A.** CK5, **B.** CK8, **C.** CK19, **D.** PCNA, **E.** Ki67, **F.** E-Cad, **G.** HER2, **H.** α-SMA, **I.** CD44, **J.** CoxIV, **K.**CD4 and **L.** CD3. SBR was calculated for **M.** each indirect IF and Ab-oligo + 2° image and compared to **N.** SBR calculated for each FL conjugated 1° antibody and Ab-oligo + IS image. 40 μm scale bars are displayed in all images.

Photocleavable linkers enable complete signal removal. Photocleavable linkers (PCL) were used as the signal removal strategy, where the size of the photocleavable linker and conjugated fluorophore were equivalent to ~2 nucleotides (nt). A study was conducted to determine if the size of the PCL and fluorophore label created steric hindrance at the 3' end of the IS binding to the DS using the exact 28 mer IS complement to the antibody conjugated DS.

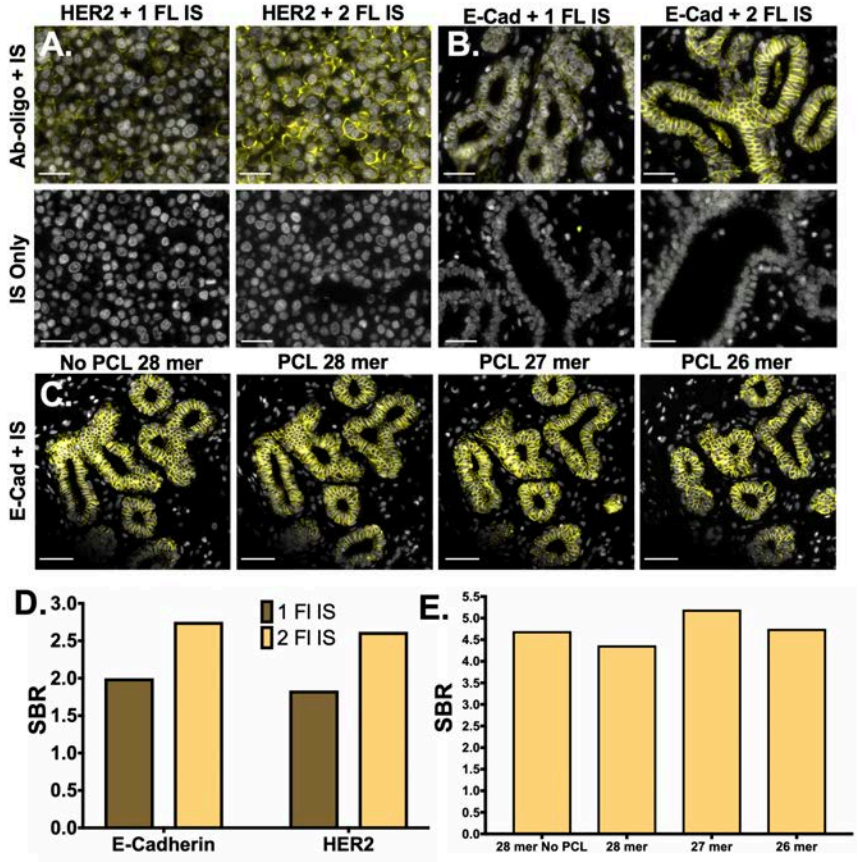

Fig. 3.3: *IS design optimization.* An IS labeled with a second fluorophore was compared to the original IS design with a single fluorophore for **A.** HER2 and **B.** E-Cad. **C.** IS length with and without a PCL was also investigated using E-Cad labeling. **D.** Images were quantified to calculate the SBR IS labeled with one or two fluorophores as well as **E.** with different oligonucleotide lengths (i.e., 26, 27 or 28 nt). 40 μm scale bars are displayed in all images.

Staining using the E-Cad Ab-oligo with a 28 nt IS sequence without PCL was compared to staining using IS of 28, 27, or 26 nt in length with PCL. Each IS was used to stain a consecutive tissue section as a negative control (**Fig. 3.3C**). Quantified mean fluorescence intensity was similar for all IS containing the PCL, regardless of sequence length (**Fig. 3.3E**). PCL signal removal was validated after each sample was treated with UV light, resulting in complete signal removal for all PCL containing IS, but maintained staining pattern in the 28 nt IS without PCL (**Fig. 3.3C** and **3.3E**). Although E-Cad staining intensity was not strongly affected by IS length, the 26 nt IS length was selected for further use to ensure that steric hindrance would not diminish Ab-oligo staining of other antigens.

Serial sections of the same test tissue per antigen (**Table 3.1**) were stained with IS containing fluorophore on both the 3' and 5' ends without PCL and with PCL (**Fig. 3.4**). Images of the staining pattern collected prior to UV light treatment demonstrated variable staining intensity with the addition of the PCL to the two fluorophore IS, with some targets showing similar mean fluorescence intensity with and without the PCL (**Fig. 3.4A**, **3.4D**, **3.4F** & **3.4J**), some showing lower mean fluorescence intensity with the PCL (**Fig. 3.4B**, **3.4C**, **3.4E**, **3.4H**, **3.4I**, **3.4K** & **3.4M**) and one showing improved mean fluorescence intensity with the PCL (**Fig. 3.4L**). Negative control slides stained with the IS only, where either the IS with or without the PCL was used, showed that no appreciable signal from non-specific staining or tissue autofluorescence contributed to overall staining intensity (**Fig. 3.4**). Antibody specific fluorescence signal was completely removed in the PCL containing IS stained samples, where signal intensity was reduced to levels akin to IS only negative control samples. As expected, the Ab-oligo staining pattern was maintained when the IS without PCL was used for staining, although some signal was lost after UV light treatment, which was likely due to photobleaching of the fluorophore label with the high energy UV light (**Fig. 3.4**).

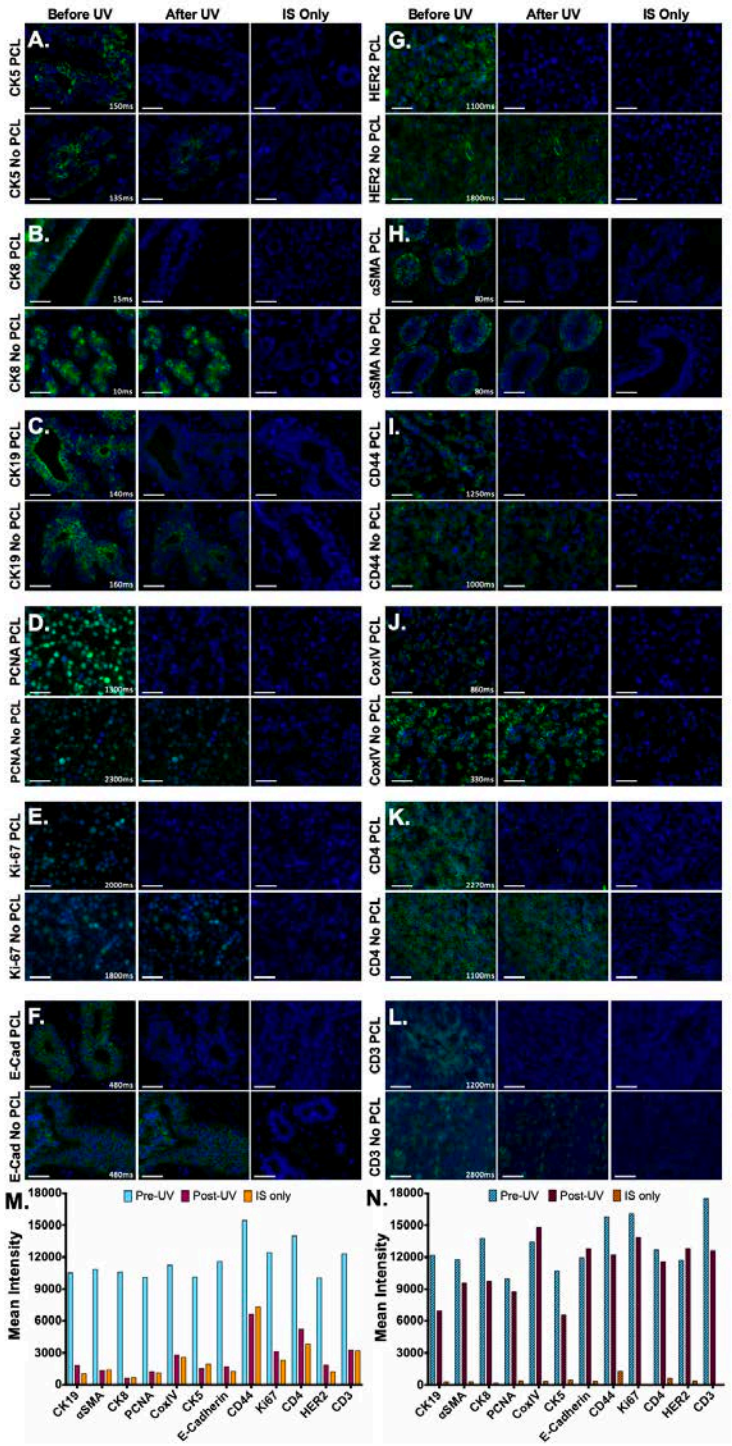

Fig. 3.4: *Ab-oligo signal removal validation using PCLs.* Ab-oligo conjugate signal removal using PCLs was validated by staining serial sections using Ab-oligo conjugate (1°) and IS without a PCL as well as Ab-oligo conjugate and IS with a PCL. Following image collection to demonstrate the Ab-oligo tissue staining pattern, each sample was treated with 15 minutes of UV light and images were again collected of each sample. Serial sections were stained with IS only and imaged as a negative control. The Ab-oligo staining pattern before and after UV treatment was verified for **A.** CK5, **B.** CK8, **C.** CK19, **D.** PCNA, **E.** Ki67, **F.** E-Cad, **G.** HER2, **H.** α-SMA, **I.** CD44, **J.** CoxIV, **K.**CD4 and **L.** CD3. The mean fluorescence intensity for each image before and after UV light treatment was quantified for samples stained **M.** with and **N.** without a PCL. 40 μm scale bars are displayed in all images.

Multicolor cyclic immunofluorescence staining & visualization. The validated set of Ab-oligo conjugates and PCL containing IS were used to generate multiplexed IF images of both a HER2+ breast cancer resection specimen (**Fig. 3.5**) and a breast cancer tissue microarray (TMA, **Fig. 3.6**). The cocktail of Ab-oligo conjugates was applied as a single stain, while IS were applied in groups of three, where each IS group had spectrally distinct fluorophore labeling. DAPI staining was used in each imaging round for registration and to monitor for any potential tissue loss throughout the cyclic staining experiment. Tissue scanning was performed in each IS staining round permitting image tiling for visualization of the entire specimen (**Fig. 3.5A**). A magnified field of view demonstrated the spatial resolution of the Ab-oligo cyCIF technique, where individual cell staining patterns were readily visualized (**Fig. 3.5B**). Staining of the HER2+ breast cancer tissue by round of IS staining showed variation in biomarker expression across the resection specimen for all interrogated biomarkers. As expected, the breast cancer epithelial cell marker HER2 as well as CK8 and CK19 were highly expressed in the breast cancer tumor nests. Proliferative cells, marked by Ki67 and PCNA were also largely localized to the breast cancer tumor nests. Immune markers, including CD3 and CD4, were localized to the periphery of the tissue sample, mostly isolated from the breast cancer epithelial cells (**Fig. 3.5A** & **3.5B**). Even with only 12 biomarkers imaged, the difficulty with simultaneous visualization become apparent as overlays of more than 4-5 colors in any single, static image were challenging to visualize and interpret. Using the QiTissue Software, static visualization was enhanced using additional visualization tools such as height maps to aid in data display (**Fig. 3.5C**).

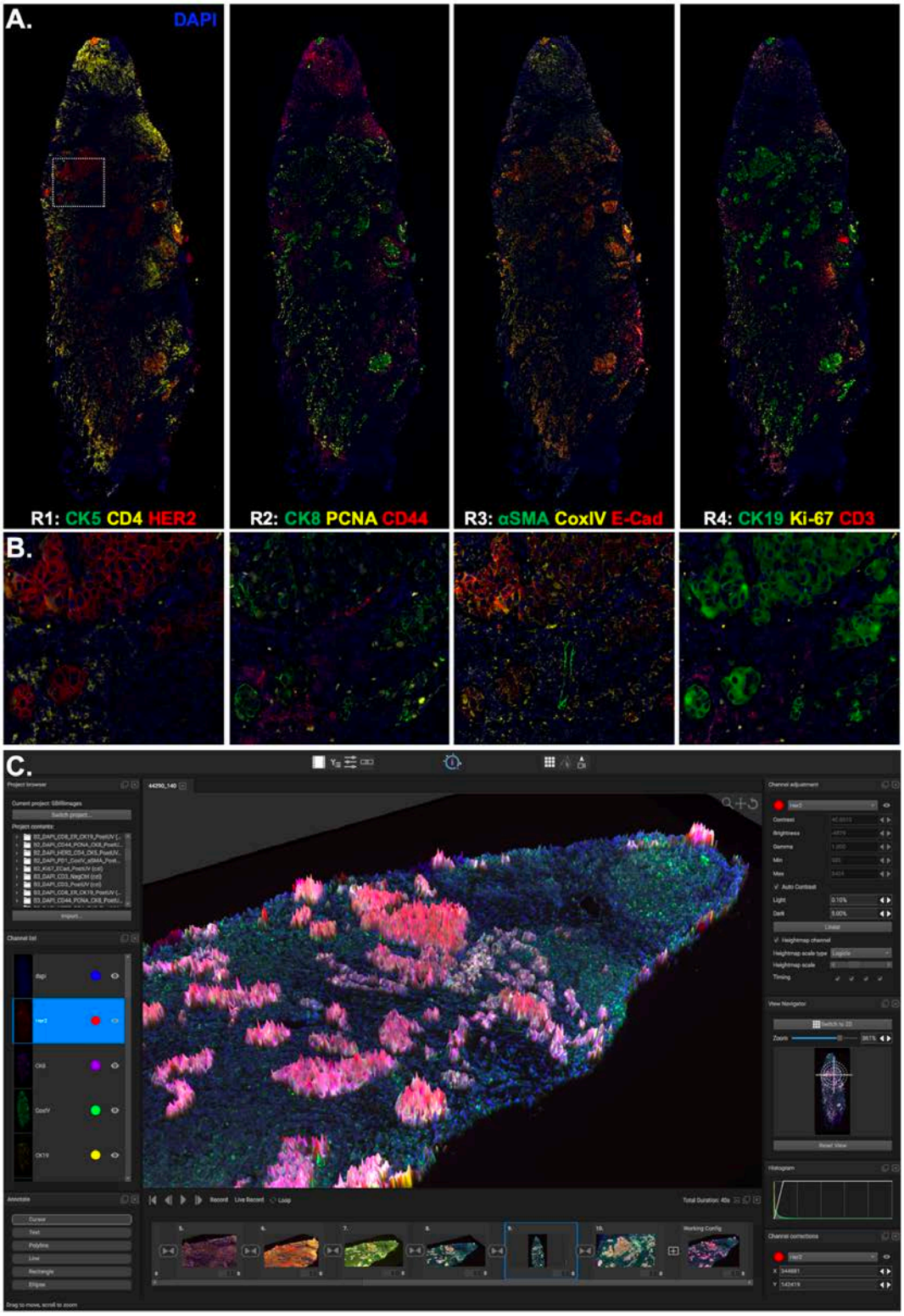

Fig. 3.5: *Multiplexed Ab-oligo cyCIF on HER2+ BC.* **A.** Tiled and stitched, whole breast cancer tissue images of Ab-oligo cyCIF are displayed by round of IS application. **B.** A magnified view of a breast cancer tumor nest within the tissue sample (white box) is displayed for a higher resolution view of the staining pattern of each marker in their respective round of imaging. **C.** QiTissue software was used to generate enhanced visualizations of this Ab-oligo cyCIF imaging data set by displaying CK8 as a height map. The height map is colorless, resulting in enhanced visualization of colocalization of markers without increased false coloring.

Multicolor cyCIF staining in a breast cancer TMA was completed using the same rounds of three color IS application and UV light treatment. However, to help demonstrate the power of cyCIF, the biomarkers were remixed into biologically relevant groups including differentiation (CK5, CK8 and CK19), proliferation (CoxIV, PCNA and Ki-67), microenvironmental (αSMA, PD-1, CD4 and CD3) and breast cancer-specific (αSMA, E-Cad, ER, CD44 and HER2) markers rather than by imaging round (**Fig. 3.6**). Visualization of the selected biomarkers on different breast cancer subtypes showed the expected distinct expression patterns for HER2+ (**Fig. 3.6A**), HER2-, ER- (**Fig. 3.6B**) and ER+ (**Fig. 3.6C**) breast cancers. As expected, the HER2+ breast cancer had the highest HER2 staining intensity, while the ER+ breast cancer had the highest ER staining intensity. CK5 was only expressed in the ER+ breast cancer, with minimal expression in either of the other two breast cancer subtypes. CK8 and CoxIV showed ubiquitous expression across the three breast cancer subtypes, while αSMA was found mainly in benign ductal breast tissues (**Fig. 3.6**). Tissue loss per round was quantified for all three TMA cores displayed by automatic counting DAPI labeled nuclei in each round of imaging resulting in an average tissue loss per round of 0.52% ± 0.37.

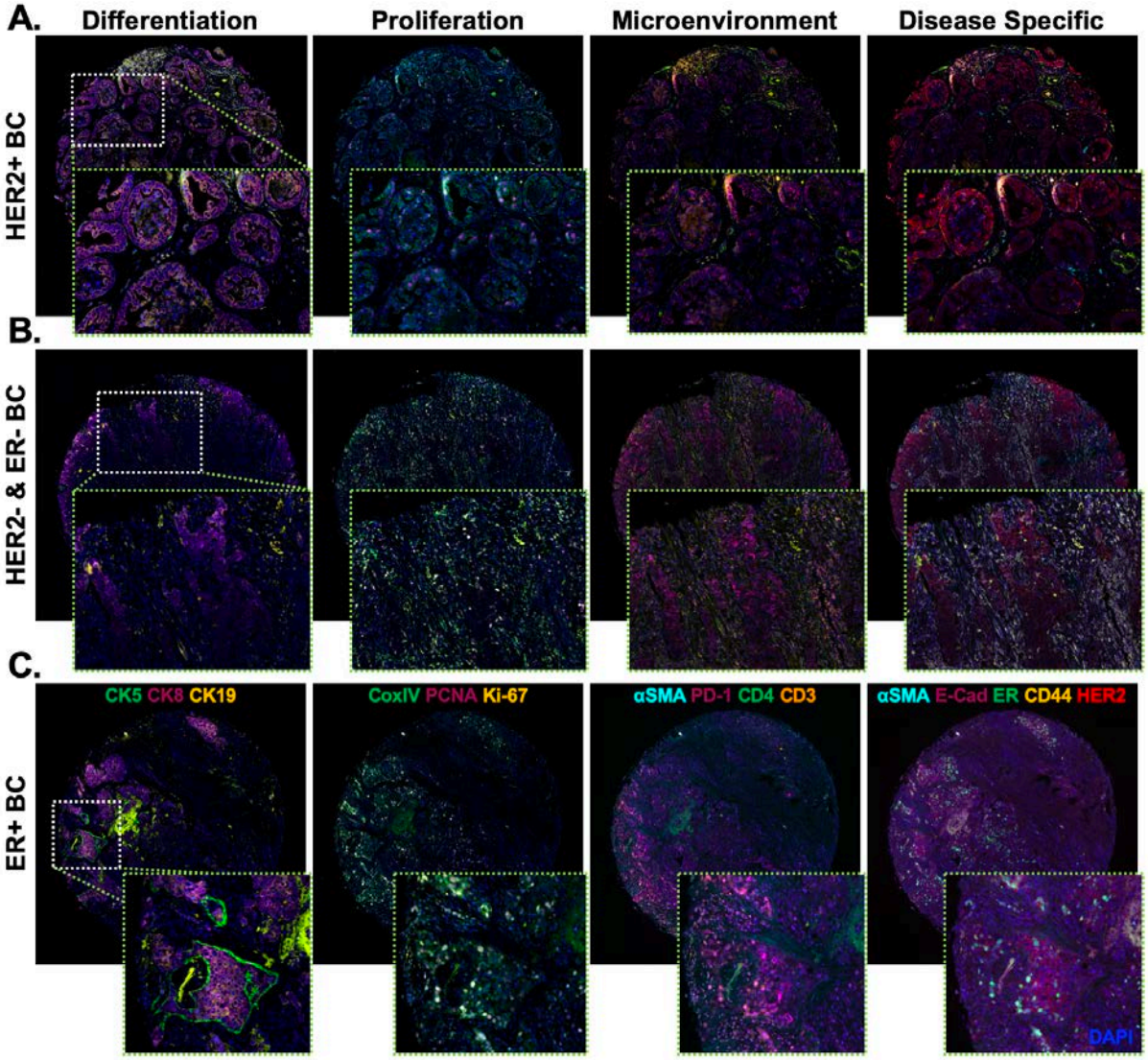

Fig. 3.6: *14-color Ab-oligo cyCIF on BC subtypes stained in a tissue microarray (TMA).* The validated Ab-oligo conjugates were used to stain a TMA containing different subtypes of BC. The biomarkers in the collected images were organized into tissue characterization panels of differentiation (CK5, CK8, CK19), proliferation (CoxIV, PCNA, Ki67), microenvironmental (α-SMA, PD-1, CD4, CD3), and disease specific (α-SMA, E-Cad, ER, CD44, HER2) biomarkers, which were then used to characterize **A.** HER2+, **B.** HER2- and ER-, and **C.** ER+ BCs.

DISCUSSION

One of the primary goals of highly multiplexed immunolabeling and imaging of cancers is to unravel the complex biology and spatial organization which give rise to heterogeneity of therapeutic response. Although there have been a number of high dimensional imaging techniques developed with the potential to interpret tumor heterogeneity, none have been adopted into the clinical histology laboratory, limiting their utility to aid in clinical decisions. Strategies using sequential rounds of biomarker staining, imaging, and destaining or antibody removal offer a potential near-term solution to build high dimensional imaging data. However, tissue damage caused by sequential rounds of labeling and signal removal along with prohibitively long processing times to adopt said strategies have prevented widespread clinical use.

The validation studies of the Ab-oligo cyCIF technology presented herein, highlight its ability to overcome the limitations of conventional immunolabeling technologies and avoid the pitfalls of alternative high dimensional cyclic staining platforms. The employment of a site directed conjugation strategy for the covalent conjugation of a unique oligonucleotide sequences (i.e., docking strands [DS]), to the carbohydrate domains on the Fc region of the antibody resulted in maintained antigen binding affinity for the majority of antibody clones used to generate the Ab-oligo conjugates. Optimization of the SBR of the Ab-oligos for detection of antigens was completed first with a titration study of the Ab-oligo conjugate to determine optimal antibody concentration (**Fig. 3.1A** & **3.1B**). While a rather high optimal antibody conjugate concentration was selected herein (i.e., 15 μg/ml) to generate maximum SBR, all tested concentrations produced positive staining pattern providing evidence that antibody staining concentrations and subsequent costs can likely be reduced. Additionally, further Ab-oligo titration is ongoing to assess optimal concentrations for other antigens. SBR optimization was also maximized through IS titration studies (**Fig. 3.1**) using an antigen localized to each cellular compartment: membrane (E-Cad), cytoplasm (α-SMA), and nucleus (Ki67). This was by design to understand if antigen location affected DS/IS hybridization and if optimal IS concentration varied with cellular compartment. An IS concentration of 350 nM was found to generate the highest SBR across markers, with little difference in intracellular localization noted (**Fig. 3.1C** & **3.1D**). Subsequent qualitative Ab-oligo staining pattern validation studies using 15 μg/ml Ab-oligo conjugate and 350 nM IS as the optimal staining methodology for all markers showed the expected target specific staining patterns for the Ab-oligo cyCIF strategy, when compared with matched indirect IF positive controls (**Fig 3.2**). Ab-oligo cyCIF sensitivity was found to be similar to conventional direct IF using antibodies with similar fluorophore to antibody conjugation ratios (**Table 3.1** and **Fig. 3.2G**).

Successful cyclic immunostaining requires robust fluorescent antigen labeling with subsequent full signal removal between staining rounds. Improved Ab-oligo fluorescent SBR was generated through the addition of a second fluorophore to the IS configuration, enhancing SBR for both HER2 and E-Cad (**Fig. 3.3A**, **3.3B**, **3.3D**). The IS length was subsequently evaluated to ensure steric hindrance with a fluorophore on the 3' end, which would require hybridization next to the antibody, was avoided. An optimal IS length of 26 nt with a fluorophore and an adjacent

photocleavable linker on each end was selected for all future studies (**Fig. 3.3C** & **3.3E**). The selection of the shortest tested length mitigated the chance for steric hindrance in high dimensional staining studies in our sequential imaging strategy.

Antibody stripping or fluorophore bleaching techniques are commonplace in cyclic immunostaining, however their use is often to the detriment to tissue integrity. Herein, we sought a mild signal removal technique that would preserve tissue integrity over multiple staining cycles. We found the incorporation of PCLs into the IS configuration to provide complete signal removal after exposure to UV light (**Fig. 3.5A-M**). Differences in overall signal intensity before and after UV treatment varied for depending on the stained antigen (**Fig. 3.5G**), however no recognizable staining pattern remained after UV signal removal, validating the utility of PCLs for cyCIF (**Fig. 3.5N**). The main reason for the differences in signal intensity following UV treatment were variation in background autofluorescence signal present in the different FFPE sample types used for validation.

Key benefits to Ab-oligo cyCIF are (1) the use of oligo labeled antibodies permits a single long antibody staining step as all Ab-oligos can be added simultaneously (2) PCLs for signal removal do not damage tissue integrity and (3) the strategy results in a simple workflow using only conventional reagents and fluorophores for ready translation to any laboratory or clinical setting. Validation and optimization of our Ab-oligo cyCIF platform enabled the extension of our technique to generate up to 14-color images on multiple HER2+ and/or ER+ BC tissue as conventional FFPE blocks (**Fig. 3.5**) or TMAs (**Fig. 3.6**). The high dimensional immunolabeling and imaging on these samples demonstrated the utility of cyCIF to visualization complex tumor heterogeneity *in situ*. Complete signal removal between sequential rounds of staining and imaging was achieved to avoid crosstalk between multiple markers labeled using the same fluorophore. Successful photocleavage and simple washing of UV light treated samples prevented accumulation of background autofluorescence as the number of staining rounds increased. Importantly, the process of signal removal by UV light treatment, multiple applications of IS, and multiple rounds of imaging did not cause any appreciable tissue damage. This observation gives motivation to further extending Ab-oligo cyCIF to higher dimensionality in future work. The simple workflow using a single antibody incubation step and sequential rounds of target imaging was validated herein. Additionally, it is important to note that all antibodies applied prior to the first round of IS application were still present in the fourth round of imaging, resulting in antibody-specific fluorescent staining patterns when labeled with their complementary IS. This validated simple workflow with mild staining and destaining conditions presents the opportunity for automated staining and imaging using emerging fluorescence microscopy technologies with robotic staining solutions.

Our validated Ab-oligo cyCIF platform employs a workflow capable of producing high dimensionality imaging from a single tissue sample without deleterious effects to tissue or requiring exotic reagents or microscopy hardware, decreasing the barrier to entry for cyCIF into the clinical setting. While biological interpretation is beyond the scope of this paper, tools for analysis and interpretation of high dimensional image data sets produced from Ab-oligo cyCIF

will be critical for clinical decision making. Several tools have been developed to perform such analyses on datasets produced by alternative multiplexed imaging technologies[29, 32, 132] and are also compatible for the analysis of Ab-oligo cyCIF data sets. These analyses simultaneously inform, with single cell resolution, protein expression distribution between cells to identify unique cell subpopulations and study what role cellular neighbors and microenvironments play in clinical outcomes. Importantly to having clinical potential, Ab-oligo cyCIF results in biomarker fluorescent labeling SBR equivalent to conventional direct IF methods validating it as a quantitative assay sensitive enough to detect clinically relevant proteins (e.g., HER2) with intertumoral expression variation. The addition of a dual fluorophore IS configuration was critical to this result and additional signal amplification studies are ongoing to further improve Ab-oligo cyCIF SBR to reach the levels of indirect IF. Furthermore, additional Ab-oligo conjugates are currently under development to address therapeutic response heterogeneity in breast, pancreatic and non-small cell lung cancers. One such application will be to quantify cellular pathway reprogramming as a mechanism of acquired resistance in response to targeted therapies. Ab-oligo targets will be extended to include total protein and phosphorylated protein targets to quantify protein signatures critical to pathways that are targets of therapeutic inhibition, where Ab-oligo cyCIF could aid in the identification of novel therapeutic strategies for a wide range of disease states.

Chapter 4

Ab-oligo cyCIF signal amplification and flexibility for increased sensitivity to low abundance antigens and rare cell types

ABSTRACT

Purpose: Advancements in our understanding of the complex, multifaceted interactions between tumor, immune and tumor microenvironmental cells has been driven by highly multiplexed imaging techniques. These techniques are capable of labeling many more biomarkers than conventional immunolabeling techniques. However, these techniques often are limited in detection sensitivity to low abundance antigens and rare cell types preventing full understanding tumor spatial heterogeneity.

Procedure: We developed and optimized a signal amplification strategy for our previously reported oligonucleotide conjugated antibodies (Ab-oligo) cyclic immunofluorescence (cyCIF) methodology. We utilized longer amplification oligos that facilitate the hybridization of more fluorescently labeled oligos than the previously reported Ab-oligo cyCIF strategy resulting in increased signal to background ratio. Staining parameters such as amplification oligo concentration, staining temperature and sequence design were optimized to generate a robust amplification technique. We also assessed the flexibility of Ab-oligo cyCIF by simultaneously imaging with indirect IF reagents, the original Ab-oligo cyCIF strategy and the Ab-oligo cyCIF amplification strategy.

Results: We successfully demonstrated that the Ab-oligo cyCIF amplification strategy produces signal to background ratio similar to that of conventional indirect IF. We also generated a 10-color image data set on a fresh-frozen cell-derived xenograft tissue section utilizing indirect IF, the original Ab-oligo cyCIF strategy and the amplification strategy. The result is a flexible, highly multiplexed imaging platform with increased detection sensitivity.

Conclusion: Herein, we demonstrated the flexibility and detection capabilities of Ab-oligo cyCIF as a methodology capable of highly multiplexed image generation through a number of strategies in order to provide sufficient detection sensitivity for rare cell types and low abundance antigens.

INTRODUCTION

Highly multiplexed imaging techniques have risen in popularity as our understanding of the significance of spatial proteomics has developed. This is particularly evident in the study of cancers, where these imaging tools are capable of measuring expression and spatial distribution of proteins of interest to define unique populations of tumor, immune and tumor microenvironmental cells.[133] In the case of immunotherapy, great advances have been made in therapeutic strategy design as highly multiplexed technologies have assisted in target identification and subsequent therapeutic response to inform on therapeutic efficacy and resistance along with the role the TME plays in both of these biological phenomena.[134, 135] Specifically, recent work performing highly multiplexed profiling of intraductal papillary mucinous neoplasms (IPMNs), a precursor to pancreatic ductal adenocarcinoma (PDAC), has revealed that the spatial proximity between epithelial cells and cytotoxic T cells is predictive in determining which patients will develop PDAC in order to aid in understanding disease progression and improved therapeutic selection in such a particularly deadly disease.[136] Further development of multiplexed imaging techniques will serve to provide more comprehensive information to improve cancer therapeutics and patient outcomes.

There exist two main modalities of highly multiplexed imaging that use either (1) antibody staining (i.e., immunohistochemistry [IHC] or immunofluorescence [IF]) or (2) mass spectrometry imaging (MSI) with rare earth metal-labeled antibodies.[30, 69-73, 75-79, 109] Cyclic antibody-based approaches are broadly performed by repeated staining, imaging and signal removal through fluorophore bleaching[73, 69, 76] or antibody stripping.[78, 110, 111] These workflows can be integrated into clinical workflows and therefore have seen broad adoption. However, repeated, lengthy antibody incubation steps limit the throughput of these techniques. Additionally, detection sensitivity is limited due to the semi-quantitative nature of IHC and decreased fluorescence signal produced by the fluorophore-labeled antibodies necessary for cyclic IF in comparison to conventional indirect IF. In contrast, MSI (e.g., MIBI,[70, 71] CyTOF,[72] etc.) is performed by applying all antibodies in a single-step as a "master-mix" and imaging for all markers is performed in a single scan. However, reagents and instrumentation costs are greater than that of antibody-based approaches. Additionally, spatial resolution is limited by the laser spot size, hampering the detection of low abundance antigens. Overcoming the limitations of these techniques, oligonucleotide (oligo) "barcoded" antibody-based highly multiplexed fluorescence imaging methodologies have emerged as a hybrid solution. In these techniques, all DNA-barcoded antibodies are stained in a single step similar to MSI, while single-cell resolution and quantitative fluorescence imaging is achieved as in conventional antibody-based highly multiplexed immunofluorescence approaches. Antibody barcoding techniques (e.g., DNA-Exchange Image,[82] Nanostring[80, 81] and CODEX[67]) have demonstrated the ability for highly multiplexed immunostaining using non-destructive signal removal techniques.

While all of these techniques have demonstrated capability for high dimensional image generation, they lack an amplification system to increase signal for markers with low abundance.

In response a number of methods of fluorescence signal amplification have been developed (e.g., Happen-based modified multiplex[137] and tyramide signal amplification[138]) where detection sensitivity has been demonstrated to be up to 10X greater than that of conventional indirect IF. These techniques meet the analytical need of increased detection sensitivity, but are limited to a maximum of seven biomarkers, which is substantially less than current cyclic immunostaining platforms. Alternatively, fluorescence-based methods of *in situ* hybridization to measure mRNA expression in tissue have been developed that utilize the mechanism of hybridization chain reaction (HCR) for signal amplification.[139, 140] In these methods, oligo probes hybridize to a complementary mRNA molecule followed by incubation of fluorophore-labeled oligo hairpins that self-assemble into a tethered amplification system. Importantly, this system has been used to measure up to 24 distinct mRNA sequences from a single tissue sample representing improved multiplexing over antibody-based signal amplification methods.[141] However, this oligo-based hybridization system has not yet been successfully translated to antibody-based immunofluorescence imaging, but offers a potential avenue for robust signal amplification and high dimensional imaging.

We have previously reported on our optimized oligonucleotide conjugated antibody (Ab-oligo) cyclic immunofluorescence (cyCIF) platform which utilizes docking strand (DS) labeled antibodies (Ab-oligos) and complementary fluorophore-labeled oligos, termed an imaging strand (IS), which hybridize for *in situ* antigen labeling. The IS are fluorophore labeled through a photocleavable linker (PCL) facilitating signal removal through exposure to UV light.[112] We demonstrated that signal to background ratio (SBR) for Ab-oligo cyCIF is improved by going from a single fluorophore on each IS (**Fig. 4.1A**) to two fluorophores on each IS (**Fig. 4.1B**). Recently, we have developed an Ab-oligo cyCIF imaging strategy to further amplify the Ab-oligo fluorescent staining patterns (**Fig. 4.1C**). In this Ab-oligo amplification strategy, an oligo partially complementary to the DS, termed the amplification strand (AmpS), is hybridized with the Ab-oliog DS. Then, fluorescence labeling is performed by staining amplification IS (Amp IS) where

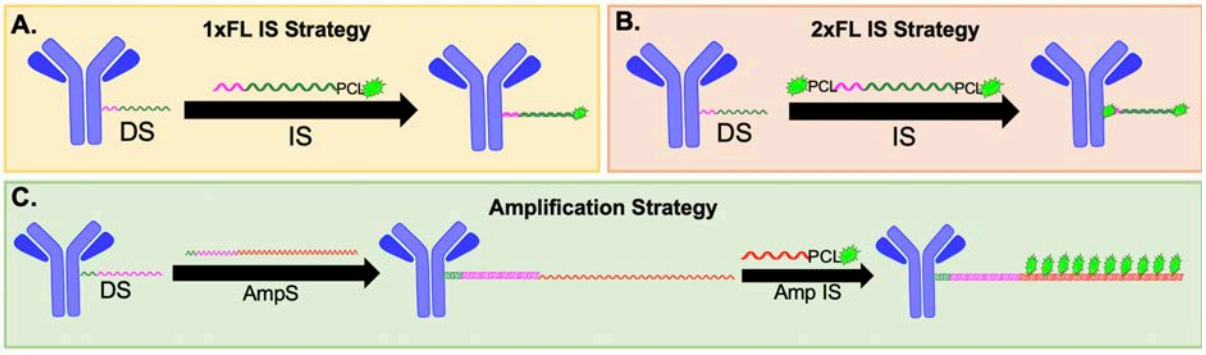

Fig. 4.1: *Ab-oligo fluorescence imaging strategies.* Multiple methods of fluorescent labeling of Ab-oligo conjugates have been investigated including **A**. a complementary imaging strand (IS) with a single fluorophore and photocleavable linker (PCL) that hybridizes the docking strand (DS) on the antibody and **B.** IS with two fluorophores and two PCLs. **C.** An amplification strategy has been developed that utilizes an amplification strand (AmpS) that is able to hybridize with up to ten amplification IS (Amp IS) that each contain a fluorophore and PCL for increased signal intensity.

there is potential for up to ten fluorophores to label a single DS, amplifying the maximum signal intensitycomparison to our previous fully complementary IS.

Described herein, we validate our Ab-oligo cyCIF amplification methodology, demonstrating its capability to generate fluorescence signal equivalent or greater than conventional indirect IF. We also, demonstrate the flexibility of the Ab-oligo cyCIF platform where multiple Ab-oligo cyCIF imaging strategies can be deployed simultaneously to selectively amplify low abundance antigens such as phosphoproteins. Additionally, we demonstrate how the Ab-oligo cyCIF platform can be integrated with conventional indirect IF as a further example to the flexibility of the platform. The optimized Ab-oligo cyCIF amplification strategy overcomes detection sensitivity limitations of other highly multiplexed platforms with the overall goal of providing sufficient sensitivity to continue to unravel the multifaceted interactions that drive the hallmarks of cancer.

MATERIALS & METHODS

Generation of oligonucleotide conjugated antibodies (Ab-oligo). Oligonucleotide (oligo) conjugated antibodies were generated as previously reported.[112] In brief, antibodies to human E-Cadherin (E-Cad), cytokeratin 5 (CK5), CK7, CK8, CK14, EGFR, Akt, pAkt, pMEK, PI3K, cleaved caspase-3, Ki-67, human epidermal growth factor receptor 2 (HER2), alpha smooth muscle actin (αSMA), CD4, CoxIV, CD68, PD1, PCNA, androgen receptor (AR), vimentin, estrogen receptor (ER) and progesterone receptor (PR) were purchased from AbCam (Cambridge, MA), Cell Signaling Technology (Danvers, MA), Biolegend (San Diego, CA) or Thermo Fisher Scientific (Waltham, MA). A unique dibenzocyclooctyne-terminated (DBCO), single-stranded oligonucleotide (docking strand [DS], 28 mer in length), used to label each antibody, was purchased from Integrated DNA Technologies (IDT, Coralville, IA). Antibody modification and oligonucleotide conjugation were completed with the SiteClick™ Antibody Azido modification kit (ThermoFisher Scientific, Waltham, MA) following the manufacturer's instructions.

Mice and cell lines. The human epidermoid carcinoma cell line, A431, EGFR mutated non-small cell lung cancer (NSCLC) cell line, HCC827, and the estrogen receptor positive human breast cancer cell line, MCF7 transfected with human epidermal growth factor 2 (HER2/neu) (MCF7-HER2),[142] were cultured in DMEM 1x (Gibco/Thermo Fisher Scientific) with 10% fetal bovine serum (FBS, Seradigm, Sanborn NY) and 1% Penicillin-Streptomycin-Glutamine (Thermo Fisher Scientific). The HER2 positive breast cancer cell line, SK-BR-3, was cultured in McCoy's 5A (Gibco/Thermo Fisher Scientific) with 10% fetal bovine serum (FBS, Seradigm, Sanborn NY) and 1% Penicillin-Streptomycin-Glutamine (Thermo Fisher Scientific). HCC827 cells were purchased from ATCC (Manassas, VA). A431 and MCF7-HER2 cells were a generous gift from Dr. Kimberley Samkoe (Dartmouth College, Hanover, NH). All cell lines were grown to ~ 90% confluence prior to use for xenograft implantation.

Athymic nude mice (Homozygous 490, Charles River Laboratories, Wilmington, MA) were purchased at 32-38 days old. After at least 48 hours of acclimation, a total of 2 mice per cell

line were subcutaneously implanted with A431, HCC827 or MCF7-HER2 cell xenografts described briefly as follows. Cells were trypsinized, counted and resuspended in their appropriate growth media to a concentration of 2 x 10^7 cells/ml. The mice were then implanted with cells into each rear flank at a final concentration of 1 x 10^6 cells/flank in 50% v/v Matrigel (Corning Inc., Corning, NY), resulting in two tumors/mouse. The mice were monitored daily after implantation for tumor growth. The tumors were allowed to grow to a maximum size of 1.2 cm^3 with growth times varying for each cell line (A431: ~2-3 weeks; MCF7-HER2: ~4-6 weeks, HCC827: ~7-8 weeks). Mice weighed ~20-25g and tumors were between 1-1.2 cm^3 prior to sacrifice and tissue collection. All xenografts were resected and flash frozen in optimal cutting temperature (OCT) compound (Fisher Scientific, Waltham, MA). MCF7-HER2 xenografts were then sent to OHSU's Histology Shared Resource where blocks were thawed and re-embedded in paraffin.

Animal care and use. All animal experiments were approved by the Oregon Health and Science University (OHSU) Institutional Animal Care and Use Committee (IACUC). All mice were hosted in the AAALAC certified OHSU vivarium, and supplied with food, water and daily inspection to monitor for pain or distress for the duration of experimentation. Mice were placed on a chlorophyll-free diet (Animal Specialties, Inc., Hubbard, OR) one week prior to tumor resection. All rodent surgical procedures, described herein, were performed under full anesthesia composed of a 90/10 mixture of ketamine/xylazine. Ketamine (Hospira Inc., Lake Forest, IL) was administered at a dose of 100 mg/kg and xylazine (AnaSed, Shenandoah, IA) was administered at dose of 10 mg/kg by intraperitoneal (IP) injection. The toe pinch method was employed to verify the depth of anesthesia prior to commencement of any surgical procedures. The standard method of euthanasia for mice was inhalation of carbon dioxide under full anesthesia at the end of each experiment. Euthanasia was confirmed by physical examination to ensure cessation of heartbeat and respiration and is consistent with the recommendations of the Panel on Euthanasia of the American Veterinary Medical Association.

Tissues & cell samples for validation. Evaluation of amplifying the fluorescence produced by Ab-oligo antibodies was validated on fresh frozen A431 xenograft tissue. 10 μM sections of each frozen block were captured onto 1x3-inch Superfrost™ Plus slides (Thermo Fisher Scientific). Validation was also performed on formalin fixed paraffin embedded (FFPE) blocks of MCF7-HER2 xenografts as well as cell buttons generated from MDA-MB-468 breast cancer cell lines generously provided by Dr. Koei Chin (Oregon Health & Science University, Portland, OR). 5 μM sections of the selected FFPE block were captured onto 1x3-inch Superfrost™ Plus slides (Thermo Fisher Scientific), which were baked at 65 °C in a hybridization oven for 30 minutes to overnight prior to commencing staining.

Antibody staining on frozen, FFPE and fixed cell samples. Primary antibody or Ab-oligo conjugate incubation was performed as previously reported for frozen tissue[143] and FFPE tissue.[112] Frozen A431 xenograft tissue sections were incubated in 2% paraformaldehyde (PFA, Sigma-Aldrich) at room temperature (RT) for 15 min and then washed with 1X PBS, pH 7.4 (3 x 5 min). The tissue was then permeabilized using 1X PBS, pH 7.4 + 0.3% Triton X-100 for 15 min at RT and washed with pH 7.4 PBS (3 x 5 min). The slides were blocked at RT for 30 min in Ab-

oligo blocking and dilution buffer which contained 2% bovine serum albumin (BSA, bioWORLD, Dublin, OH), 0.5 mg/mL sheared salmon sperm DNA (ThermoFisher) and 0.5% dextran sulfate (Sigma-Aldrich) in 1X PBS, pH 7.4. Primary antibodies were diluted to 15 µg/mL in blocking buffer and incubated on the A431 xenograft tissue sections overnight at 4 °C. The staining solution was removed and the cells were washed with 2X saline-sodium citrate (SSC) buffer, pH 7 (VWR, Radnor, PA) for 3 x 5 min. The tissues were incubated with 2% PFA for 15 min at RT and then washed with 2X SSC (3 x 5 min). Secondary antibody or IS were then diluted to 350 nM - 56 µM in imaging strand (IS) dilution buffer containing 2% BSA, 0.5 mg/mL sheared salmon sperm DNA and 0.5% dextran sulfate in 2X SSC buffer and incubated on the tissues for 45 min at RT, protected from light for the remainder of the staining procedure. The excess IS was then washed with 2X SSC (3 x 5 min). The tissues were stained with 300 nM DAPI for 10 min at RT after which they were washed with 2X SSC (2 x 5 min) and cover slipped prior to imaging.

The baked MCF7-HER2 xenograft and MDA-MB-468 cell button FFPE tissue slides were deparaffinized at room temperature (RT) in xylenes (2 x 10 min washes). The tissue was then gradually rehydrated in ethanol and water solutions as follows: 100% ethanol (2 x 10 min), 95% ethanol (1 x 5 min), 70% ethanol (1 x 5 min), then 50% ethanol (1 x 5 min). The tissue was then rinsed in 100% deionized water (diH_2O) followed by a wash in 1X PBS, pH 7.4 for 10 minutes. A two-step antigen retrieval procedure was performed in a Pascal Pressure Cooker (Dako, Santa Clara, CA). RT solutions of 10 mM sodium citrate, pH 6, 1X tris hydrochloride (HCl), pH 8 and diH_2O were placed in the pressure cooker in three individual plastic buckets immersed in 500 mL of diH_2O, which covered the bottom of the chamber. The slides were immersed in the sodium citrate buffer and the pressure cooker lid was secured. The temperature was increased to 125 °C over a 15 min period, where the pressure reached ~15 psi. The pressure cooker was removed from heat, and the temperature and pressure were allowed to decrease to 90 °C and 0 psi respectively over ~25 min. The residual pressure was released as the lid was removed and the slides were rinsed in the hot diH_2O. The slides were immediately placed in the hot tris-HCl buffer, where they were incubated for 10 min with the lid on the pressure cooker. The slides were then transferred back to the hot diH_2O and brought back to RT by slow addition of RT water to the vessel. After 5 min in RT diH_2O, the slides were washed in PBS, pH 7.4 at RT for an additional 5 min. The slides were blocked at RT for 30 min in Ab-oligo blocking and dilution buffer which contained 2% bovine serum albumin (BSA, bioWORLD, Dublin, OH), 0.5 mg/mL sheared salmon sperm DNA (ThermoFisher) and 0.5% dextran sulfate (Sigma-Aldrich) in 1X PBS, pH 7.4. Primary antibodies were diluted to 15 µg/mL in blocking buffer and incubated on the FFPE tissue sections overnight at 4 °C. The staining solution was removed and the cells were washed with 2X saline-sodium citrate (SSC) buffer, pH 7 (VWR, Radnor, PA) for 3 x 5 min. The tissues were then incubated with 2% PFA for 15 min at RT and then washed with 2X SSC (3 x 5 min). Secondary antibody or IS were diluted to 350 nM - 56 µM in IS dilution buffer and incubated on the tissues for 45 min at RT, protected from light for the remainder of the staining procedure. Excess IS was removed by washing with 2X SSC (3 x 5 min). The tissues were stained with 300 nM DAPI for 10 min at RT after which they were washed with 2X SSC (2 x 5 min) and cover slipped prior to imaging.

SK-BR-3 cells were seeded onto 96-well glass bottom plates (Cellvis, Mountain View, CA) at 10,000 cells per well and grown to ~70% confluence for ~60 hours (h) at 37 °C and 5% CO_2. Cells were fixed for 15 minutes (min) in 4% PFA at RT. PFA was removed and cells were wash with 1X PBS, pH 7.4 (3 x 5 min) and stored with 0.05% sodium azide (NaN_3) at 4 °C until needed for staining. Prior to staining, the cells were washed with PBS (3 x 5 min) to remove NaN_3. In pilot studies, the cells were permeabilized in 0.5% polyoxyethylene(10) octylphenyl ether (Triton X-100, Millipore) for 15 min at RT followed by washing in PBS (3 x 5 min). This step was omitted following completion of staining optimization studies. The cells were blocked for 30 min at RT with 2% BSA, 0.5 mg/mL sheared salmon sperm DNA, 0.5% dextran sulfate, and 0.05% Tween 20, which was termed "blocking buffer." Ab-oligos were diluted to 15 µg/mL in blocking buffer and incubated with SK-BR-3 cells overnight at 4 °C. Staining solution was removed and cells were washed in PBS (3 x 5 mins). Cells were post-fixed in 2% PFA for 15 min at RT, followed by washing in 2X SSC. Secondary antibody and IS were diluted in IS dilution buffer to 350 nM. Secondary antibody or IS was incubated with the cells for 45 min at RT with gentle shaking, protected from light for the remainder of the staining procedure. The staining solution was removed and the cells were washed with PBS (3 x 5 min). The cells were stained with 300 nM DAPI for 10 min at RT after which they were washed with PBS (2 x 5 min) prior to imaging.

Fluorescence Microscopy of Tissue Sections. Cells stained in 96 well plates were imaged on a Zeiss AxioObserver microscope with an AxioCam 506 camera (Carl Zeiss AG, Oberkochen, Germany). Frozen and FFPE tissue sections were imaged on a Zeiss AxioImager.M2 microscope equipped with an XY motorized scanning stage (Carl Zeiss AG) and a 14-bit CCD CoolSNAP HQ2 camera (Photometrics, Tucson, AZ). Filter sets were selected based on the IS-labeled fluorophore excitation and emission characteristics. Three channels were used for fluorescence image capture, specific to fluorophore-labeled IS, and include the following Zeiss filter sets: EGFP (FITC/Cy2), Cy3/TRITC and Cy5. The following bandpass (BP) filters were used to filter excitation light: 470/40 (PF), 545/25 (PF), 620/60 (PF) for AF488, AF546, and AF647, respectively. The following BP filters were used to filter emission light: 525/50, 605/70, 700/75 for AF488, AF546, and AF647, respectively. To collect DAPI images, excitation light was filtered using a Zeiss 405/40 BP filter. All images collected on the AxioObserver were at 40X (Plan-Apochromat, 0.95A) magnification. For frozen and FFPE tissue experiments imaged on the AxioImager.M2 microscope, the excitation and emission light were filtered as previously described and images were collected at either 20X (Plan-Apochromat, 0.8A) or 40X (Plan-Apochromat, 0.95A) magnification.[112] Signal to background ratio (SBR) calculations were performed to quantify difference between staining and signal removal conditions as previously described.[112]

Ab-oligo fluorescence signal amplification. To validate the method of amplifying fluorescence signal using the Ab-oligo conjugates, three groups were used for comparison including: (1) conventional indirect immunofluorescence with unconjugated primary and fluorophore conjugated secondary antibody, (2) the Ab-oligo conjugate plus the complementary fluorophore conjugated imaging strand (IS) with a fluorophore at both the 3' and 5' ends of the

oligo[112] and (3) the Ab-oligo conjugate plus the partially complementary 198 nt amplification strand (AmpS) plus the 15 nt fluorophore conjugated amplification IS (Amp IS) complementary to the AmpS with one fluorophore at the 3' end. The previously described overall Ab-oligo staining procedure was used for each group, where only the final fluorescence labeling steps differed as explained below.

For group (1), the conjugated secondary antibody was added at 350 nM and incubated at RT protected from light. The secondary antibody was removed and samples were washed in 2X saline-sodium citrate (SSC) buffer, pH 7 (VWR, Radnor, PA) for 3 x 5 min. For group (2) the complementary IS was diluted in IS dilution buffer containing 2% BSA, 0.5 mg/mL sheared salmon sperm DNA and 0.5% dextran sulfate in 2X SSC buffer. The samples were incubated with IS at RT protected from light for 45 min. The IS was removed and the samples were washed in 2X SSC buffer (3 x 5 min). For group (3), the partially complementary AmpS was added at 350 nM and incubated at RT for 45 min. The AmpS was removed and samples washed in 2X SSC buffer (3 x 5 min). Then the Amp IS complementary to the AmpS was added at concentrations ranging from 350 nM – 56 μM depending on experimental design and incubated at RT for 45 min protected from light. DAPI was applied to all stained samples at 300 nM for 10 min at RT and the samples were then washed in 2X SSC buffer (2 x 5 min). All stained slides were mounted in Fluoromount-G (Southern Biotech, Birmingham, AL) and cover-slipped for imaging.

Amplification IS (Amp IS) molar excess titration. The previously detailed FFPE tissue antibody staining procedure was used to stain MCF7-HER2 xenograft tissue with HER2 primary antibody or Ab-oligo conjugate. A secondary antibody labeled with Alexa Fluor 546 (AF546) or complementary AmpS diluted in IS dilution buffer to 350 nM was added to tissues stained with HER2 primary antibody or Ab-oligo conjugate, respectively. Slides stained with HER2 Ab-oligo conjugate were then incubated with Amp IS labeled with AF546 diluted in IS dilution buffer to 350 nM - 56 μM. A negative control was also generated for each sample where they were processed through the complete staining protocol, but only secondary antibody or AmpS and Amp IS were added to the tissues to assess background fluorescence. The images produced were used to calculate SBR where signal was measured from the images stained with primary antibody + secondary antibody or Ab-oligo + AmpS + Amp IS and each samples background measured from its respective negative control. Fluorescence signal intensity for each image was quantified in ImageJ v1.51 (National Institute of Health, Bethesda, MD).

Amplification strand (AmpS) heating. The previously detailed FFPE tissue antibody staining procedure was used to stain MCF7-HER2 xenograft tissue with HER2 primary antibody or Ab-oligo conjugate. The tissue stained with the HER2 primary antibody was labeled with 350 nM of AF546 conjugated secondary antibody. One tissue section stained with HER2 Ab-oligo conjugate was incubated with 350 nM of AmpS followed by 350 nM of Amp IS. Another tissue section stained with HER2 Ab-oligo conjugate was incubated with 350 nM of AmpS that was heated at 85 °C for 3 min prior to staining in an effort to decrease the formation of hairpins and other secondary structures that long oligos have a propensity to form. Following AmpS incubation, 350 nM Amp IS was stained onto the tissues. Negative controls for each sample were tissues

stained with fluorophore-labeled secondary antibody or AmpS + Amp IS only. SBR for each tissue was calculated as described above.

Amplification validation for varied cellular compartment markers. Antibody staining studies assessing the optimized Ab-oligo amplification strategy were completed using two groups including (1) conventional indirect immunofluorescence with unconjugated primary + fluorophore conjugated secondary antibody and (2) the Ab-oligo conjugate + AmpS + Amp IS. The AmpS was heated to 85 °C for 3 min prior to tissue incubation and the Amp IS added at 20X molar excess with respect to the AmpS. Indirect IF staining pattern served as a positive control for qualitative comparison to Ab-oligo amplification strategy staining pattern. Negative controls for each sample and SBR ratios for each image were generated as described above.

Optimal docking strand (DS) oligo sequence design for antibody conjugation. Docking strands (DS) were evaluated for potential to form secondary structures using the IDT OligoAnalyzer™ Tool (Coralville, IA). Briefly, oligo sequences were analyzed with the hairpin function where the potential for secondary structure formation was calculated. If an oligo had a high potential for secondary structure formation, nucleotides involved in the hairpin were iteratively changed and tested until no hairpin structure could be predicted. The sequence was then tested for self-dimerization potential and again iteratively adjusted until no self-dimerization was predicted. Three DS sequences, KpnIB, SalIC and PvuIIA, were identified to have strong potential for secondary structure formation and were re-designed with this process to reduce the probability of secondary structure formation. The new DS sequences were then conjugated to HER2 primary antibody as described above. Fixed SK-BR-3 cells were stained for HER2, as described above with either conventional indirect IF using unconjugated HER2 primary antibody, the HER2 Ab-oligo conjugate with the original DS design or the HER2 Ab-oligo conjugate with the new DS design. Fluorescence imaging was performed on a on a Zeiss AxioObserver and fluorescence intensity quantified for each image as described above.

Highly Multiplexed Image Generation with Indirect IF and Ab-oligo cyCIF. A HCC827 xenograft tissue section was incubated in 2% PFA at RT for 15 min and then washed with 1X PBS, pH 7.4 (3 x 5 min). The tissue was permeabilized using 1X PBS, pH 7.4 + 0.3% Triton X-100 for 15 min at RT and washed with pH 7.4 PBS (3 x 5 min). The slides were blocked at RT for 30 min in Ab-oligo blocking and dilution buffer which contained 2% BSA, 0.5 mg/mL sheared salmon sperm DNA and 0.5% dextran sulfate in 1X PBS, pH 7.4. Each tissue section was covered with 40 µL of unconjugated pEGFR antibody diluted to a concentration of 15 µg/mL and incubated for 1h at RT. An additional tissue section was incubated with blocking buffer without primary antibody to serve as a negative control. Excess pEGFR antibody was removed by washing with 2X SSC buffer, pH 7 for 3 x 5 min. Antibody was then fixed on each tissue section through a 15 min incubation of 2% PFA at RT for 15 min and then washed with 2X SSC pH 7 (3 x 5 min). pEGFR was labeled with donkey anti-rabbit secondary conjugated to AF750 (dRb750). The secondary antibodies were diluted in a dilution buffer containing 2% BSA, 0.5 mg/mL sheared salmon sperm DNA and 0.5% dextran sulfate in 2X SSC buffer. The dRb750 was diluted to a final protein concentration of 350 nM. Each tissue section, including the negative control, was covered

with 40 µL of the diluted secondary antibody and incubated for 45 min at RT in a humidified chamber protected from the light. Excess secondary antibody was removed by washing with 2X SSC buffer (3 x 5 min). Then, to facilitate Ab-oligo cyCIF imaging, the nine Ab-oligo antibodies (**Table 4.1**) were mixed at a concentration of 15 µg/mL per antibody into a single master mix. Each tissue section was covered with 40 µL of the diluted antibody cocktail and incubated at 4 °C overnight in a humidified chamber. The negative control slide was once again incubated with blocking buffer without any antibody. The next day, the sections were washed with 2X SSC buffer (3 x 5 min). The Ab-oligo conjugates stained on the tissue sections were fixed in 2% PFA for 15 min at RT, then washed again in 2X SSC buffer (3 x 5 min). To facilitate cyCIF imaging, the Ab-oligo conjugates were imaged through two different strategies. The first was performed as

Table 4.1: *Flexible cyCIF imaging antibody panel.*

Marker Category	Protein	Fluorescence Imaging Strategy
Tumor Area	CK8	Ab-oligo 2xFL IS
	E-Cad	Ab-oligo 2xFL IS
Tumor Viability	Ki67	Ab-oligo 2xFL IS
	CC3	Ab-oligo amplification strategy
EGFR Signaling Pathway	*EGFR*	Ab-oligo 2xFL IS
	pEGFR	Indirect Immunofluorescence (IF)
	pMEK	Ab-oligo amplification strategy
	PI3K	Ab-oligo 2xFL IS
	AKT	Ab-oligo amplification strategy
	pAKT	Ab-oligo amplification strategy

previously described where complementary imaging strands (IS) with fluorophores (AF488, AF546 or AF647) at both the 3' and 5' end of the IS and two photocleavable linkers located adjacent to the fluorophores were utilized to label Ab-oligo conjugates.[112] The second strategy employed the amplification strategy described above where AmpS and Amp IS were incubated on tissues at 350 nM and 7 µM, respectively for each marker.

Notably, cycles of imaging and signal removal were performed using both Ab-oligo fluorescence strategies simultaneously. The strategy using IS with two fluorophores and two photocleavable linkers was applied for labeling E-Cad, Ki67, CK8, EGFR and PI3K. The Ab-oligo amplification strategy was used to label pAkt, CC3, pMEK and Akt. First, AmpS for all markers to be imaged in a given round were diluted to 350 nM in dilution buffer containing 2% BSA, 0.5 mg/mL sheared salmon sperm DNA and 0.5% dextran sulfate in 2X SSC buffer. The AmpS mixture was then heated to 85 °C for 3 min. Then any 26 nt, 2xPCL-FL IS to be used in that round were added to the mixture for a final concentration of 350 nM of each 2xPCL-FL IS. 40 µL of the diluted oligo cocktail was applied to each slide and incubated at RT for 45 min and tissues were protected from light for the remainder of the staining procedure. Unbound 26 nt IS and AmpS were removed by washing with 2X SSC buffer (3 x 5 min). Amp IS was then diluted to a final

concentration of 7 µM and 40 µL was dispensed onto each tissue and incubated at RT for 45 min. Unbound Amp IS was removed by washing with 2X SSC buffer (3 x 5 min). DAPI (Thermo Fisher Scientific) was then applied to all stained samples at 300 nM for 10 min at RT and the samples were washed in 2X SSC buffer (2 x 5 min). All stained slides were mounted in Fluoromount-G (Southern Biotech, Birmingham, AL) and cover-slipped for imaging.

Images were collected on a Zeiss AxioScan.Z1 in the DAPI, AF488, AF546, AF647, AF750 channels. All stained slides were then treated with UV light for 15 minutes followed by washing 10 times with 0.1X SSC and remounted with Fluoromount-G. Finally, the slides were imaged with the same settings used prior to UV treatment to confirm complete signal removal. Subsequent rounds of IS addition, imaging and signal removal were repeated until all Ab-oligo conjugates were imaged.

RESULTS

Amplification IS molar excess titration. Optimal Ab-oligo amplification oligo staining concentrations were evaluated on tissue positive for HER2 (**Fig. 4.2**) where a titration of the molar ratio of AmpS to Amp IS was performed from 1:1-160:1 and compared to conventional indirect IF staining of HER2. All samples produced HER2 specific staining patterns (**Fig. 4.2A**). In the negative control samples containing no primary antibody or Ab-oligo conjugate, background fluorescence increased in the sample stained with a molar ratio of 80X and 160X molar excess of Amp IS (**Fig. 4.2B**). Quantification of HER2 SBR was performed by using an antibody stained tissue as the foreground signal and the corresponding negative control with no antibody as the background signal. In all images the highest SBR was generated in tissue stained with the Ab-oligo conjugate at 20X molar excess of Amp IS (**Fig 4.2C**). The next highest SBR was generated using conventional indirect IF stained tissue that showed a ~6% lower SBR. SBR decreased in tissues stained with greater molar excess of IS.

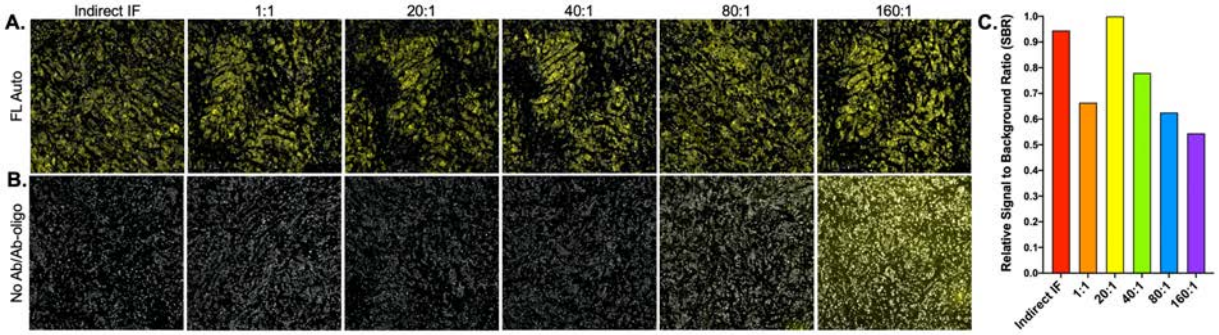

Fig. 4.2: *Ab-oligo amplification oligo titration.* **A.** MCF7-HER2 xenograft FFPE tissue sections were stained with either HER2 primary antibody for indirect immunofluorescent staining or HER2 Ab-oligo conjugate where a titration of molar excess of Amp IS to AmpS was performed from 1:1-160:1. **B.** Negative controls for each sample were stained with only fluorophore labeled secondary antibody or the respective concentrations of AmpS and Amp IS. **C.** Image quantification was performed to calculate SBR for all staining conditions.

Amplification strand (AmpS) heating. Methods of improving SBR produced by the Ab-oligo cyCIF amplification strategy were assessed on MCF7-HER2 xenograft FFPE tissue (**Fig. 4.3**). Tissues stained with HER2 Ab-oligo conjugate were labeled with AmpS that was kept at RT prior to tissue incubation or AmpS heated to 85 °C for 3 min prior to tissue incubation followed by incubation of 1X molar excess of Amp IS. The Ab-oligo conjugate-stained tissues were compared to tissues stained with conventional indirect IF staining of HER2. All stained samples produced HER2 specific staining pattern (**Fig. 4.3A**) although some visible background was present in the negative control for the Ab-oligo-stained tissue where the AmpS was not heated prior to incubation (**Fig. 4.3B**). SBR calculation for all images show indirect IF has the highest SBR while the Ab-oligo-stained tissue where AmpS was heated prior to incubation displayed a ~10% lower SBR while the no AmpS heating sample had a ~59% lower SBR (**Fig. 4.3C**).

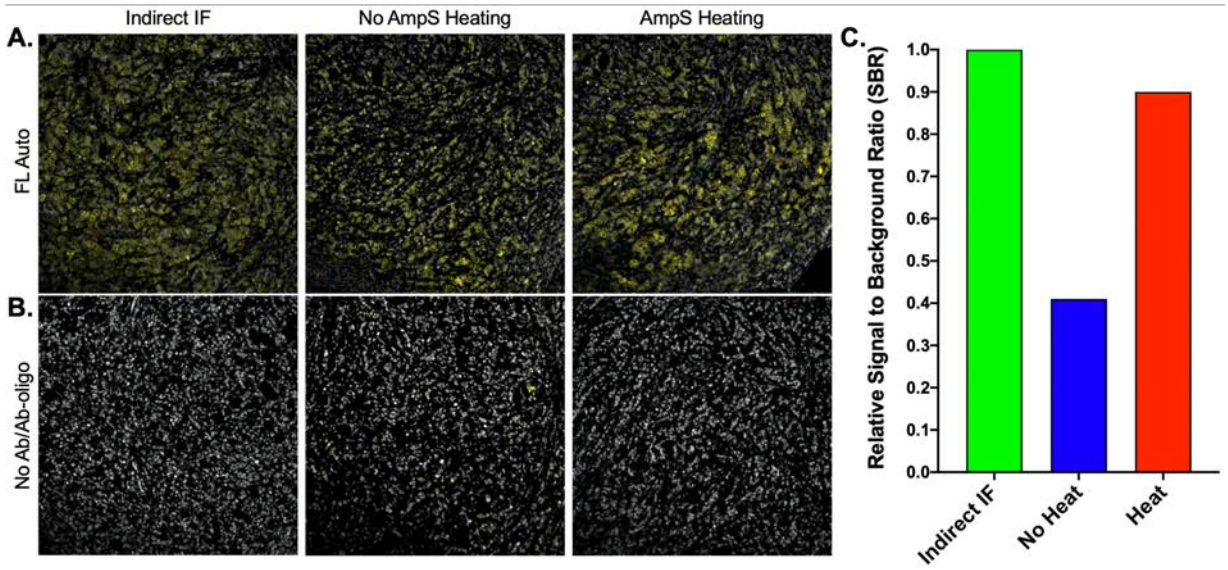

Fig. 4.3: *Amplification strand (AmpS) heating.* **A.** MCF7-HER2 xenograft FFPE tissue sections were stained with either HER2 primary antibody for indirect immunofluorescent staining or HER2 Ab-oligo conjugate where AmpS was either kept at RT prior to application or heated to 85 °C prior to staining. **B.** Negative controls for each sample were stained with only fluorophore labeled secondary antibody or the respective AmpS staining conditions and equivalent Amp IS concentrations. **C.** Image quantification was performed to calculate SBR for all staining conditions.

Optimized amplification strategy validation. After optimization of staining parameters for the Ab-oligo amplification strategy, validation of the technique was performed on EGFR, pEGFR and Ki67 (**Fig. 4.4**). Ab-oligo amplification of each marker was compared to both conventional indirect IF and Ab-oligo staining using IS with 2 fluorophores (2xFL IS). For EGFR, images from all samples are displayed with auto-contrast settings to visualize the EGFR-specific staining pattern produced by each method in A431 frozen xenograft tissue sections (**Fig. 4.4A**). The image contrast settings were then all normalized to the image with the greatest signal, the tissue stained with the Ab-oligo amplification strategy (**Fig. 4.4B**). Visually, the EGFR-specific fluorescence signals produced by indirect IF and the Ab-oligo were similar, while the signal produced by the 2xFL IS was much lower. A similar result was seen with pEGFR where marker specific staining pattern was seen with all staining methods in A431 frozen xenograft tissue

sections (**Fig. 4.4C**). The Ab-oligo amplification strategy produced the highest fluorescence signal as observed qualitatively when all images were set to equivalent contrast settings (**Fig. 4.4D**). The Ab-oligo amplification strategy was validated for Ki67 in MDA-MB-468 FFPE cell button sections, where marker specific staining pattern was observed for all staining methods (**Fig. 4.4E**). Images were normalized to the contrast settings of indirect IF image, where the amplification strategy produced the next highest fluorescent signal followed by the 2xFL IS (**Fig. 4.4F**). SBR quantification of each staining strategy in tissues stained for EGFR revealed that the amplification strategy produced a ~5% higher SBR than indirect IF and a 42% higher SBR than the 2xFL IS (**Fig. 4.4G**). SBR calculations for pEGFR-stained tissues revealed though that indirect IF stained tissue had an ~18% greater SBR than the amplification strategy and ~78% greater SBR than the 2xFL IS (**Fig. 4.4H**). Quantification of Ki67 staining SBR showed the indirect IF image has the highest SBR, ~58% and ~77% greater than SBR of the amplification strategy and 2xFL IS strategy, respectively (**Fig. 4.4I**).

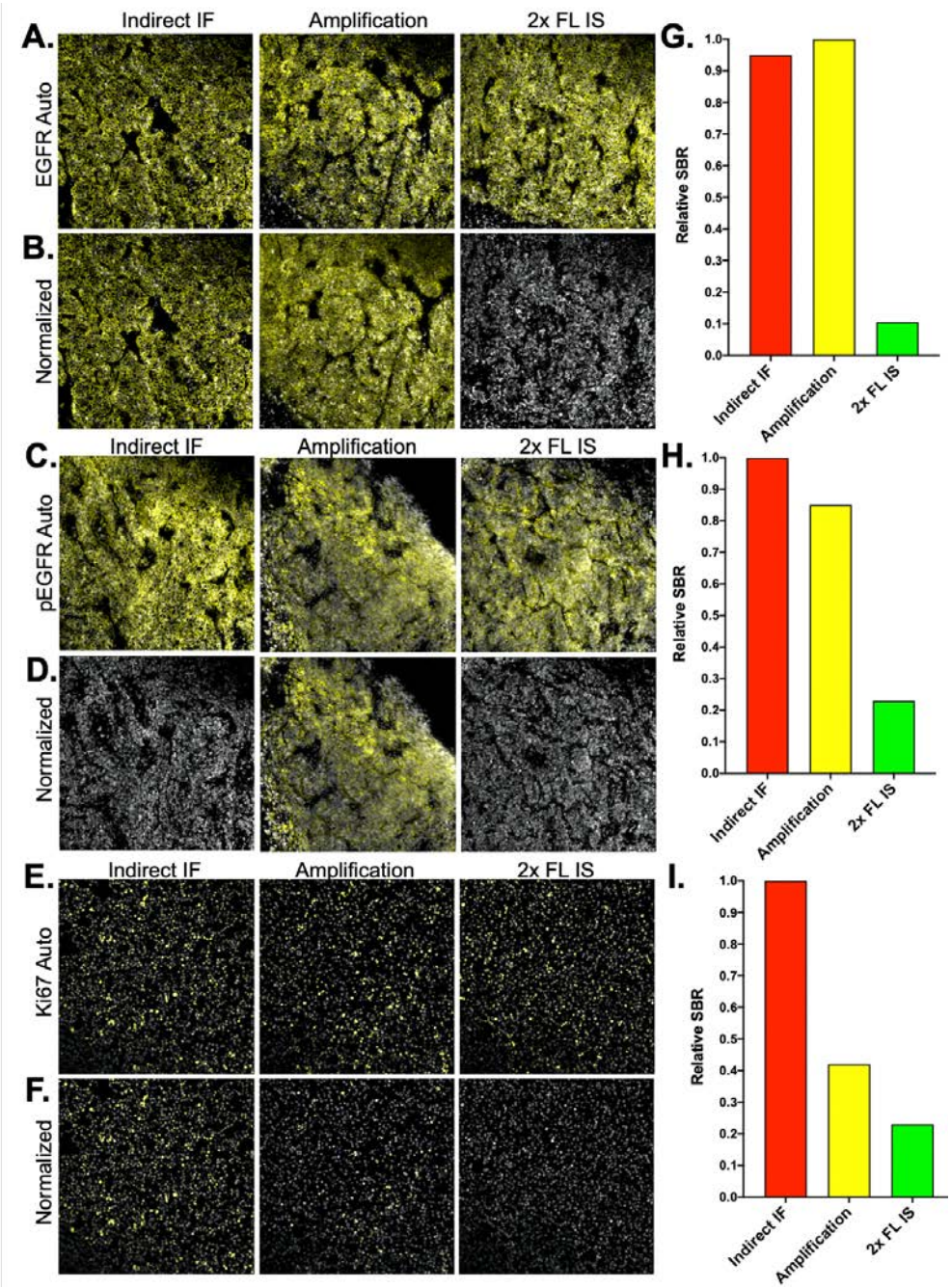

Fig. 4.4: *Ab-oligo amplification strategy evaluation.* The staining pattern and signal to background (SBR) produced by the Ab-oligo amplification strategy was assessed by comparing it to conventional indirect IF and the Ab-oligo conjugate detected using the complementary imaging strand with 2 fluorophores (2xFL IS). **A.** EGFR-specific staining pattern was verified for all staining methods and **B.** signal intensity qualitatively assessed for a membrane bound marker. Similarly, **C.** pEGFR staining pattern and **D.** visual signal intensity evaluation was performed to assess amplification of a cytosolic protein. **E.** Ki67 staining pattern and **F.** signal intensity were also evaluated for amplification of a nuclear marker. Staining pattern verification images are displayed with auto-contrast settings for visualization and signal intensity comparison images are normalized to all have equivalent display settings. SBR was calculated for all images stained for **G.** EGFR, **H.** pEGFR and **I.** Ki67.

Further validation of the optimized Ab-oligo strategy was performed on Ab-oligo conjugates for the following 16 markers: human epidermal growth factor 2 (HER2), alpha smooth muscle actin (αSMA), CD4, cytokeratin 5 (CK5), CK8, CoxIV, CD68, PD1, PCNA, CK7, CK14, androgen receptor (AR), Vimentin, estrogen receptor (ER), progesterone receptor (PR) and E-Cadherin (E-Cad, **Fig. 4.5**). The SBR of HER2, CK8, CK7, CK14, AR, Vimentin and PR were greater than that of conventional indirect IF. The remaining nine Ab-oligo conjugates (αSMA, CD4, CK5, CoxIV, CD68, PD1, PCNA, ER and E-Cad) produced SBR less than that of conventional indirect IF. Of those nine Ab-oligo conjugates, five (αSMA, CD4, CoxIV, CD68 and ER) produced SBR that was at least ~20% lower than that of indirect IF. Thus, all Ab-oligo conjugates stained with the Ab-oligo amplification strategy provided positive staining and sufficient signal for visualization, but performance of the amplification strategy varied.

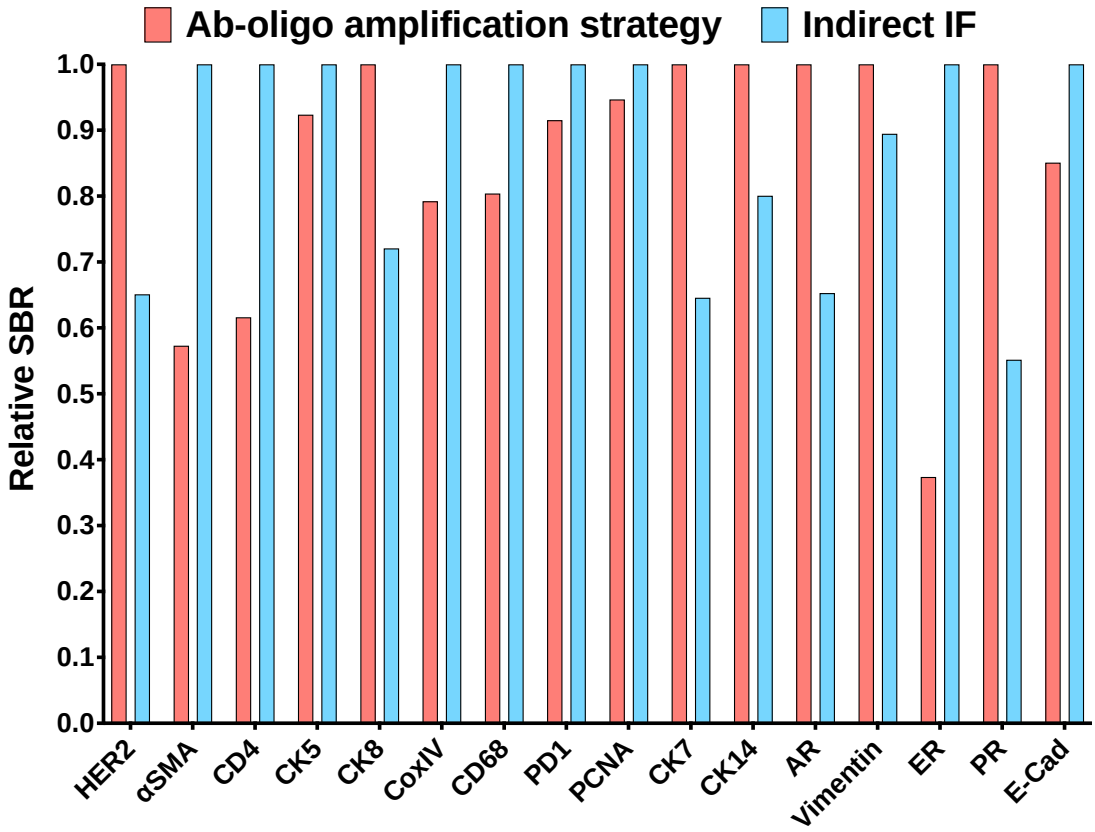

Fig. 4.5: *Ab-oligo amplification strategy SBR variation.* Comparison of SBR (images not displayed) produced by conventional indirect IF and the Ab-oligo amplification strategy revealed heterogeneity in signal amplification performance. All markers displayed were stained with the optimal staining conditions identified by the studies described above where AmpS was heated to 85 °C prior to incubation on tissue. Amp IS was added at a 20X molar excess to AmpS.

Optimization of DS oligo sequence design. The Ab-oligo amplification strategy was assessed for the HER2 Ab-oligo conjugates using a new DS design for the sequences KpnIB, SalIC and PvuIIA to minimize the occurrence of secondary structures. The new DS designed Ab-oligo conjugates were compared to HER2 labeled with conventional indirect IF and the original HER2 Ab-oligo conjugate. All indirect IF samples and samples stained with either the old or new DS

sequences and the optimized amplification strategy produced HER2 specific staining pattern (**Fig. 4.6A**). Quantification of the fluorescence intensity for each image revealed that in all cases the indirect IF image produced the highest fluorescence intensity (**Fig. 4.6B**). All new DS designs generated improved fluorescence signal through the Ab-oligo amplification strategy than the original DS designs. No new DS sequence produced a fluorescence intensity less than 50% of that produced by indirect IF stained cells while the original DS sequences all produced fluorescence intensity > 70% below than that of conventional indirect IF.

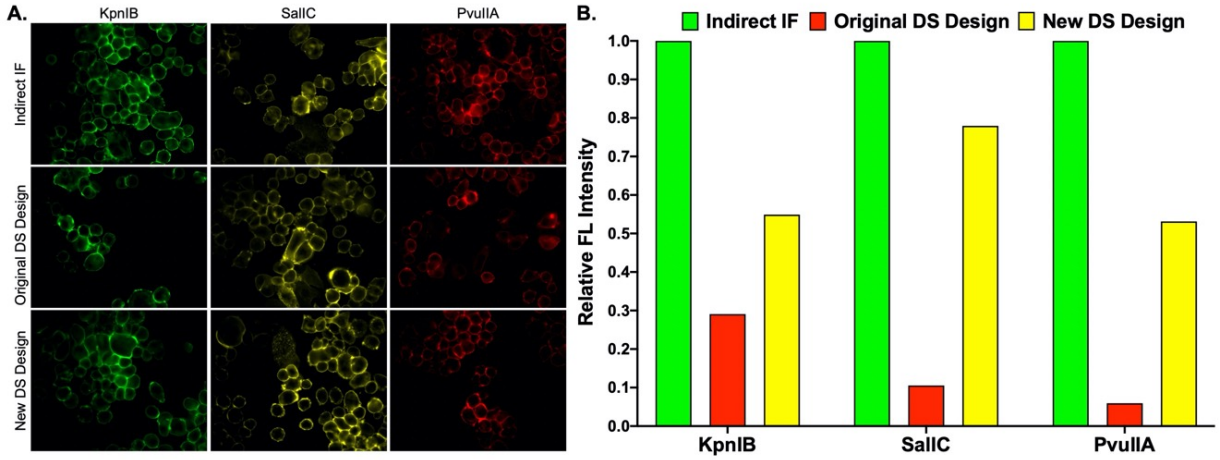

Fig. 4.6: *Optimized docking strand (DS) sequence design.* **A.** Fixed cells were stained for HER2 using conventional indirect IF and HER2 Ab-oligo conjugates containing either the old or new KpnIB, SalIC and PvuIIA DS sequence. All images are set to auto-contrast settings for visualization of HER2-specific staining pattern. **B.** Fluorescence intensity was quantified for each image for comparison of fluorescence intensity between indirect IF, old DS sequence design and the new DS sequence design.

Highly multiplexed image generation with Ab-oligo cyCIF and indirect IF. The validated set of antibodies, both unconjugated primary and Ab-oligo conjugate (**Table 4.1**), were used to generate a 10-color image on a frozen HCC827 xenograft tissue section (**Fig. 4.7**). Unconjugated primary antibody for pEGFR and AF750 labeled secondary were applied first. The master-mix of Ab-oligo conjugates was then incubated in a single staining step followed and IS applied in groups of three using either 2xFL IS or the Ab-oligo amplification strategy. More specifically, E-Cad, Ki67, CK8, EGFR and PI3K were imaged using 2xFL IS while pAkt, CC3, pMEK and Akt were all imaged using the optimized Ab-oligo amplification strategy as described above. Tissue scanning was performed in each staining round for visualization of the specimen with one representative field of view displayed where individual cell staining patterns were visualized. Marker specific staining pattern was seen for all antibodies imaged regardless of staining method where indirect IF staining for pEGFR was successfully performed before any Ab-oligo conjugate was present on the tissue. Additionally, both the 2xFL IS and Ab-oligo amplification strategy were employed simultaneously in a single round of imaging without any deleterious effects on producing accurate antigen labeling. Due to the relative homogeneity of xenografts, there was overlap in the staining pattern for some of the markers especially the EGFR signaling pathway proteins EGFR, pEGFR, Akt, pAkt, PI3K and pMEK. E-Cad and CK8,

commonly expressed in epithelial cells, provided a spatial map for the HCC827 cells. Further, Ki67 and CC3, marking proliferating and apoptotic cells, respectively, are expressed in distinct

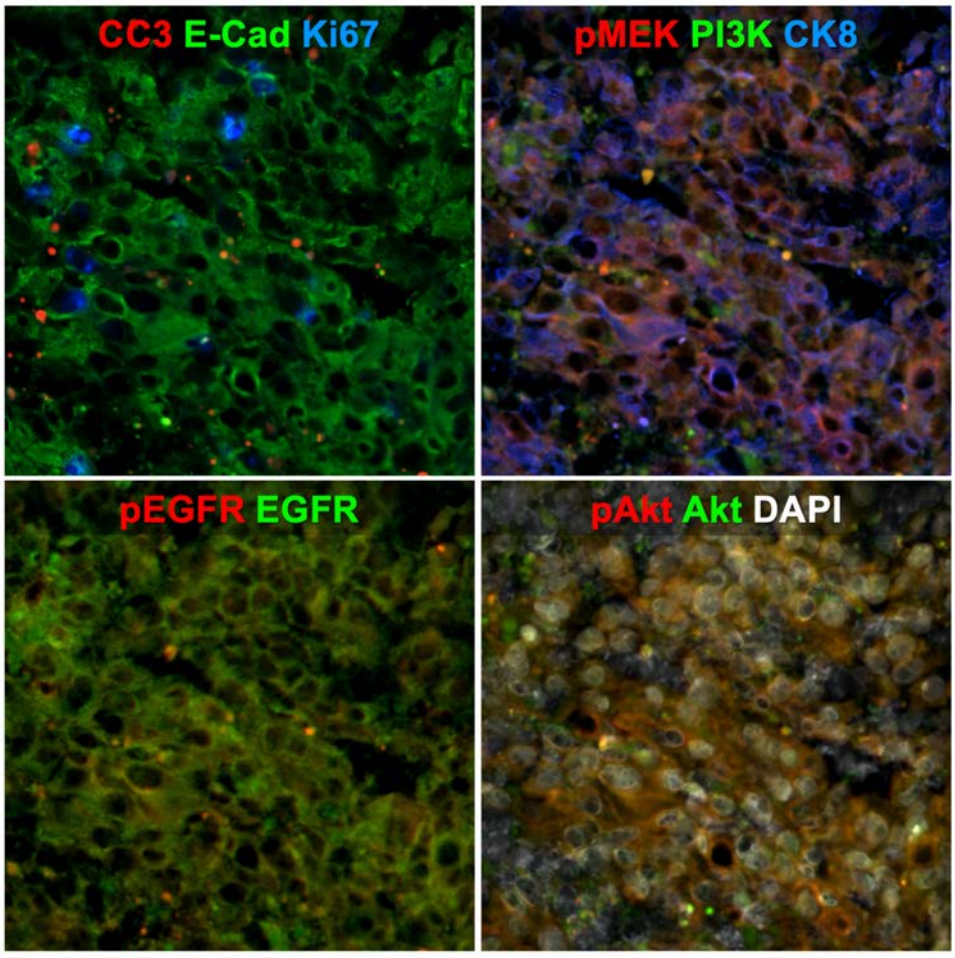

Fig. 4.7: *Highly multiplexed cyCIF imaging of HCC827 xenograft frozen tissue.* A 10-color image was produced on a frozen HCC827 xenograft where pEGFR was imaged with indirect IF and all other markers were imaged with Ab-oligo conjugates. E-Cad, Ki67, CK8, EGFR and PI3K were imaged with 2xFL IS and pAkt, cleaved caspase 3 (CC3), pMEK and Akt were imaged with the optimized Ab-oligo amplification strategy.

cells from one another where DAPI staining provides this spatial context.

DISCUSSION

One the critical components to a robust highly multiplexed imaging platform is detection sensitivity sufficient for detecting low abundance antigens and rare cell subpopulations. This is crucial in the context of the overall goal of building a comprehensive spatial proteomic characterization of a tumor and its microenvironment. A wide variety of highly multiplexed imaging technologies have been developed with this goal in mind and have demonstrated ability to interpret the spatial context of tumor composition in order to inform improved therapeutic strategies. However, both conventional antibody-based and mass spectrometry imaging (MSI) techniques for high dimensional image generation lack amplification strategies for low abundance

antigens. This limits their potential detection sensitivity for rare cell subpopulations and low abundance antigens.

The validation studies of the Ab-oligo cyCIF amplification strategy presented herein, demonstrate its ability to achieve equivalent sensitivity to conventional indirect IF (**Fig. 4.1**). Optimization of the SBR produced by the Ab-oligo cyCIF amplification strategy was first performed with a titration study to identify the molar excess of Amp IS required to maximize staining intensity while minimizing background (**Fig. 4.2**). The optimal molar ratio of Amp IS to AmpS selected was 20:1 which produced marker specific staining pattern (**Fig. 4.2A**) and no visible background fluorescence in the biomarkers tested (**Fig. 4.2B**). Additionally, 20X molar excess of Amp IS demonstrated SBR greater than that of indirect IF (**Fig. 4.2C**). While a rather high molar excess was selected representing increased reagent cost, the 1X molar excess also produced marker-specific staining. Further titration on a per marker basis is ongoing to identify optimal concentrations in an effort to reduce reagent costs. An additional factor in selecting 20X molar excess of Amp IS is that each fluorophore (i.e., AF488, AF546, AF647 and AF750) were assigned a specific Amp IS sequence meaning that Ab-oligo conjugates were assigned a specific channel for amplification. Therefore, in order to prevent cross-talk between the different markers across rounds of imaging, 20X molar excess of Amp IS is applied in order to saturate all AmpS binding sites in each round of imaging. This, by design, reduces additional reagent costs of purchasing a unique Amp IS for each marker which helps to offset the additional reagent cost associated with using high concentrations of Amp IS in each imaging round. Next, optimal AmpS staining parameters were identified to maximize signal amplification by preventing the long oligo strands from forming secondary structures, decreasing efficient hybridization with Amp IS. It was observed that heating AmpS to 85 °C for 3 min prior to applying it to the tissue improved the SBR, a step common in protocols for polymerase chain reaction (PCR) assays for denaturation of oligo templates prior to measurements.[144] This step was therefore integrated into the Ab-oligo cyCIF amplification strategy to mitigate the chance for secondary structure formation of AmpS (**Fig. 4.3C**).

Evaluation of optimized Ab-oligo cyCIF amplification strategy staining parameters (e.g., AmpS heating and 20x molar excess of Amp IS) was performed in a variety of markers with varied efficiency. Ab-oligo amplification of EGFR and pEGFR Ab-oligo conjugates resulted in similar SBR to conventional indirect IF stained tissue (**Fig. 4.4G** & **4.4H**). However, amplification of Ki67 Ab-oligo conjugate resulted in a SBR more similar to that generated with 2xFL IS than conventional indirect IF (**Fig. 4.4I**). Notably, EGFR and pEGFR are expressed in the membrane and cytosol, respectively, while Ki67 is localized to the nucleus suggesting that potentially steric hindrance of the longer AmpS may prevent efficient amplification of nuclear markers. Additionally, Ki67 staining pattern was more disparate than that of EGFR and pEGFR so further refinement of analysis methods to quantify only Ki67 positive pixels could improve evaluation of amplification strategy performance. However, expanded validation of the amplification strategy to a wide variety of markers revealed no relationship between marker localization and amplification performance as compared to conventional indirect IF (**Fig. 4.5**). For example, Ab-

oligo amplification of PCNA, another nuclear marker, produced a SBR within ~10% of conventional indirect IF. In contrast, amplification of CD4 Ab-oligo conjugate, a membrane bound marker, resulted in a SBR ~40% less than that of conventional indirect IF. Additionally, this evaluation of amplification performance across markers also indicated that not all markers are candidates for amplification, where either amplification alone did not improve SBR or amplification was unnecessary for more abundant antigens such as cytokeratin markers (e.g., CK5, CK8, CK7 and CK14).

This result prompted further investigation into the design of the docking strand (DS) sequences conjugated to the antibodies. It was determined through evaluation of oligo sequence composition that some DS sequences had higher potential to form secondary structures such as stem loops that can form when two regions of the same strand are complementary to one another.[145] Three DS sequences, KpnIB, SalIC and PvuIIA, who all possessed high probability for stem loop formation were re-designed to decrease their propensity for secondary structure formation (**Fig. 4.6**). Both the original and new DS design produced marker specific staining pattern for all sequences when stained with the Ab-oligo amplification strategy (**Fig. 4.6A**). However, all three new DS designs showed higher fluorescence intensity than their respective original design (**Fig. 4.6B**). This resulted in increased attention to DS sequence design for future Ab-oligo conjugates to mitigate stem loop formation potential.

A key benefit to Ab-oligo cyCIF is its flexibility to alter the imaging strategy on a per marker basis, where not all markers required amplification. Additionally, the 2xFL IS strategy and amplification strategy could be readily performed simultaneously on the same sample. Furthermore, the Ab-oligo cyCIF workflow is sufficiently flexible to integrate multiple immunofluorescence techniques at once such as conventional indirect and direct IF. Validation of the flexibility of our Ab-oligo cyCIF platform resulted in the generation of a 10-color image on a HCC827 xenograft tissue section where conventional indirect IF along with the Ab-oligo imaging strategies using either the 2xFL IS or the amplification strategies were imaged simultaneously (**Fig. 4.7**). pEGFR was labeled via indirect IF, where it was stained first to avoid cross-reactivity between antibodies of the same host. This first antibody staining step did not disrupt the subsequent staining of Ab-oligo conjugates where cycles of three Ab-oligo conjugates were imaged per round. The first round of imaging included three Ab-oligo conjugates along with pEGFR, but since pEGFR signal could not be removed all subsequent rounds of imaging were done with three markers per round. Importantly, no interactions occurred between the 2xFL IS and the AmpS that were incubated simultaneously, potentially in part due to the heating of the AmpS that denatured any potential complexes formed between the different oligos. For example, the staining patterns of cleaved caspase 3 (CC3) and CK8, which were stained using the amplification and 2xFL IS strategies, respectively were found to maintain specificity.

While the study described herein validate the Ab-oligo amplification strategy and flexibility of Ab-oligo cyCIF, the methodology presented does have some limitations. Regarding the amplification strategy, one drawback to its application is that it adds additional protocol time slowing data generation. Additionally, there is additional reagent cost associated with employing

the amplification strategy that should be considered as well. In order to overcome this, it is crucial that the Ab-oligo cyCIF imaging strategy, either conventional or amplification, is judiciously selected so that only markers that produce low signal and require amplification are amplified in order to minimize the additional protocol time and reagent cost associated with a study. Another limitation of the methodology described is that while the flexibility of Ab-oligo cyCIF to integrate multiple highly multiplexed imaging techniques onto a single tissue section can help prevent redundant antibody validation for the same marker in each technology, this means that multiple signal removal methods must be applied, further increasing data collection time and protocol complexity. For example, use of both Ab-oligo and conventional direct and/or indirect immunofluorescence reagents will require both UV light for signal removal as well as the chemical quenching signal removal technique commonly used in other highly multiplexed immunostaining technologies. However, identification of a single signal removal technique for all applied immunostaining techniques is under investigation to overcome this hurdle.

The demonstrated flexibility of the Ab-oligo cyCIF platform opens possibility for integration with other immunofluorescence techniques such as fluorophore-labeled antibodies. Conjugation of oligos to antibodies involves increased reagent cost and expertise to synthesize while many fluorophore-conjugated antibodies are available for purchase from major antibody vendors. However, while the staining workflow may remain relatively similar when integrating techniques, an inherent drawback is the need to use signal removal methods potentially more harmful to tissue integrity such as fluorophore bleaching. It is therefore necessary to consider each marker for its detection requirements to decide if an amplification strategy may be needed for sufficient signal generation and if conjugation has successfully been performed to that antibody previously. These options for labeling methods offer practical options for high dimensional characterizations of tumor tissue using a variety of well validated techniques, each with their own respective strengths and weaknesses. The flexible Ab-oligo cyCIF platform offers an avenue to increase the number of detectable markers on a single tissue sample and therefore further advances spatial proteomic characterization of complex tumor tissues.

Chapter 5

TRIPODD: A novel fluorescence imaging platform for *in situ* quantification of drug distribution and therapeutic response

This manuscript was originally published in *Molecular Imaging and Biology*. McMahon NP, Solanki A, Wang LG, Montaño AR, Jones JA, Samkoe KS, Tichauer KM, Gibbs SL. TRIPODD: A Novel Fluorescence Imaging Platform for In Situ Quantification of Drug Distribution and Therapeutic Response. Mol Imaging Biol. 2021 Mar 9.

ABSTRACT

Purpose: Personalized medicine has largely failed to produce curative therapies in advanced cancer patients. Evaluation of *in situ* drug target availability (DTA) concomitant with local protein expression is critical to an accurate assessment of therapeutic efficacy, but tools capable of both are currently lacking.

Procedure: We developed and optimized a fluorescence imaging platform termed TRIPODD (**T**herapeutic **R**esponse **I**maging through **P**roteomic and **O**ptical **D**rug **D**istribution), resulting in the only methodology capable of simultaneous quantification of single-cell DTA and protein expression with preserved spatial context within a tumor. Using TRIPODD, we demonstrate the feasibility of combining two complementary fluorescence imaging techniques, intracellular paired agent imaging (iPAI) and cyclic immunofluorescence (cyCIF) conducted with oligonucleotide conjugated antibodies (Ab-oligos) on tissue samples.

Results: We successfully performed sequential imaging on a single tissue section of iPAI to capture single cell DTA and local protein expression heterogeneity using Ab-oligo cyCIF. Fluorescence imaging data acquisition was followed by spatial registration resulting in high dimensional data correlating DTA to protein expression at the single cell level where uptake of a targeted probe alone was not well correlated to protein expression.

Conclusion: Herein, we demonstrated the utility of TRIPODD as a powerful imaging platform capable of interpreting tumor heterogeneity for a mechanistic understanding of therapeutic response and resistance through quantification of drug target availability and proteomic response with preserved spatial context at single cell resolution.

INTRODUCTION

Molecularly targeted therapy, powered by large-scale cancer genomic and proteomic studies, has been largely unsuccessful in producing curative treatment. Extensive genomic sequencing efforts have identified tyrosine kinase inhibitor (TKI) drug targets; however, the heterogeneous nature of the primary tumors and their metastatic sites drives the acquisition of resistance to TKI-based therapies in the vast majority of patients. This is especially evident in advanced cancer patients where genomic heterogeneity represents a significant hurdle in the design of durable treatment regimens to address therapeutic resistance.[23-26] Notably, DNA and RNA analyses of single patients are indirect measures of functional cell-signaling proteins – the actual target of the majority of molecular therapeutics.[146] Proteomics has since emerged as a powerful tool in cancer therapy prediction and evaluation, where the significance of protein expression, function, protein-protein interactions and spatial organization of key tumor biomarkers has been directly validated.[30, 32, 67, 75, 76] However, a major obstacle to overcoming resistance is a lack of understanding of the dynamic cancer ecosystem, highlighted by the multifaceted interactions with the tumor, its microenvironment (TME)[102, 103] and the heterogeneous populations of immune and stromal cells.[147, 148] In response, significant efforts to interpret these complex systems within the spatial context of the tumor to overcome therapeutic resistance are underway. As an example, highly multiplexed proteomic imaging of triple-negative breast cancers illuminated the significance of the spatial proximity of tumor and immune cells to one another where cellular composition, spatial arrangement and expression of immune regulatory proteins were correlated to overall survival.[149] Importantly, this study led to the identification of distinct tumor-immune architectures which hold the potential for earlier identification of patients who are most likely to respond to immune checkpoint therapy, a characteristic not currently used when stratifying patients in clinical trials. This work has motivated further clinical investigation into tumor-immune microenvironment spatial organization to understand if this relationship can inform therapeutic strategy design to overcome immune inhibition. While recent advances in methodologies to perform high dimensional profiling of tumor architecture and composition are encouraging, a crucial variable that is not routinely considered in current spatial analyses is drug distribution and engagement. Successful therapy is dictated by the duration, completeness and heterogeneity of drug target availability (DTA) and engagement in the complex disease setting.[13, 19] While tools exist to quantify local protein expression of a tumor (i.e., cyclic immunostaining), tools to quantify critical drug efficacy metrics like molecularly targeted therapies' distribution and protein engagement, concomitant with local protein expression and TME response, have not been fully realized.

Insufficient DTA and off-target binding are typically assessed by bulk sampling of plasma or tissues, resulting in sample averages that homogenize the important spatial variation in cell-to-cell drug distribution, target binding and off-target effects.[20-22] In response, an assortment of small molecule drugs with labeling modifications have been generated (e.g., fluorescent, biotin and photoclickable labels) to facilitate direct visualization of tissue distribution and target

engagement.[20, 33-36] Conversely, drug target proteins have themselves been genetically modified, enabling visualization.[19, 37] While useful, modifications can vastly alter drug distribution or target engagement. To overcome this difficulty, numerous label-free methods have also been developed including mass spectrometry imaging, assessment of drug targets in tissue lysates, cellular thermal shift assay and positron emission tomography.[38-43] However, DTA quantification necessitates accounting for both the drug that binds to its target as well as the drug that accumulates in the cells and tissues in a nonspecific manner.[28]

While targeted uptake is the goal of drug development, all drugs have some degree of untargeted accumulation attributable to drug affinity, biodistribution, pharmacokinetics, and/or metabolism.[44, 45] To facilitate quantification of specific and nonspecific accumulation of targeted drugs in tissue, we have adapted a technique from autoradiography termed Paired Agent Imaging

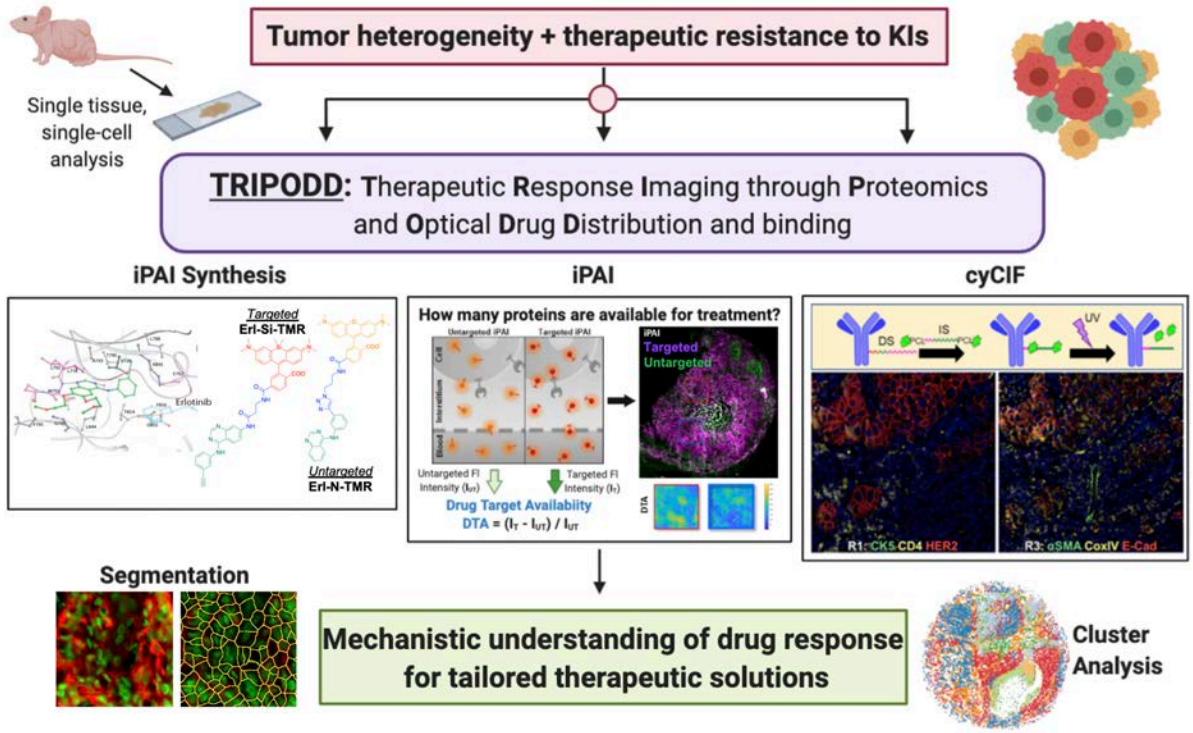

Fig. 5.1: ***T**herapeutic **R**esponse **I**maging through **P**roteomics and **O**ptical **D**rug **D**istribution and binding (TRIPODD).* TRIPODD is a novel fluorescence imaging toolbox which enables in situ measurement of drug target availability (DTA) and spatially intact proteomic signatures by combining iPAI and cyCIF onto a single tissue section. iPAI is facilitated by the synthesis of fluorescently labeled targeted and untargeted, spectrally distinct small molecule therapeutics guided by the protein crystal structure.[1] Fluorescence imaging of both the targeted and untargeted iPAI probes enables quantification of the number of proteins available for treatment using iPAI to calculate DTA heterogeneity. Following iPAI imaging, cyCIF staining using oligonucleotide conjugated antibodies can be utilized to quantify proteomic signatures. Single cell, spatially resolved DTA and proteomic analysis will facilitate mechanistic understanding of drug response to enable design of improved therapeutic solutions.

(PAI). PAI was originally created for quantitative *in vivo* imaging, where nonspecific accumulation of protein-based affinity reagents was observed to dominate malignant tissue signals.[46] The PAI approach hypothesized that the nonspecific accumulation of a molecularly

targeted, radiolabeled antibody could be corrected for by normalizing its signal to the signal of a co-administered, control antibody, labeled with an isotope of different energy. The dual isotope labeling of the targeted and control antibodies permitted energy windowing for detection of both individual signals simultaneously, where the control antibody was used to correct for the dominant nonspecific uptake in malignant tissues. This technique has been reinvigorated by the optics community, where spectrally-distinct targeted and untargeted imaging agents are used to correct for nonspecific uptake, providing quantitative assessment of receptor density.[47-63] Herein, we have extended the PAI technique from fluorescently labeled proteins measuring extracellular receptors to fluorescently labeled cell permeant, small molecule therapeutics to detect intracellular targets. Thus, termed intracellular PAI (iPAI), this novel technique uses spectrally-distinct, fluorescently-labeled targeted and untargeted small-molecule drug derivatives, such as TKIs. By collecting images of the targeted and untargeted agents *in vivo*, we can calculate the number of drug targets actively engaged with the therapeutic, aiding in prediction of *effective* dose. Additionally, although our technique relies on fluorescently-labeled drugs for quantification, all treatment is completed with the parent drug, thus iPAI is classified as a label-free method, permitting quantification of the interaction between the parent drug and its native target. DTA quantification permits interpretation of intra- and inter-tumoral heterogeneity of available drug targets, a crucial step in the mechanistic unraveling of the complexities of resistance.

Requisite for a complete mechanistic assessment of therapeutic response is to simultaneously measure the proteomic response in the same tissue where DTA heterogeneity can be correlated on a cell-by-cell basis to perturbed protein expression. Conventional antibody staining techniques (i.e., immunofluorescence [IF] or immunohistochemistry [IHC]) measure protein expression and spatial distribution but lack the dimensionality to measure cell viability, signaling perturbations and TME interactions on a single sample. In response to this need, cyclic immunostaining techniques have been developed, including our cyclic IF technique, utilizing oligonucleotide labeled antibodies (Ab-oligo cyCIF) to generate highly multiplexed images on a single sample.[67, 80-83, 112] In this validation study, we apply our complementary iPAI and Ab-oligo cyCIF techniques to the same tissue sample to validate our novel fluorescence imaging platform, **T**herapeutic **R**esponse **I**maging through **P**roteomic and **O**ptical **D**rug **D**istribution (**TRIPODD**, **Fig. 5.1**). TRIPODD facilitates simultaneous single-cell quantification of DTA and the associated tumor biology through accurate segmentation of spatially aligned tumor cells based on Ab-oligo cyCIF. To date, TRIPODD is the only methodology to visualize and quantify the complex interactions that define effective cancer therapy, a critical unmet analytical need. In these proof-of-concept studies, xenografts with varied epidermal growth factor receptor (EGFR) expression, the molecular target of erlotinib, were examined as our model system to demonstrate the utility of the TRIPODD methodology.

MATERIALS & METHODS

Synthesis of fluorescently labeled erlotinib. The targeted and untargeted intracellular paired agent imaging (iPAI) probes used in this study were derivatives of erlotinib (Erl), a first generation, reversible TKI targeting EGFR. Synthesis of the erlotinib iPAI probes has been previously described.[150] Briefly, site selection for synthetic modifications of erlotinib to generate the targeted and untargeted drug derivatives was guided by the structure of the parent drug bound to the EGFR crystal structure.[1, 151] The spectrally-distinct fluorophores, tetramethylrhodamine (TMR) and silicon-TMR (Si-TMR), were selected for probe labeling due to overall charge, charge distribution, molecular weight and structural similarity between the two fluorophores to maintain biodistribution similarity. The two probes synthesized were (1) Erl-SiTMR used as the cell membrane permeant iPAI targeted agent with a maximum emission peak at 660 nm and (2) Erl-TMR used as the cell membrane permeant iPAI untargeted agent with a maximum emission peak at 565 nm.

Generation of oligonucleotide conjugated antibodies (Ab-oligo) for cyCIF. Oligonucleotide (oligo) conjugated antibodies were generated as previously reported.[112] In brief, monoclonal antibodies to cytokeratin 5 (CK5), CK8, phospho-EGFR (pEGFR), E-Cadherin (E-Cad), and Ki-67 were purchased from AbCam (Cambridge, UK) and Cell Signaling Technology (Danvers, MA). A unique dibenzocyclooctyne-terminated (DBCO), single-stranded oligonucleotide (docking strand [DS], 28 mer in length), used to label each antibody, was purchased from Integrated DNA Technologies (IDT, Coralville, IA). Antibody modification and oligonucleotide conjugation were completed with the SiteClick™ Antibody Azido modification kit (ThermoFisher Scientific, Waltham, MA) following the manufacturer's instructions.

Cell lines. The human epidermoid carcinoma cancer cell line, A431, was generously provided by Dr. Kimberley Samkoe at Dartmouth College (Hanover, NH). The human lung adenocarcinoma cell line, HCC827, and human colorectal adenocarcinoma cell line, SW620, were purchased from ATCC (Manassas, VA) and maintained mycoplasma free at passage numbers <25 for all studies. The cell lines were expanded in their respective optimal growth media (A431: DMEM [ThermoFisher Scientific] + 10% fetal bovine serum [FBS, VWR Scientific, Radnor, PA] + 1% penicillin/streptomycin/glutamine [ThermoFisher Scientific]; HCC827: RPMI 1640 [ThermoFisher Scientific] + 10% FBS + 1% penicillin/streptomycin/glutamine; SW620: Leibovitz L-15 [ThermoFisher Scientific] + 10% FBS + 1% penicillin/streptomycin/glutamine) and stored at 37 °C in either a 5% (A431 and HCC827) or 0% (SW620) CO_2 incubator.

Animal care and use. All animal experiments were approved by the Oregon Health and Science University (OHSU) Institutional Animal Care and Use Committee (IACUC). All mice were hosted in the AAALAC certified OHSU vivarium, and supplied with food, water and daily inspection to monitor for pain or distress for the duration of experimentation. Mice were placed on a chlorophyll-free diet (Animal Specialties, Inc., Hubbard, OR) one week prior to tumor resection. All rodent surgical procedures, described herein, were performed under full anesthesia composed of a 90/10 mixture of ketamine/xylazine. Ketamine (Hospira Inc., Lake Forest, IL) was

administered at a dose of 100 mg/kg and xylazine (AnaSed, Shenandoah, IA) was administered at dose of 10 mg/kg by intraperitoneal (IP) injection. The toe pinch method was employed to verify the depth of anesthesia prior to commencement of any surgical procedures. The standard method of euthanasia for mice was inhalation of carbon dioxide under full anesthesia at the end of each experiment. Euthanasia was confirmed by physical examination to ensure cessation of heartbeat and respiration and is consistent with the recommendations of the Panel on Euthanasia of the American Veterinary Medical Association.

Mouse Xenograft Models. Mixed male and female athymic nude mice (Homozygous 490, Charles River Laboratories, Wilmington, MA) were purchased at 32-38 days old. After at least 48 hours of acclimation, a total of 13 mice were subcutaneously implanted with A431, HCC827 or SW620 cell xenografts described briefly as follows. Cells were trypsinized, counted and resuspended in their appropriate growth media to a concentration of 2 x 10^7 cells/ml. The mice were then implanted with cells into each rear flank at a final concentration of 1 x 10^6 cells/flank in 50% v/v Matrigel (Corning Inc., Corning, NY), resulting in two tumors/mouse. A total of n = 5 nude mice each were implanted for A431 cell line derived xenograft (CDX) models, n=5 mice implanted for HCC827 CDX models and a total of n = 3 nude mice were implanted for SW620 CDX models. The mice were monitored daily after implantation for tumor growth. The tumors were allowed to grow to a maximum size of 1.2 cm^3 with growth times varying for each cell line (A431: ~2-3 weeks, HCC827: ~7-8 weeks, SW620: ~4 weeks). Mice weighed ~20-25g at the time of iPAI agent administration prior to sacrifice and tissue collection.

When tumors reached 1-1.2 cm^3, the Erl-SiTMR and Erl-TMR iPAI agents were injected simultaneously via tail vein injection to n = 3 of each CDX mouse model at 2.5-3.5 mg/kg for both the targeted and untargeted iPAI probes. As controls for the study, an HCC827 CDX bearing mouse was co-injected with the SiTMR and TMR fluorophores without conjugation to erlotinib at matched molarities to the labeled iPAI probe (80.4 nmol and 78.0 nmol for SiTMR and TMR, respectively). An additional HCC827 CDX bearing mouse was injected with vehicle without fluorophores (i.e., vehicle only) as a control to assess tissue autofluorescence. The remaining n = 2 A431 CDX mice were used in a competitive binding study with the parent erlotinib drug administered prior to the erlotinib iPAI agents. These n=2 A431 CDX bearing mice were injected via the tail vein with 2.5 mg/kg of erlotinib 24 hours before simultaneous tail vein injection of 2.5 mg/kg each of parent erlotinib, targeted (Erl-SiTMR) and untargeted (Erl-TMR) iPAI agents. Injection vehicle for all systemically administered TKI and iPAI probes was a co-solvent mixture of a ratio of 10% dimethyl sulfoxide ([DMSO], Sigma-Aldrich, St. Louis, MO), 5% Kolliphor (Sigma-Aldrich), and 85% of 75% mixture of FBS/PBS (VWR Scientific). For all CDX models, tumors were resected four hours after systemic administration of the iPAI agents or parent fluorophore and flash frozen in optimal cutting temperature (OCT) compound (Fisher Scientific, Waltham, MA).

Flow Cytometry. A431, HCC827 and SW620 cells were trypsinized, counted, and fixed in 4% paraformaldehyde (PFA) for 10 min. A 3 min permeabilization step (0.5% Triton-X) was followed by 2 x 5 min washes in phosphate buffered saline (PBS) and then 2 x 10^6 cells per cell

line were blocked for 15 min with 5% FBS. Without removing the blocking buffer, the cells were then incubated with 5 mg/ml cetuximab (Eli Lilly, Indianapolis, IN) directly conjugated to Alexa Fluor 647 ([AF647], 1:1.7 antibody to fluorophore conjugation ratio). The cells were washed 1 x 5 min with PBS + 0.1% Tween 20, followed by 2 x 5 min PBS washes, and finally resuspended in fresh PBS prior to analysis on a Becton Dickinson LSR Fortessa (Becton, Dickinson and Company, Franklin Lakes, NJ). The flow cytometer was configured with a 640-1 (670/30) Cy5 channel to detect AF647. A minimum of 1 x 10^5 cells were counted for each sample. To quantify EGFR receptor number, Quantum™ Alexa Fluor® 647 molecules of equivalent soluble fluorophore (MESF) beads (Bangs Laboratories, Inc., Fishers, IN) were quantified prior to the cellular samples.

Fluorescence microscopy. Frozen blocks were sectioned at 10 μm thickness (Leica Biosystems cryostat, Wetzlar, Germany) onto SuperFrost Plus glass slides (ThermoFisher). Fluorescence images of whole tissue sections were acquired on a Zeiss AxioScan.Z1 microscope (Carl Zeiss AG, Oberkochen, Germany) equipped with a Colibri 7 light source (Carl Zeiss AG) and Orca Flash4 v.2 (Hamamatsu Photonics, Hamamatsu, Shizouka, Japan). Images were collected using the following filter sets: Zeiss 38HE (Cy2/AF488 [Carl Zeiss AG]), Zeiss 43HE (Cy3/AF555 [Carl Zeiss AG]), Zeiss 50 (Cy5/AF647 [Carl Zeiss AG]) and Chroma 49007-ET-Cy7 (Cy7/AF750 [Chroma Technology Corporation, Bellows Falls, VT]). Excitation light was filtered using the following bandpass (BP) filters: 470/40 (38HE), 550/25 (43HE), 640/30 (50) and 710/75 (49007-ET-Cy7) for Cy2, Cy3, Cy5 and Cy7 channels, respectively. Emission light was filtered using the following BP filters: 525/50 (38HE), 605/70 (43HE), 690/50 (50) and 810/90 (49007-ET-Cy7) for Cy2, Cy3, Cy5 and Cy7 channels, respectively. Images were captured at 20X (Plan-Apochromat, 0.8NA) magnification, where image tiles with 10% overlap were stitched together using the Zeiss Zen software to produce a single tissue map.

Validation of tumor iPAI agent distribution. To assess the homogeneity of iPAI agent distribution throughout the tumors, three 10 μm thick sections were collected from a single frozen HCC827 xenograft tissue block that had been co-administered targeted and untargeted iPAI probes. The three sections were collected at the following depths relative to one another: 0 μm (Section 1), 10 μm (Section 2) and 50 μm (Section 5). The targeted iPAI probe (Erl-SiTMR) was imaged in the Cy5 channel, the untargeted iPAI probe (Erl-TMR) was imaged in the Cy3 channel and tissue autofluorescence, used to generate a focus map, was imaged in the Cy2 channel. After image acquisition, a custom MATLAB script (10.5281/zenodo.4004647) was used to calculate DTA images on a per pixel basis for each tissue image. DTA was calculated as

$$\text{Drug Target Availability (DTA)} = \frac{\mathrm{I_T} - \frac{I_{UT}}{SF}}{\frac{I_{UT}}{SF}} \qquad (1)$$

where $\mathrm{I_T}$ is the targeted iPAI probe fluorescence intensity, $\mathrm{I_{UT}}$ is the untargeted iPAI probe fluorescence intensity and SF is a scaling factor to account for signal intensity difference between the target and untargeted probes caused by collection in their respective imaging channels. The scaling factor was determined by imaging the targeted and untargeted probes at titrated

concentrations on the Zeiss AxioScan.Z1 to generate a linear calibration trend line for each probe. The scaling factor was then calculated as the ratio of the slope of the untargeted probe trend line to the slope of the targeted probe trend line and is built into the MATLAB analysis script. DTA for each tissue section was quantified by calculating the tissue mean DTA by manual segmentation of the tissue in ImageJ v1.51 (National Institute of Health, Bethesda, MD) and extracting the mean DTA from the tissue sections. The mean fluorescence signal or DTA value from each section was divided by the highest mean fluorescence or DTA value, respectively, to calculate relative fluorescence intensity or DTA values. The built-in MATLAB function, histogram(), was used to plot histograms of the fluorescence signal or DTA values on a per pixel basis where probability for each pixel value was calculated and plotted in order to normalize for tissue size. Notably, zero-value pixels located in the background areas of images were excluded for accurate tissue pixel value probability quantification.

***Ex vivo* iPAI imaging of varied EGFR expressing xenograft tissue.** Frozen A431, HCC827 and SW620 iPAI xenograft tissue blocks along with frozen HCC827 xenograft blocks of fluorophore (FL) only and vehicle only injected tissues were sectioned at 10 μm thickness with one section adhered to each slide. The tissue sections were imaged on a Zeiss AxioScan.Z1, where images were again collected in the Cy5 (Erl-SiTMR), Cy3 (Erl-TMR) and Cy2 (autofluorescence used to generate focus maps) channels. Mean fluorescence intensity for each image was calculated in ImageJ through manual segmentation of the tissue. The relative fluorescence intensity for each image was calculated by dividing the mean fluorescence intensity of an image by the highest mean fluorescence intensity of that particular image channel (i.e., Cy5 and Cy3). The previously described MATLAB script was used to calculate DTA images for the A431, HCC827 and SW620 iPAI injected tissues as well as the FL only injected tissues (Equation 1). Relative fluorescence intensity and DTA values along with the generation of a histogram comparing the DTA images of the displayed A431, HCC827 and SW620 tissue sections were calculated following the same protocol as described above. To account for inter-animal variability, n=3 tumors from each CDX model, each collected from a different mouse, were analyzed and bar plots comparing tissue sections with standard deviation were generated in Prism v7.0 (GraphPad, San Diego, CA).

Competitive binding study between parent erlotinib and iPAI derivatives. A431 xenograft bearing mice (n=2) were systemically administered parent erlotinib (2.5 mg/kg) 24 hours prior to systemic administration of equivalent doses of both parent erlotinib and the erlotinib iPAI probes (all at 2.5 mg/kg) four hours prior to sacrifice and tumor resection. Frozen A431 xenograft tissue sections from n=3 tumors injected with both parent erlotinib TKI and erlotinib iPAI probes were sectioned at 10 μm thickness with one section adhered to each slide for this analysis. For equivalent group size comparison, competitive binding tissue (n=3 tumors) was compared to tissue administered with only erlotinib iPAI probes that was collected from n=3 tumors as previously described. The tissue sections were imaged on a Zeiss AxioScan.Z1, where images were again collected in the Cy5 (Erl-SiTMR), Cy3 (Erl-TMR) and Cy2 (autofluorescence used to generate focus maps) channels. Mean fluorescence intensity for each image was calculated in ImageJ through manual segmentation of the tissue. The relative fluorescence intensities for each image

were calculated by dividing the mean fluorescence intensity of an image by the highest mean fluorescence intensity of that particular image channel (i.e., Cy5 and Cy3). The previously described MATLAB script was used to calculate DTA images for the tissue co-injected with erlotinib and erlotinib iPAI derivatives as well as tissue with only erlotinib iPAI derivatives present (Equation 1). Relative fluorescence signal, DTA values and histograms were calculated following the same protocol as described above. Bar plots comparing tissue sections from n=3 tumors with standard deviation were generated in Prism v7.0 (GraphPad, San Diego, CA).

Ab-oligo cyCIF frozen tissue staining and imaging. Following iPAI fluorescence microscopy of A431 xenograft tissue sections, signal removal was performed by washing with 1X PBS, pH 7.4 (3 x 5 min). A subsequent whole tissue image was captured to confirm signal removal to the level of tissue autofluorescence. The coverslip was then removed and the tissue was incubated in 2% paraformaldehyde (PFA, Sigma-Aldrich) at room temperature (RT) for 15 min and then washed with 1X PBS, pH 7.4 (3 x 5 min). The tissue was then permeabilized using 1X PBS, pH 7.4 + 0.3% Triton X-100 for 15 min at RT and washed with pH 7.4 PBS (3 x 5 min). The slides were blocked at RT for 30 min in Ab-oligo blocking and dilution buffer which contained 2% bovine serum albumin (BSA, bioWORLD, Dublin, OH), 0.5 mg/mL sheared salmon sperm DNA (ThermoFisher) and 0.5% dextran sulfate (Sigma-Aldrich) in 1X PBS, pH 7.4. Five selected Ab-oligo conjugates were combined into a single cocktail solution and diluted in the Ab-oligo blocking and dilution buffer to a final protein concentration for each conjugate of 15 μg/mL. The A431 tissue sections were covered with 40 μL of the diluted Ab-oligo conjugate cocktail, or blocking and dilution buffer without Ab-oligo conjugates as a negative control, and incubated at 4 °C overnight in a humidified chamber. The next day, the sections were washed with 2X saline-sodium citrate (SSC) buffer, pH 7 (VWR, Radnor, PA) for 3 x 5 min. The sections were fixed in 2% PFA for 15 min at RT, then washed again in 2X SSC buffer (3 x 5 min). The tissue stained with the Ab-oligo conjugates was labeled with complementary imaging strands (IS) with distinct fluorophore labels in rounds, where 350 nM IS concentration was used per IS for *in situ* labeling. Serial sections were used for staining with the cocktail of Ab-oligo or rounds of IS only application without Ab-oligo incubation as a negative control. Ab-oligo targets for imaging were selected for either tumor viability assessment (CK8, CoxIV, Ki67), tumor biology (pEGFR) or cell segmentation (E-Cad). A DNA-selective fluorogenic dye optimized for imaging in the Cy2 channel, Nuclear Green (AbCam), was applied to the slides at a final concentration of 100 nM for 10 min at RT before washing with 2x SCC (2 x 5 min). The stained slides were imaged on a Zeiss AxioScan.Z1. Images were collected in all 4 channels (Cy2, Cy3, Cy5, Cy7). The antibodies imaged in each round were as follows: Round 1: pEGFR (Cy3) and E-Cad (Cy7), Round 2: Ki67 (Cy3), CK8 (Cy7) and Round 3: CoxIV (Cy3). Nuclear Green was imaged in the Cy2 channel in all rounds. All stained slides were treated with ultraviolet (UV) light after each round for 15 mins through the coverslip followed by washing 10 times with 0.1X SSC and remounted with Fluoromount-G. Finally, the slides were imaged with the same settings used prior to UV treatment to quantify any remaining signal. Subsequent rounds of IS addition, imaging and signal removal

were repeated until all Ab-oligo conjugates were imaged. Tumor viability was confirmed with standard histology by hematoxylin and eosin (H&E) staining.

Quantification of single-cell drug target availability (DTA). After iPAI and Ab-oligo cyCIF data were collected from the same A431 tissue section, all images were spatially registered. First, the Ab-oligo cyCIF data captured across rounds of staining and imaging was automatically registered with a custom MATLAB script that used the Nuclear Green image in each round to map and then register images with accurate alignment of cell nuclei.[152] The untargeted (Erl-TMR) and targeted (Erl-SiTMR) probe images were then manually registered to the first cyCIF round Nuclear Green image with the built-in spatial transformation structure function, tform() (MATLAB). To enable single-cell DTA quantification, cell segmentation was performed with the publicly available cell segmentation toolkit, ilastik[131] v2.0 (European Molecular Biology Laboratory). For accurate cell segmentation, images of Nuclear Green signal and E-Cadherin were used to define each nucleus and cell membrane, respectively. Then, a pixel classifier was trained in the Pixel Classification pipeline to identify all pixels into one of three classes: nucleus, cell boundary or background area. After pixel classification was complete, a map of each pixel with its identity was integrated into the "Boundary-based Segmentation with Multi-cut" pipeline. A watershed algorithm was then run to plant watershed seeds in the nucleus of each cell, which were allowed to grow until a watershed encountered a pixel identified as a cell membrane pixel. A training step was then initiated where a subset of predicted cell boundaries was labeled as accurate or inaccurate to train the classifier that was then applied to further improve the accuracy of the final segmentation mask. The final segmentation mask was then loaded into the "Object Classification" pipeline where a classifier was trained to identify cells as either a cell or an object in a background area of the image. After applying the classifier to the segmentation mask, data for each object was exported as a comma separated variable (CSV) file that included object identity as either cell or background, the x- and y-coordinate of the center of mass of each object, and the fluorescence intensity of the Nuclear Green, E-Cadherin and both the untargeted and targeted iPAI signals. To calculate single-cell DTA values, the ratiometric calculation for DTA was performed on all objects identified as a cell using the untargeted and targeted iPAI probe signals in each cell (Eq. 1). Next, the x- and y-coordinate of the center of mass and DTA value for each cell was loaded into MATLAB and plotted using the spatial information for x- and y-axis and a color "heat" map was generated to represent the DTA value for each individual cell.

Statistical Analysis. Fluorescence intensity and calculated DTA data are presented as mean ± standard deviation and marked with asterisks for statistical significance. Fluorescence intensity of iPAI and calculated DTA of xenograft tissue type with varied EGFR expression was compared to all other xenograft tissue types individually where significance was tested for using a one-way analysis of variance (ANOVA) followed by Fisher's least significant difference (LSD) multiple comparison test. The α value was set to 0.05 for all analyses. iPAI fluorescence intensity and calculated DTA from tissues in the competitive binding study were compared between parent erlotinib and iPAI derivative administration with an unpaired t-test where the α value was set to

0.05. P-values for significance are denoted by the number of asterisks as follows: *p < 0.05, **p < 0.01, ***p < 0.001, and ****p < 0.0001. All statistical analyses were completed using Prism.

RESULTS

Validation of tumor iPAI probe distribution throughout the tissue volume. iPAI probe distribution was quantified using tissue sections from an HCC827 tumor collected at different depths relative to the tumor edge labeled as 10 µm (section 1, tumor edge), 20 µm (section 2, serial section) and 50 µm (section 5) that were imaged for Erl-SiTMR and Erl-TMR fluorescence signal (**Fig. 5.2A** & **5.2B**). The targeted and untargeted images were used to calculate DTA tissue maps (**Fig. 5.2C**). Tissue morphology was similar between adjacent sections 1 and 2, while there was a substantial decrease in tissue section size for the more distant section 5. Relative fluorescence intensity of the targeted probe signal in each tissue section was calculated where section 1 showed the highest targeted probe signal, while sections section 2 and 5 showed a small decrease with 94% and 95% of the relative intensity, respectively (**Fig. 5.2A**). Relative fluorescence intensities of the untargeted probe were also calculated where section 5 showed the greatest untargeted probe signal followed by section 1, with a 3% lower relative intensity, and section 2 with an 8% lower relative signal intensity (**Fig. 5.2B**). Relative DTA calculations showed section 1 with the highest DTA while sections 2 and 3 had only a 2% decrease with similar overall spatial patterning in calculated DTA values (**Fig. 5.2C**). Examination of pixel probability histograms of all three tissue sections

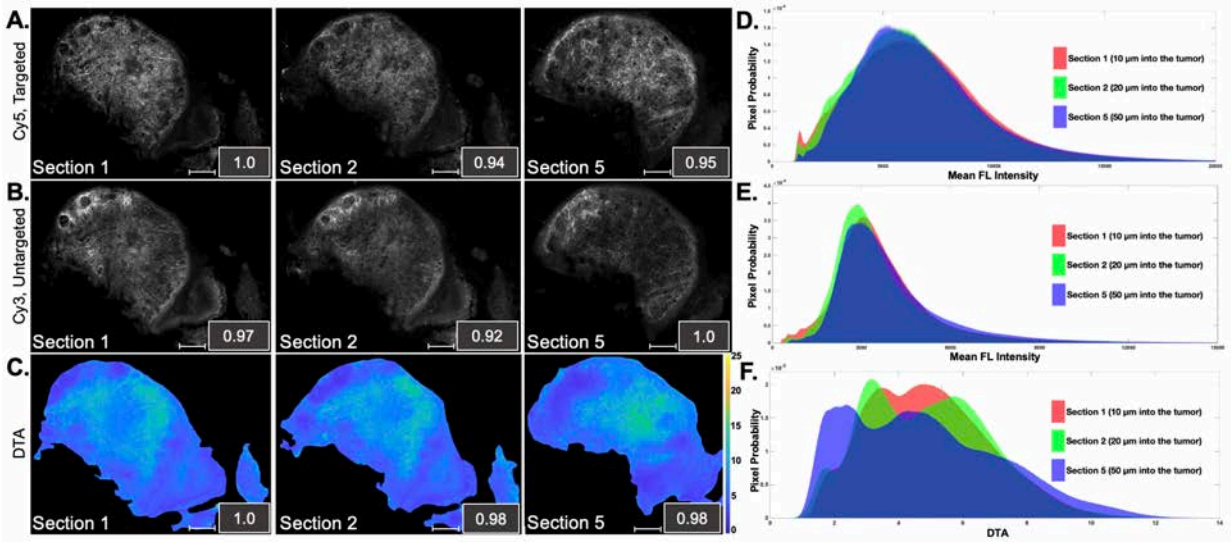

Fig. 5.2: *DTA signatures are spatially and quantitatively similar throughout CDX tumors*. HCC827 xenograft tissues were serially cryosectioned at 10 (Section 1), 20 (Section 2) and 50 µm (Section 5) into the same tumor tissue block. Fluorescence images of the **A.** targeted channel (Cy5) and **B.** untargeted channel (Cy3) were collected and are displayed with auto contrast. For quantitative comparison the inset values indicate the relative intensity normalized across sections for each imaging channel (i.e., Cy3 and Cy5). These targeted and untargeted images were used to calculate **C.** DTA tissue maps, which are displayed at the same contrast levels with relative intensity normalized across the sections displayed as inset values. Additionally, pixel probability histograms were calculated for the **D.** targeted channel, **E.** untargeted channel and F. DTA tissue maps for quantitative comparison. Scale bars = 440 µm.

again demonstrated the similarity of signal in all channels. The targeted and untargeted channel histograms displayed significant overlap of the histograms from all three tissue images (**Fig. 5.2D** & **5.2E**). Pixel probability histograms of the DTA tissue maps display large areas of overlap in support of the calculated relative DTA values, however there were unique histogram shapes for each DTA tissue map (**Fig. 5.2F**).

Quantification of DTA in varied EGFR expressing tissues. Quantification of the distribution of targeted and untargeted iPAI probes was performed in xenograft tissues with varied endogenous EGFR expression *in vitro* (**Fig. 5.3**). EGFR number for each cell line, as quantified

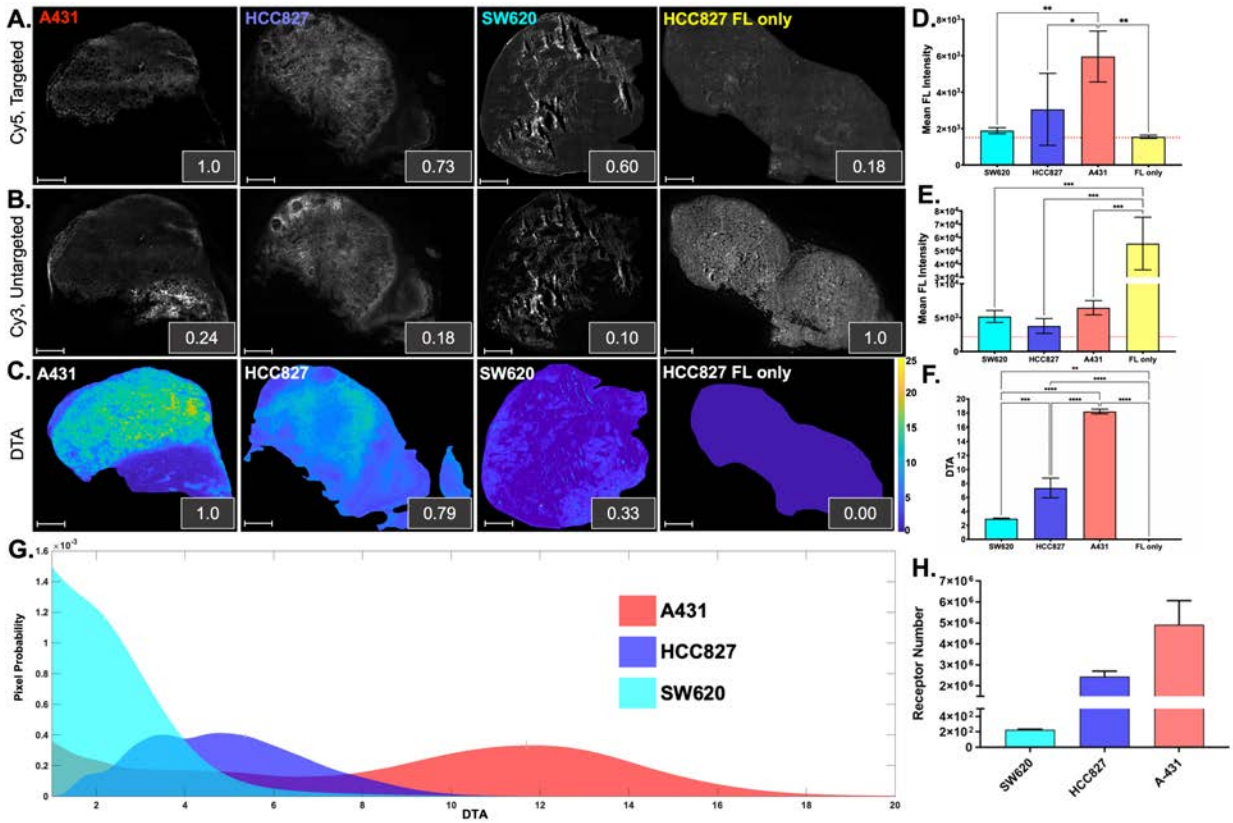

Fig. 5.3: *iPAI enables quantification of DTA.* Systemically administered doses of either iPAI agent or parent fluorophore only for the **A.** targeted (Si-TMR, imaged in the Cy5 channel) and **B.** untargeted (TMR, imaged in the Cy3 channel) iPAI probes allowed for comparison of probe uptake in representative (from n=3 tumors per CDX) A431, HCC827 and SW620 tissue sections all displayed with auto-contrast. Inset values represent relative signal intensity normalized across imaging channels. Targeted and untargeted tissue images enabled calculation of **C.** DTA spatial maps and relative DTA values (insets) for each representative tissue section with all images displayed at the same contrast levels. Assessment of **D.** targeted and **E.** untargeted probe uptake variability to compare all analyzed tumors was performed. The red dashed line indicates the level of tissue autofluorescence (AF) as quantified from HCC827 xenograft tissue following a vehicle only injection. **F.** DTA was also quantified across all tumors to assess inter-tumoral variability. Data are presented as mean ± standard deviation and are marked with asterisks for statistical significance. Data for each tissue type was compared to all other tissue types where significance was tested using a one-way ANOVA followed by Fisher's LSD multiple comparison test, where *$p < 0.05$, **$p < 0.01$, ***$p < 0.001$, and ****$p < 0.0001$. **G.** DTA pixel probability histograms were calculated for each DTA tissue maps for quantitative comparison of each tissue type's DTA signature. **H.** Quantification of EGFR expression in SW620, HCC827 and A431cells was performed by flow cytometry. Scale bars = 440 μm.

by flow cytometry, demonstrated high EGFR expression for A431 (average EGFR per cell = $4.9x10^6$), mid-level EGFR expression for HCC827 (average EGFR per cell = $2.4x10^6$) and low EGFR expression by SW620 (average EGFR per cell = $2.3x10^2$, **Fig. 5.3H**). Whole tissue section fluorescence images were used to quantify the mean fluorescence signal intensities in the Cy5 (targeted) and Cy3 (untargeted) channels and used to calculate the relative fluorescence intensities for the displayed, representative images from n=3 mice. Relative targeted iPAI probe fluorescence intensity was greatest in A431 xenograft tissue, where HCC827 and SW620 xenograft tissue had 27% and 40% lower targeted iPAI probe signals, respectively. The fluorophore (FL) only control tissue imaged in the Cy5 channel resulted in relative fluorescence intensity lower than all iPAI probe administered tissues (**Fig. 5.3A**). In the untargeted images (i.e., Cy3 channel, **Fig. 5.3B**), the tissue section with the highest relative fluorescence intensity was the HCC827 TMR FL only control tissue with a relative intensity at least 76% higher than all other tissues. The A431 tissue showed the highest untargeted iPAI probe signal when compared to HCC827 and SW620 iPAI probed injected tissues (**Fig. 5.3B**). Notably, the disparity amongst the untargeted iPAI probe uptake as measured by relative fluorescence intensity was appreciably less than the difference in targeted iPAI probe uptake. DTA tissue maps were calculated and scaled equivalently for the A431, HCC827 and SW620 iPAI probe administered tissues as well as the HCC827 FL only administered tissue section (**Fig. 5.3C**). Correlating with quantified EGFR expression, A431 generated the highest relative DTA value and was 21% greater than the relative DTA of HCC827 iPAI administered tissue. The difference in relative DTA between these tissues represents a 6% correction for nonspecific accumulation of the targeted iPAI probe in A431 tissue that had a 27% greater targeted iPAI probe signal than the HCC827 tissue. An even greater correction for nonspecific accumulation of targeted iPAI probe was seen in the SW620 tissue where relative DTA was 77% less than that of A431, while the relative intensity of the targeted iPAI probe in SW620 tissue was only 40% less than A431 tissue. HCC827 FL only injected control tissue had the lowest relative intensity, where there was no measurable DTA demonstrating the equivalent biodistribution of the SiTMR and TMR labels.

The average and standard deviation of the mean fluorescence intensity was calculated from the targeted and untargeted images for all tumor tissue (**Fig. 5.3D** & **5.3E**). For the targeted probe, a significant difference between A431 and SW620 tissues was observed ($p < 0.01$). Autofluorescence in the Cy5 channel of vehicle only injected tissue generated similar fluorescence signal to the nonspecific accumulation of the SiTMR FL only (**Fig. 5.3D**, *red dashed line*). For the untargeted probe, no significant difference between tumors that received iPAI agents existed indicating similar uptake of untargeted probe in all tumors (**Fig. 5.3E**). However, a significant difference in the untargeted channel did exist between tumors that received iPAI agent and the FL only tissue ($p <0.001$). Importantly, comparison of average DTA values across all tissue sections displayed a significant difference in mean DTA between all tissue types (at least $p < 0.001$, **Fig. 5.3F**). DTA pixel value probability histograms were generated for the displayed A431, HCC827 and SW620 tissue sections (**Fig. 5.3G**). As expected, A431 possessed the greatest DTA peak probability in comparison to HCC827 and SW620. HCC827 displayed the next highest peak DTA

probability followed by SW620. Notably, all histograms showed overlap in pixel probabilities, demonstrating DTA heterogeneity in all tissue sections. The ranking of relative and average DTA values showed the DTA signatures of A431, HCC827 and SW620 were aligned with the flow cytometry quantified EGFR expression *in vitro* (**Fig. 5.3H**).

Extension of iPAI to measure DTA in treated tissue. Assessment of the sensitivity of iPAI to measure DTA variation in the presence or absence of parent erlotinib was performed on A431 xenograft tissue that was administered either the erlotinib iPAI probe pair only or the erlotinib iPAI probe pair as well as the parent erlotinib TKI. This competitive binding study also served to confirm that the targeted iPAI probe competes for the same protein binding site(s) as the parent erlotinib drug. Targeted and untargeted iPAI probe intensity was measured from whole tissue section images and relative fluorescence intensities were calculated for each representative image (**Fig. 5.4A** & **5.4B**). The relative targeted iPAI probe intensity was highest in the A431 tissue following erlotinib iPAI probe administration without parent erlotinib, as expected. The A431 tissue that was administered both the erlotinib iPAI probes and erlotinib parent TKI had a

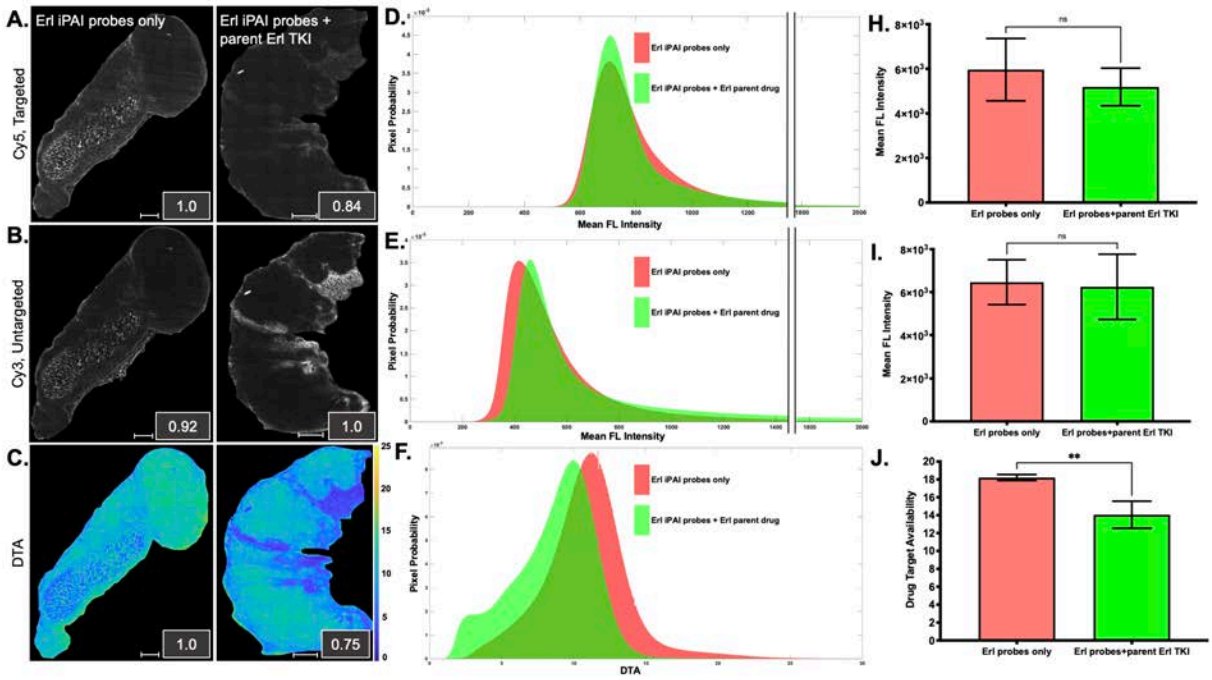

Fig. 5.4: *DTA signatures are sensitive to the presence of parent drug.* Comparison of **A.** targeted and **B.** untargeted iPAI probe uptake was performed by imaging tissue sections following administration of either iPAI probes only or tissue with iPAI probes in combination with parent erlotinib, where all representative tissue images (n=3 per group) are displayed with auto contrast. **C.** DTA tissue maps were calculated and displayed scaled equivalently with relative DTA quantified as inset values. Mean fluorescence (FL) intensity pixel probability histograms of the **D.** targeted probe, **E.** untargeted probe and **F.** DTA tissue maps provided a quantitative view of the signal changes. Quantification of **H.** targeted and **I.** untargeted probe uptake variability across tumors (n=3 per group) was performed. **J.** DTA was quantified across all tumors to assess the effect of co-injection of parent erlotinib with the iPAI probes. Data are presented as mean ± standard deviation and are marked with asterisks for statistical significance. The two groups were compared to one another where significance was tested for using an unpaired t-test, where **p<0.01. Scale bar = 440 μm.

16% lower relative targeted iPAI probe intensity (**Fig. 5.4A**). In contrast, the relative untargeted iPAI probe signal was 8% higher in the A431 tissue administered both erlotinib iPAI probe and parent erlotinib than in the A431 tissue with only iPAI probe administration (**Fig. 5.4B**). DTA tissue maps were calculated for each tissue section and scaled equivalently (**Fig. 5.4C**). Calculated relative DTA showed a 25% increase in the tissue administered the erlotinib iPAI probes only vs. co-administration with parent erlotinib demonstrating that the targeted iPAI probe competes for the same binding sites as the parent erlotinib. In comparison to the relative targeted iPAI probe intensities alone, the difference in DTA values represented a 9% correction for nonspecific accumulation of the targeted probe. For quantitative comparison of the tissue sections, pixel probability histograms were calculated on a per channel basis from the mean fluorescence intensity of each image (**Fig. 5.4D** & **5.4E**). Pixel probabilities of fluorescence intensity images in the targeted channel showed significant overlap with a small region of higher probability for higher fluorescence signal pixels in the tissue administered the iPAI probes alone (**Fig. 5.4D**). The untargeted pixel probability histogram showed the tissue with both iPAI probe and parent Erl TKI administration had regions of increased probability for greater fluorescence intensity compared to the tissue section with iPAI probes alone (**Fig. 5.4E**). DTA pixel probability value histogram comparisons of each tissue section showed an increased probability for DTA values in the tissue with iPAI probes administration alone in comparison to tissue with co-administered erlotinib parent drug and iPAI probes (**Fig. 5.4F**). The average and standard deviation of the mean fluorescence intensity was calculated from the targeted and untargeted images for all analyzed tumor tissue (n=3, **Fig. 5.4H** & **5.4I**). For the targeted and untargeted probe, no significant difference was observed between tissue with iPAI probes alone when compared to tissue with both erlotinib parent TKI and iPAI probes administered. Notably, a significant difference did exist between the DTA values of tissue with either iPAI probes only or both erlotinib parent TKI and iPAI probes ($p<0.01$).

Single-cell iPAI and Ab-oligo cyCIF analysis. Sequential cyCIF analysis was performed on a previously characterized section of iPAI administered A431 xenograft tissue (**Fig. 5.5**). Qualitative analysis of the targeted iPAI probe distribution in the tissue section showed probe uptake largely constrained to the viable tumor region (**Fig. 5.5A**). Tumor viability was confirmed with H&E staining (**Fig. 5.5A**, inset). In contrast, the untargeted probe demonstrated substantial uptake in the necrotic core of the xenograft as confirmed by H&E staining (**Fig. 5.5B**, inset). DTA values were highest in the viable tumor region and there was notable removal of the sectioning artifacts versus the targeted and untargeted iPAI images (**Fig. 5.5C**). After iPAI signal removal, five-biomarker Ab-oligo cyCIF imaging was performed and images were registered to facilitate visualization of each marker in its native spatial context (**Fig. 5.5D**). Ab-oligo cyCIF imaging measured EGFR signaling (pEGFR), proliferation (Ki67), mitochondrial abundance (CoxIV), cell adhesion (E-Cad) and cell state (CK8). Ab-oligo cyCIF staining enabled cell segmentation to be performed using cell nucleus and boundary information, facilitating extraction of both the targeted and untargeted iPAI probes fluorescent intensity within each cell. Subsequently, ratiometric

calculation of DTA for each cell was performed and plotted based on the position of the cell within the tissue with notable variation in DTA between cells (**Fig. 5.5E**).

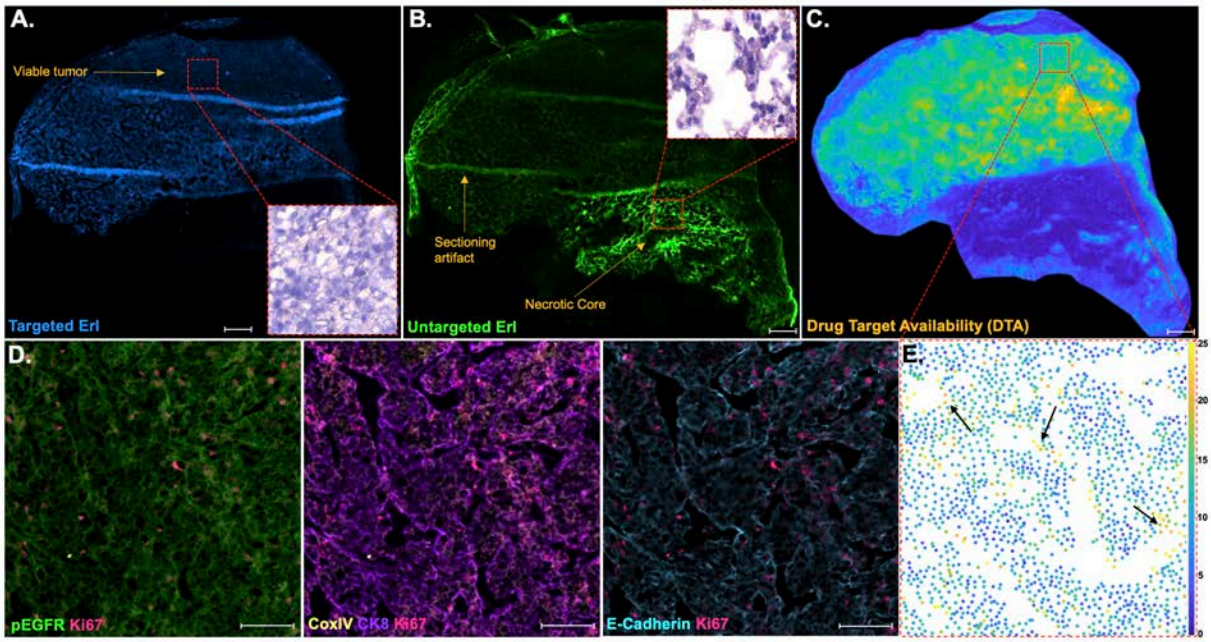

Fig. 5.5: *Proof of concept TRIPODD analysis.* **A.** Targeted and **B.** untargeted Erl iPAI images in excised tissue from A431 CDX enabled **C.** DTA heterogeneity visualization. Sectioning artifact were present in cut section and visible in the targeted and untargeted Erl iPAI images. Notably, sectioning artifacts were removed in the calculated ratiometric DTA image. Tumor viability was confirmed by H&E histology (**A&B**, insets). iPAI reagents were readily removed with a simple saline wash, rendering the tissue ready for **D.** cyCIF antibody staining (pEGFR [green], Ki67 [magenta], E-Cadherin [cyan], CoxIV [yellow] and CK8 [purple]). Nuclear stain (i.e., DAPI, data not shown) and cell membrane markers were utilized to segment individual cells for **E.** spatially patterned DTA, where higher DTA was seen in regions with lower cellular density indicating potential nearby vasculature (black arrows). Scale bar = 110 μm displayed in **A-C**. Scale bar = 22 μm displayed in **D**.

DISCUSSION

Fully realized personalized medicine will include curated drug selection as well as tailored dosages and treatment schedules uniquely designed to target inter- and intra-tumoral heterogeneity, reduce toxicity and improve overall survival. This will require new tools to quantify therapeutic efficacy and the corresponding resistance mechanisms in the design of effective treatment strategies. Our novel fluorescence imaging platform, TRIPODD, combines the complementary iPAI and Ab-oligo cyCIF imaging technologies to provide a powerful platform for *in situ* quantification of drug distribution and phenotypic changes to tune treatment regimens for therapeutic efficacy while minimizing toxicity. TRIPODD will facilitate a broader mechanistic understanding of therapeutic response with single-cell resolution to inform innovative treatment strategies (**Fig. 5.1**).

Validation of the TRIPODD technique and analysis pipeline was completed herein. The distribution of iPAI probes and calculated DTA at different depths within a tumor was quantified

to determine spatial pattern similarity across a CDX to guide tumor volume analysis from a single xenograft section required for accurate DTA characterization (**Fig. 5.2**). While some variation was seen in mean fluorescence intensity between sampled sections, the calculated mean DTA value only varied by 2% between sections. Importantly, spatial DTA patterns were maintained throughout the sampled 50-μm volume, where higher DTA was seen in the central portion of the tumor vs. the outer ring of the xenograft section (**Fig. 5.2C**). Notably, examination of the pixel probability histograms of fluorescence and DTA images further exemplified the similarity of fluorescent signal intensity and DTA values where significant overlap of histograms was clearly demonstrated (**Fig. 5.2D-5.2F**). For the purposes of this validation study, these results demonstrate through quantification of relative and pixel level signal intensities, that subsequent single tissue section analysis of CDX tumors will be sufficient for acquiring a representative DTA signature of the entire tumor. Given the validity of minimal tissue analysis for representative biological information, all subsequent studies herein analyzed a single tissue section from each tumor.

Xenograft tissues with varied EGFR expression levels that were administered targeted iPAI agents showed decreased fluorescence intensity with decreasing EGFR expression in representative images (**Fig. 5.3A**). However, quantification of targeted probe signal in all tumors revealed significant variability in targeted probe uptake across tissue types where overlap in standard deviation was present (**Fig. 5.3D**). EGFR expression was more than four orders-of-magnitude lower in the SW620 versus the A431 or HCC827 xenograft tissues (**Fig. 5.3H**), thus the relatively high targeted iPAI probe uptake was unexpected (**Fig. 5.3A**). Correction for nonspecific uptake using the untargeted iPAI probe (**Fig. 5.3B**) resulted in substantially decreased DTA signal (**Fig. 5.3C** & **5.3F**) and thus improved correlation with the quantified EGFR expression. This result supports the use of the untargeted probe to correct for nonspecific drug uptake, where calculation of DTA improves *in vivo* quantification (**Fig. 5.3B** & **5.3C**). To assess the influence of the fluorophore label on the targeted and untargeted iPAI probe uptake and biodistribution, the fluorophores (i.e., SiTMR and TMR) were co-administered to mice bearing HCC827 xenografts. While fluorescence intensity between the parent fluorophores in the tissue differed substantially, the overall xenograft tissue distribution was nearly identical as DTA calculations exhibited no detectable values across the entire tissue section (**Fig. 5.3A-5.3C**). Notably, when the pixel probabilities of the DTA values were plotted as a histogram, there was partial overlap between the DTA value probabilities in all three xenograft types, an observation not immediately apparent from examining the tissue image maps. Additionally, the histogram shapes across the three xenografts types were variable. While HCC827 showed the tightest DTA distribution, the A431 showed a broad distribution of DTA probability values, suggesting that drug accumulation and target availability is not spatially equivalent even in relatively homogeneous CDX models and may provide insight into intra-tumoral therapeutic response heterogeneity (**Fig. 5.3G**).

Sensitivity validation of the iPAI technique to detect the presence of parent TKI by equating decreased DTA signal (i.e., occupied binding sites prohibiting Erl iPAI probe binding) in tissue was performed on A431 xenograft tissue with administration of either the iPAI probe pair

alone or in combination with the erlotinib parent drug (**Fig. 5.4**). Quantification of the targeted and untargeted iPAI probe fluorescence intensity revealed a greater decrease in targeted signal intensity vs. untargeted signal intensity when co-administered with parent erlotinib (**Fig. 5.4A** & **5.4B**). Pixel probability histograms of fluorescence intensity support this observation although it is noteworthy that the histogram of the targeted signals shows marginal difference in the two tissues (**Fig. 5.4D**). Calculated DTA for each tissue showed further difference between the tissues administered the erlotinib iPAI probes alone vs. the iPAI probes in the presence of the parent drug, with a 25% higher relative DTA value (**Fig. 5.4C**). This demonstrates that the parent erlotinib and the targeted erlotinib iPAI probe compete for the same protein binding site(s), validating the maintained targeted behavior of our fluorescently labeled targeted iPAI probe. This result was further supported by the DTA pixel probability histograms where there was a clear shift in peak pixel probability with increased DTA values in the tissue that received the iPAI probe pair only (**Fig. 5.4F**). Importantly, no significant difference existed between the mean tissue uptake of the targeted probe with either iPAI probe only or with erlotinib parent TKI and iPAI probe (**Fig. 5.4H**). However, a significant difference did exist between the two groups when mean DTA was calculated and compared (**Fig. 5.4J**). Thus, the ratiometric DTA calculation further exemplified the difference between tissue administered the iPAI probes alone versus the iPAI probes in the presence of the parent drug demonstrating the necessity to account for nonspecific accumulation on a per tumor basis to ensure accurate quantification. Additionally, the 25% decrease in relative DTA in the tissue with co-administered parent erlotinib and iPAI probe pair compared to tissue with the iPAI probe pair alone indicated that the targeted erlotinib iPAI probe and parent erlotinib compete for the same intracellular binding site, highlighting the utility of TRIPODD to quantify tissues treated for longer time courses in future studies.

As proof of concept for the TRIPODD analysis pipeline, sequential iPAI followed by Ab-oligo cyCIF was performed on an A431 xenograft tissue section (**Fig. 5.5**). Following iPAI imaging (**Fig. 5.5A-5.5C**) and probe removal, Ab-oligo cyCIF antibody staining was completed using a master mix of pEGFR, Ki67, E-Cad, CoxIV and CK8, detected using rounds of complementary IS labeling (**Fig. 5.5D**). The iPAI and cyCIF data sets were spatially aligned to facilitate single cell quantification of DTA for biologically relevant spatial context. cyCIF imaging data yielded a cell segmentation map, facilitating feature extraction of the fluorescence signal from the targeted and untargeted iPAI probes in each cell for quantification of DTA on a per cell basis while maintaining the spatial context of the individual cells. These DTA maps demonstrated the inherent intra-tumoral heterogeneity, where neighboring cells could have drastically different DTA values (**Fig. 5.5E**), showing the potential of TRIPODD as an imaging platform capable of interpreting intra-tumor DTA and proteomic response heterogeneity with conserved spatial context to enable quantitative assessment of therapeutic response on a cell-by-cell basis. One potential driver of the heterogeneous DTA values is dysfunctional tumor vasculature arising from the hypoxic environment in the tumor as cells rapidly divide and overexpress vascular endothelial growth factor A (VEGF-A).[108] A future application of TRIPODD for assessing novel therapeutic strategies will be monitoring combination TKI therapy in the presence of TME modulators (e.g.,

bevacizumab),[153] where it is hypothesized that improve efficacy is the result of improved drug delivery, a metric that can be measured by decreased intra-tumoral DTA heterogeneity, after tumor vasculature normalization.[154] The capability of TRIPODD to quantify drug delivery and local proteomic therapeutic response all while maintaining their spatial context is a critically unmet analytical need and represents a significant opportunity for improved therapeutic strategy design through high dimensional analysis of the tumor ecosystem.

Further development of TRIPODD platform will require application of the workflow on tissues treated with clinically relevant courses of TKI therapy to assess variation in DTA in the context of proteomic response to targeted therapy, where longitudinal monitoring of tumor evolution in different treatment cohorts will provide the ability to design and further evaluate novel therapeutic strategies. Further development of the TRIPODD platform will require longitudinal evaluation of responsive and non-responsive tissues treated with clinically relevant courses of TKI therapy to assess variation in DTA in the context of proteomic response to targeted therapy. Additionally, future TRIPODD optimization studies will enable assessment of how the tumor microenvironment, which includes a dysfunctional tumor vasculature, is linked to DTA and subsequent therapeutic efficacy.[108] The tumor model systems utilized in treatment studies will include patient derived xenografts and immunocompetent mouse models, allowing interrogation of clinically relevant tumor-immune microenvironment interactions in relation to DTA and local proteomic response. Additionally, the extension of iPAI from probes targeting transmembrane proteins such as EGFR to intracellular targets will enhance the utility of the TRIPODD technique. This extension will be important for assessing combination treatment strategies targeting EGFR and downstream proteins of interest implicated in cancer specific mechanisms of resistance through cell signaling pathway reprogramming. Important to continued development of TRIPODD, the cyCIF antibody panel will be expanded to include immune, vasculature and downstream cell signaling proteins in the EGFR signaling cascade in order to evaluate proteomic response in these tumor settings. Notably, TRIPODD could be readily combined with additional label-free imaging modalities such as collagen autofluorescence[155, 156] and second harmonic generation[157, 158] to image changes in tissue metabolism and matrix proteins, providing additional insight into the tumor microenvironment. The novel TRIPODD imaging platform is capable of monitoring a variety of treatment conditions in a broad spectrum of diseased tissue systems to provide mechanistic understating of therapeutic response and resistance and could be further expanded to include other novel imaging methods.

Chapter 6

In situ single-cell therapeutic response imaging facilitated by the TRIPODD fluorescence imaging platform

ABSTRACT

Purpose: Small molecule drugs such as tyrosine kinase inhibitors (TKIs) targeting tumoral molecular dependencies have become standard of care for numerous cancer types such as epidermal growth factor receptor mutated (EGFRmut+) non-small cell lung cancer (NSCLC) where EGFR TKIs (e.g., erlotinib, osimertinib) have demonstrated improved therapeutic outcomes EGFR TKIs produce over platinum-based chemotherapy. However, tumors largely develop resistance to TKI therapy resulting in disease progression. Currently, the relationship between *in situ* drug target availability (DTA) and local protein expression cannot be characterized by current analytical tools despite being crucial to mechanistic understanding of therapeutic efficacy.

Procedure: We have previously reported our fluorescence imaging platform termed TRIPODD (**T**herapeutic **R**esponse **I**maging through **P**roteomic and **O**ptical **D**rug **D**istribution) that is capable of simultaneous quantification of single-cell DTA and protein expression with preserved spatial context within a tumor. TRIPODD combines two complementary fluorescence imaging techniques, intracellular paired agent imaging (iPAI) to measure DTA and cyclic immunofluorescence (cyCIF) conducted with oligonucleotide conjugated antibodies (Ab-oligos) for proteomic expression quantification on tissue samples. Optimization of TRIPODD tissue collection and analysis herein, facilitates extension of the platform to analyze therapeutic response through single-cell DTA and proteomic response imaging.

Results: We successfully performed sequential imaging of iPAI and cyCIF for high dimensional image data generation to quantify single-cell DTA and local protein expression on tissues treated with erlotinib. Spatial registration and cell segmentation resulted in high dimensional data capable of mechanistic characterization of erlotinib kinetics.

Conclusion: Herein, we demonstrated the capability of TRIPODD to perform therapeutic response imaging to monitor mechanisms of erlotinib response kinetics relating signaling inhibition, DTA, proliferation and apoptosis with preserved spatial context at single cell resolution.

INTRODUCTION

The targeted-therapy era of cancer treatment has delivered significant progress in improving patient survival rates by exploiting cellular vulnerabilities present in malignant tissues. Some of the most common targeted vulnerabilities are cell signaling pathway kinases that are deregulated in many cancers.[2] For example, the discovery that ~15% of all non-small cell lung cancer (NSCLC) exhibit dependance on epidermal growth factor (EGFR) signaling has led to the development of tyrosine kinase inhibitors (TKI) targeting EGFR signaling. Phase III trials have consistently shown superior efficacy of first- (i.e., erlotinib) and second-generation (i.e., afatinib) TKIs over standard chemotherapies (i.e., platinum-based) for patients with EGFR-mutated (EGFRmut+) NSCLC, improving progression-free survival (PFS) from 6 to up to 15 months.[90-94] However, tumor evolution and subsequent disease progression are still inevitable, most commonly the result of a T790M mutation in EGFR exon 20, which sterically hinders binding of both first- and second-generation EGFR TKIs.[17] A third-generation EGFR TKI, osimertinib, overcomes this resistance mechanism resulting in superior efficacy and garnered FDA approval in 2018 as a first-line treatment option regardless of T790M mutational status.[95, 96] As with other targeted therapies, enthusiasm for initial robust response rates was tempered by inexorable disease progression due to adaptive resistance mechanisms.[97] Notably, mechanistic diversity of therapeutic resistance is further reinforced by the 10-20% of EGFRmut+ NSCLC patients that do not respond to first-line EGFR targeted therapy, where the de novo resistance mechanism(s) are not fully understood, but are thought to relate to *in vivo* pharmacokinetics and could potentially be treated using combination therapy.[99, 159] It has been proposed that contributing factors to therapeutic failure include insufficient drug target availability (DTA) and off-target activity, however, effective tools to quantify and validate intracellular drug delivery and target engagement are lacking.[11, 38]

Typically, insufficient DTA and off-target activity are assessed by bulk sampling (e.g., plasma analysis, western blot [WB]), which are not representative of the variable cell-to-cell drug distribution, target binding and off-target effects.[20-22] Drug delivery characterization in the context of a highly dynamic tumor microenvironment (e.g., dysfunctional vasculature, hypoxic regions, dense extracellular matrix, immune infiltrate, epithelial mesenchymal transition [EMT], cancer stem cells [CSC], etc.), is a key missing component in most drug efficacy studies as it requires *in situ* spatial interpretation that exceeds current analytical capabilities.[27] Furthermore, therapeutic efficacy can be correlated to the spatial organization of tumor, immune, and stromal cells. As such, significant efforts are underway to interpret therapeutic response heterogeneity within these complex environments.[28-32] Numerous labeled small molecule drugs have been generated (e.g., fluorescent, biotin and photoclickable labels) to facilitate direct visualization of tissue distribution and target engagement.[20, 33-36] Conversely, druggable protein targets have also been genetically modified to enable direct visualization.[19, 37] While useful, modifications can vastly alter drug distribution or target engagement. In response, various label-free methods have been developed, including mass spectrometry imaging (MSI), cellular thermal shift assay (CETSA) and positron emission tomography (PET).[38-43] However, quantification of available drug targets necessitates

accounting for both on-target drug binding and non-specific accumulation in the cells and tissues due to drug affinity, biodistribution, pharmacokinetics and metabolism.[28, 44, 45]

To facilitate quantification of specific and non-specific targeted drug accumulation in tissue, we have adapted a technique from autoradiography termed Paired Agent Imaging (PAI). PAI was created for quantitative *in vivo* imaging, where non-specific accumulation of protein-based, radiolabeled affinity reagents dominated malignant tissue signals, but could be corrected for by normalizing the targeted signal to the signal of a co-administered, control antibody labeled with an isotope of different energy.[46] This technique has been reinvigorated, where spectrally-distinct targeted and untargeted imaging agents are used to correct for non-specific uptake to quantify drug target availability (DTA; also called "binding potential").[47-63] Importantly, while the modification necessary to prevent targeted binding has the potential to change off-target binding of the untargeted agent, previous work has demonstrated DTA to remain a relatively quantitative measure.[143] We have expanded the PAI technique to be capable of measuring intracellular targets with the use of spectrally-distinct, fluorescently-labeled drug derivatives, such as TKIs. DTA is calculated by collecting images of targeted and untargeted agents in order to perform ratiometric imaging between the two fluorescence signals. The ratiometric imaging performed in iPAI satisfies the requirement of accounting for both the drug that binds to its target as well as the drug that accumulates in the cells and tissues in a non-specific or untargeted manner when calculating DTA. The goal of a targeted therapeutic is to achieve only on-target binding, but in the complex tumor setting there is always some degree of untargeted accumulation which can vary on a cell-by-cell basis in heterogeneous diseases such as NSCLC. Notably, although our technique relies on fluorescently-labeled drugs for quantification, all treatment is completed with the parent drug and is thus classified as a label-free method with quantitative assessment of the interaction of the parent drug with its native target.

In addition to assays for directly measuring target engagement, biomarkers are a popular proxy measure for target occupancy that have been demonstrated to reliably give insight into interactions between a drug and its target *in vivo*. If a drug produces an expected therapeutic effect on its target biomarker, then the mechanism is assumed to be sufficiently tested and validated as an effective therapeutic. Additionally, common proteomic assays (e.g., conventional immunohistochemistry [IHC] or immunofluorescence [IF]) for assessing biomarker are able to provide *in situ* spatial context to therapeutic effect. However, these assays are limited to measuring 2-5 antigens on single time which has led to the evolution of a number of highly multiplexed immunostaining techniques using two main methods: (1) conventional antibody staining (i.e., IF or IHC) in a cyclic fashion[67, 68] or (2) MSI using rare earth metal labeled antibodies.[30, 69-79] While both of these approaches provide high-dimensional spatial proteomic tissue maps, they are inherently limited due to their destructive signal removal methods in cyclic imaging workflows and limited sensitivity to low abundance antigens using MSI. In response we have optimized a technique utilizing oligonucleotide conjugated antibodies (Ab-oligo) to perform cyclic immunofluorescence (cyCIF).[84] In Ab-oligo cyCIF, a single stranded docking strand is covalently conjugated to the antibody, where detection is completed *in situ* through a complementary,

fluorescently labeled oligonucleotide sequence.[84] Our Ab-oligo cyCIF platform is capable of quantifying tumor plasticity/stemness, cell signaling pathway and phenotypic changes on a single-cell basis while retaining spatial organization in the dynamic TME, which is critical to understand therapeutic response and resistance heterogeneity.

Importantly, while assays capable of directly measuring DTA or indirectly through biomarker response to a therapeutic are critical to discerning the efficacy of a drug, the ideal assay requires concomitant measurement of: 1) the extent and heterogeneity of DTA across a tissue as well as 2) drug interactions with the drug target protein along with off-target effects that allow for correlations to be made between efficacy, toxicity and dosing.[38] To bridge this unmet analytical gap, we have previously reported our novel fluorescence imaging platform, **T**herapeutic **R**esponse **I**maging through **P**roteomic and **O**ptical **D**rug **D**istribution (**TRIPODD**).[143] TRIPODD facilitates simultaneous single-cell quantification of DTA with iPAI and the associated tumor biology through accurate segmentation of spatially aligned tumor cells based on Ab-oligo cyCIF. Described herein, we validated administration kinetics of the iPAI probes and extended TRIPODD to correlate erlotinib therapeutic effect kinetics as measured by changes in DTA and EGFR signaling pathway protein expression in EGFRmut+ NSCLC xenografts to demonstrate the capability of TRIPODD to facilitate mechanistic understanding of therapeutic response.

MATERIALS & METHODS

Synthesis of fluorescently labeled erlotinib. The targeted and untargeted iPAI probes used in this study were derivatives of erlotinib (Erl), a first generation, reversible TKI targeting EGFR. Briefly, site selection for synthetic modifications of erlotinib to generate the targeted and untargeted drug derivatives was guided by the structure of the parent drug bound to the EGFR crystal structure.[1, 151] Our novel Oregon Fluors (OF), OF552 and OF649, were selected for probe labeling due to their spectral separation, overall charge, charge distribution, molecular weight, structural similarity and stability in varied biological environments. This new class of tetramethylrhodamine (TMR)/silicon-TMR (Si-TMR) probe derivatives enable maintained biodistribution similarity between the targeted and untargeted probes, while improving stability in varied biological environments (Wang, *et al*, 2021, in review). The two probes synthesized were (1) Erl-OF649 used as the cell membrane permeant iPAI targeted agent with a maximum excitation/emission peak at 649/668 nm and (2) Erl-OF552 used as the cell membrane permeant iPAI untargeted agent with a maximum excitation/emission peak at 552/575 nm.

Antibody Conjugation and Validation for cyCIF. A 10-antibody panel using unconjugated, oligo conjugated and fluorophore conjugated antibodies was generated and validated for the Ab-oligo cyCIF workflow (**Table 6.1**). Oligonucleotide conjugated antibodies (Ab-oligo) were generated as previously reported.[112] In brief, antibodies to human E-Cadherin (E-Cad), cytokeratin 8 (CK8), EGFR, Akt, pAkt, pMEK, PI3K, cleaved caspase-3 (CC3) and Ki-67 were purchased from AbCam (Cambridge, UK) and Cell Signaling Technology (Danvers, MA). A unique dibenzocyclooctyne-terminated (DBCO), single-stranded oligonucleotide (docking

strand [DS], 28 mer in length), used to label antibodies, was purchased from Integrated DNA Technologies (IDT, Coralville, IA). Antibody modification and oligonucleotide conjugation were completed with the SiteClick^{TM} Antibody Azido modification kit (ThermoFisher Scientific, Waltham, MA) following the manufacturer's instructions. A primary antibody reactive to mouse CD31 antigens (AbCam) was directly conjugated to AlexaFluor546 (AF546) NHS ester (Thermo Fisher Scientific). The starting antibody concentration was determined by measuring the absorbance at 280 nm prior to any conjugation chemistry. The primary antibody was purified of any storage buffers (e.g., BSA) and buffer exchanged into 1X PBS, pH 8.0 with a 10 kDa Amicon filter (EMD Millipore, Burlington, MA). AF546 NHS was resuspended at 10 mM in anhydrous dimethyl sulfoxide (DMSO) and added to the antibody at a ratio of 10 fluorophore molecules to 1 antibody in a reaction volume of 1 mL. The mixture was rocked gently at 4 °C for three hours protected from light. The antibody conjugate was then purified with a 10 kDa Amicon filter. Absorbance was measured at 280 and 546 nm to calculate the antibody-fluorophore conjugate concentration, respectively. A primary antibody reactive to human phospho-EGFR (CST, pEGFR) was purchased to be used for indirect immunofluorescence with a donkey anti-rabbit secondary antibody conjugated to AF750.

Table 6.1: *Validated antibody panel for multiplex cyCIF imaging.*

Marker Category	Protein	Fluorescence Imaging Strategy
Tumor Area	CK8	Ab-oligo 2xFL IS
	E-Cad	Ab-oligo 2xFL IS
Tumor Viability	Ki67	Ab-oligo 2xFL IS
	CASP3	Ab-oligo amplification strategy
EGFR Signaling Pathway	*EGFR*	Ab-oligo 2xFL IS
	pEGFR	Indirect Immunofluorescence (IF)
	pMEK	Ab-oligo amplification strategy
	PI3K	Ab-oligo 2xFL IS
	AKT	Ab-oligo amplification strategy
	pAKT	Ab-oligo amplification strategy

Cell lines. The human lung adenocarcinoma cell line, HCC827, the human pancreatic ductal adenocarcinoma cell line, PANC-1, and human the colorectal adenocarcinoma cell line, SW620, were purchased from ATCC (Manassas, VA) and maintained mycoplasma free at passage numbers <25 for all studies. The cell lines were expanded in their respective optimal growth media (HCC827: RPMI 1640 [ThermoFisher Scientific] + 10% FBS + 1% penicillin/streptomycin/glutamine; PANC-1: DMEM [ThermoFisher Scientific] + 10% FBS + 1% penicillin/streptomycin/glutamine; SW620: Leibovitz L-15 [ThermoFisher Scientific] + 10% FBS + 1% penicillin/streptomycin/glutamine) and stored at 37 °C in either a 5% (HCC827 and PANC-1) or 0% (SW620) CO_2 incubator.

Animal care and use. All animal experiments were approved by the Oregon Health and Science University (OHSU) Institutional Animal Care and Use Committee (IACUC). All mice

were hosted in the AAALAC certified OHSU vivarium, and supplied with food, water and daily inspection to monitor for pain or distress for the duration of experimentation. Mice were placed on a chlorophyll-free diet (Animal Specialties, Inc., Hubbard, OR) one week prior to tumor resection. All rodent surgical procedures, described herein, were performed under full anesthesia composed of a 90/10 mixture of ketamine/xylazine. Ketamine (Hospira Inc., Lake Forest, IL) was administered at a dose of 100 mg/kg and xylazine (AnaSed, Shenandoah, IA) was administered at dose of 10 mg/kg by intraperitoneal (IP) injection. The toe pinch method was employed to verify the depth of anesthesia prior to commencement of any surgical procedures. The standard method of euthanasia for mice was inhalation of carbon dioxide under full anesthesia at the end of each experiment. Euthanasia was confirmed by physical examination to ensure cessation of heartbeat and respiration and is consistent with the recommendations of the Panel on Euthanasia of the American Veterinary Medical Association.

Mouse Xenograft Models. Mixed male and female athymic nude mice (Homozygous 490, Charles River Laboratories, Wilmington, MA) were purchased at 32-38 days old. After at least 48 hours of acclimation, mice were subcutaneously implanted with HCC827, PANC-1 or SW620 cell xenografts described briefly as follows. Cells were trypsinized, counted and resuspended in their appropriate growth media to a concentration of 2 x 10^7 cells/ml. The mice were then implanted with cells into each rear flank at a final concentration of 1 x 10^6 cells/flank in 50% v/v Matrigel (Corning Inc., Corning, NY), resulting in two tumors/mouse. A total of n = 35 nude mice were implanted for HCC827 cell derived xenograft (CDX) models and a n = 7 nude mice each were implanted for PANC-1 and SW620 CDX models. The mice were monitored daily after implantation for tumor growth. Tumors were allowed to grow to a maximum size of 1.2 cm^3 with growth times varying for each cell line (HCC827: ~7-8 weeks; PANC-1 and SW620: ~4 weeks). Mice weighed ~20-25g and tumors were between 1-1.2 cm^3 at the time of iPAI agent administration prior to sacrifice and tissue collection.

Flow Cytometry. HCC827, PANC-1 and SW620 cells were trypsinized, counted, and fixed in 4% paraformaldehyde (PFA) for 10 min. A three min permeabilized step (0.5% Triton-X) was followed by 2 x 5 min washes in phosphate buffered saline (PBS) and then 2 x 10^6 cells per cell line were blocked for 15 min with 5% FBS. Without removing blocking buffer, the cells were then incubated with 5 mg/ml cetuximab directly conjugated to AF647 (1:1.7 antibody to fluorophore conjugation ratio). The cells were washed 1 x 5 min with PBS + 0.1% Tween 20, followed by 2 x 5 min PBS washes, and finally resuspended in fresh PBS prior to analysis on a Becton Dickinson LSR Fortessa (Becton, Dickinson and Company, Franklin Lakes, NJ). The flow cytometer was configured with a 640-1 (670/30) Cy5 channel to detect AF647. A minimum of 1 x 10^5 cells were counted for each sample. To quantify EGFR receptor number, Quantum™ Alexa Fluor® 647 molecules of equivalent soluble fluorophore (MESF) beads (Bangs Laboratories, Inc., Fishers, IN) were quantified prior to the cellular samples.

Fluorescence microscopy of Tissue Sections. All fluorescence microscopy of tissue sections described herein was performed as follows. Frozen tissue blocks were sectioned at 10 μm thickness (Leica Biosystems cryostat, Wetzlar, Germany) onto SuperFrost Plus glass slides

(ThermoFisher). Fluorescence images of whole tissue sections were acquired on a Zeiss AxioScan.Z1 microscope (Carl Zeiss AG, Oberkochen, Germany) equipped with a Colibri 7 light source (Carl Zeiss AG) and Orca Flash4 v.2 (Hamamatsu Photonics, Shizouka, Japan). Images were collected using the following filter sets: Zeiss 38HE (Cy2/AF488 [Carl Zeiss AG]), Zeiss 43HE (Cy3/AF555 [Carl Zeiss AG]), Zeiss 50 (Cy5/AF647 [Carl Zeiss AG]) and Chroma 49007-ET-Cy7 (Cy7/AF750 [Chroma Technology Corporation, Bellows Falls, VT]). Excitation light was filtered using the following bandpass (BP) filters: 470/40 (38HE), 550/25 (43HE), 640/30 (50) and 710/75 (49007-ET-Cy7) for Cy2, Cy3, Cy5 and Cy7 channels, respectively. Emission light was filtered using the following BP filters: 525/50 (38HE), 605/70 (43HE), 690/50 (50) and 810/90 (49007-ET-Cy7) for Cy2, Cy3, Cy5 and Cy7 channels, respectively. DAPI was imaged using a Semrock filter set (Zeiss), where excitation was filtered at 405 nm and emission filtered using a 410/480 BP filter. Images were captured at 20X (Plan-Apochromat, 0.8NA) magnification, where image tiles with 10% overlap were stitched together using the Zeiss Zen software to produce a single tissue map.

Pharmacokinetic Study of iPAI Agents. To characterize the pharmacokinetic activity of iPAI agents, the Erl-OF649 and Erl-OF552 iPAI agents were injected simultaneously via tail vein injection into n = 12 HCC827 CDX bearing mice at 2.5 mg/kg for both the targeted and untargeted iPAI agents. N=3 mice were sacrificed and tumors resected at either 15 minutes (min), 30 min, 60 min, 120 min, 240 min or 480 min after iPAI agent injection and flash frozen in optimal cutting temperature (OCT) compound (Fisher Scientific, Waltham, MA). Injection vehicle for all systemically administered TKI and iPAI probes was a co-solvent mixture of a ratio of 10% dimethyl sulfoxide ([DMSO], Sigma-Aldrich, St. Louis, MO), 5% Kolliphor (Sigma-Aldrich), and 85% of 75% FBS/PBS (VWR Scientific). A 10 μm thick tissue section from each frozen tissue block was collected and imaged as described above. The targeted iPAI probe was imaged in the Cy5 channel, the untargeted iPAI probe was imaged in the Cy3 channel and tissue autofluorescence, used to generate a focus map, was imaged in the Cy2 channel. After image acquisition, a custom MATLAB script (10.5281/zenodo.4004647) was used to calculate DTA images on a per pixel basis for each tissue image. DTA, as previously reported,[143] was calculated as

$$\text{Drug Target Availability (DTA)} = \frac{\mathrm{I_T} - \frac{I_{UT}}{SF}}{\frac{I_{UT}}{SF}} \qquad (1)$$

where $\mathrm{I_T}$ is the targeted iPAI probe fluorescence intensity, $\mathrm{I_{UT}}$ is the untargeted iPAI probe fluorescence intensity and SF is a scaling factor to account for signal intensity difference between the target and untargeted probes. The scaling factor was quantified by imaging the targeted and untargeted probes at titrated concentrations on the Zeiss AxioScan.Z1 to generate a linear calibration trend line for each probe, where the scaling factor was calculated as the ratio of the slope of the untargeted probe trend line to the slope the targeted probe trend line and is built into the MATLAB analysis script. Targeted probe, untargeted probe and DTA signal for each tissue section was quantified by manual segmentation of the tissue in ImageJ v1.51 (National Institute of

Health, Bethesda, MD) and extracting the mean value for each channel from the tissue sections. The mean fluorescence signal or DTA value from each section was divided by the highest mean fluorescence or DTA value, respectively, to calculate relative fluorescence intensity or DTA values. Box and whisker plots comparing tissue sections resected at different times after iPAI agent injection were generated in Prism v9.0 (GraphPad, San Diego, CA).

Pharmacodynamic Study of iPAI Agents. The pharmacodynamics of iPAI agents was assessed in HCC827, PANC-1 and SW620 CDX mouse models where the targeted and untargeted iPAI agents were simultaneously injected via tail vein at 5, 2.5 or 1.25 mg/kg for both targeted and untargeted iPAI agents. For equivalent group size comparison, each dose group was comprised of n=2 mice per CDX model. The same co-solvent mixture was used for systemic administration of all TKI and iPAI probes. For all CDX models, tumors were resected four hours after systemic administration and flash frozen in OCT compound. An additional n=1 mouse per CDX model was injected with injection co-solvent vehicle only to assess tissue autofluorescence in each CDX model. A 10 μm thick tissue section was collected from each frozen tissue block and tissues were imaged on a Zeiss AxioScan.Z1, where images were collected in the Cy5 (targeted iPAI agent), Cy3 (untargeted iPAI agent) and Cy2 (autofluorescence used to generate focus map) channels. Mean fluorescence intensity for each image was calculated in ImageJ through manual segmentation of the tissue. The relative fluorescence intensities for each image were calculated by dividing the mean fluorescence intensity of an image by the highest mean fluorescence intensity of that particular image channel (i.e., Cy5 and Cy3). The previously described MATLAB script was used to calculate DTA images for the HCC827, PANC-1 and SW620 iPAI injected tissues (Equation 1). Box and whisker plots comparing tumor types were generated in Prism v9.0.

To identify the iPAI dose that provided quantitative imaging, the targeted probe, untargeted probe and DTA signals on all collected tissue sections were correlated to their EGFR and pEGFR protein expression as measured by indirect immunofluorescence. Following iPAI microscopy of all tissue sections from the three CDX models in all dose groups (n=2 mice/CDX/dose group [6 mice/CDX]) as described above, iPAI agents were removed with 3 x 5 min saline wash rendering the tissue available for indirect immunofluorescent staining. Each tissue section was then stained following the protocol described below with primary EGFR (Erbitux, Eli Lilly, Indianapolis, IN) and pEGFR antibodies purchased from the Oregon Health and Science University (OHSU) Pharmacy and CST, respectively. The stained slides were mounted with Fluoromount-G (Southern Biotech, Birmingham, AL) and cover-slipped for imaging. The stained slides were imaged on a Zeiss AxioScan.Z1 in the DAPI, Cy3 and Cy5 channels. EGFR and pEGFR signals for each tissue section were quantified by manual segmentation of the tissue in ImageJ v1.51, where the mean value for each channel was calculated. Scatter plots and Pearson's correlations for all dose groups correlating EGFR and pEGFR expression to targeted probe, untargeted probe and DTA signal were generated in Prism v9.0.

Erlotinib Treatment of HCC827 Xenografts. TRIPODD was used to investigate the kinetics of therapeutic response to erlotinib in HCC827 CDX bearing mice. When tumors reached a minimum size of 150 mm^3, n=13 mice were randomly assigned to a treatment group (n = 10

mice) or the untreated control group (n = 3 mice). Then, n = 9 of the mice selected for treatment were further randomly divided into groups where tumors were resected 6 h, 12 h or 24 h (n = 3 per time point) after erlotinib administration. Erlotinib was dissolved in 0.3% weight/volume of sodium carboxymethylcellulose (Sigma-Aldrich) and 0.1% volume/volume of Tween 80 (Sigma-Aldrich) in PBS (VWR Scientific) and administered by oral gavage as a single dose of 50 mg/kg.[160, 161] As determined by PK and PD studies, iPAI probes were systemically administered at 2.5 mg/kg 4 h prior to tumor resection for all groups. The remaining n=1 mouse in the treatment group was dosed with erlotinib for 6 h, but no iPAI agent was administered in order to assess any changes to tumor tissue autofluorescence following erlotinib treatment. After resection, all tumors (n = 26 tumor, 2 tumors/mouse) were flash frozen in OCT compound.

DTA Quantification of Erlotinib Treatment Study. A 10 μm thick tissue section was collected from each frozen tissue block and imaged on a Zeiss AxioScan.Z1, where images were collected in the Cy5 (targeted iPAI agent), Cy3 (untargeted iPAI agent) and Cy2 (autofluorescence used to generate focus map) channels. The previously described MATLAB script was used to calculate DTA images for tissue sections (Equation 1).[143]

Ab-oligo cyCIF Imaging of Erlotinib Treatment Kinetics. Following iPAI microscopy of tissue sections, iPAI agents were removed with 3 x 5 min saline wash rendering the tissue available for Ab-oligo cyCIF imaging. Each tissue section was incubated in 2% PFA at room temperature (RT) for 15 min and then washed with 1X PBS, pH 7.4 (3 x 5 min). The tissue was then permeabilized using 1X PBS, pH 7.4 + 0.3% Triton X-100 for 15 min at RT and washed with pH 7.4 PBS (3 x 5 min). The slides were blocked at RT for 30 min in Ab-oligo blocking and dilution buffer which contained 2% bovine serum albumin (BSA, bioWORLD, Dublin, OH), 0.5 mg/mL sheared salmon sperm DNA (ThermoFisher) and 0.5% dextran sulfate (Sigma-Aldrich) in 1X PBS, pH 7.4. Each tissue section was covered with 40 μL of unconjugated pEGFR antibody diluted to a concentration of 15 μg/mL and incubated for 1h at RT. An additional tissue section was incubated with blocking buffer without primary antibody to serve as a negative control. Excess pEGFR antibody was removed by washing with 2X SSC buffer, pH 7 for 3 x 5 min. Each tissue section was then fixed through a 15 min incubation of 2% PFA at RT and washed with 2X SSC pH 7 (3 x 5 min). pEGFR was labeled with donkey anti-rabbit secondary antibody conjugated to AF750 (dRb750). The secondary antibodies were diluted in dilution buffer containing 2% BSA, 0.5 mg/mL sheared salmon sperm DNA and 0.5% dextran sulfate in 2X SSC buffer. The dRb750 was diluted to a final protein concentration of 350 nM. Each tissue section, including the negative control, was covered with 40 μL of the diluted secondary antibody and incubated for 45 min at RT in a humidified chamber protected from the light. Excess secondary antibody was removed by washing with 2X SSC buffer for 3 x 5 min. Then to facilitate Ab-oligo cyCIF imaging, the nine Ab-oligo conjugates (**Table 6.1**) were mixed at a concentration of 15 μg/mL per antibody into a single cocktail. Each tissue section was covered with 40 μL of the diluted antibody cocktail and incubated at 4 °C overnight in a humidified chamber. The negative control slide was once again incubated with blocking buffer without any antibody. The next day, the sections were washed with

2X SSC buffer, pH for 3 x 5 min. The sections were fixed in 2% PFA for 15 min at RT, then washed again in 2X SSC buffer (3 x 5 min).

Cycles of IS application, imaging and signal removal were performed to specifically label E-Cad, Ki67, pAkt, CK8, CASP3, pMEK, EGFR, PI3K and Akt. Each marker was fluorescently labeled using one of two unique IS labeling strategies. The first, previously reported strategy employed the use of a 26 nt IS with a fluorophore conjugated through a photocleavable linker (PCL) at both the 3' and 5' ends of the oligo.[112] This strategy was applied for labeling E-Cad, Ki67, CK8, EGFR and PI3K. A second strategy was incorporated into this study as a means of amplifying the fluorescence signal of lower abundance markers. In this strategy a 198 nt oligo termed an amplification strand (AmpS) was first applied to tissue sections after Ab-oligo conjugate incubation. The AmpS contained a 26 nt region that was complementary to the DS on the Ab-oligo conjugates followed by a series of repeating 15 nt sequences with a 2 nt spacer between each repeating unit. Following AmpS incubation, complementary 15 nt amplification IS (Amp IS) with a fluorophore conjugated through the PCL at the 3' end were added to the tissue at a molar ratio of 20:1 which provided the potential for a 5X increase in signal in comparison to Ab-oligo conjugates labeled with 26 nt IS. This strategy was employed to label pAkt, CASP3, pMEK and Akt. Importantly, these two strategies were used simultaneously in rounds of imaging as follows. First, AmpS for all markers to be imaged in a given round were diluted to 350 nM in dilution buffer containing 2% BSA, 0.5 mg/mL sheared salmon sperm DNA and 0.5% dextran sulfate in 2X SSC buffer. The mixture was then heated to 85 °C for 3 min in an effort to decrease formation of hairpins and other secondary structures. Then any 26 nt, 2xPCL-FL IS were added to the mixture for a final concentration of 350 nM of each IS. 40 μL of the diluted oligo cocktail was applied to each slide and incubated at RT for 45 min while protected from light. Unbound 26 nt IS and AmpS was removed by washing with 2X SSC buffer (3 x 5 min). Then Amp IS was diluted to a final concentration of 7 μM and 40 μL dispensed onto each tissue. The Amp IS was incubated at RT for 45 min while protected from light. Unbound Amp IS was removed by washing with 2X SSC buffer (3 x 5 min). DAPI was then applied to all stained samples at 300 nM for 10 min at RT and the samples were washed in 2X SSC buffer (2 x 5 min). All stained slides were mounted with Fluoromount-G and cover-slipped for imaging.

Images were collected on a Zeiss AxioScan.Z1 in the DAPI, AF488, AF546, AF647, and AF750 channels for each round of staining. All stained slides were then treated with UV light for 15 minutes followed by washing 10 times with 0.1X SSC and remounted with Fluoromount-G. Finally, the slides were imaged with the same settings used prior to UV treatment to confirm complete signal removal. Subsequent rounds of IS addition, imaging and signal removal were repeated until all Ab-oligo conjugates were imaged.

TRIPODD Analysis of Erlotinib Therapeutic Response Kinetics. After iPAI and Ab-oligo cyCIF data was collected from each tissue section, the image datasets for each tissue section were spatially registered. Ab-oligo cyCIF was registered with a previously reported MATLAB script.[152] The targeted and untargeted iPAI agent images along with the generated DTA tissue map for each tissue section were then manually registered to the E-Cad images with the built-in ImageJ

registration plugin, "Align image by line ROI." To enable spatially-oriented, single-cell quantification of targeted iPAI probe, untargeted iPAI probe and DTA signal along with expression of all antibodies, cell segmentation was performed with QiTissue Software (QiBiotech Inc, Raleigh, NC) which included feature extraction of the mean intensity of each marker within each cell. To ensure quantification of only xenograft tissue and exclude mouse stromal tissue, manual gating was performed in QiTissue where only E-Cad positive cells were selected for further analysis. Violin plots were then generated in Prism v9.0 based on the single-cell expression values for pEGFR, DTA, Ki67 and CC3 for comparison of therapeutic effect in each group.

RESULTS

Pharmacokinetic evaluation of iPAI agents in HCC827 xenograft tissues. iPAI probe pharmacokinetics were characterized in HCC827 xenograft tissues that were resected 15, 30, 60, 120, 240 or 480 min after systemic administration of 2.5 mg/kg of the targeted and untargeted iPAI

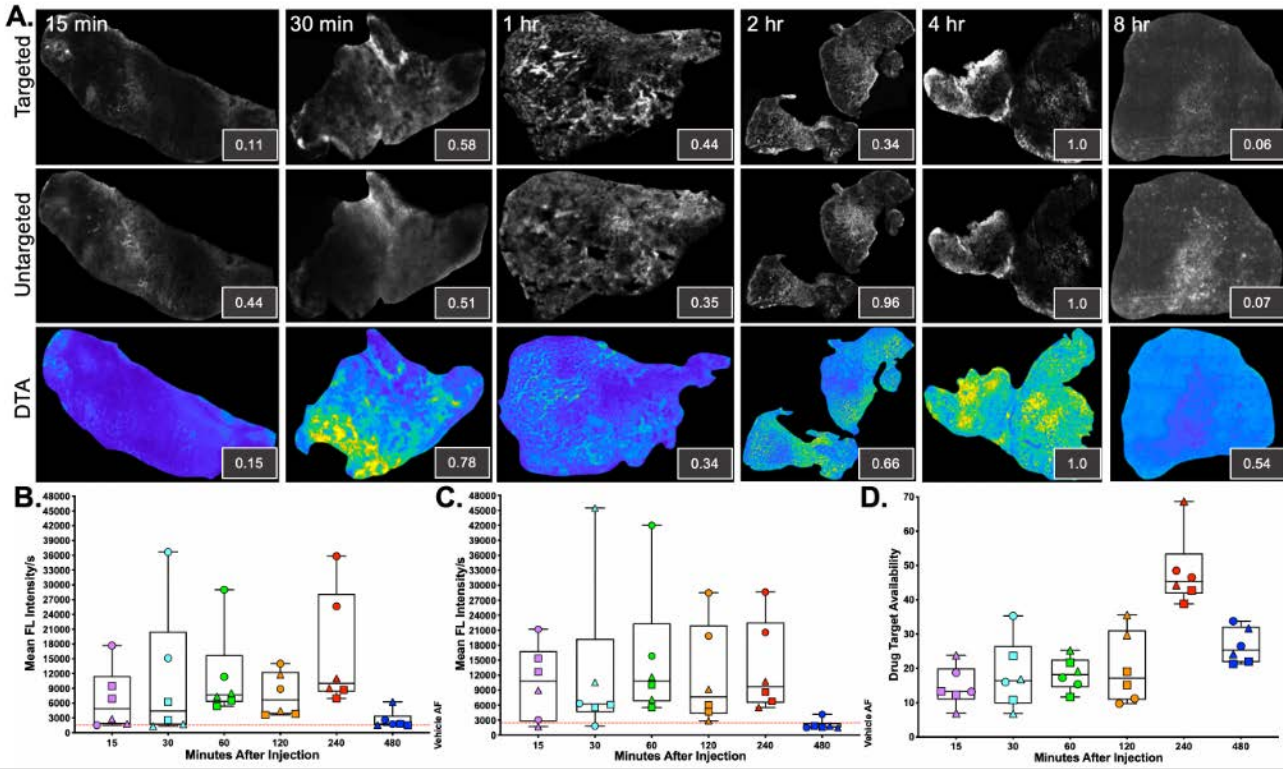

Fig. 6.1: *Pharmacokinetic characterization of iPAI probes and DTA.* HCC827 CDX mice were systemically administered 2.5 mg/kg of the targeted and untargeted iPAI probes and resected after 15, 30, 60, 120, 240 or 480 min. **A.** Representative fluorescence images of tumor tissue sections (from n=4 tumors per timepoint) of the targeted, untargeted and generated DTA tissue maps are displayed with the targeted and untargeted images displayed with auto-contrast levels for visualization while the DTA tissue maps are scaled equivalently. Relative signal intensities for each imaging channel (insets) for each representative tissue section were calculated. Assessment of **B.** targeted and **C.** untargeted probe uptake as well as **D.** DTA variability to compare all analyzed tumors was performed. Points of the same shape signify that the tumors were taken from the same mouse at each timepoint. The red dashed line indicates the level of tissue autofluorescence as quantified from HCC827 xenograft tissue following a vehicle only injection.

probes (**Fig. 6.1**). Whole tissue section fluorescence images from tumors (n=3 mice/timepoint, 2 tumors/mouse) were used to quantify the mean signal intensities in the Cy5 (targeted) and Cy3 (untargeted) channels to generate DTA tissue maps. All targeted and untargeted tissue images are displayed with auto-contrast. The targeted and untargeted images were then used to generate DTA maps and mean DTA for each image was calculated. All targeted and untargeted images are displayed with unique contrast settings to enable visualization while DTA tissue images are displayed with equivalent contrast settings. In the displayed representative images, the 4 h time point produced the highest relative targeted, untargeted and DTA signals (**Fig. 6.1A**). In the summary data, the highest median targeted fluorescence was at the 240 min timepoint (**Fig. 6.1B**). The untargeted channel saw similar median intensities at 60, 120 and 240 min although at 120 min there was a tissue section with fluorescence below the autofluorescence level (**Fig. 6.1C**). In the DTA channel, the 240 min timepoint produced the highest median DTA from all tissue sections analyzed (**Fig. 6.1D**).

Pharmacodynamic assessment of iPAI agents in varied EGFR expressing tissues. iPAI agent pharmacodynamic activity was quantified in xenograft tissues with varied endogenous EGFR expression *in vitro* (**Fig. 6.2**). EGFR number for each cell line, as quantified by flow cytometry, demonstrated high EGFR expression for HCC827 (average EGFR per cell = $2.4x10^6$), mid-level EGFR expression for PANC-1 (average EGFR per cell = $6.7x10^5$) and low EGFR expression by SW620 (average EGFR per cell = $2.3x10^2$, **Fig. 6.2G**). Whole tissue section fluorescence images collected from tumors (n=4/dose/CDX) administered with 5, 2.5 or 1.25 mg/kg of each iPAI agent were used to quantify the mean fluorescence signal intensities in the Cy5 (targeted) and Cy3 (untargeted) channels. All targeted and untargeted tissue images are displayed with auto-contrast. The targeted and untargeted images were used to both generate DTA maps and quantify mean DTA for each tumor. All targeted and untargeted images are displayed with unique contrast settings to enable visualization while DTA tissue images are displayed with equivalent contrast settings. Relative fluorescence or DTA values were calculated per imaging channel for the displayed, representative images. In the 1.25 mg/kg dose group, PANC-1 had the highest relative targeted and untargeted iPAI agent fluorescence intensity as well as the highest relative DTA value (**Fig. 6.2A**). The representative image of the HCC827 xenograft tumor section in the 2.5 mg/kg group showed the highest relative targeted fluorescence in the 2.5 mg/kg cohort as well as the highest relative DTA of all displayed tissue sections (**Fig. 6.2B**). The displayed SW620 tumor section in the 2.5 mg/kg group produced the highest relative untargeted fluorescence within the dose group. The 5 mg/kg dose group showed the highest relative targeted and untargeted fluorescence intensities from the displayed SW620 tumor section (**Fig. 6.2C**). The SW620 tissue sections also produced the highest relative DTA in comparison to the displayed PANC-1 and HCC827 tumor sections in the 5 mg/kg dose group.

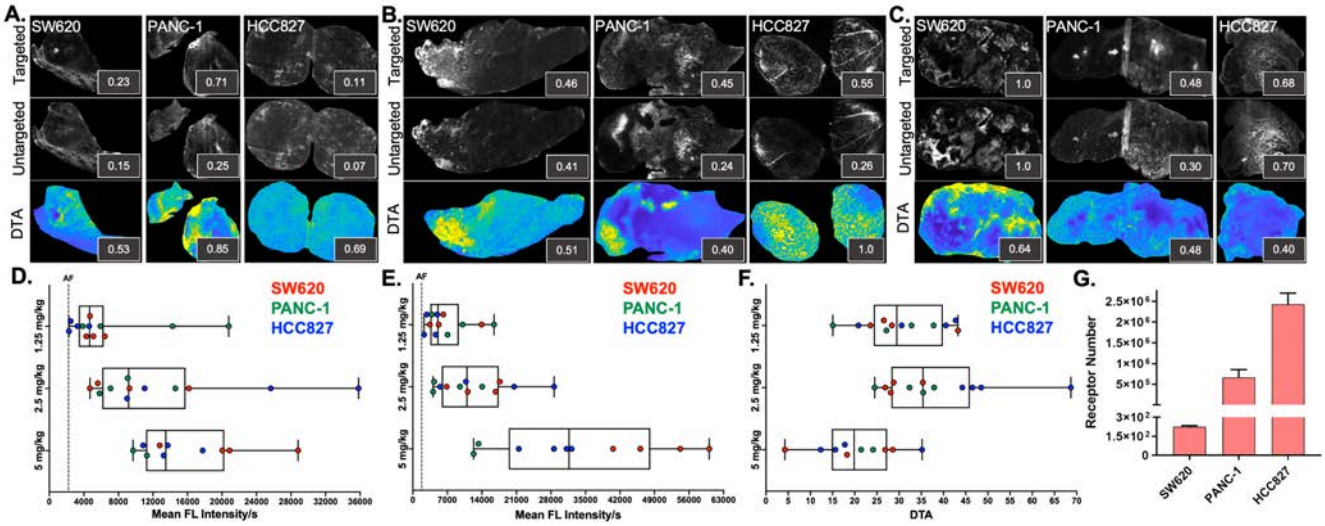

Fig. 6.2: *Pharmacodynamic assessment of iPAI probes in xenografts with varied EGFR expression*. HCC827, PANC-1 and SW620 CDX mice were systemically administered with **A.** 1.25 mg/kg, **B.** 2.5 mg/kg or **C.** 5 mg/kg of the targeted and untargeted iPAI probes and resected 4 hours after injection. Representative images of targeted and untargeted probe uptake from (from n=4 tumors per CDX per dose) HCC827, PANC-1 and SW620 tissue sections are all displayed with auto-contrast. Inset values represent relative signal intensity normalized across imaging channels. Targeted and untargeted tissue images enabled calculation of DTA spatial maps and relative DTA values (insets) for each representative tissue section with all images displayed at the same contrast levels. Assessment of **D.** targeted and **E.** untargeted probe uptake as well as **F.** DTA variability to compare all analyzed tumors was performed. **G.** Quantification of EGFR expression in SW620, PANC-1 and HCC827 cells was performed by flow cytometry.

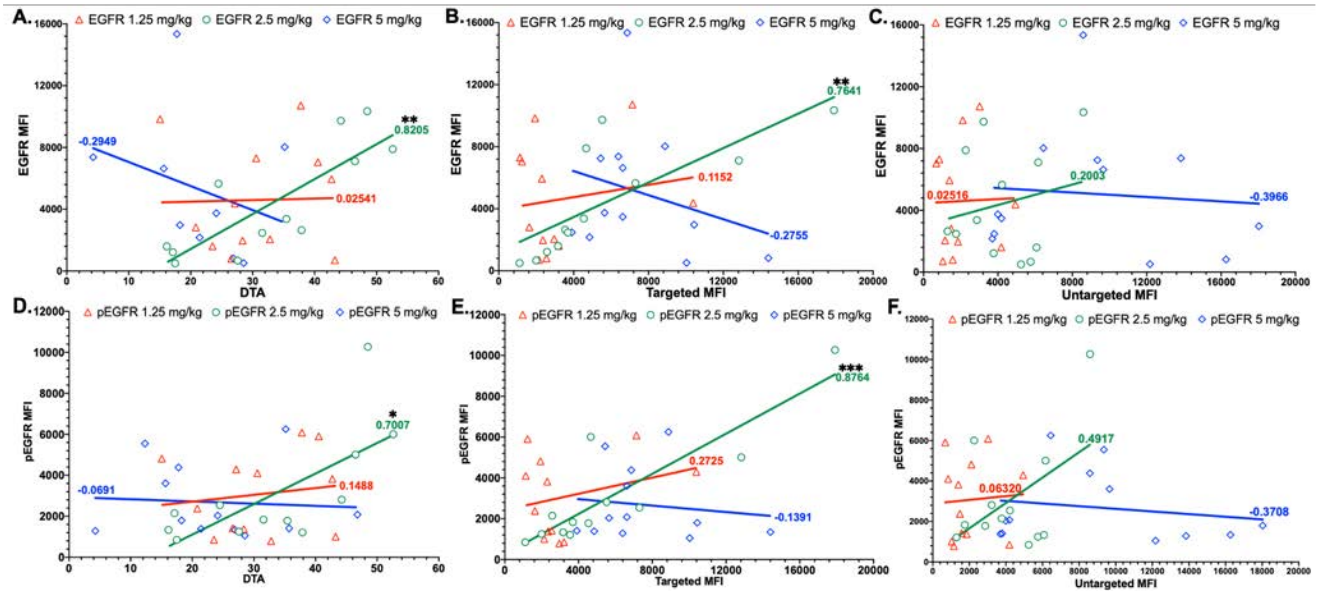

Fig. 6.3: *Pearson's correlation of iPAI signal to EGFR expression*. Pearson correlation coefficients were generated to compare EGFR expression to **A.** DTA, **B.** targeted probe and **C.** untargeted probe signal. Pearson correlation coefficients were also calculated to study the relationship between pEGFR expression and **D.** DTA, **E.** targeted probe and **F.** untargeted probe. Solid lines represent the linear regression trendline and are the color of their respective dose group. (*$p < 0.05$, **$p < 0.01$ and ***$p < 0.001$.

The minimum, maximum and median values were calculated from the targeted, untargeted and DTA images for all tumor tissue in all dose groups (**Fig. 6.2D-F**). For the targeted and untargeted probes, a positively correlated dose dependent relationship with median was found (**Fig. 6.2D** & **6.2E**). There was also a dose dependent relationship between maximum and minimum fluorescence intensity in the untargeted channel. In contrast, the targeted channel of the 2.5 mg/kg dose group showed tissues with the highest fluorescent signal and a dose dependent relationship only existed for the minimum fluorescence intensity. In the DTA channel, the highest median and maximum DTA values were in the 2.5 mg/kg dose group (**Fig. 6.2F**).

To assess the relationship between iPAI dose and EGFR expression, all tissues from all CDXs were immunostained to quantify EGFR and pEGFR expression. Pearson's correlation was then calculated and scatterplots were utilized to compare EGFR and pEGFR expression to DTA, targeted probe and untargeted probe signals (**Fig. 6.3**). In the DTA and targeted channel, only the 2.5 mg/kg dose group demonstrated significant correlation between EGFR and pEGFR expression to either DTA or targeted probe signal (**Fig. 6.3A, 6.3B, 6.3D** & **6.3E**). In the untargeted probe channel, there were no significant correlations calculated between the untargeted probe signal to EGFR or pEGFR expression in any dose group (**Fig. 6.3C** & **6.3F**).

TRIPODD analysis of erlotinib therapeutic effect kinetics in HCC827 xenografts. Erlotinib therapeutic effect kinetics were assessed in HCC827 CDX mice (n=9) treated with 50 mg/kg of erlotinib via oral gavage. iPAI probes were administered at 2.5 mg/kg 4 h prior to sacrifice, where mice (n=3/time point) were sacrificed at 6, 12, or 24 h after erlotinib dosing. The erlotinib treated cohorts were compared to an untreated cohort (n=3) that were only administered with 2.5 mg/kg iPAI agents. Tissue sections from each tumor were imaged for the iPAI targeted and untargeted fluorescence intensity followed by the 10-antibody panel (**Table 6.1**). Registration of all image sets facilitated simultaneous visualization of the fluorescence staining pattern of all antibodies and the generated DTA tissue map for each tissue section (**Fig. 6.4**), where each stained biomarker is displayed at equivalent contrast settings for qualitative assessment. The untreated tissue showed minimal CC3 staining and positive staining for Ki67 as well as the EGFR signaling cascade proteins (e.g., EGFR/pEGFR, Akt/pAkt, pMEK and PI3K [**Fig. 6.4A**]). In the 6h treatment group both Ki67 and CC3 were positive in varied cells, while all signaling proteins showed similar staining intensity to the untreated group (**Fig. 6.4B**). 12h after erlotinib treatment, there was positive CC3 and Ki67 signal, while the downstream protein targets of erlotinib had decreased expression (**Fig. 6.4C**). 24h after erlotinib treatment, CC3 expression was abundant while EGFR signaling cascade proteins had returned to the expression level of the untreated group (**Fig. 6.4D**).

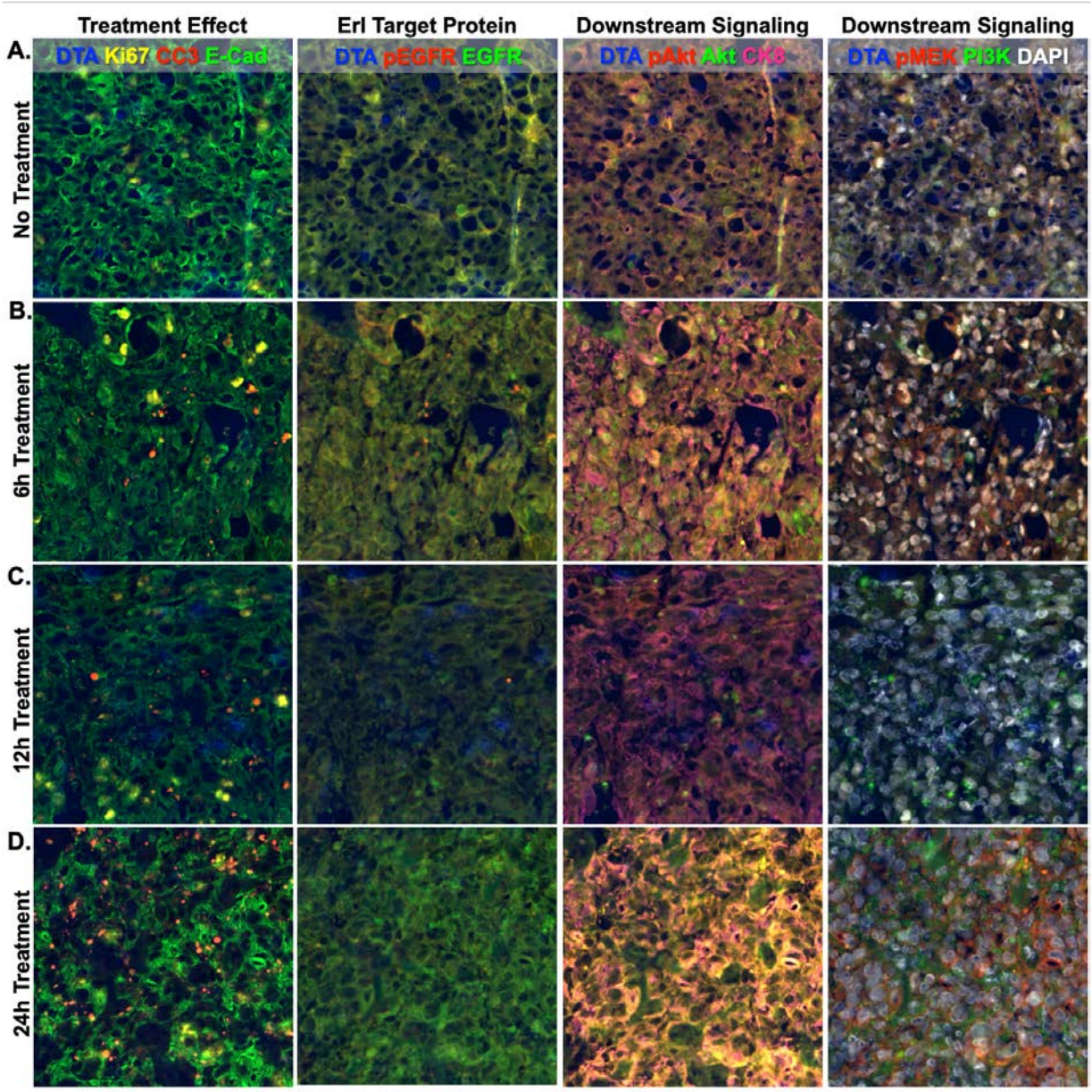

Fig. 6.4: *TRIPODD imaging of erlotinib treated tissues.* Representative regions of interest from whole tissue images of HCC827 xenografts imaged with multiplexed cyCIF are displayed based on treatment as **A.** No treatment/untreated, **B.** 6h Treatment, **C.** 12h Treatment or **D.** 24h Treatment. Markers displayed in each image are organized to have similar biological relevance and set to equivalent contrast settings across treatment groups. QiTissue software was used to generate high dimensional visualizations of the cyCIF imaging data sets.

Single-cell quantification facilitated by cell segmentation was performed for pEGFR, DTA, Ki67 and CC3 to evaluate the kinetics of erlotinib therapeutic effect (**Fig. 6.5**). Therapeutic inhibition of pEGFR by erlotinib was observed as median pEGFR expression decreases at 6h after erlotinib dosing and further reduced 12h after treatment although overlap in expression levels exists across all time points (**Fig. 6.5A**). 24h after erlotinib treatment, median pEGFR expression increased to a level greater than that of the untreated group indicating erlotinib-based inhibition had expired. Median DTA was highest in the untreated tissues while DTA decreases with time

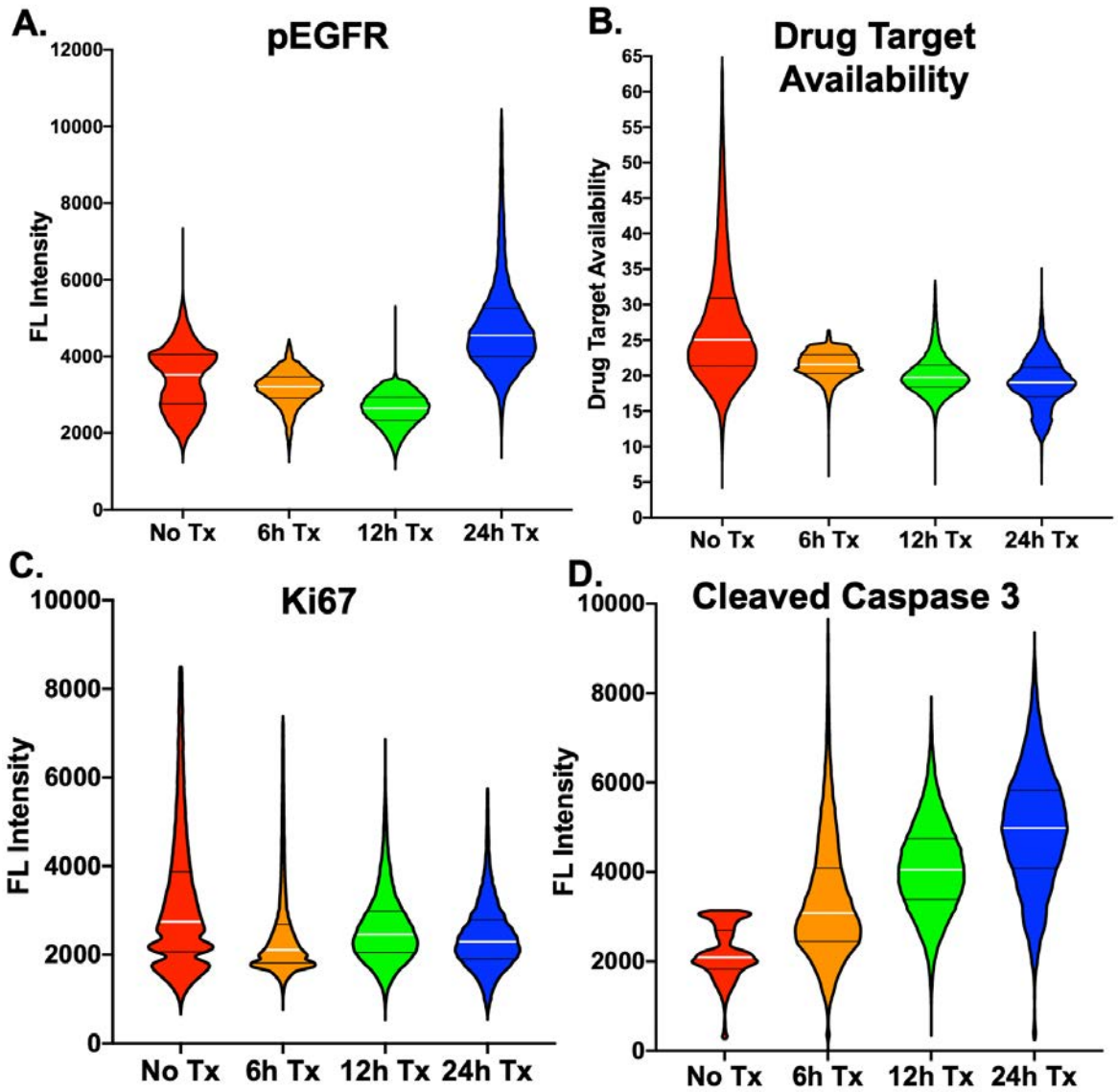

Fig. 6.5: *Single-cell quantification of erlotinib therapeutic kinetics.* Cell segmentation performed in QiTissue facilitated single-cell quantification across treatment groups for known markers of erlotinib therapeutic response and DTA. **A.** pEGFR expression decreased after erlotinib treatment through 12h and returned to above no treatment levels after 24h. **B.** DTA decreased after treatment for all timepoints. **C.** Ki67 expression was lowest 6h after treatment, but remained below no treatment levels through 24h. **D.** Cleaved caspase 3 (CC3) increased in a treatment-time dependent manner.

where median DTA was lowest 24h after erlotinib dosing (**Fig. 6.5B**). Median Ki67 expression was also highest in the untreated group and lowest 6h after erlotinib dosing (**Fig. 6.5C**). In contrast, CC3 expression was lowest in the untreated tissues and increased with time after treatment where median CC3 expression was highest 24h after erlotinib treatment (**Fig. 6.4D**).

DISCUSSION

Targeted therapeutics (e.g., erlotinib) that aim to inhibit molecular dependencies present in tumors often outperform previous standards of care such as platinum-based chemotherapy and improve overall survival for patients. However, therapeutic response is often transient as tumors evolve to escape therapeutic inhibition through a number of routes. Crucially, current methodologies are unable to unravel the multifaceted routes by which a therapeutic can fail, such as insufficient drug delivery and cell signaling pathway reprogramming as a mechanism of resistance. Our previously reported novel fluorescence imaging platform, TRIPODD, is capable of generating a mechanistic understanding of therapeutic response and resistance that correlates drug target availability (DTA) and proteomic therapeutic response to inform on therapeutic strategy design. Optimization if iPAI and extension of the TRIPODD platform to analyze erlotinib therapeutic response kinetics were preformed herein as a proof-of-concept demonstration of the capability of TRIPODD to perform therapeutic response imaging.

The optimal time to resect tissues after systemic iPAI agent administration was performed through a pharmacokinetic study of the iPAI agents. Distribution of the iPAI probes and calculated DTA at the various timepoints after injection were quantified to determine variation in signal intensity over time to ensure tissue resection was performed at the optimal timepoint (**Fig. 6.1**). Variation was observed in DTA and fluorescence intensity between and within timepoints, but only tumors resected after 60 min and 240 min did not have targeted or untargeted images at the autofluorescence level of the injection vehicle (**Fig. 6.1B** & **6.1C**). Importantly, the highest median DTA was at the 240 min timepoint which led to its selection as the optimal timepoint to resect tissue after iPAI administration (**Fig. 6.1D**). Due to the dynamic kinetics of *in vivo* distribution of iPAI agents, 240 min afforded more time for sufficient distribution of the probes than 60 min.

Xenografts with varied EGFR expression levels, HCC827, PANC-1 and SW620, that were administered with varied doses of iPAI agents displayed a dose dependent relationship between median targeted and untargeted probe fluorescence intensity (**Fig. 6.2D** & **6.2E**). None of the iPAI dose groups displayed a correlation between targeted or untargeted probe signal and known EGFR expression. Notably, the 1.25 mg/kg dose group produced tissues with fluorescence near that of tissue autofluorescence. Further, the SW620 tissues had the majority of the highest targeted and untargeted signals in the 5 mg/kg group suggesting that quantitative imaging is not achieved with the highest dose group. Additionally, in the 5mg/kg group, it may be that the SW620 CDX experienced elevated non-specific accumulation of both the targeted and untargeted probes, and thus the generated DTA values in that dose group do not correlate with EGFR expression. This indicates that relative quantitative imaging is not achieved with 5 mg/kg of iPAI agents (**Fig. 6.2D-**

F). Importantly, iPAI based correction for non-specific uptake in the 2.5 mg/kg group was observed where the highest EGFR-expressing tissue, HCC827 (**Fig. 6.2G**), produced DTA values greater than that of any tissues indicating quantitative imaging may be produced at that dose (**Fig. 6.2F**). To confirm this, a study to correlate EGFR and pEGFR expression to iPAI signal in all tissues analyzed in the pharmacodynamic study was performed (**Fig. 6.3**). Both EGFR and pEGFR expression was significantly correlated to DTA and targeted signal in the 2.5 mg/kg group while no correlation was seen for any other dose group (**Fig. 6.3A, 6.3B, 6.3D** & **6.3E**). No correlation was seen for any dose in the untargeted channel as was expected due to the untargeted probe accumulating non-specifically (**Fig. 6.3C** & **6.3F**). Additionally, the slopes of the majority of trendlines produced in the untargeted channel were low signifying that untargeted probe signal alone has minimal relationship to expression of the targeted probe protein target. This result suggests that potentially 1.25 mg/kg of iPAI agents does not produce fluorescence signal that is adequately above the background signal, which is necessary to produce relatively quantitative information. Although the 5 mg/kg dose group produced greater median fluorescence intensity in the targeted and untargeted channels, the 2.5 mg/kg dose resulted in both the most quantitative receptor imaging and a lower iPAI dose to prevent saturation of probe binding sites, which could result in non-quantitative imaging. 2.5 mg/kg was therefore selected as the optimal dose for iPAI administration. While this study provides evidence for selection of 2.5 mg/kg as the optimal dose for iPAI administration, the data produced is noisy, as is not unexpected for *in vivo* model systems, so additional data points could be added in future studies to further strengthen the findings.

Extension of TRIPODD to analyze erlotinib therapeutic response kinetics was performed on HCC827 xenograft tissue sections that were either not treated or treated with erlotinib and resected 6, 12 or 24 h after erlotinib dosing (**Fig. 6.4**). Following iPAI, multiplexed cyCIF integrating both indirect IF and Ab-oligo methodologies was performed using a 10-antibody table (**Table 6.1**). In representative images, increased cell death, labeled with cleaved caspase 3 (CC3), was visualized in treated tissues over the untreated tissues indicating erlotinib was having an anti-tumor effect (**Fig. 6.4A-6.4D**). Notably, EGFR, pEGFR and downstream proteins appear to accumulate more intracellularly in the treated tissues than the untreated tissues, most clearly observed in the 6h treated tissue (**Fig. 6.4B**). Erlotinib has previously been reported to cause internalization of EGFR in EGFRmut+ cells and further demonstrates that erlotinib was having a therapeutic effect on the HCC827 xenografts.[162] Quantification of single-cell expression of pEGFR revealed the lowest median pEGFR value in tissues treated with erlotinib for 12 h (**Fig. 6.5A**). Notably, pEGFR expression recovered 24 h after erlotinib therapy indicating that erlotinib was no longer preventing ATP binding to the intracellular domain of EGFR. Interestingly, although pEGFR expression recovered, DTA after 24 h remained reduced compared to untreated tissues which was consistent with previous findings of the off-rate of erlotinib in relation to EGFR phosphorylation. (**Fig. 6.5B**).[163] This may be explained in part by the fact that erlotinib can bind to both the active and inactive conformations of EGFR.[164] This means that while EGFR phosphorylation may be occurring, it does not necessarily signify that erlotinib is no longer bound within the tumor. Additionally, it has been confirmed via liquid chromatography mass

spectrometry (LC-MS) that erlotinib can be detected within a tumor 24 h after a single erlotinib dose.[165] Kinetics of erlotinib cycling from EGFR may also further explain this finding where it has been demonstrated that pEGFR expression does not necessarily correlate to kinase occupancy by erlotinib, but rather downstream protein expression (e.g., pAkt, pMEK) provides a better correlation between therapeutic effect and kinase occupancy.[166] Further evidence of erlotinib therapeutic effect was the decrease in proliferation, measured by Ki67 expression, and the increase in cell apoptosis, measured by CC3 (**Fig. 6.5C** & **6.5D**). Interestingly, both showed evidence of erlotinib therapeutic effect at 24 h even after pEGFR expression recovered at the same timepoint. However, it has previously been demonstrated *in vitro* that HCC827 cells still exhibit decreased Ki67 expression 24 h after erlotinib treatment giving support to this finding.[167] Further *in vitro* studies have also shown CC3 expression to be elevated after 24h of a single dose of erlotinib.[167] The capability of TRIPODD to monitor *in situ* erlotinib therapeutic response kinetics represents a significant opportunity for improved therapeutic strategy design in future studies.

While this study provides demonstration of the capability of TRIPODD to perform therapeutic response imaging correlating DTA and proteomic markers of drug response, there are some limitations herein. While decrease in DTA after erlotinib treatment was reasonable given the non-selective nature of erlotinib binding to both active and inactive EGFR conformations, additional study of tissues resected at later timepoints will be necessary to confirm this finding. These tissues are currently under investigation. Additionally, while Ki67 and CC3 produced predicted expression trends over time, further refinement of the analysis pipeline will need to be performed to identify cells positive for each marker. This will facilitate quantification of the change in the proportion of cells that are marker-positive for high resolution quantification of cell populational changes. Ki67 and CC3 quantification performed in this study provided the expected trends, but the calculated median expression for each is skewed by populations of Ki67 and CC3 negative cells. This will require accurate thresholding for binary decision making of biomarker positivity, a non-trivial process where batch effect normalization must be considered to produce robust results. Finally, future studies applying TRIPODD to identify novel therapeutic strategies will require expansion of cyCIF staining panel beyond the limited panel applied herein for validation purposes.

Continued development of the TRIPODD platform will require increasingly complex model systems for evaluation of therapeutic response and resistance along with longitudinal treatment studies that progress beyond the single erlotinib dose treatment study reported herein. While xenograft models applied in this study provide a useful, largely homogenous system for validation purposes, they lack TME components (i.e., stromal and immune cells) known to have an influence in therapeutic outcomes in numerous cancers such as EGFRmut+ NSCLC.[168] Patient derived xenografts (PDX) and orthotopically implanted xenografts both provide model systems that will allow for investigation into the role that the TME plays in therapeutic response. One potential therapeutic strategy to be investigated in model systems such as these would be combination therapy with osimertinib, a third generation EGFR TKI, and bevacizumab, a VEGF-A inhibitor. Recent studies have also demonstrated prolonged progression free survival (PFS) by

combining bevacizumab with EGFR TKIs due to improved TME access.[169-171] However, the localized tumor response and hypothesized drug penetration improvement has not been fully characterized given the limitations with current analytical tools. The novel TRIPODD imaging platform offers an opportunity to characterize mechanisms of therapeutic response and resistance within the context of a broad spectrum of solid tumor models to unravel the relationship between drug binding, proteomic response and therapeutic outcome.

ACKNOWLEDGEMENTS

We would like to thank Drs. Stefanie Kaech Petrie and Crystal Shaw as well as Mr. Brian Jenkins in the Advanced Light Microscopy Core at the Jungers Center at Oregon Health and Science University (OHSU) for expert technical assistance with fluorescence microscopy studies. This work was funded by an ASPIRE Award from the Mark Foundation for Cancer Research (Gibbs).

Chapter 7

Summary and Future Perspectives

SUMMARY

Fully realized personalized therapy will include curated drug selection for mono- and combination therapy designed to target intratumoral heterogeneity, reduce toxicity and improve overall survival.[172] Protein kinases are one common drug target as deregulation of kinase function in cell signaling pathways is implicated in numerous cancers.[2] In response, highly specific kinase inhibitors (KIs) have been developed for personalized therapy.[3] Though nearly 50 KIs have been FDA-approved,[4] KI monotherapy is seldom curative, often owing to intratumoral heterogeneity and acquired resistance. To combat this, therapies must be tailored to known resistance mechanisms to efficiently and effectively engage with their targets to exploit cellular vulnerabilities.[17, 18] A successful therapeutic must engage with its drug target in the dynamic and complex disease setting, where subsequent efficacy is dictated by the duration, completeness and homogeneity of DTA and subsequent drug target occupancy.[13, 19] However, standard tools (e.g., plasma analysis, western blot [WB]) are bulk in nature,[38] and no established technology exists to quantify KI target engagement, concomitant with single cell protein expression, response heterogeneity and identification of cellular vulnerabilities for therapy.[13, 19]

One example of this is in the case of lung cancer, an aggressive disease and the leading cause of cancer death worldwide, with ~1.8 million fatalities in 2018.[88] The combination of asymptomatic presentation and insufficient screening methods accounts for the near uniformly late stage-diagnoses, leaving most lung cancer patients with few curative options. While smoking is the number one predictor of disease occurrence, 15% of all lung cancer patients have never smoked,[89] where non-small cell lung cancer (NSCLC) is the most commonly diagnosed subtype in this population. The discovery of NSCLC dependence on epidermal growth factor receptor (EGFR) signaling and the development of targeted EGFR tyrosine kinase inhibitors (TKIs) has revolutionized treatment outcomes for patients harboring these genetic abnormalities. Clinical trials have consistently shown superior efficacy of first- (i.e., gefitinib or erlotinib), second- (i.e., afatinib) and third-generation (i.e., osimertinib) TKIs over standard chemotherapies (i.e., platinum-based) for patients with EGFR-mutated (EGFRmut+) NSCLC, improving progression-free survival (PFS) from 6 to up to 15 months.[17, 90-96] As with the vast majority of targeted therapies, enthusiasm for initial robust response rates is tempered by inexorable disease progression. Three distinct acquired resistance mechanisms limit the duration of NSCLC response to osimertinib treatment: (1) cell signaling pathway reprogramming (e.g., *MET* or *HER2* amplifications), (2) additional EGFR mutations (e.g., C797S) and (3) phenotypic changes (e.g., transition from NSCLC to small cell lung cancer).[97] Notably, while these mechanisms are the most commonly recognized, it is understood that the full spectrum of *de novo* and acquired resistance mechanisms in response to therapy are even more diverse and not yet fully characterized using available screening tools.[98]

This thesis focuses on the development of a novel fluorescence imaging platform, TRIPODD (**T**herapeutic **R**esponse **I**maging through **P**roteomics and **O**ptical **D**rug **D**istribution and binding) combining intracellular paired agent imaging (iPAI) and oligonucleotide conjugate antibody cyclic immunofluorescence (Ab-oligo cyCIF) on a single tissue section for mechanistic

understanding of therapeutic response.[112, 143] TRIPODD facilitates simultaneous single-cell quantification of DTA through iPAI and the associated tumor biology through accurate segmentation of spatially aligned tumor cells based on Ab-oligo cyCIF, a critically unmet analytical need. TRIPODD overcomes the limitations of other methodologies for quantifying DTA with iPAI on a cell-by-cell level allowing for interrogation of the role drug distribution plays in therapeutic response. This is powered by Ab-oligo cyCIF which facilitates cell segmentation for single cell feature expression of DTA along with local protein expression, all within the spatial context of the tumor. The work presented herein has sought to develop the TRIPODD platform in an effort to generate a robust preclinical tool for evaluating novel therapeutic strategies. In this thesis, optimization and validation of iPAI and Ab-oligo cyCIF have motivated their integration into the TRIPODD pipeline.

A number of highly-multiplexed immunostaining techniques have been developed as a means for quantitative, spatial proteomics to fully elucidate and characterize proximity interactions between cells of all functions that drive tumor evolution in response to therapy.[30, 69-73, 75-79, 109 73, 69, 76 78, 110, 111] In **chapter 2**, oligo conjugation to antibody and signal removal method optimization for the development of Ab-oligo cyCIF is described. A robust method for oligo labeling antibodies was identified that utilizes a site-directed conjugation method which demonstrated superior success rate over non-specific conjugation methods. Additionally, fluorescence signal removal was achieved by utilizing ultraviolet (UV) light to cleave fluorophores present on oligos complementary to those labeling a particular antibody. This method was chosen for Ab-oligo cyCIF based on its superior speed and non-destructive nature over alternative methods that were less robust and potentially damaging to tissue antigenicity.

Based on the success of the optimization of oligo conjugation and fluorescence signal removal methods, in **chapter 3** we sought to further expand and optimize Ab-oligo staining and imaging parameters to generate a high-dimensional image data set characterizing multiple breast cancer tissue samples.[112] Ab-oligo cyCIF exploits *in situ* hybridization of complementary oligonucleotides for biomarker labeling and the oligo modifications to facilitate signal removal for sequential rounds of fluorescent tagging and imaging. In our technology, a single stranded oligo (docking strand, DS) is conjugated to the primary antibody. Subsequent introduction of a complementary single stranded oligo (imaging strand, IS) conjugated to a conventional Alexa Fluor (AF) fluorophore (e.g., AF488, AF546, and AF647) facilitated specific on tissue fluorescent labeling through *in situ* hybridization and imaging with any conventional fluorescence microscope. The presence of a photocleavable linker (PCL) between the fluorophore and oligo sequence facilitated signal removal to levels of autofluorescence after UV light exposure prior to subsequent staining cycles. We generated a library of Ab-oligo reagents and optimized the staining parameters to ensure sufficient signal-to-background ratio (SBR) was produced for antigen detection. This included titration studies of Ab-oligo conjugates and IS as well as increasing the number of fluorophores on each IS from one to two. We then generated 14-marker image sets characterizing different breast cancer subtypes, which included human epidermal growth factor 2 positive (HER2+), estrogen receptor positive (ER+) and HER2- and ER- tumors.

While Ab-oligo cyCIF produced similar SBR to that of directly labeled antibodies utilized in other cyclic immunofluorescence approaches,[69, 73, 76, 86, 92, 93] there remained a need to increase sensitivity to lower abundance antigens (e.g., phosphoproteins) that are of interest when characterizing therapeutic response and resistance. **Chapter 4** is focused on the development of an Ab-oligo cyCIF amplification method for increased sensitivity to low abundance antigens along with flexibility of the cyCIF platform. This signal amplification technique utilizes a longer amplification oligo strand (AmpS) that hybridizes to its complementary DS on an Ab-oligo conjugate. The AmpS can then be fluorescently labeled with up to 10 amplification IS (Amp IS), each labeled with a fluorophore and a PCL. Development of the Ab-oligo amplification strategy required titration studies of the amplification oligos along with optimization of AmpS staining parameters. Further, improved design of DS oligos was performed to ensure robust amplification was achieved for all antibodies regardless of its DS sequence. Additionally, the flexibility of the Ab-oligo cyCIF platform was demonstrated by integrating conventional indirect IF reagents onto the same slide as Ab-oligo conjugates in order to generate a 10-biomarker image on a tissue section from a xenograft model of EGFRmut+ NSCLC. Importantly, the amplification strategy was employed simultaneously with the original IS design that had two fluorophores and two PCLs allowing for a flexible imaging strategy that could be readily adjusted on a per antibody basis.

In **chapter 5**, we demonstrate the feasibility of performing sequential iPAI and Ab-oligo cyCIF on a single tissue section to validate the TRIPODD platform. In this validation study, we demonstrate that iPAI agents can be systemically administered to mice bearing xenografts with varied EGFR expression where subsequent imaging of resected tissue sections produced quantitative receptor imaging through DTA calculations. The iPAI methodology was also extended to demonstrate its ability to detect the presence of the parent drug of the iPAI agents which was erlotinib in this study. The *in vivo* competitive binding study performed showed that DTA decreases when parent erlotinib drug was present within the tissue. This motivated future treatment studies as DTA was a reliable metric for measuring drug distribution. In validation of the TRIPODD platform, iPAI was performed on a tissue section and then, on the same tissue section, iPAI agents were removed with a saline wash and Ab-oligo cyCIF was performed. Crucial to the TRIPODD platform, we spatially registered the iPAI and Ab-oligo cyCIF image sets which enabled single-cell DTA quantification.

Following validation of the TRIPODD platform, we advanced this platform in **chapter 6** to monitor erlotinib therapeutic response kinetics in EGFRmut+ NSCLC xenograft models. We optimized the iPAI agent dose and tissue resection time to ensure the quantitative nature of the DTA metric. The optimized iPAI methodology was then applied to xenograft mice that were either not treated or treated with a single dose of erlotinib. iPAI agents were administered 4h prior to tissue resection that was performed either 6h, 12h or 24h after erlotinib therapy. After iPAI of all tissue, a 10-marker cyCIF panel was applied to each tissue section to characterize tumor biology and viability and monitor the epidermal growth factor (EGFR) signaling pathway. Single-cell quantification of phospho-EGFR (pEGFR) revealed that pEGFR expression was decreased through 12h of erlotinib treatment, but recovered at 24h. Interestingly, DTA was decreased for all

timepoints in comparison indicating that erlotinib was still present in the tissue even if pEGFR expression was present. Proliferation also decreased and cell apoptosis increased in treated tissues as was expected in the erlotinib sensitive model system used. This advancement of the TRIPODD platform was a demonstration of its capability to perform *in situ* therapeutic response imaging with single-cell resolution.

FUTURE PERSPECTIVES

Fully realized personalized medicine has the potential to provide curative therapeutic solutions for many advanced cancer patients. Novel therapeutic strategies that will achieve this will require methodologies to fully characterize drug distribution and proteomic effects within the spatial context of a tumor to generate mechanistic understandings of therapeutic success and failure. The work presented herein developing the TRIPODD platform represents a potential analytical solution to this challenge in therapeutic response imaging. The application of this platform technology to a wide spectrum of cancers could provide improved preclinical study of therapeutics prior to clinical application to increase effective therapeutic strategy discovery. However, aspects of the TRIPODD platform require further study in order to fully develop the analytical potential of the technology.

First, to ensure the DTA metric is a reliable one for assessing drug distribution in treated tissues, additional analysis of treated tissues should be performed. Studies to be performed could be treating xenograft bearing mice with a single dose of erlotinib where tissue is resected at time points later than those described in **chapter 6** (e.g., 48h, 96h, etc.). Evidence suggests that erlotinib can remain in the tumor tissue even after target inhibition (pEGFR) has ceased,[164-166] but confirmation is required. This could be further interrogated with more conventional technologies, such as with liquid chromatography-mass spectrometry (LC-MS), in order to quantify the pharmacokinetics of erlotinib within the tumor. Also, in an effort to continue to improve the quantitative nature of the DTA metric, refinement to the iPAI tissue analysis process will need to be explored. This will include the addition of a background subtraction step into the DTA calculation process to ensure no skewing of the DTA quantification occurs due to varying autofluorescence levels in different tissue types and/or treatment settings. To do this, average background autofluorescence data would need to be collected for each tissue type studied from tissue sections that were injected with vehicle only.

Additionally, further development in the Ab-oligo cyCIF methodology is necessary to ensure it can be capable of characterizing a broad range of tumor types and therapeutic contexts. This will require expansion of the validated Ab-oligo conjugate library to include additional markers such as those necessary to identify immune cells. The cell-derived xenograft model systems described herein lack an immune component, but advancement of TRIPODD will require model systems with immune cell populations (e.g., patient-derived xenografts) to be applied that more accurately replicate the tumor microenvironment within patients. Additionally, the flexibility of the Ab-oligo cyCIF methodology should be further explored to continue to increase the efficiency of the assay. This will involve chemical synthesis of photocleavable linkers directly

linked to fluorophores that can then be directly conjugated to antibodies. This offers a potential avenue to avoid the reagent costs of docking strand (DS) oligos to be conjugated to antibodies, fluorophore-labeled imaging strand (IS) oligos complementary to the DS and site-directed conjugation kits. Theoretically, these directly labeled antibodies will produce a similar signal intensity to Ab-oligo conjugates labeled with IS containing two fluorophores while also potentially decreasing background by not introducing oligos to the tissue. Additionally, conjugation of fluorophores labeled with PCLs to antibodies can be completed in a single day while the site directed conjugation process typically takes three days to complete. Therefore, the rate of Ab-oligo panel expansion can also increase through this technique. This also will result in a technology that is more agile to the study of different tumor types that require different marker panels for proteomic characterization.

In terms of TRIPODD analysis pipeline development, a couple crucial current features of the TRIPODD platform must be addressed to advance the platform to a point where it can have predictive power in therapeutic strategy design. The first is that a ground truth to the DTA metric must be established, where the relationship between receptor abundance and calculated DTA needs to be identified. Inherently, this is a limitation to the platform as this relationship must be re-assessed each time a new tissue is studied, but nonetheless will further improve the robustness of the platform. In a similar fashion, the trend between drug bound to its target and DTA must be established where methods such as LC-MS will enable such evaluation. This, however, is an additional challenge in the flexibility of the TRIPODD platform as these studies will need to be performed for each new drug and treated tissue. After these metrics have been assessed to improve the quantitative nature of TRIPODD, it will be vital to expand the single-cell quantification of DTA and proteomic expression to have a spatial proximity analysis component. This will require continued investigation into spatial proximity analysis tools, some which have been previously reported and are currently under investigation for incorporation into the TRIPODD analysis platform.[173] As TRIPODD is applied to more complex model systems, the spatial proximity between different cell types (i.e., tumor, immune and microenvironmental cells) will be vital in unraveling the mechanisms of therapeutic response and resistance. With the growing popularity of immunotherapy, further analysis of these spatial interactions will be requisite for successful application of immunotherapy to patients as has been previously reported.[125, 126] It is also possible that TRIPODD could be extended to human tissue samples that are collected and then *ex vivo* stained with iPAI agents followed by iPAI agent removal and Ab-oligo cyCIF imaging. This will enable assessment of DTA and how proteomic expression correlates within the spatial context of the tumor. This type of *ex vivo* study does however have the limitation that the tissue is fixed when it is stained with the iPAI agents so the functional biology of drug uptake cannot be considered. Apart from this limitation, this study design does offer a potential avenue to increase the translational impact of the TRIPODD platform where predictions can be made based on TRIPODD analysis to be compared to real world clinical outcomes. Additionally, these human tissues could potentially be developed into PDX models for a more dynamic, *in vivo* model system for

assessment that would pair the *ex vivo* study of the tissues for a full characterization of therapeutic response in clinically relevant tissue samples.

CONCLUSION

Personalized medicine utilizing curated selections of molecularly targeted therapeutics has the potential to revolutionize the paradigm of cancer treatment and drastically improve patient outcomes. The studies described in this thesis have yielded a novel fluorescence imaging platform, TRIPODD, capable of therapeutic response imaging characterizing both drug binding and proteomic response to treatment. Through the innovations developed herein, we anticipate further expansion and application of TRIPODD to a number of tumor contexts to assess novel therapeutic strategies.

REFERENCES

1. Johnson, L.N. Protein kinase inhibitors: contributions from structure to clinical compounds. *Q Rev Biophys* **42**, 1-40 (2009).
2. Bhullar, K.S. et al. Kinase-targeted cancer therapies: progress, challenges and future directions. *Mol Cancer* **17**, 48 (2018).
3. Zhang, J., Yang, P.L. & Gray, N.S. Targeting cancer with small molecule kinase inhibitors. *Nat Rev Cancer* **9**, 28-39 (2009).
4. Roskoski, R. Properties of FDA-approved small molecule protein kinase inhibitors. *Pharmacol Res* **144**, 19-50 (2019).
5. Gerlinger, M. et al. Intratumor heterogeneity and branched evolution revealed by multiregion sequencing. *The New England journal of medicine* **366**, 883-892 (2012).
6. de Bruin, E.C. et al. Spatial and temporal diversity in genomic instability processes defines lung cancer evolution. *Science* **346**, 251-256 (2014).
7. Zhang, J. et al. Intratumor heterogeneity in localized lung adenocarcinomas delineated by multiregion sequencing. *Science* **346**, 256-259 (2014).
8. Piotrowska, Z. et al. Heterogeneity Underlies the Emergence of EGFRT790 Wild-Type Clones Following Treatment of T790M-Positive Cancers with a Third-Generation EGFR Inhibitor. *Cancer Discov* **5**, 713-722 (2015).
9. Sequist, L.V. et al. Genotypic and histological evolution of lung cancers acquiring resistance to EGFR inhibitors. *Science translational medicine* **3**, 75ra26 (2011).
10. Yu, H.A. et al. Analysis of tumor specimens at the time of acquired resistance to EGFR-TKI therapy in 155 patients with EGFR-mutant lung cancers. *Clinical cancer research : an official journal of the American Association for Cancer Research* **19**, 2240-2247 (2013).
11. Stefaniak, J. & Huber, K.V.M. Importance of Quantifying Drug-Target Engagement in Cells. *ACS Medicinal Chemistry Letters* **11**, 403-406 (2020).
12. Cook, D. et al. Lessons learned from the fate of AstraZeneca's drug pipeline: a five-dimensional framework. *Nat Rev Drug Discov* **13**, 419-431 (2014).
13. Bunnage, M.E., Chekler, E.L. & Jones, L.H. Target validation using chemical probes. *Nat Chem Biol* **9**, 195-199 (2013).
14. Ramirez, M. et al. Diverse drug-resistance mechanisms can emerge from drug-tolerant cancer persister cells. *Nature Communications* **7**, 10690 (2016).
15. Mullard, A. Stemming the tide of drug resistance in cancer. *Nat Rev Drug Discov* **19**, 221-223 (2020).
16. La Monica, S. et al. Trastuzumab emtansine delays and overcomes resistance to the third-generation EGFR-TKI osimertinib in NSCLC EGFR mutated cell lines. *J Exp Clin Cancer Res* **36**, 174 (2017).
17. Lim, S.M., Syn, N.L., Cho, B.C. & Soo, R.A. Acquired resistance to EGFR targeted therapy in non-small cell lung cancer: Mechanisms and therapeutic strategies. *Cancer Treat Rev* **65**, 1-10 (2018).
18. Bayat Mokhtari, R. et al. Combination therapy in combating cancer. *Oncotarget* **8**, 38022-38043 (2017).
19. Dubach, J.M. et al. Quantitating drug-target engagement in single cells in vitro and in vivo. *Nat Chem Biol* **13**, 168-173 (2017).

20. Rutkowska, A. et al. A Modular Probe Strategy for Drug Localization, Target Identification and Target Occupancy Measurement on Single Cell Level. *ACS Chem Biol* **11**, 2541-2550 (2016).
21. Arrowsmith, J. & Miller, P. Trial watch: phase II and phase III attrition rates 2011-2012. *Nat Rev Drug Discov* **12**, 569 (2013).
22. Allison, M. Reinventing clinical trials. *Nature biotechnology* **30**, 41-49 (2012).
23. Collisson, E.A., Cho, R.J. & Gray, J.W. What are we learning from the cancer genome? *Nature reviews. Clinical oncology* **9**, 621-630 (2012).
24. Garraway, L.A. & Lander, E.S. Lessons from the cancer genome. *Cell* **153**, 17-37 (2013).
25. Konieczkowski, D.J., Johannessen, C.M. & Garraway, L.A. A Convergence-Based Framework for Cancer Drug Resistance. *Cancer cell* **33**, 801-815 (2018).
26. Yap, T.A., Omlin, A. & de Bono, J.S. Development of therapeutic combinations targeting major cancer signaling pathways. *Journal of clinical oncology : official journal of the American Society of Clinical Oncology* **31**, 1592-1605 (2013).
27. Dewhirst, M.W. & Secomb, T.W. Transport of drugs from blood vessels to tumour tissue. *Nat Rev Cancer* **17**, 738-750 (2017).
28. Budayeva, H.G. & Kirkpatrick, D.S. Monitoring protein communities and their responses to therapeutics. *Nat Rev Drug Discov* (2020).
29. Jackson, H.W. et al. The single-cell pathology landscape of breast cancer. *Nature* **578**, 615-620 (2020).
30. Keren, L. et al. MIBI-TOF: A multiplexed imaging platform relates cellular phenotypes and tissue structure. *Sci Adv* **5**, eaax5851 (2019).
31. Levine, J.H. et al. Data-Driven Phenotypic Dissection of AML Reveals Progenitor-like Cells that Correlate with Prognosis. *Cell* **162**, 184-197 (2015).
32. Wagner, J. et al. A Single-Cell Atlas of the Tumor and Immune Ecosystem of Human Breast Cancer. *Cell* **177**, 1330-1345 e1318 (2019).
33. Miller, M.A. et al. Tumour-associated macrophages act as a slow-release reservoir of nano-therapeutic Pt(IV) pro-drug. *Nat Commun* **6**, 8692 (2015).
34. Gao, M. et al. Chemical genetics strategy identifies an HCV NS5A inhibitor with a potent clinical effect. *Nature* **465**, 96-100 (2010).
35. Honigberg, L.A. et al. The Bruton tyrosine kinase inhibitor PCI-32765 blocks B-cell activation and is efficacious in models of autoimmune disease and B-cell malignancy. *Proceedings of the National Academy of Sciences of the United States of America* **107**, 13075-13080 (2010).
36. Cohen, M.S., Hadjivassiliou, H. & Taunton, J. A clickable inhibitor reveals context-dependent autoactivation of p90 RSK. *Nat Chem Biol* **3**, 156-160 (2007).
37. Stadler, C. et al. Immunofluorescence and fluorescent-protein tagging show high correlation for protein localization in mammalian cells. *Nature methods* **10**, 315-323 (2013).
38. Simon, G.M., Niphakis, M.J. & Cravatt, B.F. Determining target engagement in living systems. *Nat Chem Biol* **9**, 200-205 (2013).
39. Fischman, A.J., Alpert, N.M. & Rubin, R.H. Pharmacokinetic imaging: a noninvasive method for determining drug distribution and action. *Clin Pharmacokinet* **41**, 581-602 (2002).

40. Lomenick, B. et al. Target identification using drug affinity responsive target stability (DARTS). *Proceedings of the National Academy of Sciences of the United States of America* **106**, 21984-21989 (2009).
41. Matthews, P.M., Rabiner, E.A., Passchier, J. & Gunn, R.N. Positron emission tomography molecular imaging for drug development. *Br J Clin Pharmacol* **73**, 175-186 (2012).
42. Martinez Molina, D. et al. Monitoring drug target engagement in cells and tissues using the cellular thermal shift assay. *Science* **341**, 84-87 (2013).
43. Munteanu, B. et al. Label-free in situ monitoring of histone deacetylase drug target engagement by matrix-assisted laser desorption ionization-mass spectrometry biotyping and imaging. *Anal Chem* **86**, 4642-4647 (2014).
44. Grimwood, S. & Hartig, P.R. Target site occupancy: emerging generalizations from clinical and preclinical studies. *Pharmacol Ther* **122**, 281-301 (2009).
45. Schurmann, M., Janning, P., Ziegler, S. & Waldmann, H. Small-Molecule Target Engagement in Cells. *Cell Chem Biol* **23**, 435-441 (2016).
46. Pressman, D., Day, E.D. & Blau, M. The use of paired labeling in the determination of tumor-localizing antibodies. *Cancer research* **17**, 845-850 (1957).
47. Baeten, J., Haller, J., Shih, H. & Ntziachristos, V. In vivo investigation of breast cancer progression by use of an internal control. *Neoplasia* **11**, 220-227 (2009).
48. Liu, J.T. et al. Quantifying cell-surface biomarker expression in thick tissues with ratiometric three-dimensional microscopy. *Biophys J* **96**, 2405-2414 (2009).
49. Pogue, B.W. et al. Imaging targeted-agent binding in vivo with two probes. *J Biomed Opt* **15**, 030513 (2010).
50. Davis, S.C., Gibbs, S.L., Gunn, J.R. & Pogue, B.W. Topical dual-stain difference imaging for rapid intra-operative tumor identification in fresh specimens. *Optics letters* **38**, 5184-5187 (2013).
51. Tichauer, K.M. et al. Tumor endothelial marker imaging in melanomas using dual-tracer fluorescence molecular imaging. *Molecular imaging and biology : MIB : the official publication of the Academy of Molecular Imaging* **16**, 372-382 (2014).
52. Tichauer, K.M. et al. Accounting for pharmacokinetic differences in dual-tracer receptor density imaging. *Phys Med Biol* **59**, 2341-2351 (2014).
53. Tichauer, K.M. et al. Microscopic lymph node tumor burden quantified by macroscopic dual-tracer molecular imaging. *Nature medicine* **20**, 1348-1353 (2014).
54. Barth, C.W., Schaefer, J.M., Rossi, V.M., Davis, S.C. & Gibbs, S.L. Optimizing fresh specimen staining for rapid identification of tumor biomarkers during surgery. *Theranostics* **7**, 4722-4734 (2017).
55. Maniwa, Y. et al. Association of p53 gene mutation and telomerase activity in resectable non-small cell lung cancer. *Chest* **120**, 589-594 (2001).
56. Tichauer, K.M. et al. Improved tumor contrast achieved by single time point dual-reporter fluorescence imaging. *J Biomed Opt* **17**, 066001 (2012).
57. Tichauer, K.M. et al. In vivo quantification of tumor receptor binding potential with dual-reporter molecular imaging. *Molecular imaging and biology : MIB : the official publication of the Academy of Molecular Imaging* **14**, 584-592 (2012).
58. Tichauer, K.M. et al. Dual-tracer background subtraction approach for fluorescent molecular tomography. *J Biomed Opt* **18**, 16003 (2013).

59. Wang, D. et al. Microscopic Delineation of Medulloblastoma Margins in a Transgenic Mouse Model Using a Topically Applied VEGFR-1 Probe. *Transl Oncol* **5**, 408-414 (2012).
60. Meng, B. et al. Topical dual-probe staining using quantum dot-labeled antibodies for identifying tumor biomarkers in fresh specimens. *PLOS ONE* **15**, e0230267 (2020).
61. House, B.J., Schaefer, J.M., Barth, C.W., Davis, S.C. & Gibbs, S.L. Diagnostic Performance of Receptor-Specific Surgical Specimen Staining Correlate with Receptor Expression Level. *Proceedings of SPIE--the International Society for Optical Engineering* **10862** (2019).
62. Folaron, M.R., Strawbridge, R.R., Samkoe, K.S., Gibbs, S.L. & Davis, S.C. Effect of staining temperature on topical dual stain imaging of tissue specimens for tumor identification. *Proceedings of SPIE--the International Society for Optical Engineering* **10862**, 108620L (2019).
63. Schaefer, J.M., Barth, C.W., Davis, S.C. & Gibbs, S.L. Diagnostic performance of receptor-specific surgical specimen staining correlates with receptor expression level. *Journal of biomedical optics* **24**, 1-9 (2019).
64. Dagogo-Jack, I. & Shaw, A.T. Tumour heterogeneity and resistance to cancer therapies. *Nat Rev Clin Oncol* **15**, 81-94 (2018).
65. McGranahan, N. & Swanton, C. Biological and therapeutic impact of intratumor heterogeneity in cancer evolution. *Cancer Cell* **27**, 15-26 (2015).
66. Bedard, P.L., Hansen, A.R., Ratain, M.J. & Siu, L.L. Tumour heterogeneity in the clinic. *Nature* **501**, 355-364 (2013).
67. Goltsev, Y. et al. Deep Profiling of Mouse Splenic Architecture with CODEX Multiplexed Imaging. *Cell* **174**, 968-981 e915 (2018).
68. Lin, J.R. et al. Highly multiplexed immunofluorescence imaging of human tissues and tumors using t-CyCIF and conventional optical microscopes. *Elife* **7** (2018).
69. Lin, J.R., Fallahi-Sichani, M. & Sorger, P.K. Highly multiplexed imaging of single cells using a high-throughput cyclic immunofluorescence method. *Nat Commun* **6**, 8390 (2015).
70. Levenson, R.M., Borowsky, A.D. & Angelo, M. Immunohistochemistry and mass spectrometry for highly multiplexed cellular molecular imaging. *Laboratory investigation; a journal of technical methods and pathology* **95**, 397-405 (2015).
71. Angelo, M. et al. Multiplexed ion beam imaging of human breast tumors. *Nature medicine* **20**, 436-442 (2014).
72. Giesen, C. et al. Highly multiplexed imaging of tumor tissues with subcellular resolution by mass cytometry. *Nature methods* **11**, 417-422 (2014).
73. Gerdes, M.J. et al. Highly multiplexed single-cell analysis of formalin-fixed, paraffin-embedded cancer tissue. *Proceedings of the National Academy of Sciences of the United States of America* **110**, 11982-11987 (2013).
74. Tsujikawa, T. et al. Quantitative Multiplex Immunohistochemistry Reveals Myeloid-Inflamed Tumor-Immune Complexity Associated with Poor Prognosis. *Cell Rep* **19**, 203-217 (2017).
75. Feng, Z. et al. Multispectral Imaging of T and B Cells in Murine Spleen and Tumor. *J Immunol* **196**, 3943-3950 (2016).
76. Lin, J.R., Fallahi-Sichani, M., Chen, J.Y. & Sorger, P.K. Cyclic Immunofluorescence (CycIF), A Highly Multiplexed Method for Single-cell Imaging. *Curr Protoc Chem Biol* **8**, 251-264 (2016).

77. Remark, R. et al. In-depth tissue profiling using multiplexed immunohistochemical consecutive staining on single slide. *Sci Immunol* **1**, aaf6925 (2016).
78. Zrazhevskiy, P. & Gao, X. Quantum dot imaging platform for single-cell molecular profiling. *Nat Commun* **4**, 1619 (2013).
79. Glass, G., Papin, J.A. & Mandell, J.W. SIMPLE: a sequential immunoperoxidase labeling and erasing method. *The journal of histochemistry and cytochemistry : official journal of the Histochemistry Society* **57**, 899-905 (2009).
80. Ullal, A.V. et al. Cancer cell profiling by barcoding allows multiplexed protein analysis in fine-needle aspirates. *Science translational medicine* **6**, 219ra219 (2014).
81. Decalf, J., Albert, M.L. & Ziai, J. New tools for pathology: a user's review of a highly multiplexed method for in situ analysis of protein and RNA expression in tissue. *The Journal of pathology* **247**, 650-661 (2019).
82. Wang, Y. et al. Rapid Sequential in Situ Multiplexing with DNA Exchange Imaging in Neuronal Cells and Tissues. *Nano Lett* **17**, 6131-6139 (2017).
83. Saka, S.K. et al. Immuno-SABER enables highly multiplexed and amplified protein imaging in tissues. *Nature biotechnology* **37**, 1080-1090 (2019).
84. McMahon, N.P. et al. Oligonucleotide conjugated antibodies permit highly multiplexed immunofluorescence for future use in clinical histopathology. *Journal of Biomedical Optics* **25**, 056004 (2020).
85. Ikeda, M., Ochibe, T. & Tohkin, M. Possible Causes of Failing to Meet Primary Endpoints: A Systematic Review of Randomized Controlled Phase 3 Clinical Trials in Patients With Non-Small Cell Lung Cancer. *Ther Innov Regul Sci* **53**, 324-331 (2019).
86. Fernandez-Lopez, C., Calleja-Hernandez, M.A., Balbino, J.E., Cabeza-Barrera, J. & Exposito-Hernandez, J. Trends in endpoint selection and result interpretation in advanced non-small cell lung cancer clinical trials published between 2000 and 2012: A retrospective cohort study. *Thorac Cancer* **10**, 904-908 (2019).
87. Fedele, M., Gualillo, O. & Vecchione, A. Animal Models of Human Pathology 2014. *Biomed Res Int* **2015**, 721348 (2015).
88. Bray, F. et al. Global cancer statistics 2018: GLOBOCAN estimates of incidence and mortality worldwide for 36 cancers in 185 countries. **68**, 394-424 (2018).
89. Arbour, K.C. & Riely, G.J. Systemic Therapy for Locally Advanced and Metastatic Non-Small Cell Lung Cancer: A Review. *JAMA* **322**, 764-774 (2019).
90. Recondo, G., Facchinetti, F., Olaussen, K.A., Besse, B. & Friboulet, L. Making the first move in EGFR-driven or ALK-driven NSCLC: first-generation or next-generation TKI? *Nat Rev Clin Oncol* **15**, 694-708 (2018).
91. Maemondo, M. et al. Gefitinib or chemotherapy for non-small-cell lung cancer with mutated EGFR. *N Engl J Med* **362**, 2380-2388 (2010).
92. Zhou, C. et al. Erlotinib versus chemotherapy as first-line treatment for patients with advanced EGFR mutation-positive non-small-cell lung cancer (OPTIMAL, CTONG-0802): a multicentre, open-label, randomised, phase 3 study. *Lancet Oncol* **12**, 735-742 (2011).
93. Sequist, L.V. et al. Phase III study of afatinib or cisplatin plus pemetrexed in patients with metastatic lung adenocarcinoma with EGFR mutations. *J Clin Oncol* **31**, 3327-3334 (2013).

94. Masters, G.A. et al. Systemic Therapy for Stage IV Non-Small-Cell Lung Cancer: American Society of Clinical Oncology Clinical Practice Guideline Update. *J Clin Oncol* **33**, 3488-3515 (2015).
95. Cross, D.A. et al. AZD9291, an irreversible EGFR TKI, overcomes T790M-mediated resistance to EGFR inhibitors in lung cancer. *Cancer Discov* **4**, 1046-1061 (2014).
96. Soria, J.C. et al. Osimertinib in Untreated EGFR-Mutated Advanced Non-Small-Cell Lung Cancer. *N Engl J Med* **378**, 113-125 (2018).
97. Facchinetti, F., Proto, C., Minari, R., Garassino, M. & Tiseo, M. Mechanisms of Resistance to Target Therapies in Non-small Cell Lung Cancer. *Handb Exp Pharmacol* **249**, 63-89 (2018).
98. Tredan, O., Galmarini, C.M., Patel, K. & Tannock, I.F. Drug resistance and the solid tumor microenvironment. *J Natl Cancer Inst* **99**, 1441-1454 (2007).
99. Vyse, S., Howitt, A. & Huang, P.H. Exploiting Synthetic Lethality and Network Biology to Overcome EGFR Inhibitor Resistance in Lung Cancer. *J Mol Biol* **429**, 1767-1786 (2017).
100. Lopes, N. et al. Digital image analysis of multiplex fluorescence IHC in colorectal cancer recognizes the prognostic value of CDX2 and its negative correlation with SOX2. *Laboratory investigation; a journal of technical methods and pathology* **100**, 120-134 (2020).
101. Truitt, M.L. & Ruggero, D. New frontiers in translational control of the cancer genome. *Nat Rev Cancer* **16**, 288-304 (2016).
102. Brockman, R.W. Mechanisms of Resistance to Anticancer Agents. *Advances in cancer research* **7**, 129-234 (1963).
103. Hanahan, D. & Weinberg, R.A. Hallmarks of cancer: the next generation. *Cell* **144**, 646-674 (2011).
104. Kalluri, R. The biology and function of fibroblasts in cancer. *Nat Rev Cancer* **16**, 582-598 (2016).
105. Seashore-Ludlow, B. et al. Harnessing Connectivity in a Large-Scale Small-Molecule Sensitivity Dataset. *Cancer Discov* **5**, 1210-1223 (2015).
106. Marcotte, R. et al. Functional Genomic Landscape of Human Breast Cancer Drivers, Vulnerabilities, and Resistance. *Cell* **164**, 293-309 (2016).
107. Li, J. et al. Characterization of Human Cancer Cell Lines by Reverse-phase Protein Arrays. *Cancer cell* **31**, 225-239 (2017).
108. Roma-Rodrigues, C., Mendes, R., Baptista, P.V. & Fernandes, A.R. Targeting Tumor Microenvironment for Cancer Therapy. *Int J Mol Sci* **20** (2019).
109. Galluzzi, L. et al. Molecular mechanisms of cell death: recommendations of the Nomenclature Committee on Cell Death 2018. *Cell Death Differ* **25**, 486-541 (2018).
110. Stack, E.C., Wang, C., Roman, K.A. & Hoyt, C.C. Multiplexed immunohistochemistry, imaging, and quantitation: a review, with an assessment of Tyramide signal amplification, multispectral imaging and multiplex analysis. *Methods* **70**, 46-58 (2014).
111. Zrazhevskiy, P., True, L.D. & Gao, X. Multicolor multicycle molecular profiling with quantum dots for single-cell analysis. *Nature protocols* **8**, 1852-1869 (2013).
112. McMahon, N.P. et al. Oligonucleotide conjugated antibodies permit highly multiplexed immunofluorescence for future use in clinical histopathology. *J Biomed Opt* **25**, 1-18 (2020).

113. Bragg, P.D. & Hou, C. Subunit composition, function, and spatial arrangement in the Ca2+-and Mg2+-activated adenosine triphosphatases of Escherichia coli and Salmonella typhimurium. *Arch Biochem Biophys* **167**, 311-321 (1975).
114. Gong, H. et al. Simple Method To Prepare Oligonucleotide-Conjugated Antibodies and Its Application in Multiplex Protein Detection in Single Cells. *Bioconjug Chem* **27**, 217-225 (2016).
115. Wong, I.Y. & Melosh, N.A. Directed Hybridization and Melting of DNA Linkers using Counterion-Screened Electric Fields. *Nano Letters* **9**, 3521-3526 (2009).
116. Ravan, H., Kashanian, S., Sanadgol, N., Badoei-Dalfard, A. & Karami, Z. Strategies for optimizing DNA hybridization on surfaces. *Anal Biochem* **444**, 41-46 (2014).
117. Noguera, D.R., Wright, E.S., Camejo, P. & Yilmaz, L.S. Mathematical tools to optimize the design of oligonucleotide probes and primers. *Applied Microbiology and Biotechnology* **98**, 9595-9608 (2014).
118. Owczarzy, R. et al. Effects of Sodium Ions on DNA Duplex Oligomers: Improved Predictions of Melting Temperatures. *Biochemistry* **43**, 3537-3554 (2004).
119. Marmur, J. & Doty, P. Determination of the base composition of deoxyribonucleic acid from its thermal denaturation temperature. *J Mol Biol* **5**, 109-118 (1962).
120. Wallace, R.B. et al. Hybridization of synthetic oligodeoxyribonucleotides to phi chi 174 DNA: the effect of single base pair mismatch. *Nucleic Acids Res* **6**, 3543-3557 (1979).
121. Probst, C.E., Zrazhevskiy, P. & Gao, X. Rapid multitarget immunomagnetic separation through programmable DNA linker displacement. *J Am Chem Soc* **133**, 17126-17129 (2011).
122. Jungmann, R. et al. Multiplexed 3D cellular super-resolution imaging with DNA-PAINT and Exchange-PAINT. *Nature methods* **11**, 313-318 (2014).
123. Eng, J. et al. Cyclic Multiplexed-Immunofluorescence (cmIF), a Highly Multiplexed Method for Single-Cell Analysis. *Methods in molecular biology* **2055**, 521-562 (2020).
124. Toki, M.I. et al. High-Plex Predictive Marker Discovery for Melanoma Immunotherapy-Treated Patients Using Digital Spatial Profiling. *Clinical cancer research : an official journal of the American Association for Cancer Research* **25**, 5503-5512 (2019).
125. Ruffell, B. & Coussens, L.M. Macrophages and therapeutic resistance in cancer. *Cancer Cell* **27**, 462-472 (2015).
126. Cogdill, A.P., Andrews, M.C. & Wargo, J.A. Hallmarks of response to immune checkpoint blockade. *Br J Cancer* **117**, 1-7 (2017).
127. Tsurui, H. et al. Seven-color fluorescence imaging of tissue samples based on Fourier spectroscopy and singular value decomposition. *The journal of histochemistry and cytochemistry : official journal of the Histochemistry Society* **48**, 653-662 (2000).
128. Lin, J.-R., Fallahi-Sichani, M. & Sorger, P.K. Highly multiplexed imaging of single cells using a high-throughput cyclic immunofluorescence method. *Nature Communications* **6** (2015).
129. Zrazhevskiy, P., True, L.D. & Gao, X. Multicolor multicycle molecular profiling with quantum dots for single-cell analysis. *Nature Protocols* **8**, 1852-1869 (2013).
130. Schubert, W. et al. Imaging cycler microscopy. *Proceedings of the National Academy of Sciences of the United States of America* **111**, E215 (2014).
131. Berg, S. et al. ilastik: interactive machine learning for (bio)image analysis. *Nature methods* **16**, 1226-1232 (2019).

132. Schapiro, D. et al. histoCAT: analysis of cell phenotypes and interactions in multiplex image cytometry data. *Nature methods* **14**, 873-876 (2017).
133. Hernandez, S. et al. Multiplex Immunofluorescence Tyramide Signal Amplification for Immune Cell Profiling of Paraffin-Embedded Tumor Tissues. *Front Mol Biosci* **8**, 667067 (2021).
134. Gorris, M.A.J. et al. Eight-Color Multiplex Immunohistochemistry for Simultaneous Detection of Multiple Immune Checkpoint Molecules within the Tumor Microenvironment. *J Immunol* **200**, 347-354 (2018).
135. Lu, S. et al. Comparison of Biomarker Modalities for Predicting Response to PD-1/PD-L1 Checkpoint Blockade: A Systematic Review and Meta-analysis. *JAMA Oncol* **5**, 1195-1204 (2019).
136. Barua, S. et al. A Functional Spatial Analysis Platform for Discovery of Immunological Interactions Predictive of Low-Grade to High-Grade Transition of Pancreatic Intraductal Papillary Mucinous Neoplasms. *Cancer Inform* **17**, 1176935118782880 (2018).
137. Levin, M., Kron, S.J., Schwartz, D. & Snyder, H. in Clinical Research (Excluding Clinical Trials) 3949-3949 (2016).
138. Parra, E.R. et al. Validation of multiplex immunofluorescence panels using multispectral microscopy for immune-profiling of formalin-fixed and paraffin-embedded human tumor tissues. *Scientific reports* **7**, 13380 (2017).
139. Dirks, R.M. & Pierce, N.A. Triggered amplification by hybridization chain reaction. *Proceedings of the National Academy of Sciences of the United States of America* **101**, 15275-15278 (2004).
140. Choi, H.M. et al. Programmable in situ amplification for multiplexed imaging of mRNA expression. *Nature biotechnology* **28**, 1208-1212 (2010).
141. Choi, H.M. et al. Mapping a multiplexed zoo of mRNA expression. *Development* **143**, 3632-3637 (2016).
142. Benz, C.C. et al. Estrogen-dependent, tamoxifen-resistant tumorigenic growth of MCF-7 cells transfected with HER2/neu. *Breast Cancer Res Treat* **24**, 85-95 (1992).
143. McMahon, N.P. et al. TRIPODD: a Novel Fluorescence Imaging Platform for In Situ Quantification of Drug Distribution and Therapeutic Response. *Molecular imaging and biology : MIB : the official publication of the Academy of Molecular Imaging* (2021).
144. Lorenz, T.C. Polymerase chain reaction: basic protocol plus troubleshooting and optimization strategies. *J Vis Exp*, e3998 (2012).
145. Farahani, N., Behmanesh, M. & Ranjbar, B. Evaluation of Rationally Designed Label-free Stem-loop DNA Probe Opening in the Presence of miR-21 by Circular Dichroism and Fluorescence Techniques. *Scientific reports* **10**, 4018 (2020).
146. Lu, Y. et al. Using reverse-phase protein arrays as pharmacodynamic assays for functional proteomics, biomarker discovery, and drug development in cancer. *Semin Oncol* **43**, 476-483 (2016).
147. McAllister, S.S. & Weinberg, R.A. Tumor-host interactions: a far-reaching relationship. *J Clin Oncol* **28**, 4022-4028 (2010).
148. Marusyk, A., Almendro, V. & Polyak, K. Intra-tumour heterogeneity: a looking glass for cancer? *Nat Rev Cancer* **12**, 323-334 (2012).
149. Keren, L. et al. A Structured Tumor-Immune Microenvironment in Triple Negative Breast Cancer Revealed by Multiplexed Ion Beam Imaging. *Cell* **174**, 1373-1387 e1319 (2018).

150. McMahon, N.P. et al. Fluorescent Imaging for In Situ Measurement of Drug Target Engagement and Cell Signaling Pathways. *Proc SPIE Int Soc Opt Eng* **11219** (2020).
151. Solanki, A. et al. Intracellular paired agent imaging enables improved evaluation of tyrosine kinase inhibitor target engagement. *Proc SPIE Int Soc Opt Eng* **11219** (2020).
152. Chang, Y.H. et al. in 2017 39th Annual International Conference of the IEEE Engineering in Medicine and Biology Society (EMBC) 672-675 (2017).
153. Li, H. et al. Addition of bevacizumab enhances antitumor activity of erlotinib against non-small cell lung cancer xenografts depending on VEGF expression. *Cancer Chemother Pharmacol* **74**, 1297-1305 (2014).
154. Yu, H.A. et al. Effect of Osimertinib and Bevacizumab on Progression-Free Survival for Patients With Metastatic EGFR-Mutant Lung Cancers: A Phase 1/2 Single-Group Open-Label Trial. *JAMA Oncol* (2020).
155. Cannon, T.M., Shah, A.T. & Skala, M.C. Autofluorescence imaging captures heterogeneous drug response differences between 2D and 3D breast cancer cultures. *Biomed Opt Express* **8**, 1911-1925 (2017).
156. Walsh, A.J. et al. Quantitative optical imaging of primary tumor organoid metabolism predicts drug response in breast cancer. *Cancer research* **74**, 5184-5194 (2014).
157. Dudenkova, V.V. et al. Examination of Collagen Structure and State by the Second Harmonic Generation Microscopy. *Biochemistry (Mosc)* **84**, S89-S107 (2019).
158. Burke, R.M., Madden, K.S., Perry, S.W., Zettel, M.L. & Brown, E.B., 3rd Tumor-associated macrophages and stromal TNF-alpha regulate collagen structure in a breast tumor model as visualized by second harmonic generation. *J Biomed Opt* **18**, 86003 (2013).
159. Lovly, C.M. & Shaw, A.T. Molecular pathways: resistance to kinase inhibitors and implications for therapeutic strategies. *Clin Cancer Res* **20**, 2249-2256 (2014).
160. Higgins, B. et al. Antitumor activity of erlotinib (OSI-774, Tarceva) alone or in combination in human non-small cell lung cancer tumor xenograft models. *Anticancer Drugs* **15**, 503-512 (2004).
161. Abraham, J. et al. Preclinical testing of erlotinib in a transgenic alveolar rhabdomyosarcoma mouse model. *Sarcoma* **2011**, 130484 (2011).
162. de Wit, M. et al. Mutation and drug-specific intracellular accumulation of EGFR predict clinical responses to tyrosine kinase inhibitors. *EBioMedicine* **56**, 102796 (2020).
163. Wood, E.R. et al. A unique structure for epidermal growth factor receptor bound to GW572016 (Lapatinib): relationships among protein conformation, inhibitor off-rate, and receptor activity in tumor cells. *Cancer research* **64**, 6652-6659 (2004).
164. Park, J.H., Liu, Y., Lemmon, M.A. & Radhakrishnan, R. Erlotinib binds both inactive and active conformations of the EGFR tyrosine kinase domain. *Biochem J* **448**, 417-423 (2012).
165. Li, H.-Q. et al. A sensitive LC-MS/MS method to determine the concentrations of erlotinib and its active metabolite OSI-420 in BALB/c nude mice plasma simultaneously and its application to a pharmacokinetic study. *Journal of Chinese Pharmaceutical Sciences* **21**, 296-303 (2012).
166. Barkovich, K.J. et al. Kinetics of inhibitor cycling underlie therapeutic disparities between EGFR-driven lung and brain cancers. *Cancer Discov* **2**, 450-457 (2012).
167. Rothenberg, S.M. et al. Inhibition of mutant EGFR in lung cancer cells triggers SOX2-FOXO6-dependent survival pathways. *Elife* **4** (2015).

168. Hwang, I. et al. Tumor-associated macrophage, angiogenesis and lymphangiogenesis markers predict prognosis of non-small cell lung cancer patients. *J Transl Med* **18**, 443 (2020).
169. Moya-Horno, I., Viteri, S., Karachaliou, N. & Rosell, R. Combination of immunotherapy with targeted therapies in advanced non-small cell lung cancer (NSCLC). *Ther Adv Med Oncol* **10**, 1758834017745012-1758834017745012 (2018).
170. Naumov, G.N. et al. Combined Vascular Endothelial Growth Factor Receptor and Epidermal Growth Factor Receptor (EGFR) Blockade Inhibits Tumor Growth in Xenograft Models of EGFR Inhibitor Resistance. *Clinical Cancer Research* **15**, 3484-3494 (2009).
171. Li, H. et al. Addition of bevacizumab enhances antitumor activity of erlotinib against non-small cell lung cancer xenografts depending on VEGF expression. *Cancer Chemother Pharmacol* **74**, 1297-1305 (2014).
172. Mathijssen, R.H.J., Sparreboom, A. & Verweij, J. Determining the optimal dose in the development of anticancer agents. *Nature Reviews Clinical Oncology* **11**, 272-281 (2014).
173. Lane, R.S. et al. IFNgamma-activated dermal lymphatic vessels inhibit cytotoxic T cells in melanoma and inflamed skin. *J Exp Med* **215**, 3057-3074 (2018).